Magnetic and Quadrupolar Ordering in (U,Np)Pd_3

Helen Claire Walker

A Thesis presented for the degree of
Doctor of Philosophy

Condensed Matter and Materials Physics
Department of Physics and Astronomy
University College London
England

November 2006

Dedicated to

Duncan

Magnetic and Quadrupolar Ordering in $(U,Np)Pd_3$

Helen Claire Walker

Submitted for the degree of Doctor of Philosophy
November 2006

Abstract

This thesis furthers our understanding of the canonical quadrupolar system UPd_3, which is unusual and interesting for several reasons. It is the only known localised uranium intermetallic, it exhibits long range quadrupolar order, and it has four phase transitions below 8 K attributed to a succession of different quadrupolar orderings of the $5f^2$ uranium electrons. The two strategies used in this work are: probing the quadrupolar order directly using X-ray resonant scattering, to determine the order parameters, and investigating how the quadrupolar order is perturbed by the substitution of neptunium for uranium through bulk thermodynamic measurements.

This is the first time that the symmetry of the quadrupolar order in UPd_3 has been examined directly, making use of the unique properties of X-ray resonant scattering, which couples directly to the quadrupoles as opposed to neutrons which only couple to the induced lattice distortions. We have been able to ascertain, through a detailed comparison between calculations and experimental data, that the $T_0 = 7.8$ K transition is to a quadrupolar ordered phase described by the anti-phase stacking of Q_{zx} quadrupoles along the $c-$axis. This, in combination with new high precision low temperature heat capacity measurements, has enabled us to place constraints on the quadrupolar operators within the crystal field model. We have also investigated the order-

ing in two of the lower temperature phases, and shown that the scattering corresponds to a more complex model.

We have also investigated $NpPd_3$ by measurements of the electrical resistivity, magnetic susceptibility and heat capacity, and demonstrated that it undergoes two phase transitions, one antiferromagnetic and the other possibly quadrupolar. In the dilute neptunium region of $(U,Np)Pd_3$ we have followed the lowering of the transition temperatures with increasing neptunium content, and shown that several observed features of $(U_{0.95}Np_{0.05})Pd_3$ are consistent with proximity to a quantum critical point, which we have associated with the suppression of a quadrupolar transition to zero temperature. This preliminary work has indicated that there is considerably more scope for investigating the $(U_{1-x}Np_x)Pd_3$ system to identify a new type of quantum critical point associated with the "squeezing out" of quadrupolar order.

Declaration

I, Helen Claire Walker, confirm that the work presented in this thesis is my own. Where information has been derived from other sources, I confirm that this has been indicated in the thesis. The work in this thesis is based on research carried out at the Condensed Matter and Materials Physics Group, the Department of Physics and Astronomy, University College London, England. No part of this thesis has been submitted elsewhere for any other degree or qualification.

Acknowledgements

I would like to thank my supervisors Prof. K. A. McEwen and Prof. D. M. McMorrow for all their assistance and inspiration, I am deeply indebted to them both. I would also like to thank everyone at the Institute for Transuranium Elements in Karlsruhe, in particular Dr J.-C. Griveau, Dr E. Colineau and Dr F. Wastin, for making me feel so welcome and introducing me to the world of Neptunium. Stuart Wilkins at the ESRF deserves special mention for putting up with my computing ineptitude and staying to help me on the beamline until hours which I never knew prior to my PhD existed, as well as being the most helpful local contact any visiting experimenter could hope for.

I am also grateful to everyone in CMMP who helped me feel at home in the big city, including Arthur Lovell, Ross Springell, Chris Howard, Mark Ellerby and Duc Le.

I thank my family: my father, who introduced me to science, my mother, who supported me even though I turned away from history, and my sister, who helped me to remember about the real world, and finally, of course, Duncan. Thank you for always welcoming me home after experiments and putting up with me over the course of this thesis.

Contents

List of Figures

List of Tables

Chapter 1

Introduction

In the past couple of decades there has been considerable interest in the orbital ordering of *d* and *f* electron systems [1 11]. The highly degenerate *f*-electron shells in actinide and rare earth systems provide a wealth of local degrees of freedom: dipolar(magnetic), quadrupolar, octupolar etc. In a localised *f*-electron system, such as UPd_3, the quadrupolar degree of freedom becomes a potential order parameter, which can lead to interesting and complex phase diagrams. Whilst, historically, the order associated with magnetic dipole moments has been studied extensively, more recently the importance of electric quadrupoles in magnetic materials has been recognized [12]. In classical electrodynamics the multipole expansion suggests that the interaction between higher order multipoles is seemingly much weaker than between dipoles. However, the interaction between multipoles is quantum mechanical in origin, and dipolar and quadrupolar interactions may be equally strong. More recently, quadrupolar order has been associated with new and interesting behaviour, such as the novel heavy Fermion state in $PrFe_4P_{12}$ [7], and the exotic superconductivity in $PrOs_4Sb_{12}$, which may be mediated by quadrupolar fluctuations [8].

In this thesis I have attempted to develop the understanding of quadrupolar interactions through the study of the canonical quadrupolar system UPd_3, its order and how it evolves with the substitution of neptunium for uranium. I present extensive X-ray Resonant Scattering studies, which have determined the order in the first quadrupolar phase, and macroscopic polycrystalline magnetisation and transport measurements of the mixed actinide system $(U,Np)Pd_3$ and $NpPd_3$.

Chapter 2

Background

2.1 Actinides

The actinide metals from actinium to nobelium, see Table 2.1 are amongst the most complex and unusual series in the periodic table, displaying properties such as magnetism, superconductivity, low melting points and numerous structural phase transitions see Figure 2.1, but due to the difficulty in handling these materials they are the least well studied. Only actinium, thorium and uranium occur naturally in the earth's crust. The spatial extent of the $5f$ electrons and their tendency to interact with ligand site electrons make the actinides the most difficult series to understand, whilst presenting opportunities for interesting behaviour.

The lanthanides are the first series in the Periodic Table to have f electrons, so that the $4f$ electron wavefunctions are orthogonal to all previous wavefunctions. Therefore the $4f$ radius can be very small while still satisfying the Pauli Principle, which often results in the electrons being localised. The physics and chemistry of the actinides differ from the lanthanides due to the extended

Table 2.1: The elements in the actinide series, the half-lives of the predominant isotopes (taken from Wikipedia) and significant transition temperatures. (T_{SC} superconducting transition temperature, T_C Curie temperature and T_N Néel temperature)

Atomic Number	Symbol	Isotope half-life	T^* / K
89	Ac	^{227}Ac 21.8 years	
90	Th	^{232}Th 1.41 × 10^{10} years	$T_{SC} = 1.4$
91	Pa	^{231}Pa 32760 years	$T_{SC} = 0.4$
92	U	^{238}U 4.5 × 10^9 years	$T_{SC} = 0.9$
		^{235}U 7 × 10^8 years	
93	Np	^{237}Np 2.14 × 10^6 years	
94	Pu	^{239}Pu 24100 years	
95	Am	^{243}Am 7370 years	$T_{SC} = 0.8$
96	Cm	^{247}Cm 1.56 × 10^7 years	$T_N = 52$
97	Bk	^{247}Bk 1380 years	$T_N = 25$
98	Cf	^{251}Cf 900 years	$T_C = 52$
99	Es	^{252}Es 472 days	
100	Fm	^{257}Fm 100 days	
101	Md	^{258}Md 52 days	
102	No	^{259}No 1 hour	

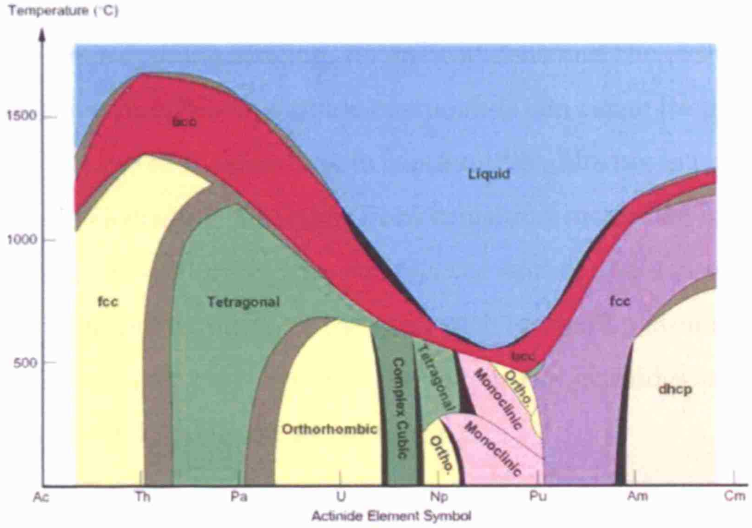

Figure 2.1: The experimentally determined connected binary phase diagram of adjacent actinide elements, an adapted version of the original in [13] taken from [14].

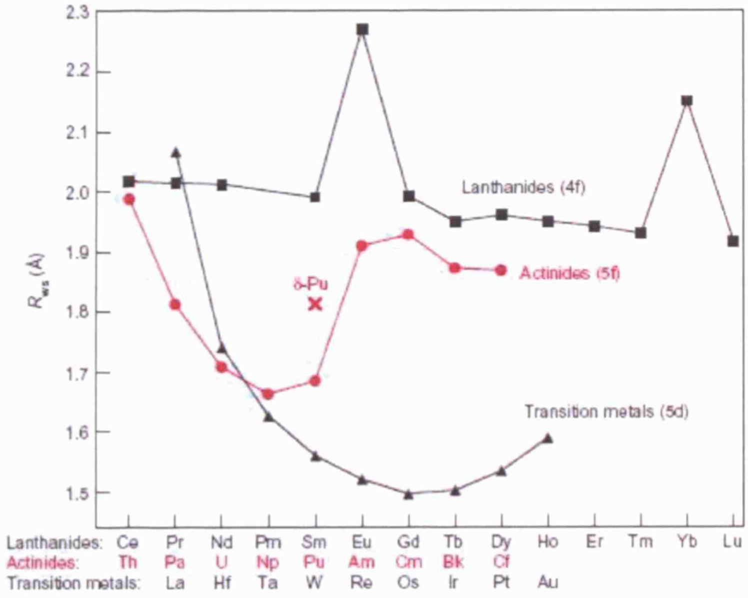

Figure 2.2: The experimental Wigner-Seitz radius of the Actinides compared with the Lanthanides and Transition Metals, showing that the light Actinide radii decrease with increasing atomic number, similar behaviour to that shown by the Transition Metal radii, but in contrast to the Lanthanides, where the radii remain approximately constant [15].

nature of the $5f$ wavefunctions. As a result, depending on the actinide ion involved, the inter-actinide spacing, its environment and the electron-electron correlations, the properties of actinide compounds can range from itinerant, as in transition metals, to localised, as in lanthanides. Moving across the series, the similarity in electron localisation from transition metal-like to lanthanide-like shows up in physical properties such as the atomic radius, see Figure 2.2. The similarities in the variation of the radii with increasing atomic number for the light actinides and transition metals, led to the actinides initially being assigned as a new 6d transition metal series.

Close to the Mott transition between itinerant and localised electrons, the cross-over in electronic properties may lead to new and unconventional behaviour. Actinide compounds are unique materials, many showing an interplay between magnetism and superconductivity, which is of interest to the wider condensed matter physics community.

2.2 Multipolar Order

There is currently much interest in the interplay between spin and orbital couplings leading to a range of interesting phenomena [16], such as Orbital Ordering, as seen in Transition Metal Oxides [17], Jahn-Teller distortions [18], as in Rare Earth spinels, and Quadrupolar Ordering, as seen in CeB_6 [19] and UPd_3. The study of multipolar interactions concerning the unfilled f-electron shell in Rare Earth and Actinide intermetallics involves the complex problems of pair interactions between different ions and the effect of the crystal field acting on an f ion. The quadrupolar pair interaction is mediated by conduction electrons, via an indirect mechanism like the RKKY interaction, and by phonons, in the case when quadrupoles are coupled strongly to the lattice.

When this interaction dominates the magneto-elastic coupling, quadrupolar ordering may occur. Depending on the sign of the pair interaction the ordering will either be ferro- or antiferroquadrupolar [12].

Quadrupolar moments are expressed as average values of the components Q_{ij} of the electric quadrupole tensor Q. They express the deviation of the $5f$ charge clouds from a perfectly spherical distribution:

$$Q_{ij} = \int \left(3r_i r_j - r^2\delta_{ij}\right) \rho(\mathbf{r})\mathrm{d}\mathbf{r}, \tag{2.1}$$

and, using the Wigner-Eckart theorem, can be seen to measure the correlation between components $\mathbf{J}_i$ and $\mathbf{J}_j$ of the total angular momentum, such that:

$$Q(3z^2 - r^2) \equiv Q_{zz} \rightarrow 3J_z^2 - J(J+1), \tag{2.2}$$

and

$$Q_{\mathrm{xy}} \rightarrow \frac{1}{2}\overline{J_x J_y} = \frac{1}{2}(J_x J_y + J_y J_x), \tag{2.3}$$

where the "overline" symmetrizes the non-commuting operators. Unlike dipole moments there is no net directionality. The quadrupole moment couples to the gradient of the electric field, as can be seen from the multipole expansion of the electrostatic energy:

$$\begin{aligned} W_E &= \int d^3x\rho(\mathbf{x})\Phi(\mathbf{x}) \\ &= q\Phi(0) - \mathbf{d}\cdot\mathbf{E} - \frac{1}{6}\sum_{ij} Q_{ij}(\delta E_i/\delta x_j)(0) + \ldots. \end{aligned} \tag{2.4}$$

where the charge q couples to the electrostatic potential and the dipole $\mathbf{d}$ to the electric field $\mathbf{E} = -\nabla\boldsymbol{\Phi}$. The wave functions of quadrupoles look like those of atomic d-orbitals, but with positive and negative lobes, and are schematically represented by ellipses, which are the simplest form reflecting the symmetry.

The different quadrupolar order parameters induce different changes in the charge distribution. The $\langle Q_{x^2-y^2}\rangle$ order parameter changes the charge

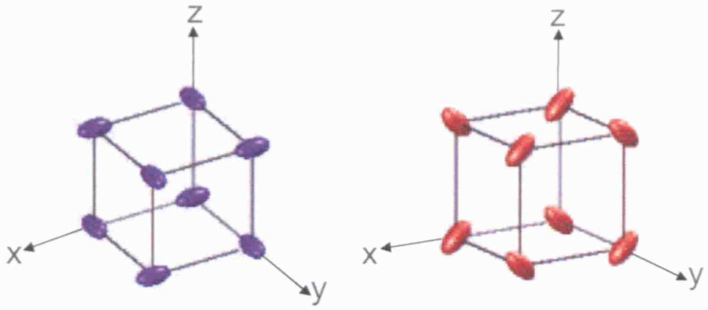

Figure 2.3: Schematic representation of $\mathcal{Q}_{x^2-y^2}$ and $\mathcal{Q}_{zx}$ on a cubic lattice.

distribution on the uranium ions from being spheroidal to ellipsoidal, and $\langle \mathcal{Q}_{zx} \rangle$ results in a rotation of this distribution about an axis in the basal plane, see Figure 2.3.

A two ion coupling between quadrupoles can be written analogous to that of the Heisenberg coupling of two magnetic dipoles [20]:

$$\mathcal{H}_{EX} = \sum_{ij} \mathcal{J}_{ij} \mathbf{J}_i \cdot \mathbf{J}_j, \tag{2.5}$$

where $\mathcal{J}_{ij}$ is the exchange constant between the ith and jth dipoles, replacing the spins with quadrupole moments. A generalised interaction Hamiltonian between lattice sites i and j can then be written as:

$$\mathcal{H}_{ij} = \sum_{k,l} \mathcal{J}_{ij}^{kl}(m) J_i^k J_j^l + \sum_{k,l} \mathcal{J}_{ij}^{kl}(Q) Q_i^k Q_j^l + \sum_{k,l} \mathcal{J}_{ij}^{kl}(O) O_i^k O_j^l + \ldots, \tag{2.6}$$

where J_i^k, Q_i^k and O_i^k are the dipolar, quadrupolar and octupolar moments at site i, and $\mathcal{J}_{ij}^{kl}(m)$, $\mathcal{J}_{ij}^{kl}(Q)$ and $\mathcal{J}_{ij}^{kl}(O)$ are the magnetic, quadrupolar and octupolar coupling constants. The lattice Hamiltonian is then given by the sum over all the pair interaction Hamiltonians, and is invariant under all symmetry operations of the lattice.

When symmetry conditions are taken into account, the quadrupolar term in the Hamiltonian can be written in the Molecular Field Approximation in terms

Table 2.2: Expression of the quadrupolar operators

Operator	Expression
$\mathcal{O}_2^0$	$3J_z^2 - J(J+1)$
$\mathcal{O}_2^2$	$J_x^2 - J_y^2 = \frac{1}{2}\left(J_+^2 + J_-^2\right)$
P_{xy}	$\frac{1}{2}\left(J_xJ_y + J_yJ_x\right) = \frac{-i}{4}\left(J_+^2 - J_-^2\right)$
P_{yz}	$\frac{1}{2}\left(J_yJ_z + J_zJ_y\right)$
$P_{zx} \equiv \mathcal{O}_2^1$	$\frac{1}{2}\left(J_zJ_x + J_xJ_z\right)$

of the quadrupolar Stevens operators and the two-ion quadrupolar parameters corresponding to the two linear combinations of quadrupolar operators, which are associated with the anisotropic normal strain modes. Hence, for example, for cubic symmetry the Hamiltonian is given by:

$$\mathcal{H}_Q = -K^{\gamma}\left(\langle\mathcal{O}_2^0\rangle\mathcal{O}_2^0 + 3\langle\mathcal{O}_2^2\rangle\mathcal{O}_2^2\right) - K^{\epsilon}\left(\langle P_{xy}\rangle P_{xy} + \langle P_{yz}\rangle P_{yz} + \langle P_{zx}\rangle P_{zx}\right), \tag{2.7}$$

where the quadrupolar operators are given in Table 2.2 and K^{γ} and K^{ϵ} are the two-ion quadrupolar parameters for tetragonal (γ) and trigonal (ϵ) strain modes [12].

Higher order multipolar terms are not necessarily insignificant and have been suggested as the primary order parameters in systems with "hidden order", such as $\mathrm{URu_2Si_2}$ and $\mathrm{NpO_2}$, but are little discussed. If the multipoles are described according to 2^n, where $n = 1$ for magnetic dipoles and $n = 2$ for electric quadrupoles, the higher order terms are $n = 3$: magnetic octupole, $n = 4$: electric hexadecapole, $n = 5$: magnetic triakontadipole, $n = 6$: electric hexacontatetrapole etc. In general, n odd terms break time reversal symmetry, while n even terms preserve time reversal symmetry. Octupoles are named after the eight magnetic poles, as shown in Figure 2.4, where there are four current eddies belonging to the magnetic field lines entering and four belonging to the lines leaving the surface, and do not have time-reversal symmetry. The

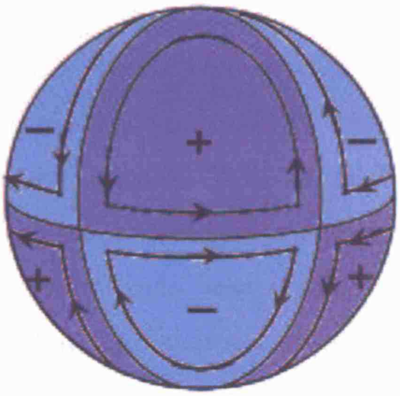

Figure 2.4: Diagrammatic representation of a free-ion T_{xyz} octupole in the $l = 2$ Hilbert space, showing the current eddies about the magnetic field lines entering and leaving the surface.

octupole in Figure 2.4 is in the $l = 2$ Hilbert space, and differs to an $l = 4$ T_{xyz} octupole, which displays more complex current eddies, with four minor eddies in a petal arrangement within the one major eddy in each octant [21]. The overall vortex pattern is the same, but the central eddy of the sub-eddies in each octant rotates counter to the others, so that the field changes direction within each octant. The magnetic fields of octupolar currents are weaker in $l = 4$ than $l = 2$ states. Hexadecapoles are time-reversal invariant and the eigenstates are similar to quadrupolar eigenstates, but with a higher number of positive and negative lobes.

Whilst octupolar order has been suggested as the primary order parameter in NpO_2 [22], which is consistent with the absence of observed magnetic order, more recent calculations suggest that the actual primary order parameter is triakontadipolar [23]. Hexadecapolar order has been proposed for the skutterudite $PrRu_4P_{12}$ [24], and a combination of higher multipolar orders has been suggested for URu_2Si_2 [21].

2.3 UPd$_3$

UPd$_3$ is a particularly interesting and unusual compound as it displays four phase transitions at low temperatures: $T_0 = 7.8$ K, $T_{+1} = 6.9$ K, $T_{-1} = 6.7$ K and $T_2 = 4.4$ K [25–27], and it is the best known example of a localised uranium intermetallic. For this reason it has been studied in great detail by a wide range of experimental techniques:- neutron [27–33] and X-ray scattering [1], photoemission [34, 35], magnetic susceptibility [36–39], heat capacity [37, 39–41], magnetostriction [42, 43] and ultrasonic techniques [25]. These transitions have been attributed to a series of quadrupolar order parameters using group theory arguments, making it one of only a small number of metallic systems exhibiting long range quadrupolar ordering.

The uranium $5f$ electrons are well localised in a $5f^2$ configuration. The localised behaviour is clearly evident from the existence of crystal field excitations first measured by Buyers *et al.*, using inelastic neutron scattering [28], and supported by intermultiplet spectroscopy results [33]. It is also indicated by the absence of a peak at the Fermi level in Ultraviolet Photoemission valence spectra and the poorly screened peak at higher binding energy than in pure uranium in the X-ray photoemission uranium $4f$ spectra [34, 35], a low γ value ranging between 2.5 [40] - 9.5 [37] mJ/K^2, and low cyclotron effective mass $0.24 - 3.62m_0$ (i.e. no evidence of hybridization between conduction and 5f electrons) [37, 39, 44]. Applying Hund's Rules, assuming Russell Saunders coupling, indicates that the ground state configuration is the $^3H_4$ multiplet ($S = 1$, $L = 5$, $J = 4$). This ground state indicates that the atomic moment should be $3.2\mu_B$, which is strongly in contrast with the measured value of $0.02\mu_B$ for the antiferromagnetically ordered moment [39]. This discrepancy could be due to the crystal field splittings, induced by the developing quadrupolar order, almost entirely quenching the moment. Since the $5f$ shells are unfilled, the uranium ions will have fluctuating magnetic dipole, electric quadrupole and higher order multipole moments. The large orbital moment means that there is strong coupling to the lattice, which helps explain why quadrupolar effects are dominant in UPd$_3$. Recently a new crystal field model has been developed which provides a qualitative understanding of the transitions and the excitations observed by inelastic neutron scattering at 2K [26].

UPd$_3$ is also interesting to study as a comparison to UPt$_3$, a heavy fermion superconductor [45]. The nearest neighbour uranium distances in the two compounds are nearly the same: UPd$_3$ $d_{U-U} = 4.106$A and UPt$_3$ $d_{U-U} = 4.132$A. However, they have different structures. UPd$_3$ is double-hexagonal close-packed while UPt$_3$ is simple hexagonal close-packed, and the Pt $5d$ wave function is more extended than the Pd $4d$ one, contributing to different band structures [46]. At least some of the U $5f$ electrons in UPt$_3$ appear to be itinerant, forming band states [47]. This goes some way to explaining why the two compounds show markedly different behaviour.

2.3.1 Crystal Structure

UPd$_3$ crystallizes in a double hexagonal close packed structure with hexagonal layers stacked ABACABAC, uranium atoms in the B and C layers possess locally hexagonal symmetry, while those in layer A have a local environment BAC indicating a quasi-cubic symmetry. The crystal structure is of the TiNi$_3$ type (see Fig. 2.5) with lattice parameters $a = 5.76$ A and $c = 9.62$ A [48], and the space group is (#194, P63/mmc). In the dhcp unit cell atoms are situated at:

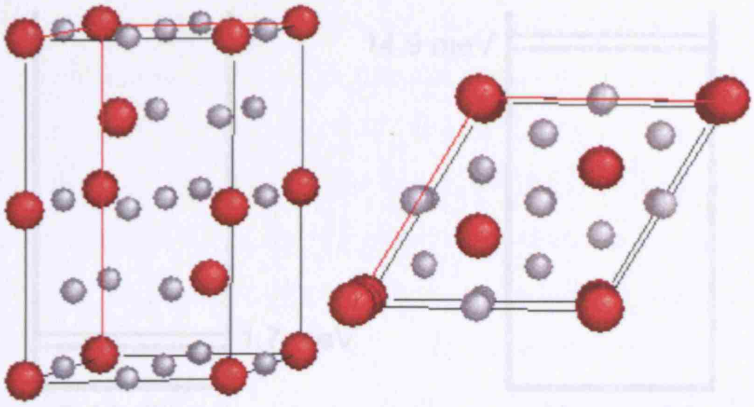

Figure 2.5: Dhcp structure of UPd$_3$ viewed from the side and from above.

U Quasi-cubic:	$(0,0,0)$	$(0,0,\frac{1}{2})$	
U Hexagonal:	$(\frac{1}{3},\frac{2}{3},\frac{3}{4})$	$(\frac{2}{3},\frac{1}{3},\frac{1}{4})$	
Pd I:	$(\frac{1}{2},0,0)$	$(0,\frac{1}{2},0)$	$(\frac{1}{2},\frac{1}{2},0)$
	$(\frac{1}{2},0,\frac{1}{2})$	$(0,\frac{1}{2},\frac{1}{2})$	$(\frac{1}{2},\frac{1}{2},\frac{1}{2})$
Pd II:	$(x,2x,\frac{1}{4})$	$(2\bar{x},\bar{x},\frac{1}{4})$	$(x,\bar{x},\frac{1}{4})$
	$(\bar{x},2\bar{x},\frac{3}{4})$	$(2x,x,\frac{3}{4})$	$(\bar{x},x,\frac{3}{4})$,

where the ideal value of parameter x is $\frac{1}{6}$ [48]. The inter-uranium distance is 4.11 Å, which is greater than the Hill Limit (3.4 Å) suggesting that the $5f$ electrons should be localised.

2.3.2 Neutron Experiments

The first inelastic neutron scattering experiments on single crystal UPd$_3$ observed three well-defined spin-excitation bands, indicating that the $5f$ electrons are localised: two strong transverse bands between 12.8 and 18.6 meV and a weak band at 1.7 meV [28]. A crystal field level scheme was developed to give the relevant transitions and to agree with the fact that up to that point no magnetic ordering down to low temperatures had been observed, which

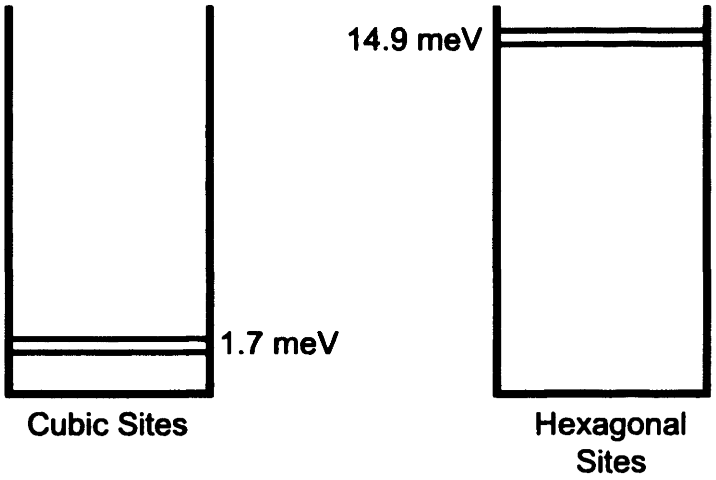

Figure 2.6: CEF level scheme developed for UPd$_3$ by Buyers and Murray [28]

required there to be a non-magnetic ground state on both sites. The strong mode around 15 meV was attributed to the hexagonal sites, with a $J_z = |0\rangle$ ground state and a $J_z = |\pm 1\rangle$ excited doublet. Using this fit, the cubic site crystal field splitting was estimated, leading to the belief that there was also a singlet ground state on the cubic sites, which was compatible with the absence of magnetic ordering (see Fig. 2.6).

A subsequent experiment using polarised neutron diffraction (PND), with the polarization **P** parallel to the scattering vector **Q**, investigated the structural and magnetic character of the phase transitions at $T_1 \sim 7$ K and $T_2 \sim 5$ K [30] that had been identified up to that time in bulk measurements [36]. The experiment made use of the fact that for neutrons polarised parallel to **Q** the origin of the Non-Spin-Flip (NSF) cross-section is entirely nuclear, whilst that for Spin-Flip (SF) scattering is purely magnetic, apart from incoherent nuclear scattering.

The temperature dependence of elastic scattering at $(h+\frac{1}{2}, 0, l)$ peaks was measured. All peaks showed an increase in the NSF scattering below T_1, with a change in the intensity below T_2, which was interpreted as the phase with

$5 < T < 7$ K incorporating a modulated lattice distortion with a wavevector of $0.5\tau_{100}$, which accompanies a quadrupolar structure. The SF data showed a distinct increase in intensity only below 4.5 K in the case of the $(\frac{1}{2}, 0, 0)$ peak, indicating that the low temperature transition is of both structural and magnetic origin, while the higher temperature transition is of non-magnetic origin. However, the diffraction peaks are not resolution limited, indicating that the order is only short range, and μSR measurements suggest that spin fluctuations may be dynamic, but appearing static within the time window of neutron scattering [49].

Group theoretical arguments applied to the $(\frac{1}{2}, 0, l)$ and $(\frac{1}{2}, 1, l)$ peak intensities established that the order parameter symmetry is B_{2g} [29]. The doubling of the unit cell means that the structure is antiferroquadrupolar (AFQ). For such a structure the allowed quadrupolar symmetry modes are δQ_{zz}, $Q_{\mathrm{x^2-y^2}}$ and Q_{zx}, where δQ_{zz} is the deviation of Q_{zz} from the average value, which cannot act as an order parameter itself as it is non-zero above T_1. Landau Theory has shown that the transition at T_1 is to an ordered phase which is triple-q, and that the phase space group is $P\bar{3}m1$.

The localised nature of the $5f$ electrons in UPd_3 in comparison to UPt_3 was confirmed using neutron intermultiplet spectroscopy [33]. Using an incident energy of 800 meV a clear excitation at a transfer of 395 meV was observed in UPd_3, while nothing was found in UPt_3. This corresponds to the electronic configuration of UPd_3 being $5f^2$, and the excitation is ascribed to a $^3H_4 \rightarrow {}^3F_2$ transition.

2.3.3 Xray Resonant Scattering Experiment

Unlike neutron and X-ray non-resonant scattering probes, which couple to the lattice distortions associated with the ordering, X-ray resonant scattering (XRS) couples directly to the quadrupolar structures. Measurements, made when only three transitions had been identified, found that resonant enhancement of scattering was observed from two peaks associated with long range quadrupolar order: (103) and (104) written in the orthorhombic notation [1]. The temperature dependence of the scattering at the two reflections indicated that between T_0 and T_1 critical fluctuations build up at (103). Then at T_1 the scattering intensity at (103) increases abruptly while there is a first order transition in the intensity at (104), and finally at T_2 there is a discontinuity in both reflections' intensities. Polarisation analysis of the intensity at the two reflections indicated that the (103) peak was predominantly in the unrotated $\pi\pi$ channel, in contrast to the (104) peak, which was mainly in the rotated $\pi\sigma$ channel. Calculations based on the resonant scattering amplitude for different quadrupolar order models were compared with the data, showing that between T_0 and T_1 the limited data was consistent with the cubic different $Q_{x^2-y^2}$ order parameter. This would be manifested as an antiphase stacking of the quadrupole moments on the cubic sites up the z-axis (see Fig. 2.7). Below T_1 comparisons of calculations and data suggested that the charge densities are rotated off axis.

2.3.4 Ultrasound

The large coupling of the acoustic strain to the ionic quadrupolar moment tensor makes ultrasound well suited to investigations of long range quadrupolar order and the quadrupole-quadrupole interaction. Ultrasound was the first

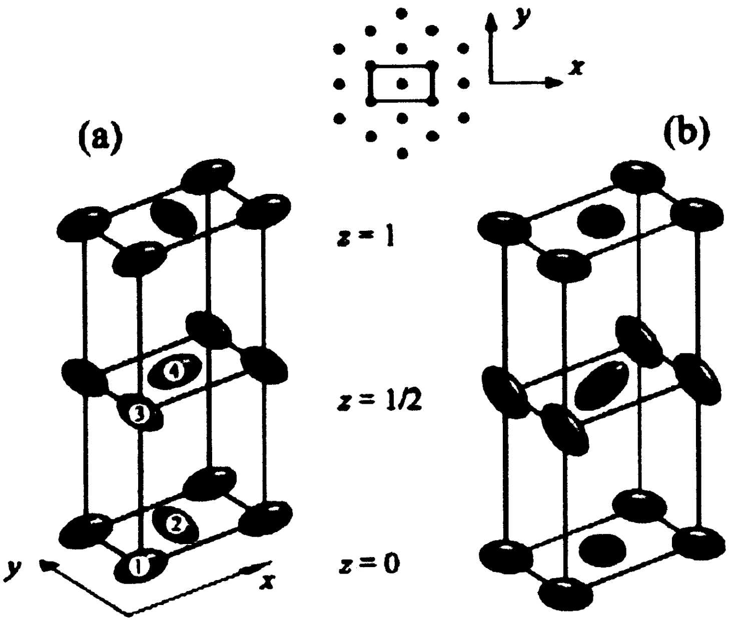

Figure 2.7: The AFQ structures in UPd_3 shown using the orthorhombic unit cell [1]. The ellipsoids on the quasicubic sites represent the U $5f$ quadrupoles. a) For $T_1 \leq T \leq T_0$ the structure was believed to be $Q_{x^2-y^2}$ with an antiphase stacking along the z axis. b) Below T_1 it was believed that the moments are rotated, introducing other order parameters.

experimental technique to identify the two distinct transitions at $T_{+1} = 6.9$ K and $T_{-1} = 6.7$ K [25]. Figure 2.8 shows that hysteresis was observed close to T_{-1} but not T_{+1} suggesting that the transition at T_{-1} is first order, while the transition at T_{+1} is likely to be second order.

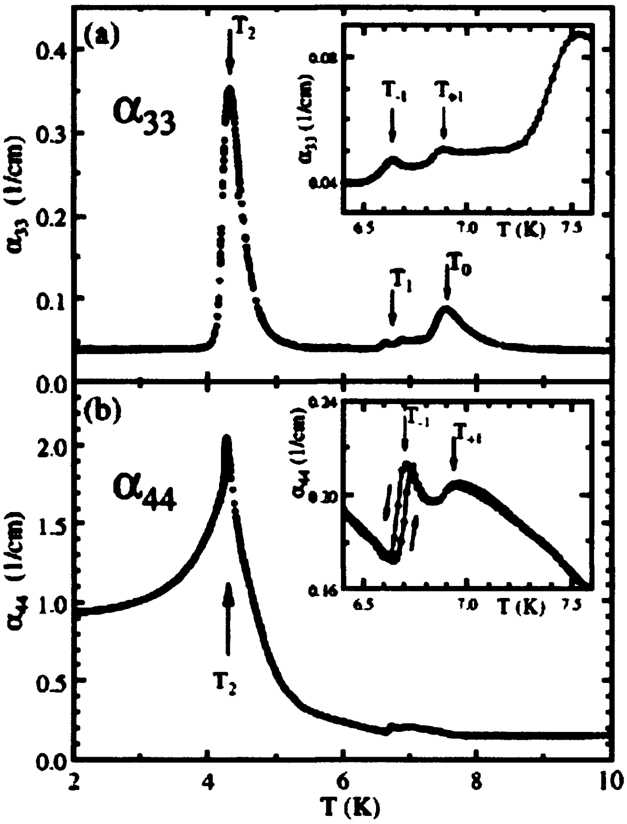

Figure 2.8: Temperature dependence of the ~ 20 MHz (a) longitudinal and (b) transverse attenuation coefficients of the C_{33} and C_{44} elastic modes in UPd$_3$ ultrasound measurements [25], providing the first evidence separating the T_{+1} and T_{-1} transitions.

Investigations of the temperature dependence of different elastic constants led to the conclusion that the four transitions, including the magnetic transition T_2, are indeed driven by quadrupolar interactions. The data supports a scheme where at T_0 the crystal symmetry changes from hexagonal to orthorhombic. Then at T_{+1} there is a second order transition from orthorhombic to monoclinic with $\langle Q_{xy} \rangle$ possibly being the significant order parameter. At

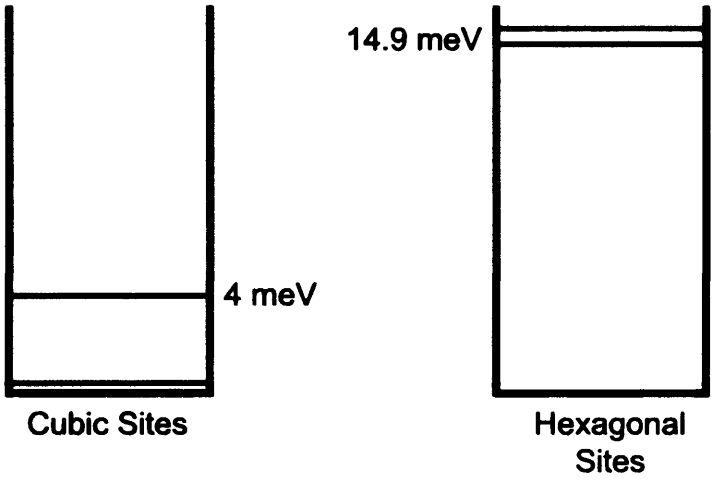

Figure 2.9: CEF level scheme developed for UPd$_3$ by K. A. McEwen *et al.* [26]

T_{-1} there is a first order transition from monoclinic to a trigonal triple-q state, followed by a probable first order transition from the trigonal triple-q state to monoclinic magnetic state at T_2, where the order parameter should be a linear combination of $\langle Q_{yz} \rangle$ and $\langle Q_{x^2-y^2} \rangle$.

2.3.5 Summary

Following a comprehensive analysis of the huge range of data, a new crystal field level scheme has been developed to explain the physics of the different phase transitions [26], see Fig. 2.9. The magnetic entropy and single crystal susceptibility data (Figure 2.10) indicate that the ground state on the quasi-cubic sites in the high temperature phase is a doublet rather than a singlet. Also a two-level system would not be able to explain the four phase transitions observed.

The two singlet ground states of the Buyers and Murray scheme [28] was in good agreement with the observed absence of magnetic ordering, while this new scheme has a magnetic doublet ground state meaning that magnetic order

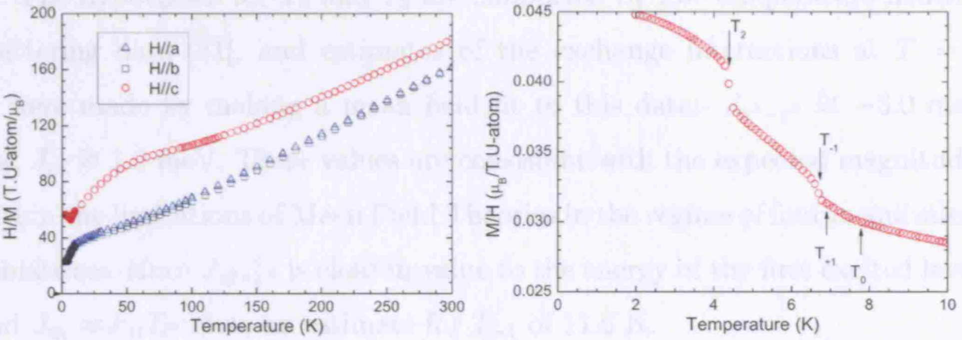

Figure 2.10: The inverse magnetic susceptibility of single crystal UPd$_3$ measured along the principal crystallographic axes, and the magnetic susceptibility between 2 and 10 K, with arrows showing the transition temperatures.

would be possible. However, the hexagonal crystal structure will lead to a geometric frustration of simple antiferromagnetism. In addition, the high strength of the quadrupolar interactions means that the quadrupolar transitions occur first preventing magnetic ordering.

The different quadrupolar order parameters lead to the cubic ground state degeneracy being lifted below 7.8 K. Using the symmetries of the different quadrupolar operators, the nature of the quadrupolar transitions have been analyzed. The scheme suggested for the phase transitions was as follows:

T_0	2nd order transition	$Q_{x^2-y^2}$ primary order parameter, only small splitting of doublet levels
T_{+1}	2nd order transition	Q_{yz} develops
T_{-1}	1st order transition	Q_{zx} primary order parameter which enhances $Q_{x^2-y^2}$ due to symmetry considerations, leads to large splitting of ground state doublet
T_2	1st order transition	Q_{yz} disappears, leaving an AFQ state with 4 sublattices with order parameters $Q_{x^2-y^2}$ and Q_{zx}

The hypotheses for T_0 and T_2 are supported by low temperature neutron scattering data [31], and estimates of the exchange interactions at $T = 0$ K were made by making a mean field fit to this data:- $J_{x^2-y^2} \cong -3.0$ meV and $J_{zx} \cong 1.0$ meV. These values are consistent with the expected magnitudes within the limitations of Mean Field Theories in the regime of four inequivalent sublattices, since $J_{x^2-y^2}$ is close in value to the energy of the first excited level, and $J_{zx} \approx k_B T_C$ gives an estimate for T_{-1} of 11.6 K.

2.4 NpPd$_3$

Dhcp NpPd$_3$ is an interesting but little studied compound, in contrast to isostructural UPd$_3$, with most of the work done published in only one paper many years ago [50], and so this literature review will take the form of a synopsis of this paper. As far as we are aware, no papers have been published relating to the mixed (U$_{1-x}$Np$_x$)Pd$_3$ system, prior to our own work.

As part of a programme investigating magnetic ordering with actinide concentration in actinide-palladium alloys and looking at the localised nature of the $5f$ electrons (the Np-Np distance is greater than the Hill Limit) magnetization, electrical resistivity, Mössbauer effect and neutron diffraction measurements were made on dhcp NpPd$_3$ between 1.5 and 300 K [50]. Samples of dhcp NpPd$_3$ were prepared by arc melting stoichiometric amounts of high purity Np and Pd metals before annealing at 1350°C for at least 85 hours to ensure that none of the cubic phase, produced on quenching, was present, which was found to be antiferromagnetic with $T_N = 55$ K.

The isofield-magnetization measurements displayed a broad peak centred on about 20 K, with the magnetization falling steeply between 20 – 35 K, see Fig. 2.11. The isotherm-magnetization curves showed no saturation down

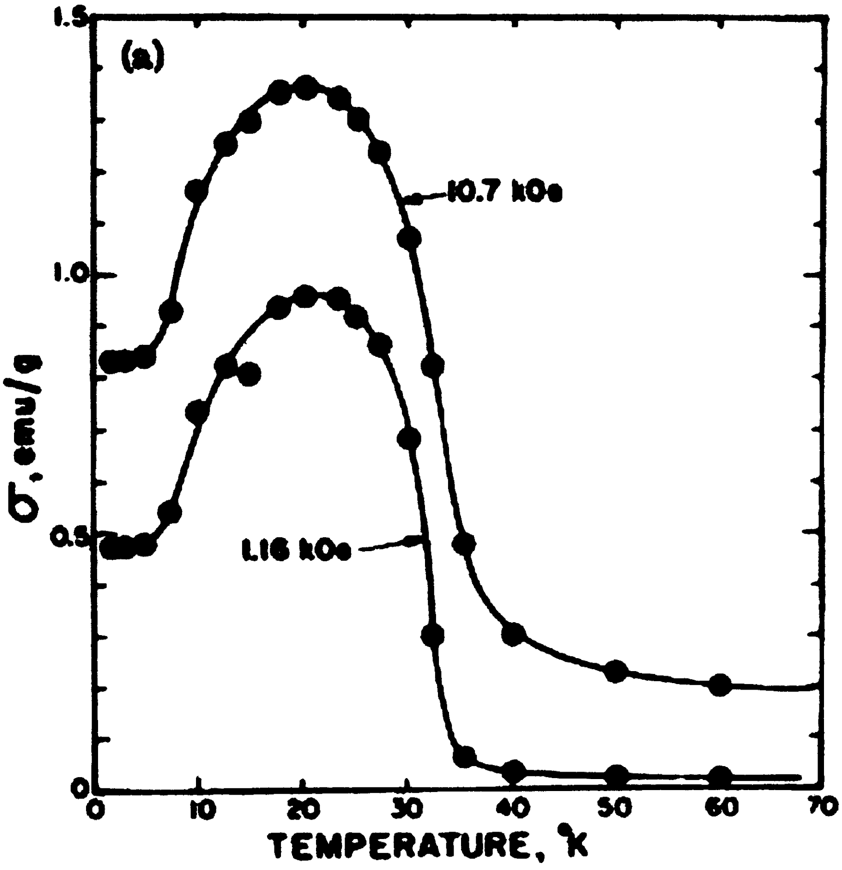

Figure 2.11: Isofield magnetization of $NpPd_3$ showing a sharp rise below 32 K, and a broad peak centred on 20 K [50].

to 1.74 K and for $T < 32$ K the susceptibility for $6 < H < 12$ kOe was almost independent of temperature. The data implied some kind of magnetic ordering near 32 K, while for temperatures in the range 100 – 300 K the susceptibility obeys a Curie-Weiss behaviour with an effective paramagnetic moment of $\mu_{eff} = (2.75 \pm 0.03)\mu_B/\mathrm{F.U.}$

The electrical resistivity increased rapidly from a residual value of 19.7 $\mu\Omega$cm to a knee at 30 K after which the gradient is reduced near the temperature at which magnetization measurements indicate some form of ordering. For $T > 50$ K the slope of the resistivity curve was found to be negative. The low temperature rapid increase in the resistivity was assigned to spin-

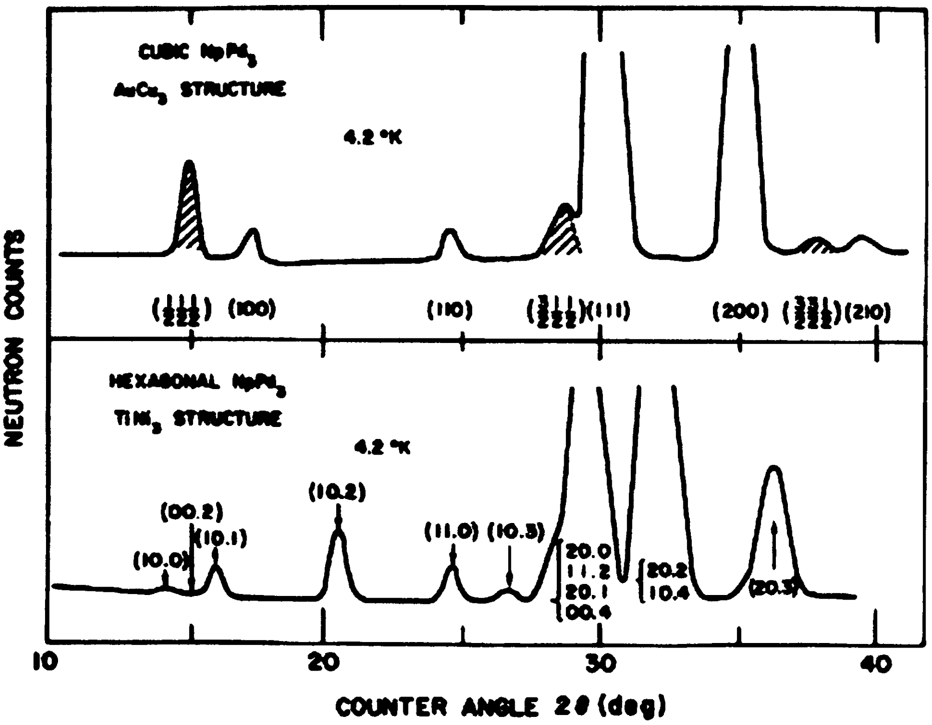

Figure 2.12: Neutron diffraction patterns for the cubic and dhcp phases of $NpPd_3$ at 4.2 K [50]. The shaded peaks in the cubic pattern are magnetic Bragg peaks due to antiferromagnetic ordering.

disorder scattering, while the high temperature negative gradient suggested spin-flip scattering and could be fitted by a Kondo-type scattering expression $\rho = A + BT + C \ln T$.

Some paramagnetic line broadening was seen close to the transition at 32 K, but no clear hyperfine structure was observed in the Mössbauer effect spectra at 4.2 K, and the authors were unsuccessful in attempting to make a fit to the data. The neutron diffraction data was identical at 78 and 4.2 K, see Fig. 2.12, meaning that no magnetic transition was observed.

The authors ascribed short range magnetic order to being responsible for the magnetization, resistivity and Mössbauer data, but could not describe the precise nature of this ordering. The fact that the features in the resistivity and magnetization are sharp implies that the onset of ordering occurs over a narrow range of only a few degrees. One possibility is that there is a small concentration of magnetic clusters distributed throughout the sample, which order antiferromagnetically at nearly the same temperature. These would polarise the surrounding Neptunium moments thus affecting bulk properties. This situation could also explain the Mössbauer behaviour. Neutrons should reveal these structures as broad peaks at incipient superlattice reflection positions, but may not have done in this case due to the use of only a small polycrystalline sample and the poor flux and resolution.

2.5 Fermi Liquid Theory, Non-Fermi Liquids and Quantum Critical Points

In 1876 Boltzmann used statistical mechanics to explain the Dulong-Petit law that the specific heat per mole of nearly any solid is approximately the same. However, by the end of the nineteenth century, numerous materials had been found to have too small a specific heat, and the low temperature specific heat was temperature dependent contradicting Boltzmann's theory. Classically each electron in a material should contribute $3k_B/2$ to the specific heat. The problem was overcome with the advent of quantum mechanics.

The Pauli Exclusion principle states that no two fermions can occupy the same quantum state. For a non-interacting system of free electrons, minimising the kinetic energy subject to Pauli's constraint produces the lowest energy state, consisting of a filled Fermi sea of occupied quantum states in momentum space within a sphere described by the Fermi energy ϵ_F and momentum $p_F = \hbar k_F$. Energy and momentum conservation during particle-hole excitations, in which an electron is promoted from below the Fermi surface to above it, result in only electrons within k_BT of ϵ_F contributing to the specific heat, with the majority of electrons lying too far below ϵ_F to reach an unoccupied state.

Whilst the problem pertaining to the low electronic heat capacity has been solved it leaves an interesting question, why should a non-interacting model work in materials where interactions are significant? The answer came from Landau's Fermi Liquid Theory (FLT) in which interactions are introduced to the electron gas as slow perturbations. The central principle of FLT is "adiabatic continuity", which postulates a one-to-one mapping of the low energy eigenstates of the interacting electrons to those of the non-interacting Fermi gas, where it is the label, in the form of the good quantum numbers, which is preserved after interactions are applied. In an interacting system the perturbed wavefunction is associated with quasiparticles, rather than the original electrons, but the spin and charge are preserved. The quasiparticles interact weakly, filling up the states to the Fermi level in the same way as the electrons in the electron gas.

Landau made two basic assumptions in his Fermi liquid theory, that to leading order in temperature the entropy is that of a Fermi gas, but the energy is not additive. The first assumption is consistent with the distribution function being unchanged as interactions are "switched on". The second assumption states that for two quasiparticles in states $(\mathbf{k},\sigma)$ and $(\mathbf{k}',\sigma')$ their total energy is not the sum of the two independent quasiparticle excitations $(\epsilon_{\mathbf{k}\sigma}+\epsilon_{\mathbf{k}'\sigma'})$, but instead

$$E = \epsilon_{\mathbf{k}\sigma} + \epsilon_{\mathbf{k}'\sigma'} + f_{\mathbf{k}\sigma,\mathbf{k}'\sigma'}, \tag{2.8}$$

where $f_{\mathbf{k}\sigma,\mathbf{k}'\sigma'}$ is the Landau interaction function. Quasiparticles also have a modified inertial mass m^* due to the back-flow in the Fermi sea when a quasiparticle moves "pushing" the ground state out of the way [51]. Using these assumptions, equilibrium properties can be calculated and shown to be similar to those for the non-interacting Fermi gas but with the modified mass m^* and the Landau parameter F_0^a, which is related to the f-function.

Fermi Liquid Theory has proved to be very successful in describing metallic behaviour at low temperatures where the quasiparticles persist, with characteristic scaling laws found for different properties in a large range of metallic systems, even in systems with the strongest electron correlations, such as UPt_3. However, over the last decade, heat capacity measurements have again posed problems for our theories of matter, as they did a century ago. The materials in which FLT fails, non-Fermi liquids, are some of the most interesting materials known, such as the high temperature superconductors and low dimensional systems.

In calculating the quasiparticle lifetime near the Fermi level in FLT it is assumed that the scattering matrix elements are independent of the momentum and energy transferred. This is valid in the limit of small energy transfers, which is usually the case given that the Pauli principle confines scattering to the vicinity of the Fermi surface. However, close to a second order phase transition, order parameter fluctuations slow down and their wavelengths increase, such that quasiparticles influence others to a greater extent resulting in a greatly enhanced scattering cross-section. Below the ordering temperature the fluctuations are locked in and the Landau quasiparticle is conserved. A transition occurring at $T = 0$ K is driven not by thermal motion, but instead by quantum fluctuations, zero-point motion, associated with Heisenberg's Uncertainty Principle, which can "melt" order. At such a transition the scattering cross section increases without constraint making the assumptions used in building Fermi Liquid theory untenable leading to its breakdown.

One of the first experimental observations of the failure of Fermi liquid theory came from heat capacity and resistivity measurements of the antiferromagnetic system $CeCu_{6-x}Au_x$ [52]. It was found that with increasing gold concentration the Sommerfeld coefficient increased, suggesting the electrons were getting heavier and heavier, until at some critical concentration it kept growing never reaching a constant as the temperature was reduced, as though the electron mass at the Fermi surface was becoming infinite. In addition the low temperature resistivity did not vary as the square of the temperature, but instead close to the critical concentration was linear in temperature. These results suggested that $CeCu_{6-x}Au_x$ was not a "normal" metal, but that quantum critical matter was a fundamentally new type of electron fluid.

In 1976 John Hertz first questioned how quantum mechanics would affect critical phenomena at a phase transition [53]. In conventional matter, electron-electron interactions are short order, and therefore electrons can be treated as individual particles moving independently. His theory introduces quantum mechanics through the inclusion of time as an imaginary dimension. At zero temperature the interactions would grow to have infinite range, while being retarded in time, such that one electron is felt by another long after it passed, making the electrons strongly correlated. This leads to droplets of incipient order associated with the transition being quantum-mechanical rather than classical. He reasoned that close to a quantum critical point the quantum droplets would eventually dominate the material resulting in quantum critical matter. The drastic properties associated with the QCP extend over a fan of phase space above absolute zero. This makes the study of quantum critical matter possible experimentally, and offers a class of materials which could display new universal electronic behaviour independent of the fine details of the individual material away from the QCP.

Quantum phase transitions have been most studied in materials where magnetism has been "squeezed out" by some tuning parameter, such as pressure, applied magnetic field or chemical pressure through doping. Antiferromagnetic

Property	Fermi liquid	Non-Fermi liquid	
		FMQCP	AFMQCP
ρ	$\rho_0 + AT^2$	$T^{5/3}$	$T^{3/2}$
C	γT	$T \ln T$	$T \ln(T/T_0)$
χ	constant	$\ln T$	$1 - \sqrt{T}$

Table 2.3: Table comparing the temperature dependence of measurable quantities for Fermi liquids and non-Fermi liquids in the vicinity of a Ferromagnetic and an Antiferromagnetic QCP.

and staggered spin alignments are more susceptible to melting by zero-point fluctuations and antiferromagnetic QCPs comprise most of the experimental literature. Ferromagnetic quantum critical points are less commonly observed, but are equally significant, for example the application of pressure to UGe_2 destroys the ferromagnetism but leads to a novel form of superconductivity with an unusual pairing mechanism [54]. The expected temperature dependences for quantum critical matter associated with ferromagnetic [51] and antiferromagnetic singularities have been calculated using Fermi's Golden Rule and the appropriate models, see Table 2.3, and show that the temperature exponents of a given property are dependent on the nature of the singularity. Experimentally the $T^{5/3}$ form for the resistivity has been observed in MnSi [55] and $ZrZn_2$ [56] when pressure suppresses $T_C \rightarrow 0$ K. However, for various antiferromagnetic systems the temperature dependence of the resistivity is less than that predicted.

There is currently considerable debate regarding a theoretical understanding of quantum criticality. While some of the experimental observations are in accordance with the theory of Hertz, other features are incompatible, for example the effects are much more significant and occur over a greater range of temperature and other tuning parameters than predicted. Additionally one of the key signifiers of quantum criticality has been shown to be E/T scaling in

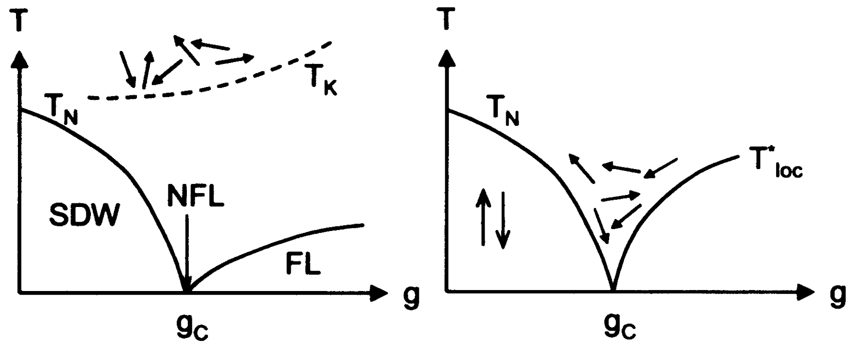

Figure 2.13: Diagram of a conventional (left) and a local (right) quantum phase transition in Kondo lattices. g is the tuning parameter relating the strength of the RKKY interaction to the Kondo energy scale, SDW is spin density wave, T_N is the Néel temperature, FL is Fermi liquid and NFL non Fermi liquid and T^*_{loc} corresponds to a local energy scale.

the dynamical susceptibility measured by inelastic neutron scattering, e.g. as in $UCu_{5-x}Pd_x$ ($x = 1$, 1.5) [57], $Ce(Rh_{0.8}Pd_{0.2})Sb$ [58] and $CeCu_{5.9}Au_{0.1}$ [59]. The observation of critical excitations over a wide range of momentum values, by Heisenberg's Uncertainty Principle, indicates that the critical excitations are highly localised in space, which is inconsistent with Hertz' theoretical treatment.

Various different ideas have been voiced to solve the problems, with some further developing Hertz' theory to take the complexity of the material into account [60], while others suggest he made inappropriate approximations [61]. Another model has been used for magnetic two dimensional insulators, in which it has been proposed that electrons in quantum critical matter break up into spin and charge components, at deconfined quantum critical points [62].

Alternatively, it is possible that a whole new framework needs to be developed for quantum phase transitions, rather than developing the theory out of that for classical phase transitions. This has led to a debate between "local" and "global" theories of quantum phase transitions, see Figure 2.13. Hertz's theory is global, based on classical criticality in which static order in space grows globally, with the addition of growth along the quantum time dimension. In local quantum critical theory, critical matter involves the growth of drops of order in time but not in space [63].

Si *et al* found that both situations emerge as solutions, when extended dynamical mean-field theory is used to examine the Kondo lattice model [63]. When spin fluctuations are three-dimensional, the lattice system orders before the local Kondo problem becomes critical, i.e. the local energy scale $\mathrm{T}^*_{\mathrm{loc}}$ is still finite, and at $T = 0$ K the local moments are completely quenched over the entire paramagnetic region and at the QCP. In this case the critical spin fluctuations form a spatially delocalised wave, and this situation corresponds to Hertz's theory. However, when the spin fluctuations are two-dimensional the lattice system orders at the point when the local problem becomes critical, i.e. $\mathrm{T}^*_{\mathrm{loc}}$ vanishes at the QCP and so two critical degrees of freedom co-exist: spatially extended fluctuations of the order parameter, and local fluctuations originating from the local moments. The resultant dynamical spin susceptibility satisfies E/T scaling, while the static susceptibility has a modified Curie-Weiss form consistent with magnetisation data for some heavy fermion metals close to quantum criticality [45, 59]. This looks promising, but one has to question how a three-dimensional system could exhibit two-dimensional excitations. In the case of $\mathrm{CeCu}_{6-x}\mathrm{Au}_x$, earlier inelastic neutron scattering experiments suggest that the magnetic fluctuations are two-dimensional [64].

It is clear that as yet there is no consensus as to a theory which is able to explain the behaviour associated with the quantum criticality observed in different systems.

2.5.1 $(M_{1-x}U_x)Pd_3$

Transport and thermodynamic measurements on the cubic $AuCu_3$-type system $Y_{0.8}U_{0.2}Pd_3$, to further investigate the evolution of the localized $5f$ behaviour with doping Y^{3+} for U^{4+}, after photoemission work which showed that the Fermi level could be tuned through removing electrons from the system [65], led to the first reports of non-Fermi Liquid behaviour [66,67]. The behaviour is manifested as the weak power law or logarithmic divergence of the electronic properties at low temperatures,

$$\Delta\rho(T)/\Delta\rho(0) \approx 1 - a(T/T_K), \tag{2.9}$$

$$\gamma(T) \equiv \Delta C(T)/T \approx -(1/bT_K)\ln(T/T_K), \tag{2.10}$$

$$\Delta\chi(T)/\Delta\chi(0) \approx 1 - c(T/T_K)^{\frac{1}{2}}, \tag{2.11}$$

where a, b and c are constants of order one. Since 1991 the system has been studied extensively with numerous different experimental techniques but there is still no theoretical consensus as to the origin of the NFL behaviour. Possible scenarios include intrinsic property mechanisms such as the Quadrupolar Kondo Effect [66] or proximity to a zero temperature second order phase transition [67] and extrinsic mechanisms due to the metallurgical inhomogeneity [68], which could lead to a distribution of different Kondo temperatures.

Non Fermi Liquid behaviour is also observed in the spin glass system $Sc_{1-x}U_xPd_3$ for $x = 0.35$ with similar properties to $Y_{1-x}U_xPd_3$, but there is a nearly homogenous U distribution within the cubic $ScPd_3$ matrix [69]. Phase diagrams for $Y_{1-x}U_xPd_3$ and $Sc_{1-x}U_xPd_3$ are shown in Figure 2.14. That the physical properties of the two systems are quite similar despite their metallurgical differences suggests that the NFL mechanism is intrinsic rather than extrinsic. Inelastic neutron scattering experiments on $Sc_{0.65}U_{0.35}Pd_3$ show that the susceptibility $\chi''(q,\omega,T)$ at all measured wavevectors (q), tempera-

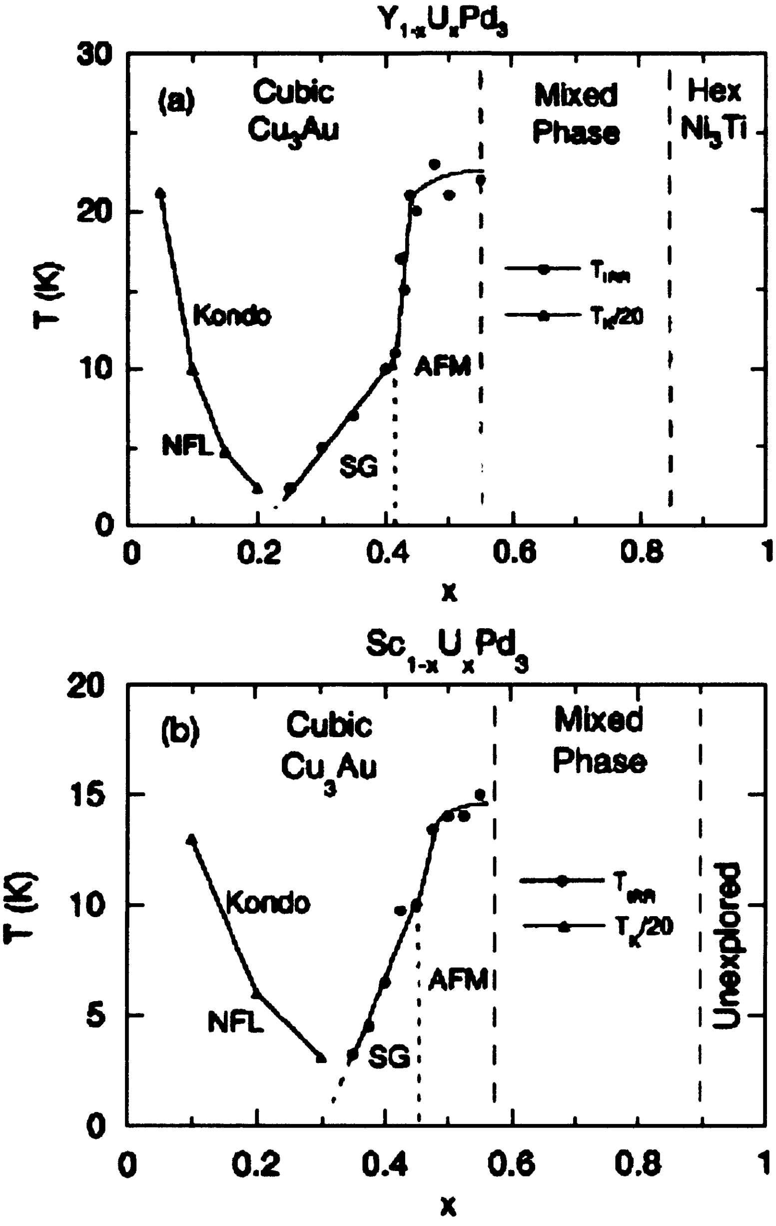

Figure 2.14: Temperature T versus Uranium concentration x phase diagram for (a) $Y_{1-x}U_xPd_3$ and (b) $Sc_{1-x}U_xPd_3$. NFL: non-Fermi liquid; SG: spin glass; AFM: antiferromagnet; T_{IRR}: irreversibility temperature (for magnetisation); T_K: Kondo Temperature. [69]

tures (T) and energies (E) obeys E/T scaling indicative of a $T = 0$ K second order phase transition [70]. Similar E/T scaling is also observed in NFL compounds near to an antiferromagnetic QCP, e.g. $\mathrm{CeCu_{6-x}Au_x}$ [59] and $\mathrm{Ce(Rh_{0.8}Pd_{0.2})Sb}$ [58], but in this case $\chi''(q, E, T)$ is wavevector independent with no spatial correlations and the scaling extends over a much larger energy range. This composition is too far removed from the antiferromagnetic region of the phase diagram, and so this quantum phase transition corresponds to the spin glass transition. It is interesting to note that NFL properties such as E/T scaling are common to systems with a QCP irrespective of the nature of the $T = 0$ K transition.

Chapter 3

X-ray Resonant Scattering

In this chapter the technique of X-ray Resonant Scattering and some of the basic theory behind it is introduced. Experimental details of X-ray Resonant Scattering Experiments performed on the ID20 beamline at the European Synchrotron Radiation Facility (ESRF) are also presented.

3.1 Introduction

X-rays are a form of electromagnetic radiation with wavelengths in the range 10^{-12} to 10^{-8} m and energies of the order of 10^{2} to 10^{6} eV. These wavelengths are on a length-scale comparable with atomic structures, unlike the wavelength of visible light, and hence crystallographic structures can be determined from the scattering of X-rays from materials. X-rays were the first tool by which such information could be inferred.

3.1.1 Conventional X-ray Sources

Classical sources of X-rays generate X-rays in one of two ways: - 1) when high energy electrons are slowed down in an anode material they produce radiation with a continuous frequency spectrum, this is Bremsstrahlung radiation; 2) when electrons recombine after the creation of empty states in the inner shells of atoms in the anode by collisions or photoionization, radiation is emitted with a sharp wavelength determined by the transition energy. The use of X-ray tubes is limited by the fact that only 1% of the energy of the absorbed electron is emitted as X-ray radiation, the rest being converted to heat [71].

3.1.2 Synchrotron Radiation

Synchrotron Radiation is the electromagnetic field radiated by relativistic accelerated charged particles. It was first observed in 1947 at the General Electric Research Laboratory in the United States in a particle accelerator [72], and was thought to be a nuisance as it led to the particles losing energy. Characterisation of this radiation showed that it was a much stronger source of X-rays. Since the first parasitic sources, synchrotron rings in combination with electron storage rings have been developed to produce brighter and brighter X-ray sources.

Particles can be made to follow a circular trajectory using the Lorentz force, where static magnetic fields are applied perpendicular to the horizontal orbital plane using bending magnets. For non-relativistic accelerated charged particles the energy flux is emitted isotropically around the acceleration in a large solid angle. Synchrotron radiation however is emitted by accelerated particles which are high energy ~GeV and have a velocity close to the speed of light making them relativistic, and so the angular distribution of the emitted

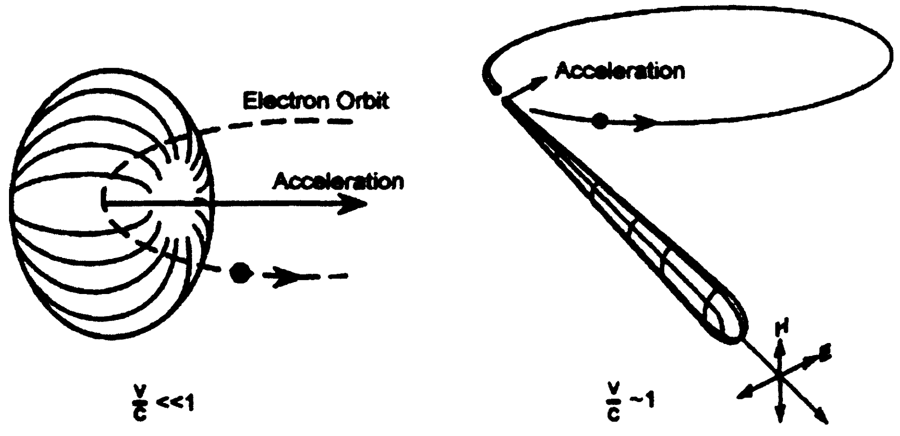

Figure 3.1: Radiation emission patterns of electrons in circular motion: case I. non-relativistic electrons - cyclotron radiation. case II. relativistic electrons - synchrotron radiation. (adapted from [74])

radiation is no longer described by a dipolar distribution [73]. Instead the relativistic transformation causes the radiation pattern to be distorted in the direction of motion, shown in Fig. 3.1.

Radiation will only be visible when the velocity of the electron is directed towards the observer. The radiation is in the form of a short burst with a timescale dependent on the radius of curvature and the velocity of the particle $\tau \sim (\mathrm{R/c})\gamma^{-3}$, where γ is the Lorentz factor $\equiv (1 - v^2/c^2)^{-1/2}$, v is the velocity in the reference frame, and c is the speed of light. The Fourier transform of this short pulse therefore shows a wide frequency spectrum, explaining why the beam is white, up to a spectral cut-off at the critical energy E_C, which characterises the spectrum. In designing a machine for synchrotron radiation, it is first necessary to choose a value for E_C as this dictates the choice of the energy of the particles, which is constrained by the magnetic fields obtainable.

Another effect of the relativistic motion is that the electric field $\boldsymbol{E}$ is contracted by the Lorentz transformation, with the result that the radiation is predominantly polarised with $\boldsymbol{E}$ in the plane of motion. If the radiation is observed in the orbit plane, it is completely linearly polarised. Observation at small angles out of the plane leads to the detected radiation being elliptically polarised.

In the straight sections in storage rings no radiation is emitted. However the use of insertion devices in these sections with periodic magnetic structures induces oscillations of the beam which causes radiation to be emitted. The spectral and spatial behaviour of the radiation is determined by the nature of the periodic structure in the insertion device [73, 75].

Wigglers are one type of insertion device (ID). They lead to trajectories which are deflected by an angle $> 1/\gamma$ and produce a radiation pattern for each electron which is the incoherent sum of the radiation fields emitted by each magnet. The brightness (flux per solid angle) of the emitted X-rays is increased by a factor corresponding to twice the number of periods of oscillation.

Undulators are another type of ID involving a spatial periodic array of magnetic dipoles which lead to trajectories deflected by an angle $< 1/\gamma$. In this case the radiation emitted from a single electron by each section of magnets sums coherently, leading to a strongly increased photon flux. (The radiation emitted by a pulse of electrons sums incoherently, whilst in a Free Electron Laser the radiation produced by a number of electrons will add coherently leading to a further increase in the beam intensity.) The increase in brightness of the radiation emitted by an undulator over a bending magnet is approximately equal to the square of the number of periods. The lower deflection angle for an undulator as opposed to a wiggler means that the beam divergence is lower, with the result that the radiation emitted by an undulator is more brilliant than from a wiggler.

Third generation sources were developed using storage rings with a low

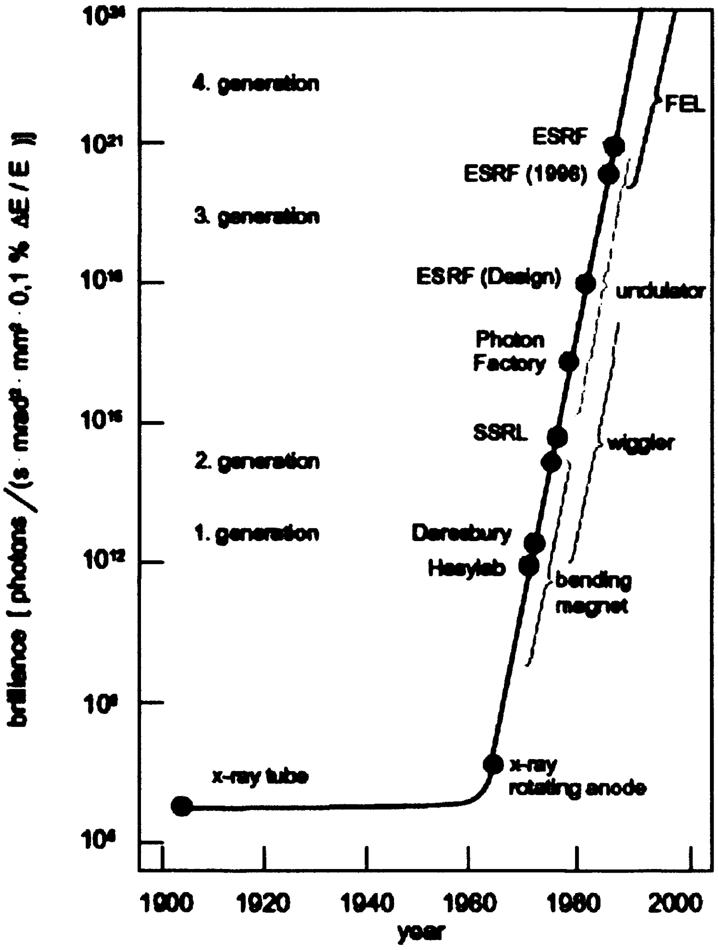

Figure 3.2: The history of the development of X-ray sources and the rise in brilliance.

emittance, i.e. propagating beams with a small cross section and angular divergence, and long straight sections to incorporate insertion devices to produce higher brilliance and a greater degree of spatial coherence. The brilliance of these third generation sources is some 10^{12} times greater than classical X-ray tubes [73], see Fig. 3.2.

The European Synchrotron Radiation Facility (ESRF) is an example of a third generation source, which operates at 6 GeV, and was the first of the hard X-ray sources to come online. Electrons are accelerated in a LINAC up to 200 MeV, before being transferred to a booster where they are accelerated up to 6 GeV. They are then injected into the storage ring where they cycle for several hours. The storage ring has a circumference of 844m. X-rays are generated by bending magnets and insertion devices, each one giving different beam characteristics. Several modes can operate in the ring depending on the number of electron bunches running at the same time, from the single bunch (X-ray pulse useful for biological samples) to uniform mode (continuous generation as used in our experiments).

3.2 X-ray Scattering in Magnetic Materials

The history of magnetic scattering is much shorter than that of classical Thomson charge scattering, but clearly X-rays do have a role to play in the study of magnetic materials since as part of the electromagnetic spectrum they will be sensitive to magnetic, as well as charge, distributions. This effect is the result of a relativistic correction and can be treated with relativistic quantum theory which takes the spin of the electrons into account [76]. In a relativistic theory the space and spin wavefunctions cannot be separated and so a perturbation of an electron by a photon will have an effect dependent on the spin. However, typically the magnetic contribution to scattering is several orders of magnitude smaller than the charge contribution [77], the intensity ratio per electron being given by

$$\frac{\mathrm{I}_{\mathrm{magnetic}}}{\mathrm{I}_{\mathrm{charge}}} = \left|\frac{\hbar\omega}{\mathrm{mc}^2}\right|^2 \tag{3.1}$$

and so it is not until recently with the advent of synchrotron sources capable of producing high brilliance beams, that magnetic x-ray scattering has become a routinely available experimental technique [76].

The magnetic contribution to scattering can be most easily identified when it does not coincide with charge scattering, i.e. when the magnetic order differs from the charge order resulting in a superlattice which produces additional peaks at forbidden positions in reciprocal space, as in an antiferromagnet [78]. However, the magnetic contribution can still be discriminated from the charge contribution even when they overlap, e.g. in ferromagnets. One method for separating the two elements is to use the interference between the imaginary part of the charge amplitude and magnetic amplitude in a sample with a complex Thomson amplitude. This can be manipulated by reversing the direction of an external magnetic field, to find the difference in intensity on changing the orientation of the magnetic moments, leading to the magnetic amplitude [79]. Alternatively the interference induced by circular polarisation can be used to look at the difference caused by a reversal of polarity to find the magnetic scattering amplitude - this is the scattering analogue of X-ray Magnetic Circular Dichroism (XMCD). In addition, magnetic scattering can be identified separately from charge scattering by using the scattered photon beam polarisation state since the two differ. Given the ratio in intensity of the two scattering mechanisms it is obvious that when investigating systems in which magnetic and charge Bragg peaks do coincide it is beneficial to look at peaks where the charge scattering is weak so as to optimise the relative magnetic contribution.

Quadrupolar order has also been observed using non-resonant X-ray Thomson scattering, for example: the spiral arrangement of the aspherical $4f$ shells detected in Holmium as early as 1969 using a laboratory source [80], and AFQ order was observed in NdMg using synchrotron radiation [81]. The great advantage of using non-resonant scattering as a probe of quadrupolar order is that it is possible to obtain the absolute value of the quadrupole moment. However, the count rate is so weak even using the high flux synchrotron radiation that, especially when combined with complicated sample environments, it can be too difficult to collect detailed data sets; and it is for this reason that very few experiments have been successfully performed to investigate quadrupolar order using this technique.

3.3 X-ray Resonant Scattering (XRS)

Large resonant enhancements of X-ray magnetic scattering signals were first reported in Holmium metal [82], when it was observed that there was a significant increase in the signal on tuning the energy through the Ho L_{III}-absorption edge. Enhancements have also been observed at M-edges, and X-ray resonant scattering has been observed in non-magnetic systems displaying orbital ordering [83] and other forms of electromagnetic multipolar order [84,85]. The huge increase in the signal to noise ratio at resonance has allowed a large variety of problems to be studied which were previously intractable.

In classical Thomson X-ray scattering the X-rays scatter from an extended distribution of free electrons such that the scattering length of an atom is simply given by $-r_0 f^0(\mathbf{Q})$, where $f^0(\mathbf{Q})$ is the atomic form factor and r_0 is the Thomson scattering length for an individual electron. The atomic form factor is the Fourier transform of the charge distribution, and is therefore a real number. When absorption processes are included the atomic scattering length becomes complex, with the imaginary part f'' proportional to the absorption cross section. However, a more complicated model than just a cloud of free electrons is required to describe some systems of interest, some of the electrons may be bound in atoms. Classically the response of these bound electrons to the driving force provided by the X-rays is one of a weighted superposition of damped harmonic oscillators [71]. This leads to dispersion corrections, real f' and imaginary f'' of the form factor:

$$f(\mathbf{Q},\omega) = f^0(\mathbf{Q}) + f'(\omega) + \imath f''(\omega) \tag{3.2}$$

These corrections are energy dependent and take their extremal values at the absorption edges, where they are known as resonant scattering terms.

Quantum mechanically resonant scattering can be seen to arise in Second Order Perturbation Theory. Taking an interaction Hamiltonian of the form:

$$\mathrm{H_I} = \frac{e\mathbf{A}\cdot\mathbf{p}}{m} + \frac{e^2 A^2}{2m}, \tag{3.3}$$

where **A** is the vector potential, **p** is the momentum, and m is the electron mass, the transition rate probability between an initial state $|i\rangle$ and a final state $|f\rangle$ of the combined photon target electron system is given in First Order Perturbation Theory by Fermi's Golden Rule:

$$\mathrm{W} = \frac{2\pi}{\hbar}|\langle f|\mathrm{H_I}|i\rangle|^2 \rho(\epsilon_f), \tag{3.4}$$

where $\rho(\epsilon_f)$ is the density of final states. The vector potential is linear in the creation and annihilation operators $\hat{a}^\dagger$ and $\hat{a}$. Therefore, the first term in the Hamiltonian which is linear in $\hat{a}^\dagger$ and $\hat{a}$, can either create or destroy a photon, but not both, and gives rise to photoelectric absorption, see Fig. 3.3(a). The second term in $\mathrm{H_I}$ is quadratic in $\hat{a}^\dagger$ and $\hat{a}$, and so can create and destroy a photon leaving the electron state unchanged, describing elastic Thomson scattering, see Fig. 3.3(b). Going to Second Order Perturbation Theory gives an additional term in the transition probability:

$$\mathrm{W} = \frac{2\pi}{\hbar}\left|\langle f|\mathrm{H_I}|i\rangle + \sum_{n=1}^{\infty}\frac{\langle f|\mathrm{H_I}|n\rangle\langle n|\mathrm{H_I}|i\rangle}{\mathrm{E_i} - \mathrm{E_n}}\right|^2 \rho(\epsilon_f). \tag{3.5}$$

Now the first term in the interaction Hamiltonian can produce scattering via an intermediate state $|n\rangle$, see Fig. 3.3(c), so that an event can be described as:

1. Incident photon destroyed

2. Electron excited into an intermediate state $|n\rangle$

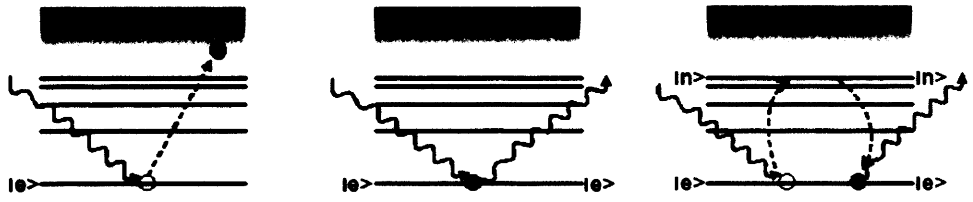

(a) Photoelectric absorption (b) Thomson scattering (c) Resonant scattering

Figure 3.3: X-ray scattering and absorption processes (modified from *Elements of Modern X-ray Physics*).

3. Electron decays back to the initial state by emission of a scattered photon in elastic processes.

Resonant behaviour occurs when the denominator tends to zero, i.e. when

$$\mathrm{E_i} = \hbar\omega + \mathrm{E_e} = \mathrm{E_n}, \tag{3.6}$$

when the incident photon energy is equal to the difference between the ground state and an intermediate state energy. This means that resonant scattering makes a good experimental probe of intermediate atomic states. Due to the Pauli Exclusion Principle, which means that an electron can only be excited into an unoccupied orbital, and the quantum mechanical selection rules, which mean that electric dipole transitions dominate, XRS probes an "exchange interaction" which is sensitive to the magnetization of the *d* and *f* bands. When multipolar interactions split an intermediate state, XRS becomes a probe of the multipolar order in a sample.

There is a clear relationship between absorption and resonant elastic scattering processes, both deriving from the same term in the Hamiltonian, and they are described by the same term in the scattering amplitude [78]. The attenuation coefficient is proportional to the imaginary part of the scattering amplitude in the forward direction, while the resonant scattering intensity is proportional to the square of the amplitude averaged over thermal, concentration and defect fluctuations. The quantities measured in the absorption and resonant scattering processes depend differently on the incident polarisation.

In a radiative transition a photon is emitted with angular momentum $J = 1$. The radiation field will be the sum of electric and magnetic multipolar contributions. Selection rules for the transition requires that total angular momentum and parity are conserved. The transition rate decreases by the order of 10^3 going up through successive multipolar transitions, such that the electric dipole transition dominates. However, in several systems electric quadrupole transitions are also significant, such as in DyB_2C_2 [11]. In UPd_3 we are interested in probing the $5f$ electrons which are directly involved in the quadrupolar order, and we therefore use the uranium M_{IV} edge which connects the core $3d_{3/2}$ states to the $5f$ states via an electric dipole transition. Fortunately, the resonant scattering cross section is easiest to calculate for $E1$ transitions.

3.3.1 Scattering Cross Section

Returning to the scattering factor in Equation (3.2), the resonant terms can be grouped to give the anomalous atomic scattering factor $f_j(\omega) = f'(\omega) + \imath f''(\omega)$, which is given by the expression

$$f_j(\omega) = \frac{m_e}{\hbar^2}\frac{1}{\hbar\omega}\sum_n \frac{(E_n - E_g)^3 M'^{*}_{ng}(j) M_{ng}(j)}{\hbar\omega - (E_n - E_g) - \imath\frac{\Gamma_n}{2}}, \tag{3.7}$$

where $\hbar\omega$ is the photon energy, m_e is the electron mass, E_g is the ground state energy, and E_n and Γ_n are the energy and inverse lifetime of the excited states. The sum is over all the excited states of the system. $M^{(\prime)}_{ng}$ are the transition matrix elements of the matter-radiation interaction

$$M^{(\prime)}_{ng}(j) = \langle \Psi_n | \hat{O}^{(\prime)} | \Psi_g(j) \rangle, \tag{3.8}$$

where $\Psi_g(j)$ is the jth atom ground state, Ψ_n is the photon-excited state. The operator $\hat{O}$ is written using the multipole expansion of the photon field up to the electric dipole ($E1$) and quadrupole ($E2$) terms

$$\hat{O}^{(\prime)} = \epsilon^{(\prime)} \cdot \mathbf{r}(1 - \frac{1}{2}\imath\mathbf{k}^{(\prime)} \cdot \mathbf{r}), \tag{3.9}$$

where $\mathbf{r}$ is the electron position from the absorbing ion, $\epsilon^{(\prime)}$ is the polarisation vector of the incident (scattered) photon and $\mathbf{k}^{(\prime)}$ the corresponding wave vector. Since $M_{ng}^{(\prime)}$ depends only on the electronic part of the operator $\hat{O}^{(\prime)}$, $\epsilon^{(\prime)}$ and $\mathbf{k}^{(\prime)}$ can be factorised out, with the result that the anomalous atomic scattering factor can be rewritten as the scalar product of two irreducible tensors:

$$f_j(\omega) = \sum_{p,q}(-)^q T_q^{(p)} F_q^{(p)}(j;\omega). \tag{3.10}$$

$T_q^{(p)}$ depends only on the incident and scattered polarisations and wave vectors, while $F_q^{(p)}$ contains all the information of the properties of the system [86].

The X-ray Resonant Magnetic Scattering (XRMS) electric dipole ($E1$) amplitude has been formulated [87] as:

$$f_{E1}^{XRMS} = \frac{3}{4|\mathbf{k}|}\left[(\hat{\epsilon}' \cdot \hat{\epsilon})F^{(0)} - \imath(\hat{\epsilon}' \times \hat{\epsilon}) \cdot \hat{\mathbf{z}}_\mathbf{n} F^{(1)} + (\hat{\epsilon}' \cdot \hat{\mathbf{z}}_\mathbf{n})(\hat{\epsilon} \cdot \hat{\mathbf{z}}_\mathbf{n})F^{(2)}\right], \tag{3.11}$$

or

$$f_{E1}^{XRMS} = f_0 + \imath f_1 + f_2, \tag{3.12}$$

where

$$f_0 = (\hat{\epsilon}' \cdot \hat{\epsilon})[F_{11} + F_{1-1}], \tag{3.13}$$

$$f_1 = -(\hat{\epsilon}' \times \hat{\epsilon}) \cdot \hat{\mathbf{z}}_\mathbf{n}[F_{11} - F_{1-1}], \tag{3.14}$$

$$f_2 = (\hat{\epsilon}' \cdot \hat{\mathbf{z}}_\mathbf{n})(\hat{\epsilon} \cdot \hat{\mathbf{z}}_\mathbf{n})[2F_{10} - F_{11} - F_{1-1}], \tag{3.15}$$

and where $\hat{\epsilon}$ and $\hat{\epsilon}'$ are the incident and scattered polarisation vectors, the terms F_{LM} describe the strength of the resonance as determined by the atomic properties of the scatterer, $\mathbf{k}$ is the incident X-ray wavevector and $\hat{\mathbf{z}}_\mathbf{n}$ is a unit vector in the direction of the magnetic moment of the nth ion. Equation (3.11) is a bilinear combination of polarisation vectors and can be rewritten in the form of a 2x2 matrix using the polarisation states σ and π as basis states, showing the polarisation dependence of the scattering [88]. When the vectors $\hat{\mathbf{k}}$, $\hat{\mathbf{k}}'$ and $\hat{\mathbf{z}}_\mathbf{n}$ are resolved into the components $\hat{\mathbf{u}}_1$, $\hat{\mathbf{u}}_2$ and $\hat{\mathbf{u}}_3$ of the diffraction plane coordinate system, see Figure 3.4, one obtains the following expression for the XRMS amplitude:

$$\begin{aligned} f_{E1}^{XRMS} = F^{(0)} & \begin{pmatrix} 1 & 0 \\ 0 & \cos 2\theta \end{pmatrix} \\ - \imath F^{(1)} & \begin{pmatrix} 0 & z_1 \cos\theta + z_3 \sin\theta \\ z_3 \sin\theta - z_1 \cos\theta & -z_2 \sin 2\theta \end{pmatrix} \\ + F^{(2)} & \begin{pmatrix} z_2^2 & -z_2(z_1 \sin\theta - z_3 \cos\theta) \\ z_2(z_1 \sin\theta + z_3 \cos\theta) & -\cos^2\theta(z_1^2 \tan^2\theta + z_3^2) \end{pmatrix}. \end{aligned} \tag{3.16}$$

As can be seen the XRMS scattering amplitude contains three terms, each consisting of a polarisation state dependent geometrical factor and a characteristic scattering ion tensor. The first term simply contributes to the charge Bragg peak, having no dependence on multipolar order. The second term probes a rank 1 tensor with odd time reversal symmetry arising from a net spin polarisation of the $5f$ states, a difference between overlap integrals, resonant energy, or lifetime for the polarisation channels. For this term to be non-zero it is clear from Equation (3.11) that the photon polarisation must be rotated such that $\hat{\epsilon} \neq \hat{\epsilon}'$, and there must be a difference in the resonance strength and therefore transition probability to the intermediate states with $M = \pm 1$. For σ-incident X-rays, the observation of scattering intensity solely in the rotated channel is one of the key signatures of XRMS. The third term in the scattering amplitude probes a rank 2 tensor with even time reversal symmetry and includes two powers of the magnetic moment, producing second harmonic magnetic satellites.

XRMS is a special case of resonant scattering, where the scattering amplitude has been calculated in a cylindrical symmetry, i.e. for a magnetic dipole moment. In general, for polarized light incident on a system with an anisotropic charge distribution described by the tensor scattering factor T, the f_2 term in Equation (3.15) is replaced by

$$f_2 = (\epsilon' \cdot \tilde{T}(Q) \cdot \epsilon)[2F_{10} - F_{11} - F_{1-1}], \tag{3.17}$$

where $\tilde{T}(Q)$ is the Fourier transform of $T(r)$. In a quadrupolar ordered system this scattering amplitude is taken to be proportional to the electric quadrupole moment [10]. The measured intensity is then simply given by [89]

$$I_{\epsilon\epsilon'} \propto |\epsilon' \cdot \tilde{T}(Q) \cdot \epsilon|^2. \tag{3.18}$$

The scattering factor $\tilde{T}(Q)$ is constructed from the individual second rank atomic scattering lengths according to the phase factor, see Appendix B.1. The anisotropic nature of the scattering is observed through the variation of the scattered intensity as a function of the azimuthal angle, Ψ, about the scattering vector. Measurements of the azimuthal dependence of XRS, see Figure 3.4 for the experimental setup, can be compared with calculations for different scattering factors, to determine the details of multipolar order.

While the formalism for XRMS and anisotropic tensor resonant scattering may be different, the two may coexist, such as in the case of $U_{0.75}Np_{0.25}O_2$, which exhibits both magnetic dipole and electric quadrupole order [10], and interference has been observed in GdB_4, which is magnetically ordered and where hybridisation distorts the valence charge distribution resulting in an anisotropic tensor susceptibility [90].

Higher order electromagnetic multipoles are not measurable using the electric dipole resonance. The magnetic octupole and electric hexadecapole can instead be probed directly using the electric quadrupole ($E2$) resonance [91,92], but this is difficult to do, due to the reduced intensity.

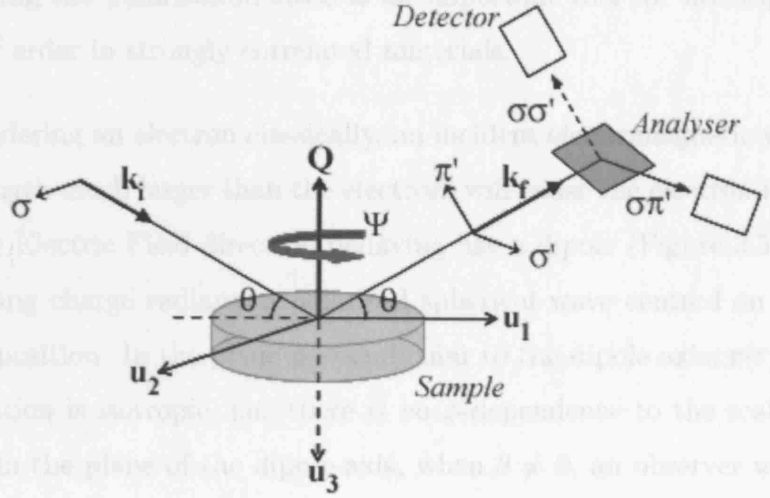

Figure 3.4: A schematic of the experimental set up for measuring the azimuthal dependence of the scattering intensity of a superlattice reflection at $\mathbf{Q}$. σ-polarised X-rays incident at an angle θ on to the sample are scattered by a vector $\mathbf{Q}$. The scattered X-rays are separated into the rotated, π, and unrotated, σ, channels by a polarisation analyser before being detected. The sample stage is rotated to give an azimuthal rotation Ψ about the scattering vector. The unit vectors $\mathbf{u}_i$ define the reference frame.

3.3.2 Polarisation Analysis

One of the most significant features of synchrotron radiation is that it is highly polarised in contrast to the unpolarised laboratory based X-ray sources. The polarisation of incident X-rays effects the angular distribution of the scattered intensity, and as the previous section has shown the XRS scattering cross section depends on the incident and scattered polarisation states. Therefore determining the polarisation state is an important tool for investigating the nature of order in strongly correlated materials.

Considering an electron classically, an incident electromagnetic wave, with a wavelength much larger than the electron, will cause the electron to oscillate along the Electric Field direction behaving like a dipole (Figure 3.5(a)). This accelerating charge radiates a polarised spherical wave centred on the mean electron position. In the plane perpendicular to the dipole axis, $\mathbf{r}(r, \theta = 0, \phi)$, the radiation is isotropic, i.e. there is no ϕ-dependence to the scattering intensity. In the plane of the dipole axis, when $\theta \neq 0$, an observer will see the acceleration of the electron, so that the scattered amplitude varies as $\cos\theta$, see Figure 3.5(b) for the polar diagram showing the angular dependence of the scattering intensity.

We now consider the case of Bragg scattering from a crystal for the two incident linear polarisation cases: π polarisation, where the incident polarisation vector lies in the plane described by the incident wavevector $\mathbf{k}$ and the scattering vector $\mathbf{q}$, and σ polarisation, where the incident polarisation vector is perpendicular to this plane. For an incident π polarised wave the scattered radiation amplitude will vary as $\cos\theta_B$, where θ_B is the Bragg angle, while for incident sigma polarised light there will be no reduction in the scattered intensity. This provides the basis for polarisation analysis.

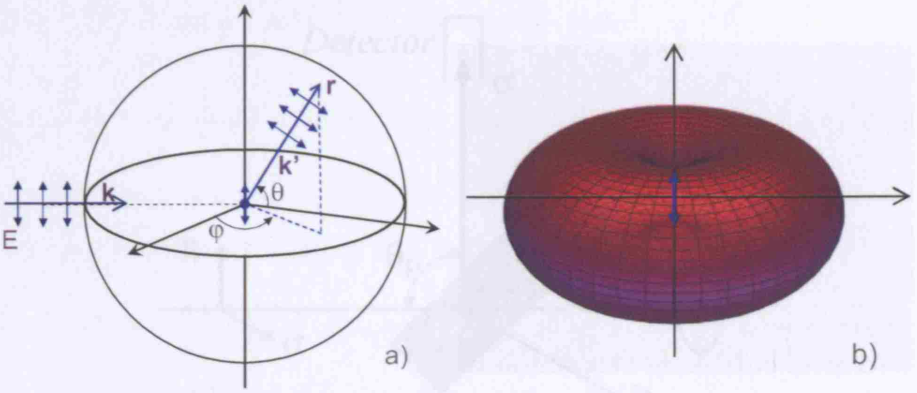

Figure 3.5: (a) Electromagnetic radiation incident on an electron will cause it to oscillate along the Electric Field direction and reradiate a polarised spherical wave centred on its mean position. (b) The angular dependence of the scattering intensity is described by the polar diagram, showing that the intensity is isotropic in the azimuthal plane, but varies as a function of θ in the plane of the dipole.

An analyser crystal is chosen to have a Bragg angle close to 90°. The angle which actually gives the best polarisation selectivity, i.e. the least feed through between polarisation states, is the Brewster angle,

$$\theta_P(\omega) = \frac{\pi}{4} - \frac{\delta(\omega)}{2}, \tag{3.19}$$

which takes the refractive index $n(\omega)$ of the crystal into account, $n(\omega) = 1 - \delta(\omega) + i\beta(\omega)$.

The polarisation state measured by the detector can be selected by rotating the analyser crystal about the incident beam (the η axis). The experimental arrangement of the polarisation analyser for detecting σ and π polarised X-rays is shown in Figure 3.6.

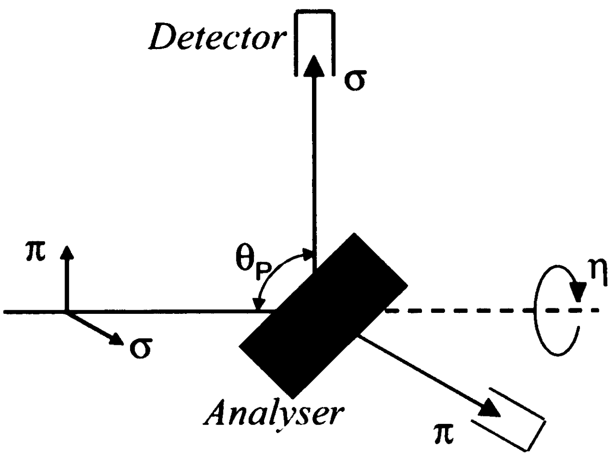

Figure 3.6: Diagram showing polarisation analysis using a crystal analyser. By rotating the crystal about the axis η, the detector can be chosen to measure either the π or σ polarised light.

3.3.3 X-ray Resonant Scattering on ID20 at ESRF

Experiments were made using the ID20 beamline at ESRF. ID20 is optimised for the study of electronic and magnetic properties of solids, in particular charge, magnetic and orbital ordering. To further this aim the instrument has a large tuneable energy range, 3 – 30 keV, very good energy resolution, i.e. $\Delta E/E < 1 \times 10^{-4}$, linear polarisation analysis of scattered photons, and can be used in conjunction with complex sample environments [93].

Ideally the X-ray beam incident on the sample should be monochromatic and linearly or circularly polarised with the unpolarised radiation minimized. Linearly polarised X-rays at energies below 20 keV are obtained on ID20 through the use of a linear undulator installed in the straight section of the storage ring. Below 20 keV the linearly polarized X-ray beam can be circularly polarised using diamond phase plates. At higher energies circular polarisation is provided by an asymmetric wiggler in the straight section of the ring.

The ID20 beamline has been designed such that:

1. the photon polarisation can be changed using a diamond phase plate;
2. experiments can be performed in either the vertical or horizontal scattering plane with analyzer crystals;
3. the front end is UHV compatible, and no graphite filters are used;
4. sensitive optical elements are supported on a girder with hydrostatic level system sensors to optimise optical alignment.

The first hutch on the beamline is the Optics hutch, containing the mirrors, monochromators, slits and monitors for intensity and beam position, see Figure 3.7. There are two mirrors with adjustable curvature covering a wide energy range, which focus the beam at the sample position and reduce the high order harmonics. The first mirror downstream from the source is water cooled (necessary to dissipate the heat load from the incident white beam) and has a curvature to provide a parallel reflected beam. The mirror reduces the vertical divergence of the X-ray beam before it is monochromated, which improves the energy resolution. ID20 has a double crystal monochromator made of two silicon (111) crystals, the first flat and cryogenically cooled, and the second sagitally focussing. The tilt and rocking angles of the second crystal are controlled by piezo actuators. The second mirror is situated after the monochromator. The photon energy can be varied by changing the incident angle onto the mirrors, which is done by changing the mirror curvature using benders.

The second hutch houses the incident beam optics and the EH1 diffractometer. The optic elements include slits, which define the beam size incident on the sample, intensity and position monitors, and attenuators, foils of aluminium, copper and lead of varying thicknesses which can be used to absorb

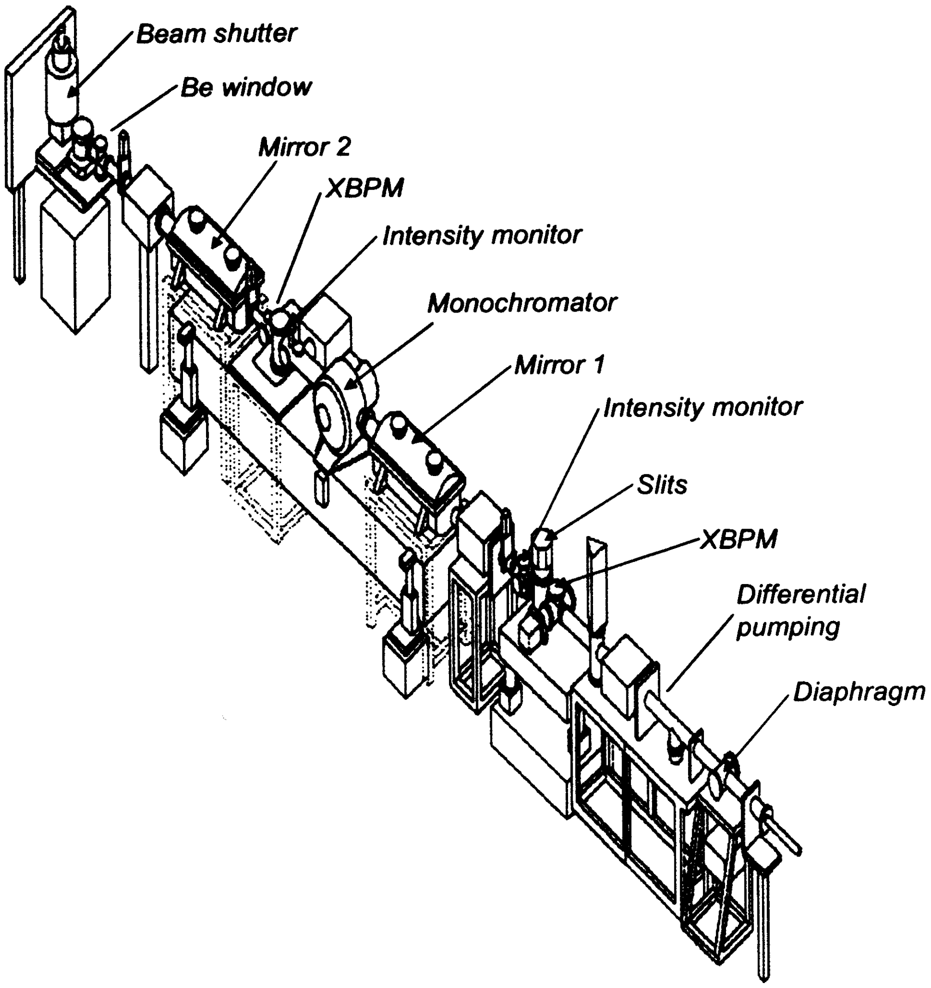

Figure 3.7: Schematic drawing of the optics elements in the first hutch on the ID20 beamline at the ESRF. (XBPM stands for X-ray beam position monitor.)

some of the beam intensity in the case of strong reflections to prevent the detectors being damaged. The monitors and detectors are avalanche photo diodes. Vacuum in the incident flight path is maintained by a Kapton window. The length of the evacuated flight path can be extended so that it is as close to the sample position as possible if necessary. The uranium M_{IV}-edge is low energy, where there is significant attenuation of the beam by the air, so the flight path through air is minimised. The EH1 diffractometer, manufactured by Microcontrôle (Newport), is a four circle diffractometer that can operate in both the horizontal and vertical scattering geometries. Azimuthal scans are performed in the vertical plane. An additional motor ρ is mounted on the χ-circle, which rotates the sample about the face normal. When the face normal is not coincident with the scattering vector, $\rho \neq \Psi$, the azimuthal angle, but the relationship between ρ and Ψ is known.

The design of the cryostat for use with the ID20 diffractometer is of vital importance for the operation of azimuthal experiments. An adapted Ricor closed cycle cryocooler with an additional Joule-Thompson stage is used, designed and built within the cryogenics laboratory at the Institute Laue Langevin. This device is capable of temperatures down to 1.7 K, and can be operated over a wide range of angles without degradation of the base temperature.

To enable polarisation analysis, an analyzer crystal must be chosen with an interplanar d-spacing which equates to an energy close to the resonant energy of the system, so that the Bragg angle is close to 90°. The crystal quality must be high, however the mosaic of the crystal must not be too small, as otherwise the small difference between the absorption edge and the energy associated with the analyser d-spacing will result in poor reflection from the analyser into the detector. For experiments at the uranium M_{IV} edge ($E = 3.725$ keV), the most suitable crystal to use is gold cut with a (111) surface ($d = 2.35454$Å, $E = 3.721$ keV), giving a Bragg angle of 87.3°. By rotating the analyzer

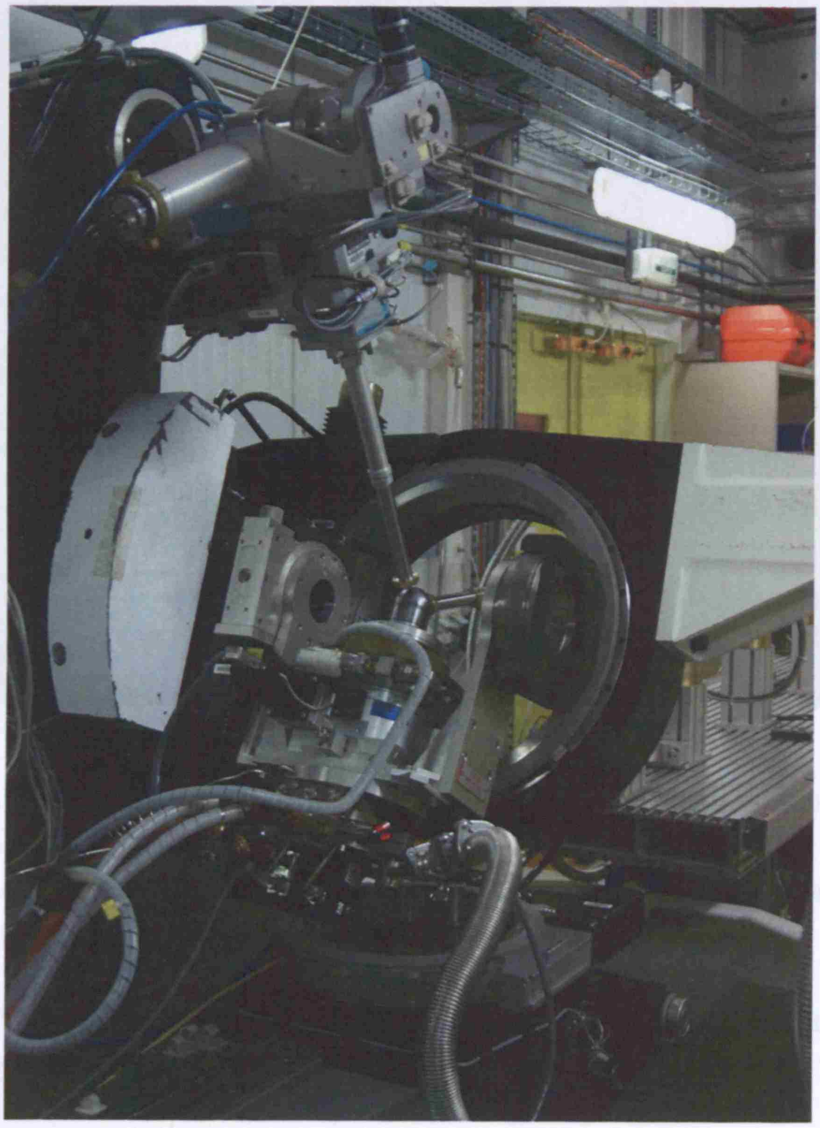

Figure 3.8: Photo of the EH1 diffractometer in the vertical scattering geometry. At the centre of the picture is the outer beryllium dome of the azimuth displex cryostat which contains the sample.

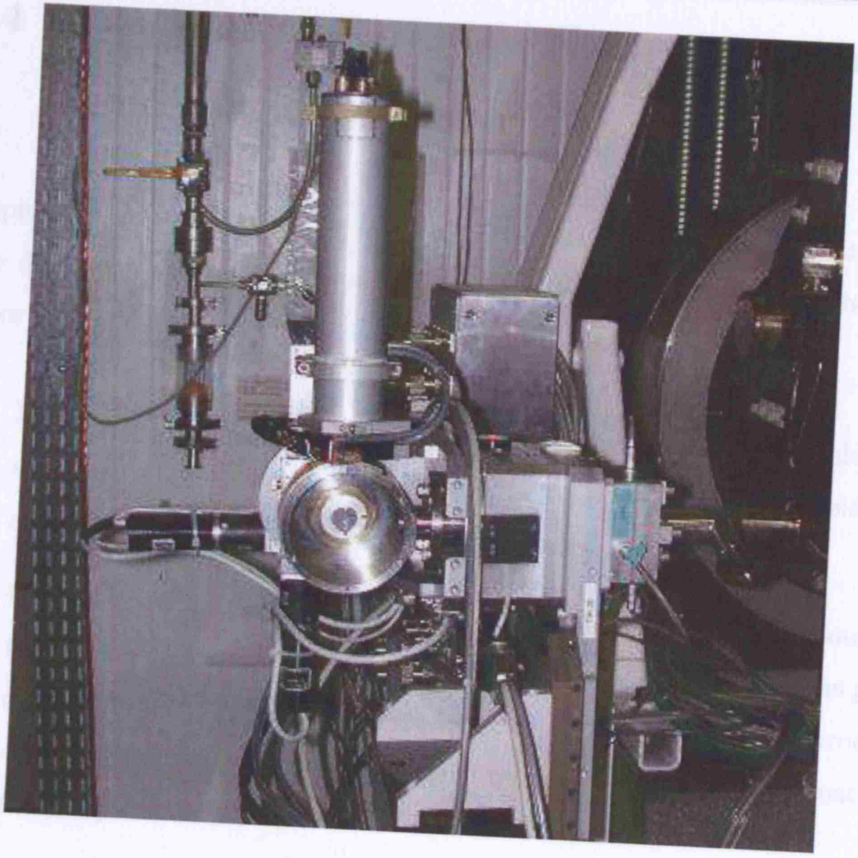

Figure 3.9: This photograph shows the polarisation analysis set up on ID20. The flight tube enters coming from the sample position to the right. The circular aperture at the centre is where the analyser crystal is inserted. The upright tube is the detector arm, which rotates through 90° about the η-axis to change the polarisation detected.

$\eta = 90°$ only the σ or the π-polarized scattered beam will be detected, see Figure 3.9.

3.4 Synchrotron X-rays vs Neutron Scattering from Magnetic Materials

Despite the obvious difficulties in using X-rays to study magnetic materials they do have a number of advantages over neutrons, the previous method of choice [78].

1. Higher Angular Resolution - this leads to higher wavelength resolution and makes it possible to investigate ordering phenomena on correlation scales of the order of microns with high accuracy.

2. Polarisation Analysis - photon beams produced in synchrotron sources are already highly linearly polarized ($\sim 98\%$), while neutron beams produced in reactors and spallation sources are unpolarized, and the process of polarisation leads to a considerable reduction in the flux incident on the sample.

3. Extinction Free Scattering - due to the weakness of non-resonant X-ray magnetic scattering, it is appropriate to interpret the scattering in terms of the First Born Approximation and no extinction correction is required.

4. Static Approximation - the energy resolution of many observations is broad with the result that inelastic events are integrated over to a good approximation, i.e. the total cross section is observed. Therefore in diffuse charge scattering the observed intensity is related to the instantaneous value of the spatial Fourier transform of the spatial distribution of scatterers.

5. Relatively small sample volumes are required. This is advantageous when investigating new materials, as large single crystals are often difficult to produce, which rules out some other experimental probes.

6. Separation of spin and orbital magnetism - it is not possible using neutrons to separate scattering orbital and spin moments merely by choice of scattering geometry, since the neutron's magnetic moment senses the total magnetisation due to spin and orbital contributions $(\mathbf{L}+2\mathbf{S})$. For magnetic X-ray scattering, however, in the dipole approximation the relative amplitudes for the spin and orbital densities are combined with geometrical prefactors in the X-ray scattering amplitude:

   $$f_{X-ray} \propto \langle \mathrm{f}|\alpha \mathbf{L}\cdot\mathbf{A}+\mathbf{s}\cdot\mathbf{B}|\mathrm{i}\rangle, \tag{3.20}$$

   where **A** and **B** are matrices depending on the incident and scattered polarisation, **L** is the orbital angular momentum, **s** is the spin moment, and $|\mathrm{i}\rangle$ and $\mathrm{f}\rangle$ are the incident and scattered states. The magnetic matrix elements $\langle M_{\alpha\beta}\rangle$ for scattering processes with incident and final polarisation vectors α and β can then be written as [94]

   $$\begin{aligned}\langle M_{mag}\rangle &= \begin{bmatrix} \langle M_{\sigma\sigma}\rangle & \langle M_{\sigma\pi}\rangle \\ \langle M_{\pi\sigma}\rangle & \langle M_{\pi\pi}\rangle \end{bmatrix} \\ &= \begin{bmatrix} S_1\sin(2\theta) & 2\sin^2[(L_2+S_2)\cos\theta+S_3\sin\theta] \\ -2\sin^2\theta[(L_2+S_2)\cos\theta-S_3\sin\theta] & \sin 2\theta[2L_1\sin^2\theta+S_1] \end{bmatrix},\end{aligned} \tag{3.21}$$

   where L_i and S_i refer to the Fourier components of the orbital and spin magnetisation densities projected onto the axes $\hat{\mathbf{u}}_i$ as defined in Figure 3.4. With a suitable choice of scattering geometries L_i and S_i can be distinguished.

7. X-ray resonant scattering is element specific, which allows the magnetic ordering of different elements within a compound to be probed individually.

However, neutrons still have some advantages over X-rays as a scattering probe.

1. The scattering cross section of an atom for X-rays is proportional to Z, the atomic number, whereas for neutrons it is non-linear with Z and varies between different isotopes of the same atom, due to the interaction with the nucleus as opposed to the electrons. This makes it possible with neutrons to sense light atoms such as hydrogen in the presence of heavier ones, and allows isotopic substitution.

2. The weak nature of the interaction between the neutron and the nucleus makes neutrons a much more deeply penetrating probe. As a result the bulk of a material is probed as opposed to just the surface region, and it is more simple to use complex sample environments, such as cryostats, magnets and pressure cells.

3. Whilst in most cases magnetic diffraction can only be performed at resonant energies using X-rays, there is no such resonant condition using neutrons. Since neutrons are spin 1/2 particles they have a magnetic moment which couples directly to the spatial variations in magnetisation in a material, and the charge and magnetic scattering cross sections are of the same order of magnitude. As a result magnetic diffraction can be performed using neutrons with a smaller wavelength, such that a much larger region of reciprocal space is accessible.

4. Neutrons and X-rays used as condensed matter probes have comparable wavelengths, however the energies are markedly different. Neutron energies vary from μeV to eV and therefore neutrons are suited to inelastic studies of lattice and magnetic excitations, enabling the determination of exchange coupling constants. Inelastic X-ray scattering is much more complicated and is not feasible for magnetic excitations.

5. The analysis of magnetic scattering by neutrons requires few corrections to the data and it is possible to measure absolute intensities, by normal-

ising to the incoherent scattering from a vanadium sample. Using the ratio of magnetic to Bragg peak intensities the magnitude of magnetic moments can be determined. The theory of magnetic neutron scattering is well established.

Chapter 4

Macroscopic Experimental Techniques

This chapter outlines the different experimental techniques used in the bulk measurements described in this thesis, and the synthesis of our polycrystalline and single crystal samples.

4.1 Sample Preparation

4.1.1 Polycrystalline samples

Polycrystalline ingots of (U,Np)Pd_3 were produced by arc-melting stoichiometric amounts of the constituent elements on a water cooled copper hearth using a zirconium getter, under an atmosphere of high purity argon. Starting materials used were in the form of 4N palladium and 3N uranium metals, and 3N neptunium metal, which was made available through a loan agreement between Lawrence Livermore National Laboratory and ITU, within the frame-

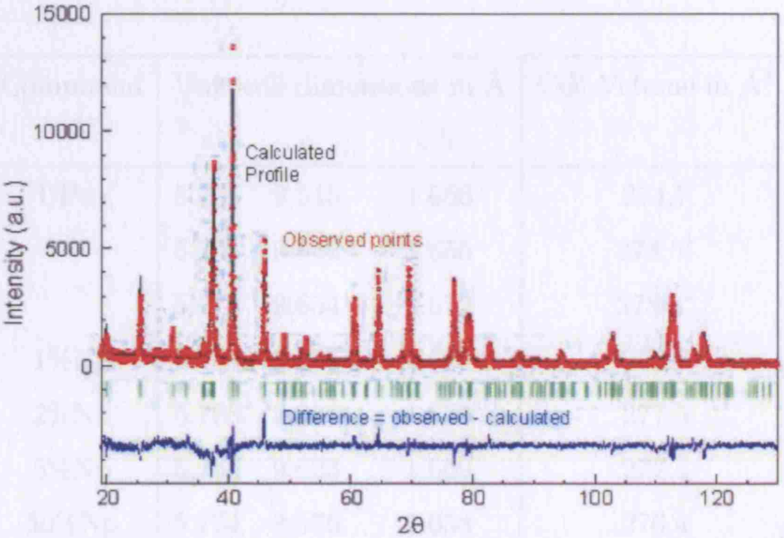

Figure 4.1: X-ray powder diffraction pattern of $NpPd_3$ ($TiNi_3$-structure). The solid line through the data is the Rietveld-type full refinement. The weighted R-factor is 6.2 % indicating the absence of other phases, e.g. the cubic phase.

work of a collaboration involving LLNL, Los Alamos National Laboratory and the US Department of Energy. ^{237}Np is an alpha emitter ($\tau_{1/2} = 2.14 \times 10^6$ years) and therefore the samples were prepared in a glove box. Homogeneity of samples was ensured by repeated turning and remelting of the buttons, followed by annealing them at 1300°C for one week. The phase purity of the samples is of great importance in the case of the doped samples, where it is important to establish that only one phase is present, and that it has the required double-hexagonal close-packed structure (dhcp), and for $NpPd_3$, which exists in one of two phases: cubic $AuCu_3$-type and dhcp $TiNi_3$-type, being the phase in which we are interested. Sample phase purity was checked using X-ray (Cu K_α) powder diffraction data collected on a Bragg-Brentano Siemens D500 diffractometer using a 2θ step size of 0.02 degrees. A Rietveld-type full profile refinement of the powder pattern for each sample checked the phase purity, see Figure 4.1 for the powder pattern with Rietveld refinement of $NpPd_3$, and gave the lattice parameters shown in Table 4.1.

Compound	Unit cell dimensions in Å			Cell Volume in Å^3
	a	c	c/a	
UPd$_3$	5.765	9.545	1.656	274.7
	5.763	9.542	1.656	274.5†
	5.775	9.654	1.672	278.8*
1%Np	5.769	9.635	1.670	277.7
2%Np	5.768	9.631	1.670	277.5
5%Np	5.766	9.623	1.669	277.1
50%Np	5.774	9.576	1.658	276.4
NpPd$_3$	5.765	9.545	1.656	274.7

Table 4.1: The structural parameters of DHCP $(U_{1-x}Np_x)Pd_3$ compounds, determined by Rietveld-type full refinement of powder XRD, prepared and measured at ITU, apart from † and ∗ [95], corresponding to Pd and U rich samples respectively.

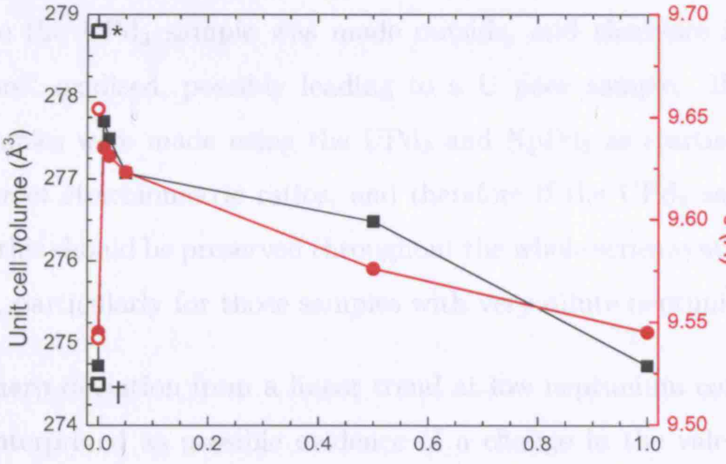

Figure 4.2: The variations of cell volume and c-axis parameter as a function of x in $(U_{1-x}Np_x)Pd_3$ do not obey Vegard's Law. The plot does not include data points taken from [95] for U rich (∗) and U poor (†) UPd$_3$ samples.

Figure 4.2 shows the cell volume and c-axis parameter of $(U_{1-x}Np_x)Pd_3$ as a function of x for the lattice parameters obtained from our powder XRD given in Table 4.1. Interestingly, the cell volume rapidly increases with the addition of just 1% neptunium before decreasing with further neptunium doping. This is not the standard behaviour and violates Vegard's Law, an approximate empirical rule which holds that the lattice constant of an alloy varies linearly as a function of the concentrations of the constituents [96].

Also given in Table 4.1 are further values for the lattice parameters of UPd_3 from the literature, reflecting the observation of a homogeneity range around the exact UPd_3 composition: 23.3 to 24.8 atomic percent uranium [95], which effects the lattice parameters significantly. Based on these measurements it could appear that our UPd_3 sample is more palladium rich. If the doped samples were more actinide rich, this could provide an explanation for the apparent violation of Vegard's Law, but all the samples were made in the same way. The samples containing Np were necessarily produced in a glovebox, while the UPd_3 sample was made outside, and therefore it may have been "more" oxidised, possibly leading to a U poor sample. However, the mixed samples were made using the UPd_3 and $NpPd_3$ as starting materials, in the correct stoichiometric ratios, and therefore if the UPd_3 sample was U deficient, this should be preserved throughout the whole series synthesised from the UPd_3, particularly for those samples with very dilute neptunium doping.

The sharp deviation from a linear trend at low neptunium concentrations may be interpreted as possible evidence of a change in the valence state of Uranium. Uranium is tetravalent in UPd_3, while neptunium is trivalent in $NpPd_3$, see Chapter 6. The ionic radius of U^{4+} is obviously smaller than that of U^{3+} (10.3 Å vs 11.6 Å), and so if the neptunium doping caused a valence change on the uranium ions, a rapid expansion of the unit cell may be expected. The possibility of an induced valence change could be investigated

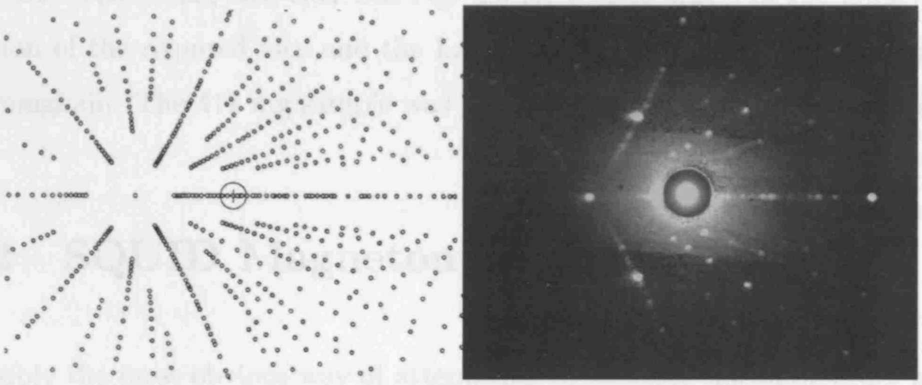

Figure 4.3: Left hand image is of the simulation obtained in Orient Express for a UPd_3 reciprocal space (207) face, and the right hand image is the Laue photograph taken in that orientation.

through photoemission and X-ray absorbtion spectroscopy. Deviations from Vegard's Law are also associated with strains within the unit cell arising from doping.

The homogeneity range also leads to questions about the actual actinide content in our samples, in particular the actual neptunium content in the nominally 1%Np sample.

4.1.2 Single crystal UPd_3

A single crystal of UPd_3 was grown using the tri-arc Czochralski pulling method [97] starting with 4N palladium and 3N uranium metals by Dr. D. Fort in the Department of Metallurgy at the University of Birmingham. The crystal was cut using a spark cutter with a reciprocal space (207) face, in orthorhombic notation, to enable the superlattice reflections of interest: (103) and (104), to be reached by only tilting the sample two degrees off-specular. *Orient Express* was used to simulate the Laue photograph, which would be obtained when the crystal was mounted in the required orientation, to ensure that the correct face was cut. See Fig. 4.3 for a comparison of the Laue simulation of the required face and the Laue photograph of the sample taken in Birmingham. The 417 mg sample was polished with 0.25 μm diamond paste.

4.2 SQUID Magnetometry

Possibly the most obvious way of attempting to measure magnetic order is to make a conventional measurement of magnetization, essentially a measurement of a sample's net magnetization divided by the sample volume. A SQUID (superconducting quantum interference device) is one of the most sensitive ways of doing this. A SQUID contains a ring made out of two superconductors separated by a thin layer ($\sim$ 1 nm) of insulating material, making up two Josephson junctions through which electron Cooper pairs tunnel, leading to a current [98]. The maximum or *critical* current depends on the temperature, and the width and material of the insulator. The magnetic flux density in the loop is quantised in flux quanta. Due to the interference between the currents passing through the two junctions the *critical* current in the loop is maximised when the applied external field is an integer multiple of the flux quantum in the ring, and minimised when the field is a half-integer multiple. By measuring the modulation of the current as a sample is moved through the ring the sample magnetic field is determined.

Magnetization measurements were carried out using a Quantum Design-SQUID magnetometer (MPMS-7) in fields up to 7 T for a range of temperatures in each sample. Magnetic susceptibility measurements were also made for T = 2 - 300 K in a range of fields for the different samples.

4.2.1 Sample encapsulation and decontamination

In SQUID measurements it is essential that the magnetic contribution from the sample holder must be as small as possible. However, since the samples are radioactive, the encapsulation must ensure that all users and instruments outside the glove boxes are protected from contamination. Within a glove box the sample is enclosed in a 20 cm long plexiglass container, which is much longer than the sample itself, but which means that as the sample is moved up and down through the SQUID, the diamagnetic plexiglass signal is constant. The plexiglass rod is then wrapped in teflon tape and sealed in a plastic envelope. It is then transferred to a second glove box, where the plastic envelope is removed, for decontamination. The teflon coated rod is sprayed with hair spray, fixing any decontamination to the teflon tape. The tape can then be removed and a Geiger counter used to check that the plexiglass rod has been decontaminated. Finally the rod is encased in a tube made of a copper nickel zinc alloy with a low paramagnetic signal. The combined encapsulation magnetic contribution of the plexiglass and alloy has been measured and modelled, and can be subtracted off from the total signal using:

$$M(T,H) = \left(3.972 \times 10^{-8} - \left(\frac{2.15 \times 10^{-7}}{T + 8.73}\right)\right) H, \tag{4.1}$$

where T is in Kelvin, H in Gauss and M in emu.

4.3 Electrical Resistivity

Electrical resistivity measurements were made using a Quantum Design PPMS (Physical Properties Measurement System) [99] in the temperature range 2 – 300 K in magnetic fields up to 9 T. The measurement uses four probes which rest on the sample, as shown in Figure 4.4. Contact is made using screws to

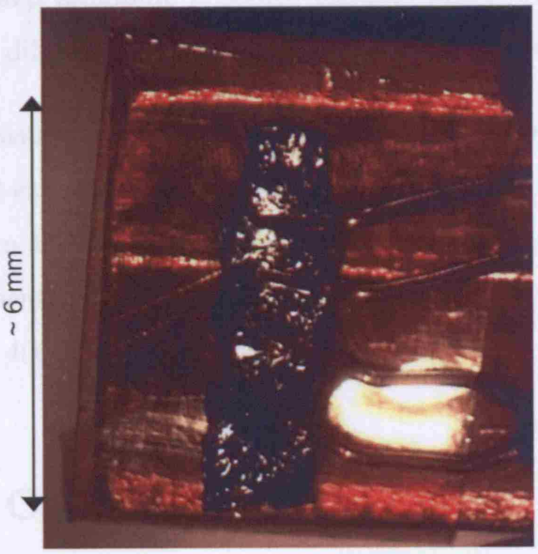

Figure 4.4: Photograph of $(U_{0.95}Np_{0.05})Pd_3$ sample with four resistivity screw contacts.

position the probes. The probes are arranged such that the outer two probes transmit the current, while the inner two measure the potential difference. The resistivity is then calculated using Ohm's Law:

$$V = I \times R \tag{4.2}$$

and the resistivity determined from the sample and probe geometry:

$$\rho = \frac{R \times A}{l} \tag{4.3}$$

Before encapsulating the sample, each contact is checked using an ohm meter. The sample is mounted onto a support which can be connected to the PPMS measurement stick, and then enclosed in a cap, before being decontaminated in the same way as the SQUID samples.

Measurements were made in AC mode, in which the current applied to the sample varies with a frequency of 50 Hz. The measured voltage is the average of the maximum and minimum absolute voltage values, which minimises the residual potential difference contributions from the electrical contacts.

Additional measurements were also made using the 4 point contacts technique with current excitations of 3.2 mA above $T = 5$ K and 1 mA below. Temperatures less than 1.5 K were obtained using 2 coupled cryompump devices (^{3}He$-^4$He). Self heating effects make it impossible to cool samples containing neptunium below 400 mK.

4.4 Heat Capacity

Specific heat measurements are also made using the QD PPMS [99] via the hybrid adiabatic relaxation method, which combines the best measurement accuracy and error analysis. Details of the experimental apparatus are given in Figure 4.5. With the addition of a ^{3}He refrigeration insert, the heat capacity can be measured over the range $T = 0.4 - 400$ K, in fields up to 9 T.

Each heat capacity measurement consists of a number of stages. First the sample platform and the puck which contains it are stabilised at the required temperature. Secondly, for a chosen length of time, power is applied to the sample platform heater, resulting in the platform temperature increasing. The power is then turned off and the platform temperature relaxes back exponentially to that of the puck. The heat capacity can then be calculated using the *two-tau model* [100], which allows the flow of heat between the platform and puck to be simulated.

A thorough description of the encapsulation of actinide samples for heat capacity measurements at the Institute for Transuranium elements has been published by Javorsky *et al.* in [101].

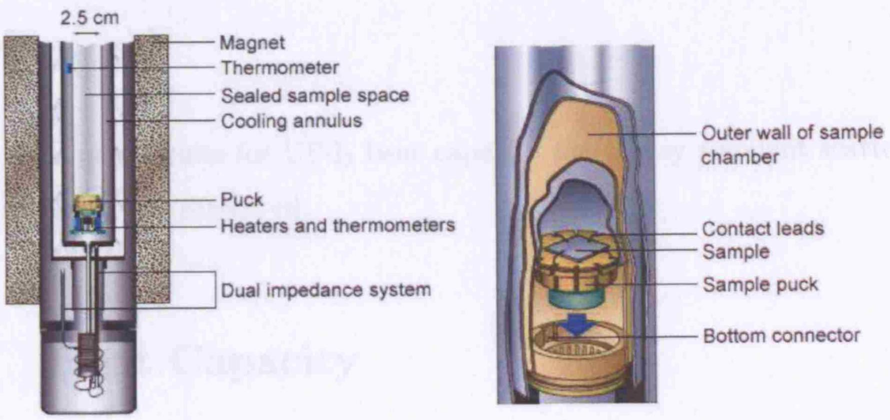

Figure 4.5: Diagrams showing details of the PPMS probe for heat capacity measurements adapted from the Quantum Design website [99].

Chapter 5

Results I - UPd_3

In this chapter results for UPd_3 heat capacity and X-ray resonant scattering measurements are presented.

5.1 Heat Capacity

Previous heat capacity experiments were made before the T_{+1} and T_{-1} transitions had been distinguished through ultrasonics measurements [25], and so new accurate heat capacity measurements have been performed to determine if the two transitions could be separated. The heat capacity of a polycrystalline sample of 51.33 mg UPd_3, synthesized as described in chapter 4.1.1, was measured from $T = 2 - 300$ K using a PPMS-9 Quantum Design calorimeter in the Actinide UserLab at the Institute for Transuranium Elements. A 16.79 mg $ThPd_3$ sample was also measured to determine the phonon contribution, since $ThPd_3$ is isostructural but non-magnetic.

Figure 5.1 a) shows C_P/T for both UPd_3 and $ThPd_3$ indicating that at temperatures greater than 50 K the heat capacity of UPd_3 is dominated by

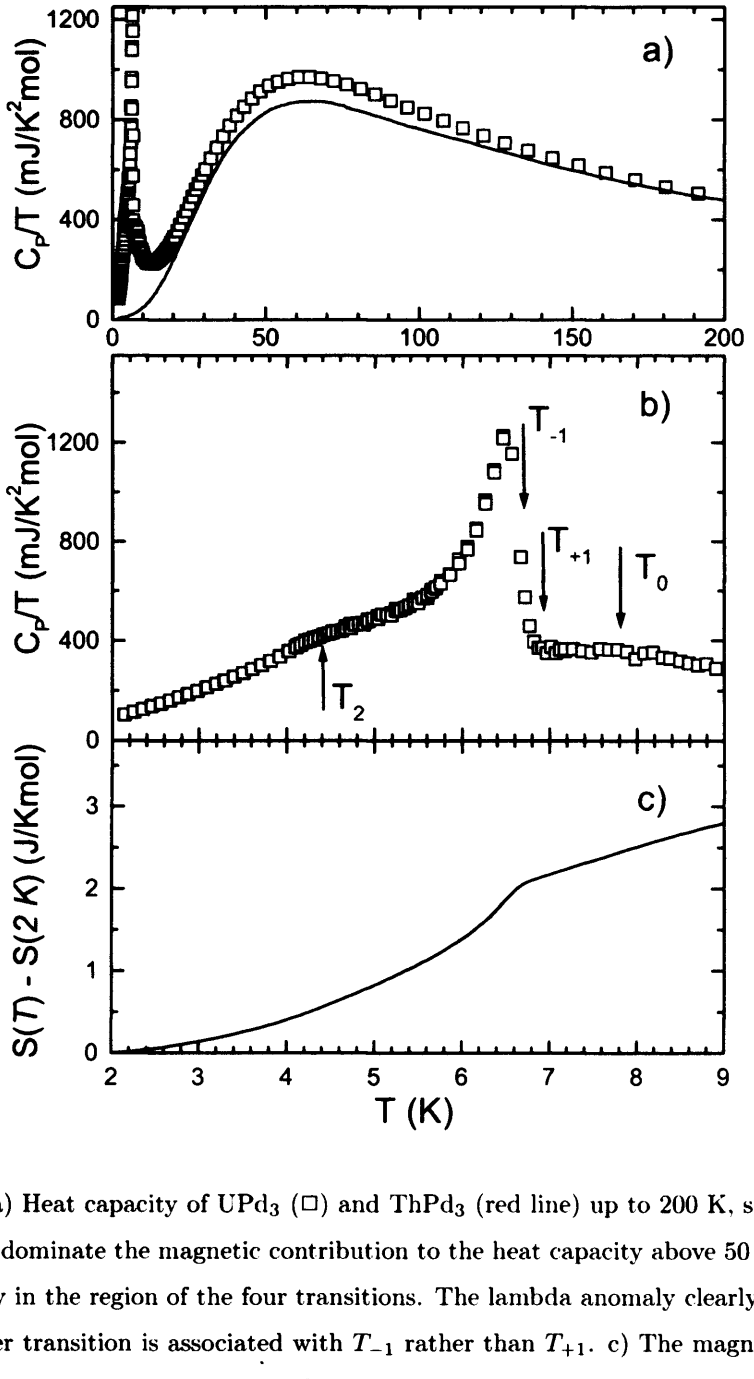

Figure 5.1: a) Heat capacity of UPd_3 (□) and $ThPd_3$ (red line) up to 200 K, showing that the phonons dominate the magnetic contribution to the heat capacity above 50 K. b) UPd_3 heat capacity in the region of the four transitions. The lambda anomaly clearly shows that the first order transition is associated with T_{-1} rather than T_{+1}. c) The magnetic entropy of UPd_3 at low temperatures deduced after subtraction of the phonon contribution given by $ThPd_3$. This shows that the significant change in entropy occurs at T_{-1}.

the phonon contribution. The low temperature data plotted in 5.1 b) reveal a clear lambda anomaly associated with the T_{-1} transition. There is a shoulder in the data at T_2 and a less well defined feature at T_0, although in plots of C_P vs T it is an obvious maximum. No clear features are associated with the T_{+1} transition.

The heat capacity of UPd_3 is the sum of different contributions:

$$\begin{aligned} C_U &= C_{mag} + C_{ph} + \gamma_U T \\ &= C_{mag} + C_{Th} - \gamma_{Th} T + \gamma_U T, \end{aligned} \tag{5.1}$$

where C_{mag} is the magnetic heat capacity, C_{ph} is the phonon contribution and γT is the electronic term. The presence of the quadrupolar transitions at low temperatures makes it very difficult to estimate the Sommerfeld coefficient, γ, in UPd_3; estimates in the literature vary between 2.5 [40] and 9.5 [37] mJ/K^2. Making a fit to the $ThPd_3$ data for

$$\frac{C}{T} = \gamma + \beta T^2, \tag{5.2}$$

gives $\gamma = 1.0 \pm 0.2$ mJ/K^{2}mol and $\beta = 0.422 \pm 0.004$ mJ/K^{4}mol, which in turn gives a Debye Temperature of $\Theta_D = 166.5 \pm 0.5$ K, the temperature above which all vibrational modes are excited [102], since

$$\beta = \frac{12\pi^4}{5\Theta_D^3} N_A k_B. \tag{5.3}$$

At high temperatures the equal thermal population of the different crystal field levels results in the magnetic entropy plateauing, as there can be no further disorder. As the magnetic heat capacity is dependent on the temperature derivative of the magnetic entropy, at high temperatures the magnetic contribution to the heat capacity tends to zero. This can be demonstrated easily using a simple two level model with an energy gap Δ. The energy of the

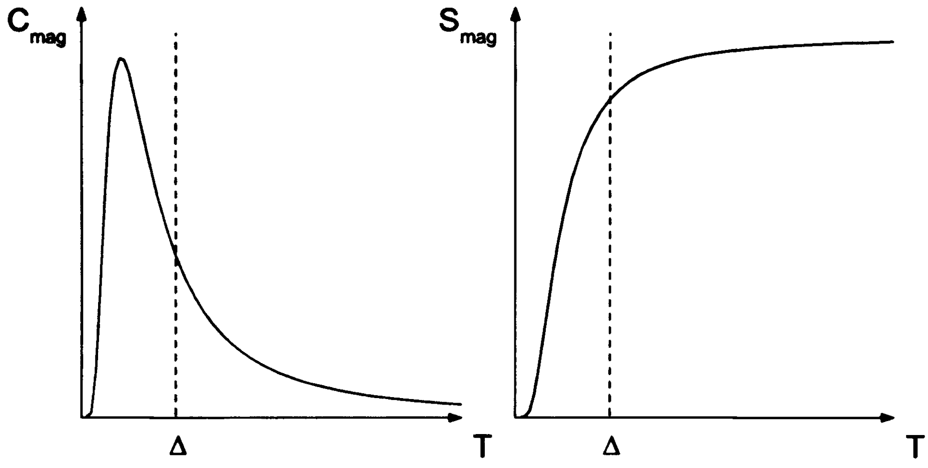

Figure 5.2: The magnetic heat capacity and entropy of a two level system with an energy gap Δ.

system as a function of temperature is then given by

$$\begin{aligned} E(T) &= \frac{\sum_i \epsilon_i \exp(-\epsilon_i/k_BT)}{\sum_i \exp(-\epsilon_i/k_BT)} \\ &= \frac{\Delta}{\exp(\Delta/k_BT)+1}. \end{aligned} \tag{5.4}$$

From this the heat capacity can be calculated using dE/dT and is shown in Figure 5.2, along with the magnetic entropy. The peak seen in C_{mag} is the Schottky anomaly. Therefore at 300 K the heat capacity of both samples is given by the electronic plus the lattice heat capacities, and at $\sim$ 100 J/Kmol is in accordance with the Dulong-Petit expression $C_V = 3nk_BN_A$ for the high temperature limit of the lattice heat capacity, since as mentioned above the electronic heat capacity of both is small.

By subtracting the phonon contribution and correcting for the electronic contribution the heat capacity associated with the crystal field levels is determined. The entropy is then calculated using

$$\Delta S(T) = S(T) - S(T = 2\text{K}) = \int_2^T \frac{C_{mag}}{T} dT, \tag{5.5}$$

and is shown in Figure 5.1c). It is clear that the only significant change in the entropy is at T_{-1}, i.e. there is only one strongly 1^{st} order phase transition. This effects the matrix elements for the order parameters. Using the three-level model for the ground state doublet:

$$\begin{aligned} |d_1\rangle &= a|4\rangle + b|1\rangle + c|-2\rangle \\ |d_2\rangle &= a|-4\rangle - b|-1\rangle + c|2\rangle \end{aligned} \tag{5.6}$$

and first excited singlet state:

$$|s\rangle = d|3\rangle + e|0\rangle - d|-3\rangle \tag{5.7}$$

on the quasi-cubic sites, developed by McEwen *et al.* [26], the operator matrices can be written as follows,

$$\begin{aligned} \hat{Q}_{\mathrm{x^2-y^2}} &= \begin{pmatrix} 0 & A & A \\ A & 0 & B \\ A & B & 0 \end{pmatrix} \quad \hat{Q}_{\mathrm{zx}} = \begin{pmatrix} 0 & A' & A' \\ A' & 0 & B' \\ A' & B' & 0 \end{pmatrix} \\ \hat{Q}_{\mathrm{xy}} &= \begin{pmatrix} 0 & -Ai & Ai \\ Ai & 0 & -Bi \\ -Ai & Bi & 0 \end{pmatrix} \quad \hat{Q}_{\mathrm{yz}} = \begin{pmatrix} 0 & A'i & -A'i \\ -A'i & 0 & B'i \\ A'i & -B'i & 0 \end{pmatrix}, \end{aligned} \tag{5.8}$$

where the $A^{(\prime)}$ terms mix the singlet with the doublet states and the $B^{(\prime)}$ terms split the doublet. It is important to note that there are only two symmetries for the four quadrupolar operators, such that a non-zero $\langle\hat{Q}_{\mathrm{x^2-y^2}}\rangle$ implies that a non-zero $\langle\hat{Q}_{\mathrm{zx}}\rangle$ will be induced, and vice versa, while a similar situation occurs for $\langle\hat{Q}_{\mathrm{xy}}\rangle$ and $\langle\hat{Q}_{\mathrm{yz}}\rangle$.

The symmetries of the $\hat{Q}_{x^2-y^2}$ and $\hat{Q}_{zx}$ operators: $\hat{Q} \neq -\hat{Q}$, mean that within Landau Theory there should be at least two first order transitions, contradicting the data which indicates that there is only one strongly first order transition at T_{-1}. Since the $B^{(\prime)}$ term splits the ground doublet, leading to entropy changes at the transition, either B or B' must be $\simeq 0$, to make $\hat{Q} = -\hat{Q}$ for either $\hat{Q}_{x^2-y^2}$ or $\hat{Q}_{zx}$, such that there can be just one strongly first order transition.

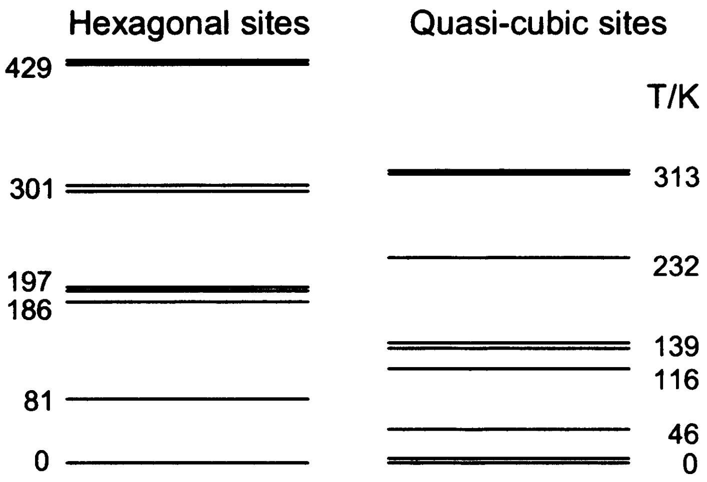

Figure 5.3: Crystal field level scheme for the hexagonal and quasi-cubic sites in UPd_3 with eigenvalues expressed as temperatures in Kelvin.

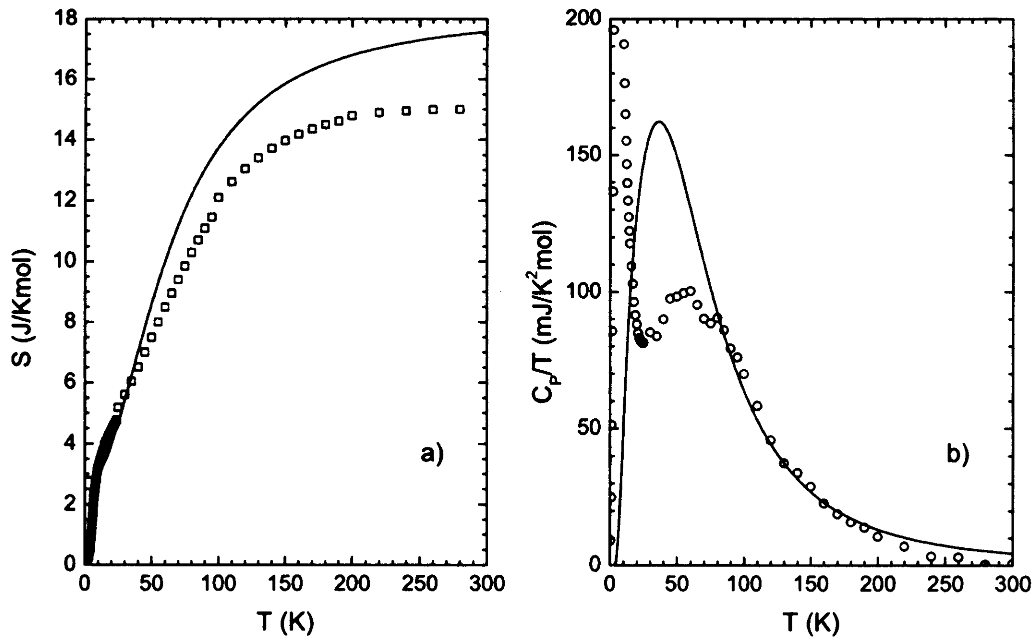

Figure 5.4: A comparison for a) the entropy and b) C_P/T of UPd_3 for our measured data and calculated values (black lines) based on the CEF scheme in Figure 5.3.

The entropy deduced from our measurements can be compared to calculations based on different energy level schemes. An example scheme deduced from inelastic neutron scattering and magnetic measurements [103] is given in Figure 5.3. Uranium is tetravalent ($5f^2$) [33], which, using Hund's Rules supposing Russell-Saunders coupling, gives $S = 1$, $L = 5$ and $J = 4$, and therefore there are 9 levels on each of the cubic and hexagonal sites. Optical spectroscopy and free-ion calculations have indicated that the ground state for U^{4+} is actually an admixture of 88% $^3H_4$ and 11% $^1G_4$ [104], arising from jj coupling, and which also has nine levels on each site type. Therefore the maximum entropy should be $R \ln 9$. Our heat capacity measurements were only made up to 300 K so that we would not expect all the levels to be equally populated, but there will be some population of the high energy levels at 300 K.

Figure 5.4 a) shows the deduced entropy from our measurements compared with the calculation based on the level scheme in Figure 5.3. There is an obvious discrepancy between the data and the calculation, there is "missing" entropy in our data. The calculated heat capacity does not include the effect of the quadrupolar order, and so does not reproduce the lambda transition. The calculated Schottky anomaly at $\sim$ 50 K based on the proposed crystal field level scheme is clearly larger than that in the data, and centred at a lower temperature, indicating that this level scheme may include too many low lying energy levels. Inelastic neutron scattering measurements are being performed to identify excitations associated with transitions between different crystal field energy levels. This should help to establish an improved crystal field level scheme on the quasi-cubic sites, but on the hexagonal sites the ground state is only dipole coupled to the first excited doublet and so neutrons cannot be used to identify the other higher energy hexagonal crystal field levels.

The heat capacity was also measured in different magnetic field strengths:

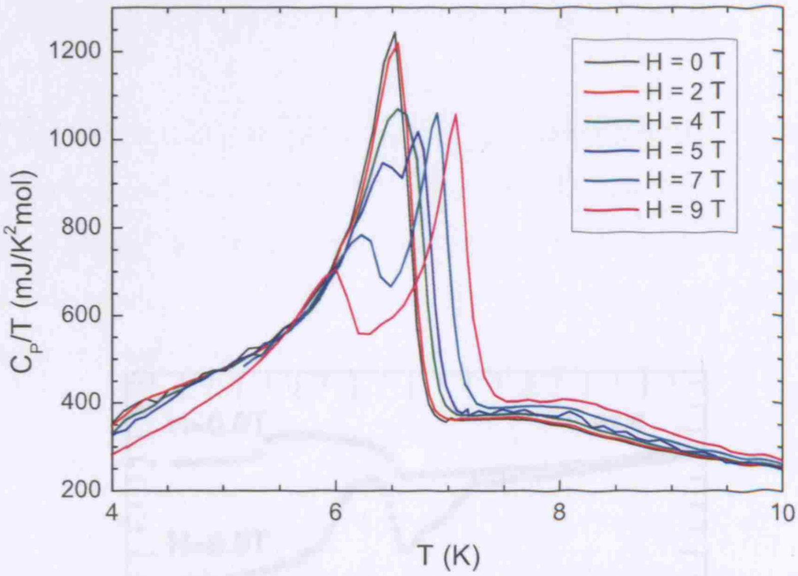

Figure 5.5: Heat capacity of polycrystalline UPd_3 in a range of magnetic fields $H = 0 - 9$ T.

$H = 0 - 9$ T, see Fig. 5.5. In fields up to 3 T, C_P/T shows very little change. In 4 T the main peak associated with T_{-1} is reduced in magnitude but slightly broader, while the features associated with the other transitions are unchanged. In 5 T the "T_{-1} peak" splits into two, while the "T_2" feature is less obvious. In higher fields the "T_{-1} peaks" split further apart, the "T_2" feature is smoothed away while the "T_0" feature becomes sharper. These measurements were made on a polycrystalline sample, which introduces a lot of complications. UPd_3 is strongly anisotropic, with clear differences in the ways that the transition temperatures evolve as a function of the magnetic field, depending on whether the field is applied axially or in the basal plane, see Figure 5.6.

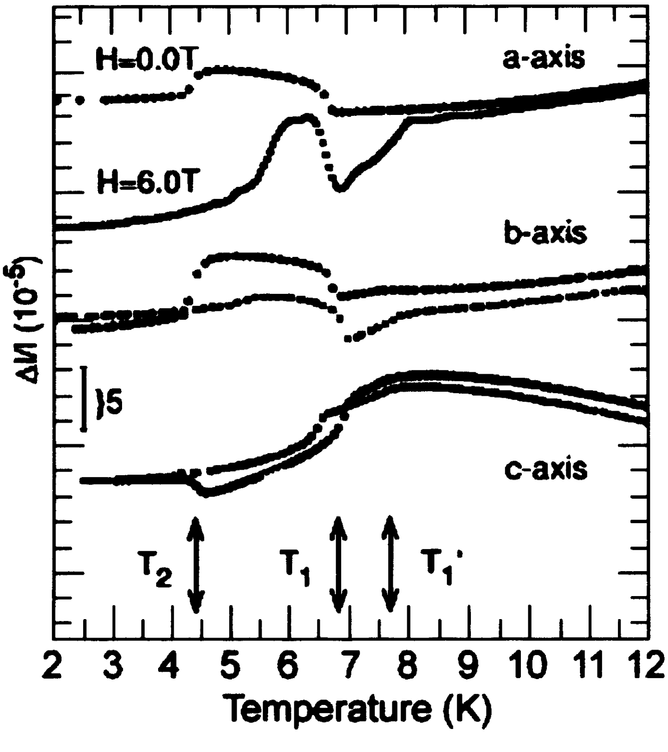

Figure 5.6: Thermal expansion of UPd_3, measured along the symmetry axes in zero field and $H = 6$ T, showing the anisotropy in the evolution of the transitions with applied field [40].

5.2 X-ray Resonant Scattering

In the following section describing our X-ray resonant scattering measurements, we have used the orthorhombic notation for the unit cell, as shown in Figure 5.7. In real space the b-axis of the orthorhombic cell is defined to be parallel to the a_2-axis of the hexagonal cell, with $|\mathbf{b}| = |\mathbf{a_2}|$, and $|\mathbf{a}| = |\mathbf{a_1}\sqrt{3}|$. The reciprocal space vectors are defined according to:

$$\mathbf{a}_\mathrm{i}^* = 2\pi\frac{\mathbf{a}_\mathrm{j} \times \mathbf{a}_\mathrm{k}}{[\mathbf{a}_\mathrm{i} \cdot \mathbf{a}_\mathrm{j} \times \mathbf{a}_\mathrm{k}]}, \qquad (5.9)$$

with the result that orthorhombic reciprocal space vector $\mathbf{a}^*$ is parallel to the hexagonal reciprocal space vector $\mathbf{a}_1^*$, but $|\mathbf{a}^*| = \frac{1}{2}|\mathbf{a}_1^*|$, such that a superlattice reflection labelled $(\frac{1}{2}03)$ in hexagonal notation, is indexed as (103) in the orthorhombic notation.

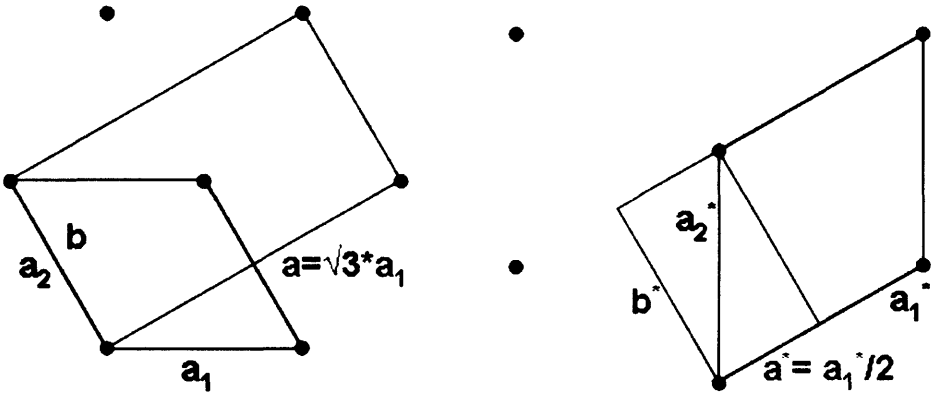

(a) Real space (b) Reciprocal space

Figure 5.7: The hexagonal and orthorhombic unit cells drawn in the basal plane in real and reciprocal space, showing how the two cells are related geometrically.

5.2.1 Temperature Dependence

In the paramagnetic phase, $T > T_0$, reflections are only observed when the scattering factor:

$$f = \sum_n l_n \exp(\imath \mathbf{Q} \cdot \mathbf{r_n}), \tag{5.10}$$

where l_n are the individual scalar atomic scattering lengths, is non-zero. Scattering factor calculations indicate that for different quadrupolar structures below T_0 the previously forbidden reflections at (103) and (104) become allowed due to the tensor nature of the individual scattering lengths. Figure 5.8 shows the Bragg and "forbidden" reflections within the Ewald sphere construction. Measurements of the temperature dependence of the resonant scattering from these superlattice reflections provides information about how the structures evolve as well as about critical phenomena, which may be able to elucidate the mechanism of the interaction between the quadrupole moments.

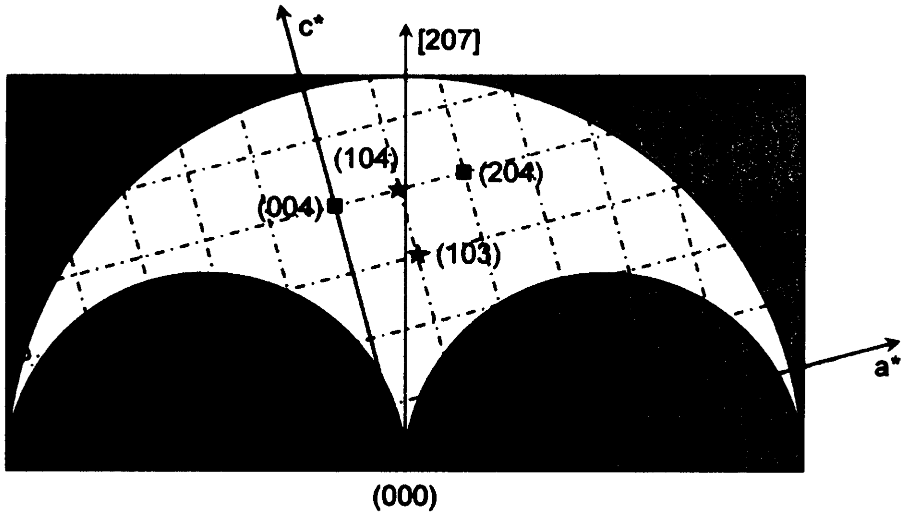

Figure 5.8: A map of the accessible region of reciprocal space in orthorhombic notation coinciding with the vertical scattering plane of the diffractometer for energies in the vicinity of the M_{IV}-edge of Uranium, defined by circles with radii k and $2k$ corresponding to transmission and reflection. Also shown are the Bragg reflections (■) and the quadrupolar reflections (★).

The ID20 diffractometer at ESRF was aligned at each of the superlattice reflections at $E = 3.726$ keV. The temperature dependence of the *unpolarised* resonant scattering was then measured by rocking theta at each temperature set point as the sample was warmed from base temperature $\sim$ 2 K. Beam heating effects were found to be negligible and there was good thermal contact to the sample, which, in combination with the thorough characterisation of the thermocouples, gives us confidence in the measurement of the sample temperature. Unfortunately, due to technical problems with the cryostat, the temperature became unstable in the critical region $T = 6.8 - 7.6$ K, with temperature variations of ±0.5 K around the target temperature for individual scans. We attempted to repeat these measurements on several occasions, but we were never able to perform the full temperature dependence measurements.

The data was fitted using a combination of a lorentzian squared (see Appendix A) and linear lineshape to find the integrated intensity, the full-width half-maximum and peak centre. Such a lineshape gave the lowest chi-squared value. The results are consistent with that published in the earlier paper by McMorrow *et al.* [1].

The normalised intensity of the (103) peak, Figure 5.9 (a), is still non-zero above T_0, but the increasing full-width half-maximum, Figure 5.9 (b), indicates that this is critical scattering due to dynamic fluctuations of short range quadrupolar order. Closer inspection of Figure 5.9 (a) indicates a possible step in the intensity associated with the T_2 transition. As discussed above, problems with the cryostat mean that we have no data at T_{+1}, and the lack of data in the vicinity of T_{-1} and T_0 makes it difficult to identify any anomalies associated with these temperatures.

Figures 5.10 (a) and (b) show the normalised integrated intensity and full-width half-maximum of the (104) reflection. Looking in detail at the intensity,

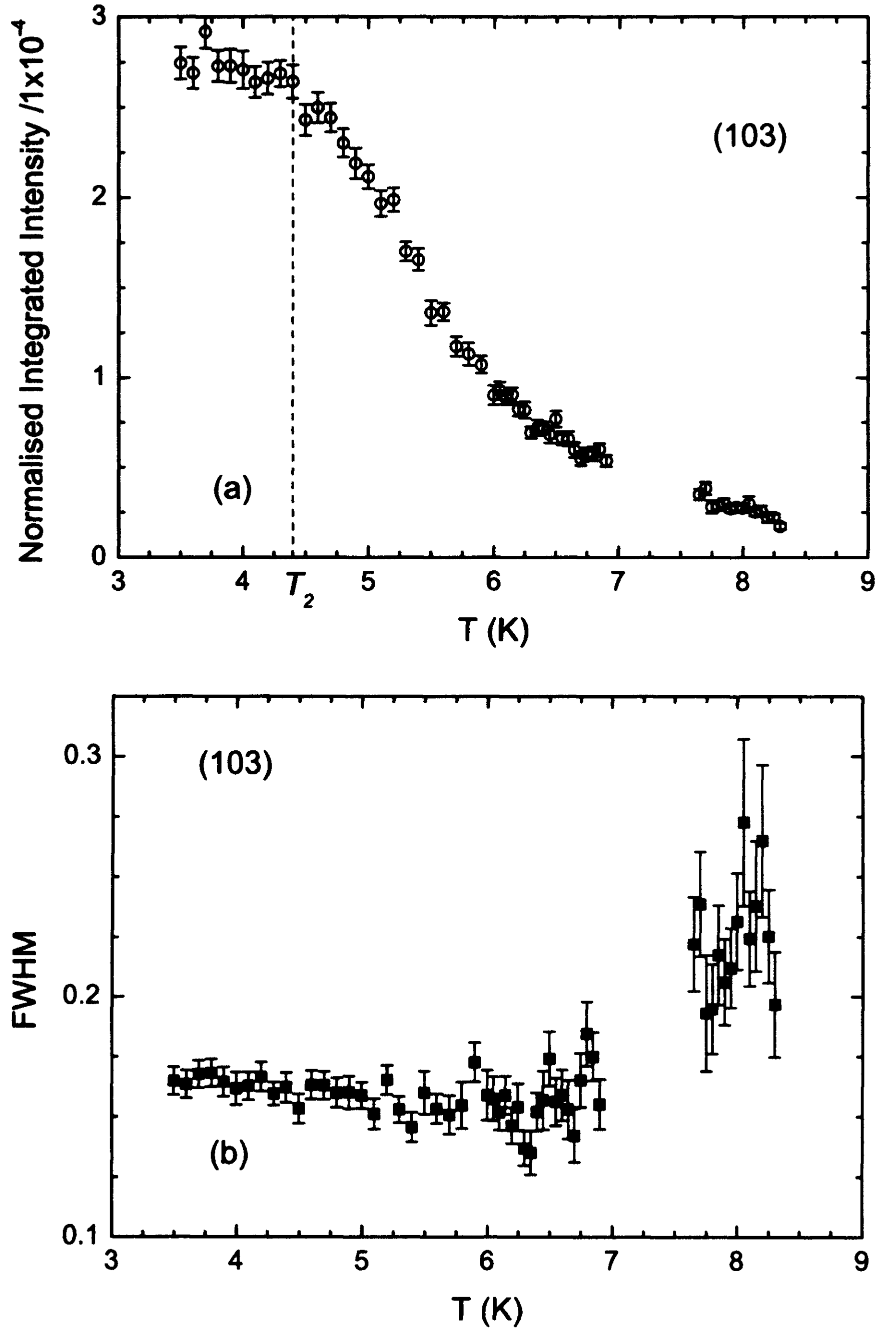

Figure 5.9: Temperature dependence of a) the integrated intensity of the (103) peak normalised to the monitor and b) its Full Width Half Maximum in UPd_3 at $\Psi = 93°$, calculated by fitting a lorentzian squared plus a linear term to θ-scans. The dashed line shown in (a) corresponds to T_2

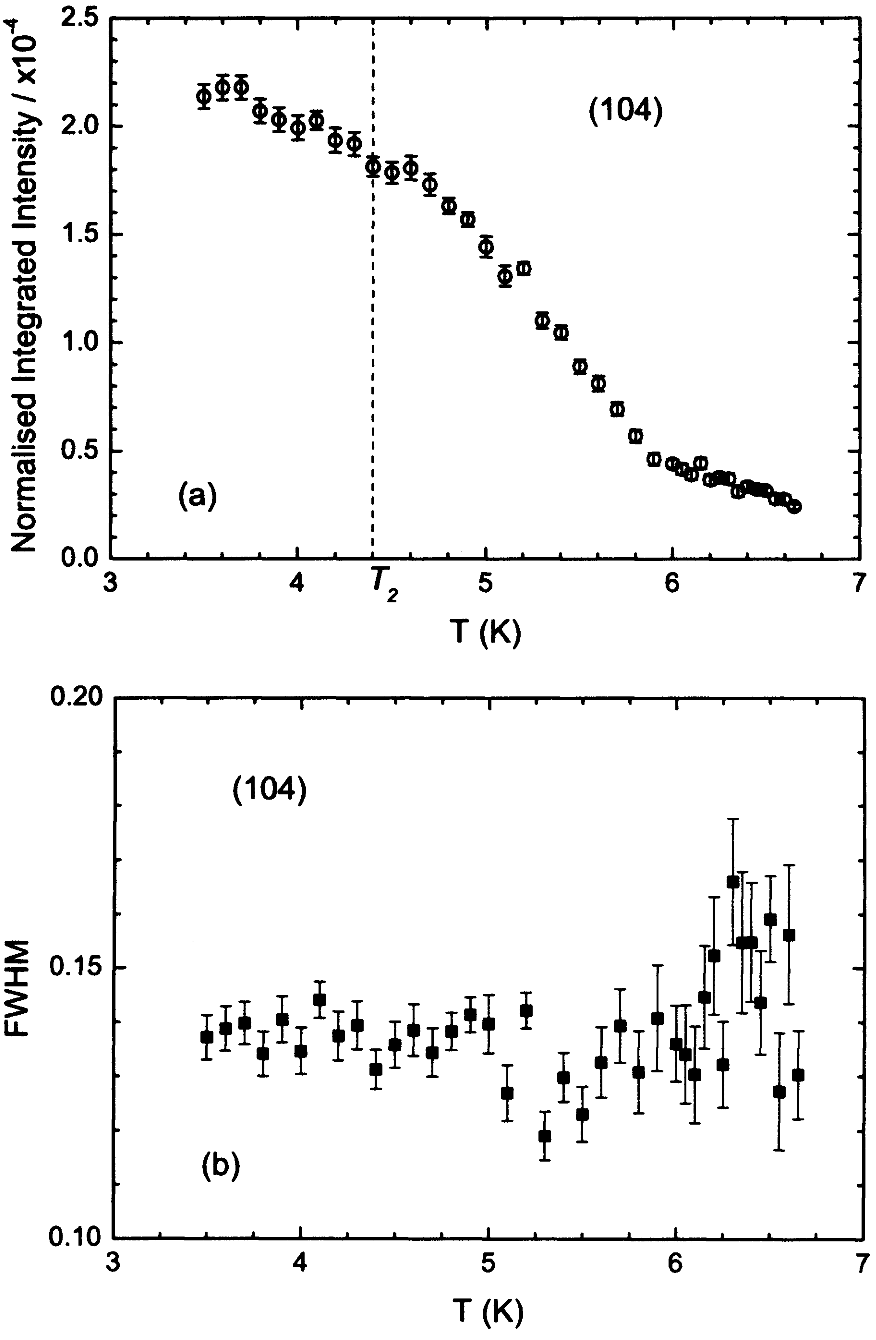

Figure 5.10: Temperature dependence of (a) the integrated intensity of the (104) peak normalised to the monitor and (b) its Full Width Half Maximum in UPd_3 at $\Psi = 93°$, calculated by fitting a lorentzian squared plus a linear term to θ-scans. The dashed line shown in (a) corresponds to T_2.

there is a suggestion that there is a small step in the data at T_2. Unfortunately the data does not extend to the $T_{\pm 1}$ transition temperatures, while no intensity is observed at this position at T_0. At the maximum temperature limit, the FWHM appears to be starting to increase, suggesting the onset of critical scattering. Also visible in Figure 5.10 (a) is a kink in the intensity at $T^* \sim 5.8$ K. This temperature is not associated with any known transition, and the origins of this anomalous feature are unknown.

5.2.2 The first quadrupolar phase: $T_{+1} < T < T_0$

The measurements as a function of temperature reveal that there is no scattering intensity at (104) in the first quadrupolar phase, while the intensity at (103) is non-zero. This indicates that the quadrupole moments on the cubic uranium sites are stacked in anti-phase along the c-axis. By measuring the count rate as a function of the incident energy a clear resonance is observed in the rotated channel, see Figure 5.11. Closer inspection of the resonance indicates the possibility of two peaks separated by less than 10 eV, in the form of a shoulder on the main resonance, which in some systems might be interpreted as being due to electric dipole ($E1$) and electric quadrupole ($E2$) resonances. Resonant scattering is also observed in the unrotated channel, but there is significant non-resonant interference. The electric dipole transitions, E1, dominate the resonant scattering cross section, connecting the core $3d_{3/2}$ states to the $5f$ states at the uranium M_{IV}-edge. If the resonance was observed only in $\sigma\pi$ this would point to a magnetic origin, while if it was only in $\sigma\sigma$ it would suggest it was due to charge scattering. That resonant scattering is seen in both channels at this energy, $E = 3.726$ keV indicates that we are probing the $5f$ electrons involved in the quadrupolar order.

To investigate the nature of the quadrupolar order in UPd$_3$, experiments

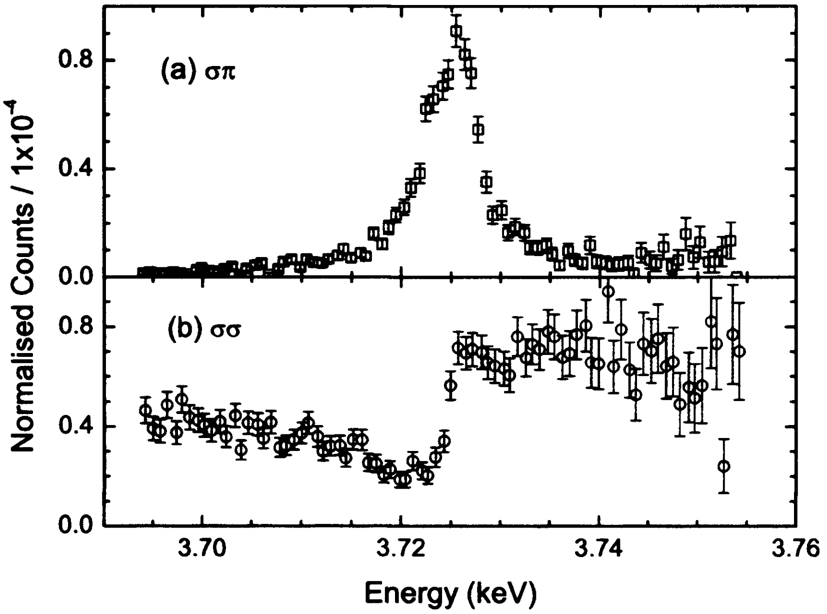

Figure 5.11: Energy scans of the (103) peak in UPd$_3$ at $T = 7.1$ K, $\Psi = 139°$ in (a) the $\sigma\pi$ channel showing resonance, with a main peak at 3.726 keV and a shoulder at ~ 3.722 keV, and (b) the $\sigma\sigma$ channel showing a significant non-resonant component.

were performed to determine how the resonant scattering intensity from a superlattice reflection varied as a function of the azimuthal angle, Ψ, see Figure 3.4. The azimuthal angle Ψ is defined relative to the reference vector $[0\bar{1}0]$. At each azimuthal angle, the sample theta angle was rocked and the intensities of the $\sigma\sigma$ and $\sigma\pi$ polarisation channels measured. As for the temperature dependence scans, the integrated peak intensities were calculated by fitting a lorentzian squared (for the peak shape) and a linear contribution (due to the background). The azimuthal dependence of the scattering intensity at the (103) reflection at $T = 7.1$ K, i.e. within the first quadrupolar phase, is shown in Figure 5.12.

The error bars shown are the output from the program which calculates the integrated intensity from the peak shape fit. Systematic errors may be introduced by the variation in absorption as a function of the azimuth angle.

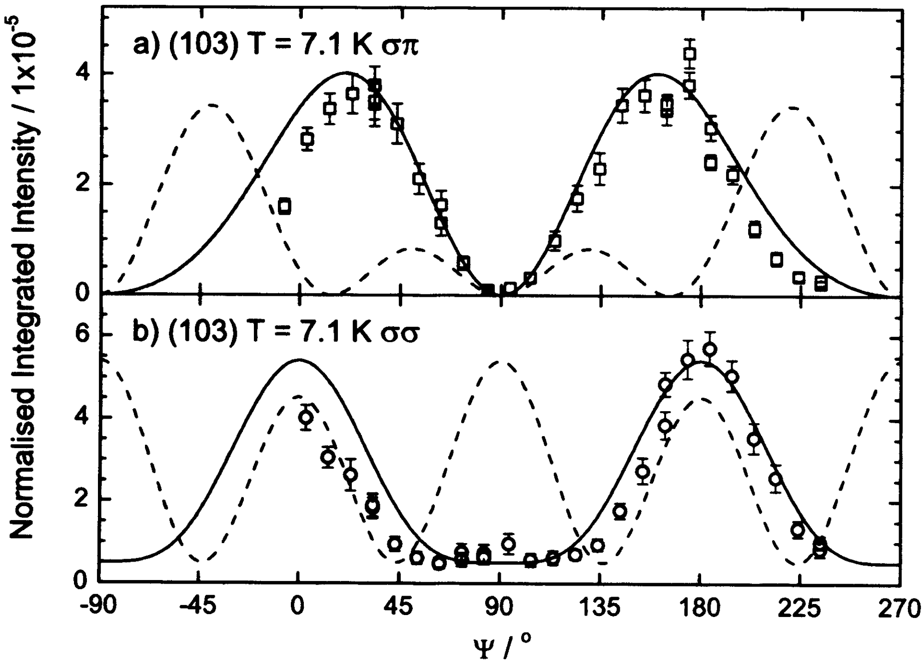

Figure 5.12: The azimuthal dependence of a) the $\sigma\pi$ and b) the $\sigma\sigma$ scattering intensities of the (103) peak in UPd3 at the U $M_{\rm IV}$ edge, at $T = 7.1$ K. Comparison is made with calculations for the Q_{zx} (solid black line) and the $Q_{x^2-y^2}$ (dashed black line) order parameters.

In this case, such errors were found to be minimal by showing that there was no significant variation in the intensity of the (004) Bragg peak as a function of Ψ. Another source of potential error on rotating the sample is due to the X-ray beam and diffractometer not being perfectly aligned, such that the incident spot traces out an arc on the sample surface, which can result in some of the diffractometer motors no longer being optimised for the superlattice reflection. At each value of Ψ before performing the theta rocking curve, θ, 2θ and χ were reoptimised, and at larger intervals we checked the transverse position of the sample stage. However, clearly there was a loss of intensity as the experiment progressed, and this can be seen in Figure 5.12 where certain data points were remeasured after moving to different values of Ψ and then returning. The difference between the two measurements at $\Psi = 174°$ gives an estimate of this source of systematic error.

The azimuthal dependence of the allowed order parameters was calculated by summing the second rank tensors T_n of the individual quasi-cubic site uranium quadrupoles to construct the resonant scattering length of the unit cell [1]

$$f = \sum_n T_n \exp(i\mathbf{Q} \cdot \mathbf{r}_n), \qquad (5.11)$$

see Appendix B.1 for details. The scattering amplitude is then given by

$$A = \epsilon' \cdot f \cdot \epsilon \qquad (5.12)$$

where the incident (ϵ) and scattered (ϵ') polarisations are transformed into the coordinate system of Blume and Gibbs [77] following the method of Wilkins *et al.* [10].

Inspection of Figure 5.12 shows that the (103) data is in excellent agreement with the above calculation for the azimuthal dependence of Q_{zx} antiferroquadrupolar order [105]. In the $\sigma\pi$ channel, note the asymmetry about $\Psi = 0°$ in both the data and Q_{zx} calculation, and that the maxima are not at $\Psi = 0, 180°$. In the $\sigma\sigma$ channel, the data and calculation show a broad minimum at 90° with symmetry about $\Psi = 0°$. Since our sample was cut with a (207) reciprocal lattice face, the scattering vector $\mathbf{Q} = (103)$ is not collinear with the face normal $(\mathbf{n})$. The σ polarisation vector is perpendicular to both $\mathbf{n}$ and $\mathbf{Q}$ so the non-collinear nature is not observed, resulting in the symmetry about $\Psi = 0°$ seen in $\sigma\sigma$ azimuthal measurements. However, the π polarisation vector lies in the plane of $\mathbf{n}$ and $\mathbf{Q}$, and the non-collinearity leads to an asymmetry in the azimuthal variation in intensity. Calculations of the Ψ dependence of the scattering intensity for the $\mathrm{Q}_{\mathrm{x}^2-\mathrm{y}^2}$, Q_{xy} and Q_{yz} order parameters do not agree with the data, as they show either the wrong periodicity, symmetry or maxima and minima positions, see Figures B.1, B.2 and B.4, and hence these order parameters can be ruled out. Q_{zx} provides a natural explanation for the macroscopic distortion to the orthorhombic cell [42] due to the splitting of the $x - y$ symmetry, see Fig. 5.13. Combining the knowledge that the transition at $T_0 = 7.8$ K is to a Q_{zx} antiferroquadrupolar ordering of the $5f^2$ electrons, with the heat capacity evidence that this transition is either second order or very weakly first order requires $B' \simeq 0$, i.e.

$$\hat{Q}_{\mathrm{zx}} = \begin{pmatrix} 0 & A' & A' \\ A' & 0 & 0 \\ A' & 0 & 0 \end{pmatrix}.$$

Previous polarised neutron diffraction [27] and X-ray resonant scattering [1] experiments revealed the wave vectors of the ordered AFQ structures, but did not allow the order parameters to be identified unambiguously. However, on the basis of the PND measurements, it was inferred that the order parameter below T_0 was $Q_{\mathrm{x}^2-\mathrm{y}^2}$. The apparent discrepancy between the above Q_{zx} result and that from the PND measurements might be explained when we take into consideration that the onset of Q_{zx} order below T_0 is expected to be accompanied by the development of a $Q_{\mathrm{x}^2-\mathrm{y}^2}$ contribution due to the symmetry

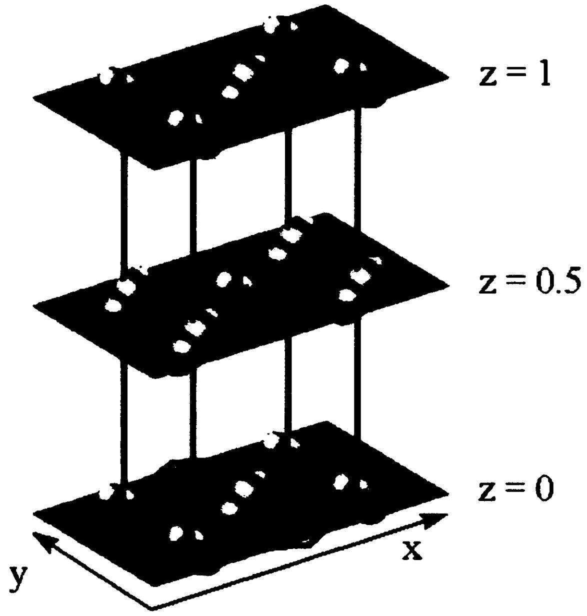

Figure 5.13: The Q_{zx} AFQ structure with antiphase stacking along the z-axis in UPd_3 at $T_{+1} < T < T_0$ in an orthorhombic unit cell. The U $5f$ quadrupole moments on the quasi-cubic sites are represented by ellipsoids.

considerations of the different quadrupolar operators [106] as described earlier in this chapter (equation (5.8)) with regard to the heat capacity data. The application of a magnetic field parallel to the real-space a-direction will induce antiferromagnetic moments aligned with the field direction in the case of $Q_{x^2-y^2}$, but not for Q_{zx}. Hence the PND experiment could only detect the contribution of $Q_{x^2-y^2}$ to the order parameter. Taking this into account a slightly better fit to the azimuthal data can be obtained by including a $Q_{x^2-y^2}$ contribution of 20% to the scattering tensor, see Figure 5.14. This is most noticeable for the $\sigma\sigma$ channel data, where the fit around $\Psi = 90°$ is significantly improved.

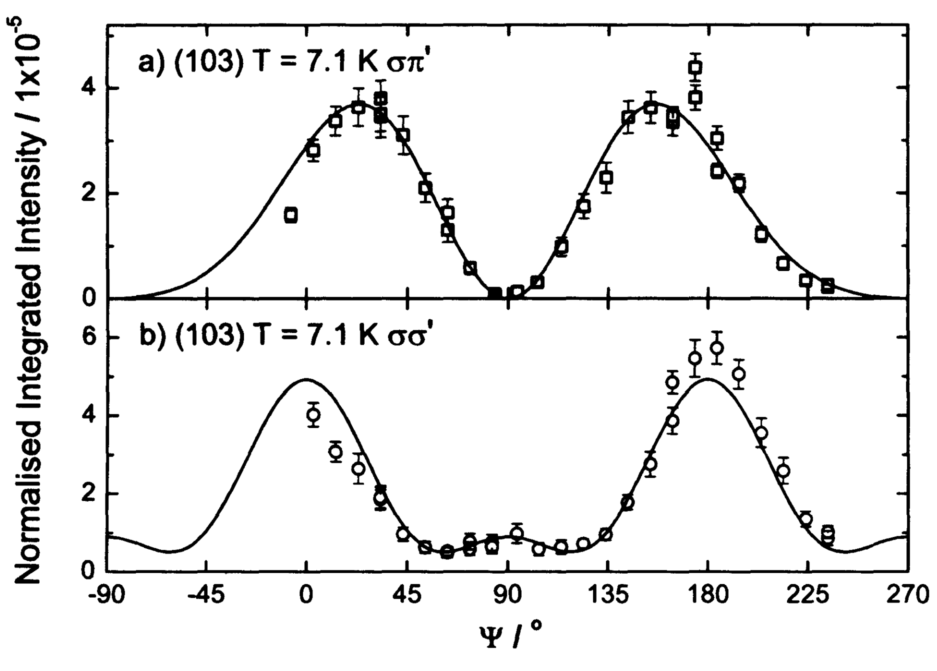

Figure 5.14: The azimuthal dependence of a) the rotated and b) the unrotated scattering from the (103) reflection in UPd_3 at $T = 7.1$ K as in Figure 5.12 with fits made allowing the Q_{zx} and $Q_{x^2-y^2}$ scattering tensor elements to vary freely.

5.2.3 $T_2 < T < T_{-1}$

UPd$_3$ is a particularly unusual compound because it displays a series of different quadrupolar ordered phases. Therefore, we were interested to observe how the azimuthal scattering dependence varied in each phase. The second quadrupolar phase lies between T_{+1} = 6.9 K and T_{-1} = 6.7 K, i.e. in a very narrow temperature range. Unfortunately it is very difficult to stabilise the cryostat within this particular range for the prolonged periods required to perform an experiment investigating the azimuthal dependence of the superlattice scattering intensity. Therefore, we next performed measurements in the third quadrupolar phase, at $T = 5.2$ K.

Energy scans in the two polarisation channels, plotted in Figure 5.15, reveal a clear resonance in $\sigma\pi$ at both (103) and (104) indicating an in-phase component to the quadrupolar order along the c-axis. These resonances are fitted well by a Lorentzian peak shape, as we would expect, since the high resolution of the diffractometer means that the peak shape is an intrinsic property of the sample. While resonance is observed in $\sigma\sigma$, there is also significant non resonant interference again. Due to time constraints we were limited as to the measurements we were able to perform, and so given the interference in $\sigma\sigma$ we decided it would be more profitable to investigate the dependence of just the $\sigma\pi$ scattering at (103) and (104). The results are presented in Figure 5.16. The dashed lines in Figure 5.16 correspond to least squares fits made to the data by varying the contributions of the different allowed quadrupole moments: Q_{zx}, $Q_{x^2-y^2}$, Q_{xy}, Q_{yz} and Q_{zz} on the quasi-cubic uranium sites.

Clearly the azimuthal dependence of the $\mathbf{Q}$ = (103) scattering at 5.2 K is more complicated than in the higher temperature Q_{zx} phase, and the AFQ order involves additional order parameters, Figure 5.16a). The least squares fit to the data indicates that the predominant order parameter is still Q_{zx}, but that

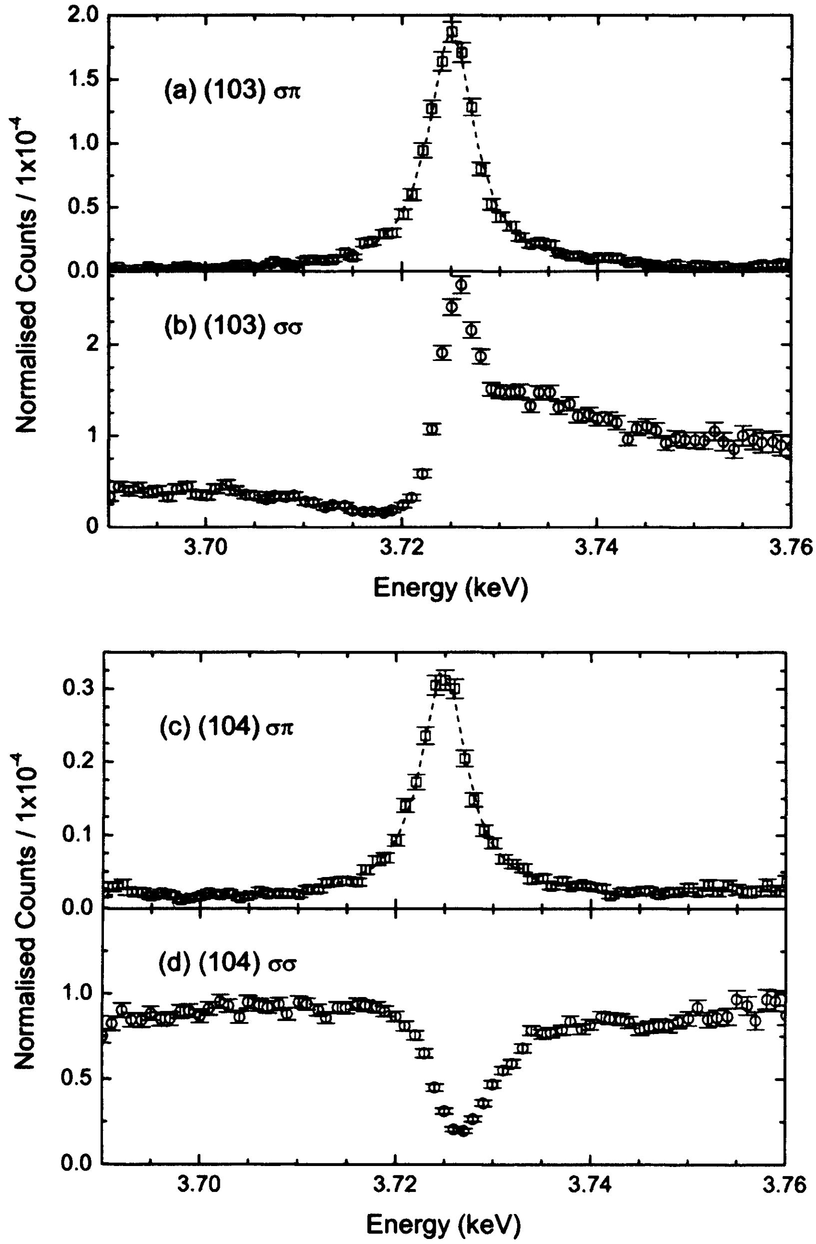

Figure 5.15: UPd$_3$ energy scans at $T = 5.2$ K of the (103) peak at $\Psi = 1.2°$ in (a) the $\sigma\pi$ channel showing resonance at $E = 3.725$ keV, and (b) the $\sigma\sigma$ channel showing a significant non-resonant component; and of the (104) peak at $\Psi = 2.7°$ in (c) the $\sigma\pi$ channel also showing resonance at $E = 3.725$ keV, and (d) the $\sigma\sigma$ channel showing interference.Both $\sigma\pi$ resonances are fitted well by a Lorentzian peak shape.

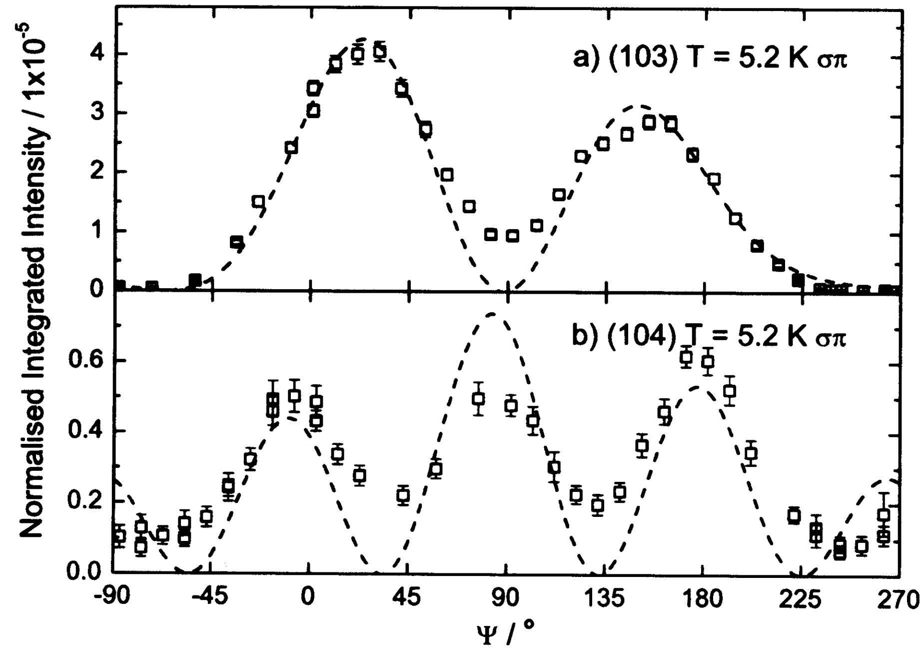

Figure 5.16: The azimuthal dependence of the $\sigma\pi$ scattered intensity from a) the (103) and b) the (104) superlattice peaks, in UPd$_3$ at the U M_{IV} edge, at T = 5.2 K. Dashed lines show least squares fits to the data as described in the text.

Q_{xy} and $Q_{x^2-y^2}$ are also present, and is derived from an anomalous scattering tensor with the order parameters present in the ratio 77:10:13 respectively. The fit to our data in Figure 5.16b), which reproduces the periodicity of the (104) data, indicates that the most significant order parameters are Q_{xy} and Q_{yz} in the ratio 2:1.

Furthering the Order Model

Quadrupoles on hexagonal sites

To improve the fit to the data it is necessary to introduce additional parameters which go beyond the scope of the current model of quadrupoles on the quasi-cubic sites. So far quadrupoles on the hexagonal sites have not been considered due to the energy level splitting between the hexagonal ground state and first excited state being so much greater at 81 K than the quadrupolar transition temperatures. However, the existence of quadrupoles on the hexagonal sites is one of the more simple ways of introducing additional model parameters.

Within the orthorhombic notation the four hexagonal sites within the unit cell are at:

$$(\frac{1}{2}\frac{1}{6}\frac{1}{4}),\quad (0\frac{2}{3}\frac{1}{4}),\quad (0\frac{1}{3}\frac{3}{4}),\quad (\frac{1}{2}\frac{5}{6}\frac{3}{4}).$$

Therefore when equation (5.11) is calculated for the (103) reflection, for certain quadrupole arrangements the resultant tensor is complex, while it remains real for all arrangements for the (104) reflection. For one particular Q_{zx} ordering of the quadrupoles on the hexagonal sites combined with the antiphase stacking of Q_{zx} order quadrupoles along the c-axis, shown in Figure 5.17, the resultant scattering factors of the (103) and (104) reflections are unchanged from those for Q_{zx} order only on the cubic sites, i.e.

$$f(103) = Q_{zx}, \quad f(104) = \mathbf{0}.$$

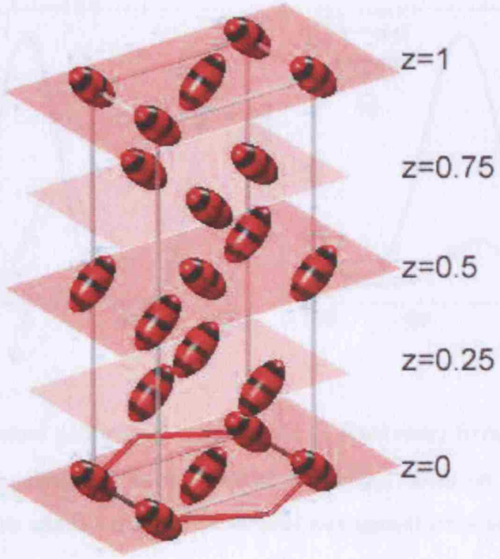

Figure 5.17: An example of a more complex periodicity of quadrupoles on cubic and hexagonal uranium sites in UPd_3, resulting in a scattering tensor unchanged from that describing the order in Figure 5.13.

Therefore it is not possible using our current data sets to distinguish between the two quadrupole configurations shown in Figures 5.13 and 5.17. To overcome this problem it would be necessary to perform experiments to measure the azimuthal variation of the scattering intensity of the (013) reflection. Figures 5.18(a) and 5.18(b) show the calculated azimuthal dependence of scattering from the (013) reflection for the two quadrupole structures shown in Figures 5.13 and 5.17, corresponding to the scattering tensors

$$f^{(a)}(013) = \begin{pmatrix} 0 & 0 & 1 \\ 0 & 0 & 0 \\ 1 & 0 & 0 \end{pmatrix},$$

$$f^{(b)}(013) = \begin{pmatrix} -1.37 + 0.57\imath & 0 & 1.46 - 0.19\imath \\ 0 & -0.92 + 0.38\imath & 0 \\ 1.46 - 0.19\imath & 0 & -1.37 + 0.57\imath \end{pmatrix}.$$

These are clearly very different; for example in $\sigma\pi$ for the cubic sites only

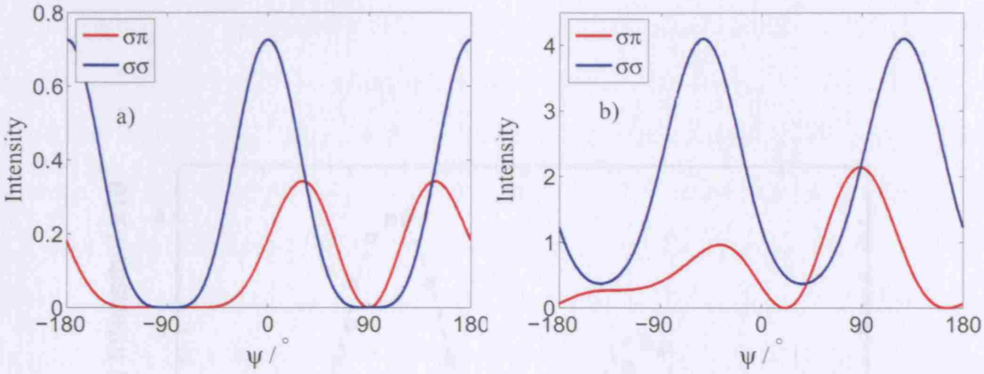

Figure 5.18: The simulated azimuthal dependence of scattering from the (013) reflection in UPd$_3$ using [100] as the azimuth reference vector for (a)Q_{zx} order on the cubic sites only and (b)quadrupoles in the zx plane on both cubic and hexagonal sites as shown in Figure 5.17.

structure there is a minimum at $\Psi = 90°$, while there is a maximum there for the cubic and hexagonal sites structure, while in $\sigma\sigma$ the oscillation in Figure 5.18(b) is shifted through Ψ relative to that in Figure 5.18(a), and its value is always greater than zero.

Figure 5.19 shows a least squares fit, with all data points weighted equally, to the $T = 5.2$ K (103) data made for a scattering tensor which is the complex weighted sum of tensors describing different orderings of the Uranium $5f^2$ electrons, $\sum_n P_n f_n$, where the multiplicative factor fitting parameters P_n and the overall intensity are allowed to vary freely, and for example

$$f_{zx} = \begin{pmatrix} 0 & 0 & 1 \\ 0 & 0 & 0 \\ 1 & 0 & 0 \end{pmatrix} .$$

Close inspection reveals that the fit to the data is very good and corresponds to $R^2 = 0.995$. The real and imaginary components of the fitting parameters are given in Table 5.1, indicating that the fit corresponds to a complex scattering tensor, which could be due to the presence of quadrupoles on the hexagonal sites.

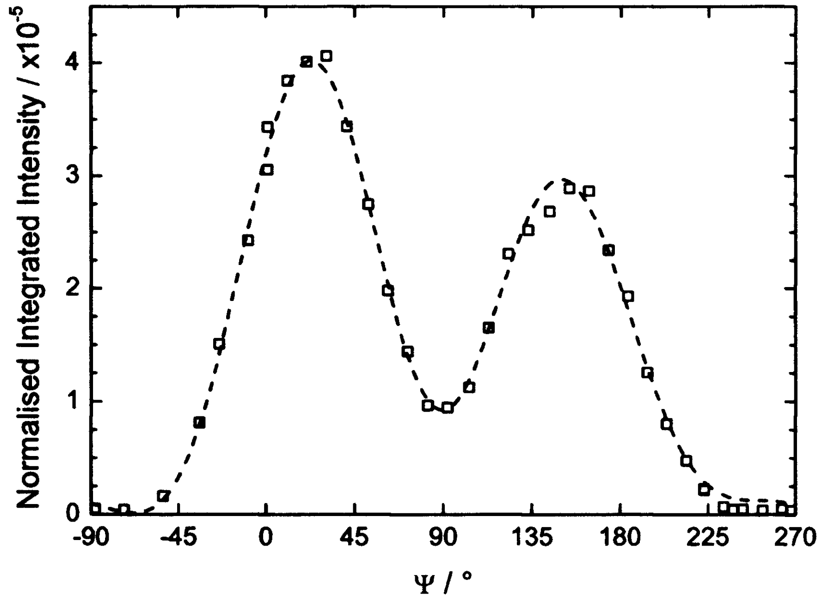

Figure 5.19: Fit to the azimuthal dependence of $\sigma\pi$ scattering intensity from the (103) reflection in UPd$_3$ at $T = 5.2$ K.

Parameter	Value	Paramater	Value
Intensity	3.91×10^{-4}	R^2	0.995
$\Re(P_{x^2-y^2})$	-6.92×10^{-2}	$\Im(P_{x^2-y^2})$	9.69×10^{-2}
$\Re(P_{xy})$	1.87×10^{-2}	$\Im(P_{xy})$	-1.40×10^{-1}
$\Re(P_{zx})$	4.67×10^{-1}	$\Im(P_{zx})$	5.99×10^{-1}
$\Re(P_{yz})$	3.27×10^{-2}	$\Im(P_{yz})$	1.19×10^{-1}
$\Re(P_{zz})$	1.90×10^{-1}	$\Im(P_{zz})$	$1.36 \times 10^{+0}$

Table 5.1: Values of the real and imaginary components of the parameters for the fit to the $\sigma\pi$ (103) UPd$_3$ azimuthal data at $T = 5.2$ K shown in Figure 5.19.

As mentioned previously the introduction of quadrupoles on the hexagonal sites does not lead to complex scattering factors for the (104) reflection. However, when a least squares fit is made to the data shown in Figure 5.16(b), allowing complex values for all the elements in the scattering factor tensor, it is found that the best fit ($R^2 = 0.976$) is achieved for a complex $F(104)$, see Figure 5.20, where the fit parameters are given in Table 5.2. It is significant to note, that for this fit and that for scattering from $\mathbf{Q} = (103)$, the imaginary components of the individual scattering tensor elements are of comparable magnitude to the real components. It should also be noted that the fitting parameters are different for the two reflections, but the relation between the order model and the scattering tensors for different reflections is not simple, and so this is to be expected. For example, in the first phase, Q_{zx} order with an antiphase c-axis stacking results in very different scattering tensors for (103) and (104).

A complex scattering tensor f requires either the tensors representing the individual quadrupoles in the cell, T_n, or the phase factor, $\exp(\imath\mathbf{Q}\cdot\mathbf{r}_n)$, to be complex, see equation (5.11). Since the individual quadrupole tensors are derived by performing $3D$ rotations away from the tensor for a $Q_{\mathrm{x}^2-\mathrm{y}^2}$ quadrupole, it is unphysical for T to be complex. Therefore the complex nature of the scattering tensor must derive from the way the different quadrupole tensors are combined according to the phase factor. With quadrupoles situated on the cubic and hexagonal sites the phase factor for $\mathbf{Q} = (104)$ is real. Therefore, within a model of purely quadrupolar order, to introduce complex numbers to the scattering tensor requires that some of the quadrupoles are not sitting at the exact positions for a dhcp unit cell, i.e. there must be some crystallographic distortion.

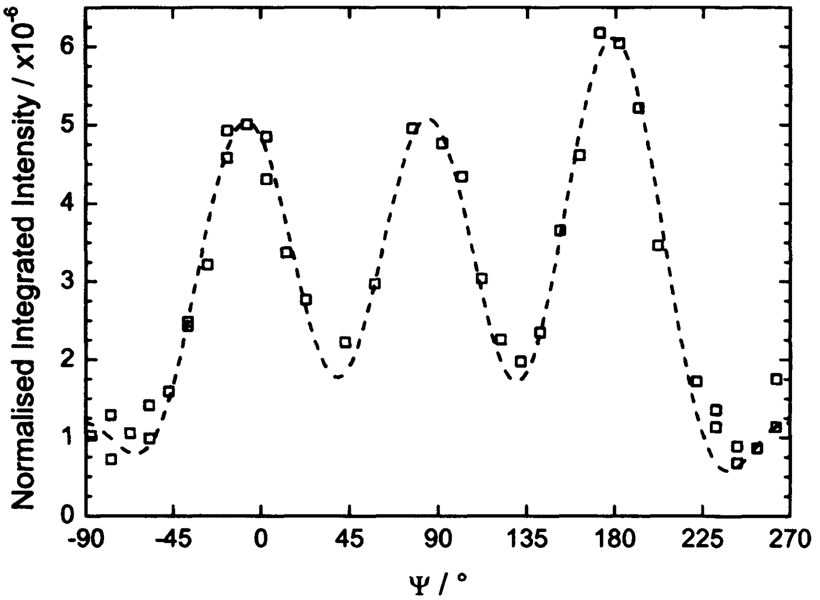

Figure 5.20: Fit to azimuthal dependence of $\sigma\pi$ scattering intensity from the (104) reflection in UPd$_3$ at $T = 5.2$ K.

Parameter	Value	Paramater	Value
Intensity	7.02×10^{-6}	R^2	0.976
$\Re(P_{x^2-y^2})$	-8.56×10^{-2}	$\Im(P_{x^2-y^2})$	1.37×10^{-1}
$\Re(P_{xy})$	-4.05×10^{-1}	$\Im(P_{xy})$	-6.67×10^{-1}
$\Re(P_{zx})$	2.19×10^{-1}	$\Im(P_{zx})$	$1.60 \times 10^{+0}$
$\Re(P_{yz})$	3.36×10^{-1}	$\Im(P_{yz})$	3.85×10^{-1}
$\Re(P_{zz})$	$2.52 \times 10^{+0}$	$\Im(P_{zz})$	$2.60 \times 10^{+0}$

Table 5.2: Values of the real and imaginary components of the parameters for the fit to the $\sigma\pi$ (104) UPd$_3$ azimuthal data at $T = 5.2$ K shown in Figure 5.20.

Crystallographic distortion

Different distortions and order parameters have been used in calculations to derive scattering tensors. In the simplest case, based on the Q_{zx} structure determined for the phase between $T_{+1} < T < T_{-1}$, a distortion of 1% along the c-axis has been applied to the location of the quasi-cubic sites with $h, k = \frac{1}{2}$, such that quadrupoles are located at:

$$(0\,0\,0),\quad (0.5\,0.5\,0.01),\quad (0\,0\,0.5),\quad (0.5\,0.5\,0.51).$$

This does not have a very large effect on the calculated scattering tensors for the two reflections:

$$\begin{aligned} f(103) = Q_{zx} &\rightarrow \begin{pmatrix} 0 & 0 & 0.99+0.09\imath \\ 0 & 0 & 0 \\ 0.99+0.09\imath & 0 & 0 \end{pmatrix} \\ f(104) = \mathbf{0} &\rightarrow \begin{pmatrix} 0.05-0.37\imath & 0 & 0 \\ 0 & 0.03-0.25\imath & 0 \\ 0 & 0 & 0.05-0.37\imath \end{pmatrix}, \end{aligned} \tag{5.13}$$

and is clearly incompatible with the fits obtained in Figures 5.19 and 5.20 and the parameters listed in Tables 5.1 and 5.2. For the same structure, but with a 5% change along the c-axis, the two scattering tensors are given by:

$$\begin{aligned} f(103) &\rightarrow \begin{pmatrix} 0 & 0 & 0.79+0.40\imath \\ 0 & 0 & 0 \\ 0.79+0.40\imath & 0 & 0 \end{pmatrix} \\ f(104) &\rightarrow \begin{pmatrix} 1.04-1.43\imath & 0 & 0 \\ 0 & 0.69-0.95\imath & 0 \\ 0 & 0 & 1.04-1.43\imath \end{pmatrix}, \end{aligned} \tag{5.14}$$

which gives comparable real and imaginary tensor elements. However, any crystallographic distortion must be very small, as a larger distortion would have been observed in previous neutron diffraction experiments and would have caused the crystal to shatter in all likelihood. For this reason it is unlikely that the azimuthal dependence of the scattering from the superlattice reflections is the result of a crystallographic distortion.

Multipolar interactions

Another alternative model for the low temperature phases, is that there is an additional multipolar order parameter. In the temperature range $T_2 < T < T_{-1}$ no magnetic ordering has been observed, which suggests that dipole order is absent. However, magnetic order would be a simple way of introducing imaginary elements into the scattering tensor through a total tensor $T = \sum_n (T_n^Q + \imath T_n^M) \exp(\imath \mathbf{Q} \cdot \mathbf{r}_n)$, where $\imath$ introduces the phase shift for magnetic scattering, T^Q is the scattering tensor describing the quadrupolar order and T^M is a rank 2 matrix representing the magnetic order following

$$T^M = \begin{pmatrix} 0 & z & -y \\ -z & 0 & x \\ y & -x & 0 \end{pmatrix}, \tag{5.15}$$

where x, y, z are the xyz components of the vector describing the dipole moment μ in the unit cell basis. $\epsilon' \cdot T^M \cdot \epsilon$ is equivalent to $(\epsilon' \times \epsilon) \cdot \mu$, the f_1 term in Equation (3.11).

When attempts are made to fit the azimuthal dependence of the scattered intensity in the $\sigma\pi$ channel for $\mathbf{Q} = (103)$ and (104) using such a tensor, where it is assumed that the real elements are associated with quadrupoles on the cubic sites and the imaginary elements are only due to a magnetic moment, a good fit is obtained for (103), Figure 5.21 $R^2 = 0.994$, but a poor fit is made to the (104) data, Figure 5.22, which does not reproduce the relative magnitudes of the maxima well, such that $R^2 = 0.714$. The fitting parameters are given in

Tables 5.3 and 5.4.

However, as discussed above, there are other possible causes of imaginary elements in the scattering tensor due to the quadrupole moments, where if f is the scattering tensor then tensor elements are such that $\Im(f_{lm}) = \Im(f_{ml})$, as opposed to $\Im(f_{lm}) = -\Im(f_{ml})$, as for the magnetic tensor. Therefore, fits have also been made to the data which take this into account, Figures 5.23 and 5.24. The fitting parameters are given in Tables 5.5 and 5.6, which give the magnitudes of the contributions from the tensors describing quadrupolar order and magnetic order. These fits are of a very similar quality to those made with a complex tensor but no magnetic component, Figures 5.19 and 5.20, and are generally better than those for which magnetic order is the only source of imaginary tensor elements, Figures 5.21 and 5.22. From these assorted fits to the data, the existence of magnetic order cannot be discounted entirely, but clearly a simple model based on a combination of a real quadrupolar tensor and a magnetic tensor cannot alone completely replicate the azimuthal dependence of the scattering data observed.

There could be higher order multipolar order parameters such as octupolar or hexadecapolar order. Magnetic octupolar order has been identified as the primary order parameter, inducing the order of electric quadrupoles as the secondary order parameter, in NpO_2 using XRS, see [22] and references therein. The octupolar order breaks time-reversal symmetry allowing the interstitial magnetic field observed in muon spin rotation measurements, while the cubic symmetry prevents the local existence of a magnetic dipole secondary order parameter, explaining why magnetic order had not been observed in Mößbauer spectroscopy or neutron diffraction experiments. Octupolar order has also been suggested as the primary order parameter behind the "hidden" order in the tetragonal system URu_2Si_2 [21]; and field induced octupoles are important for understanding the complex phase diagram of the cubic system CeB_6 [6]. To

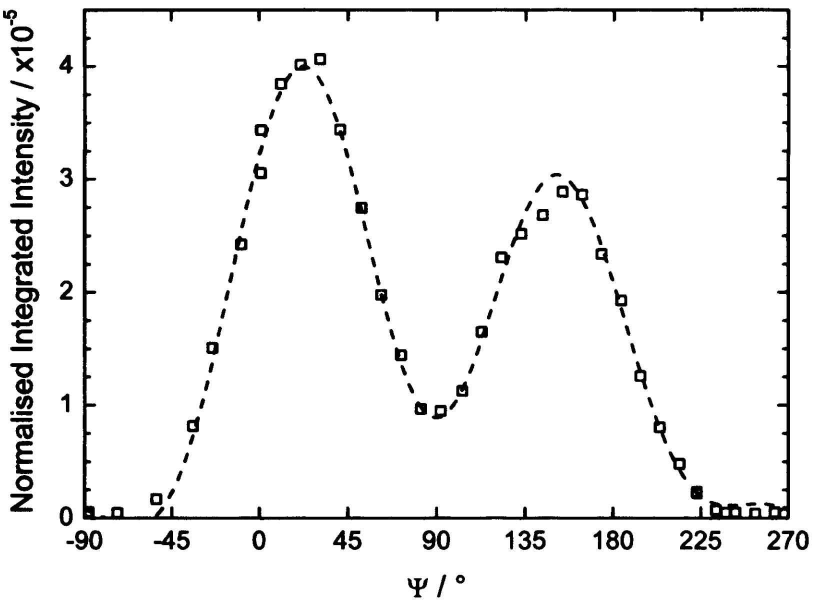

Figure 5.21: Fit to azimuthal dependence of $\sigma\pi$ scattering intensity from the (103) reflection in UPd$_3$ at $T = 5.2$ K assuming magnetic and quadrupolar order.

Parameter	Value	Parameter	Value
Intensity	3.42×10^{-4}	R^2	0.994
P_{xy}	1.02×10^{-1}	P_{m_z}	-2.23×10^{-1}
P_{zx}	$1.20 \times 10^{+0}$	P_{m_y}	2.55×10^{-1}
P_{yz}	2.25×10^{-1}	P_{m_x}	7.70×10^{-1}
$P_{x^2-y^2}$	2.83×10^{-1}	P_{zz}	4.58×10^{-1}

Table 5.3: Values of the parameters for a fit to the $\sigma\pi$ (103) UPd$_3$ azimuthal data at $T = 5.2$ K shown in Figure 5.21 for scattering from quadrupole and dipole moments.

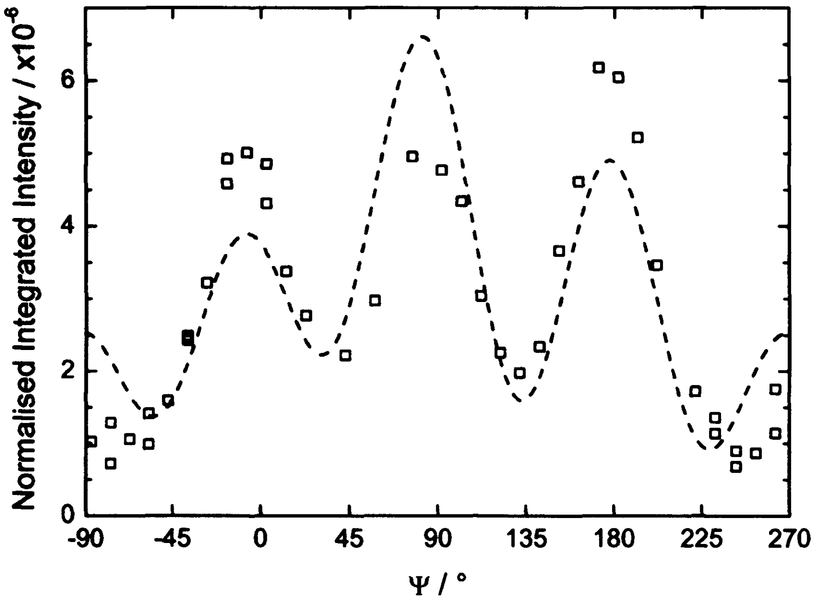

Figure 5.22: Fit to azimuthal dependence of $\sigma\pi$ scattering intensity from the (104) reflection in UPd$_3$ at $T = 5.2$ K assuming magnetic and quadrupolar order.

Parameter	Value	Parameter	Value
Intensity	1.09×10^{-5}	R^2	0.714
P_{xy}	6.35×10^{-1}	P_{m_z}	4.86×10^{-1}
P_{zx}	3.83×10^{-1}	P_{m_y}	-7.76×10^{-2}
P_{yz}	-3.42×10^{-1}	P_{m_x}	2.10×10^{-1}
$P_{x^2-y^2}$	1.52×10^{-1}	P_{zz}	$1.47 \times 10^{+0}$

Table 5.4: Values of the parameters for a dipole and quadrupole moment fit to the $\sigma\pi$ (104) UPd$_3$ azimuthal data at $T = 5.2$ K shown in Figure 5.22 for scattering from quadrupole and dipole moments.

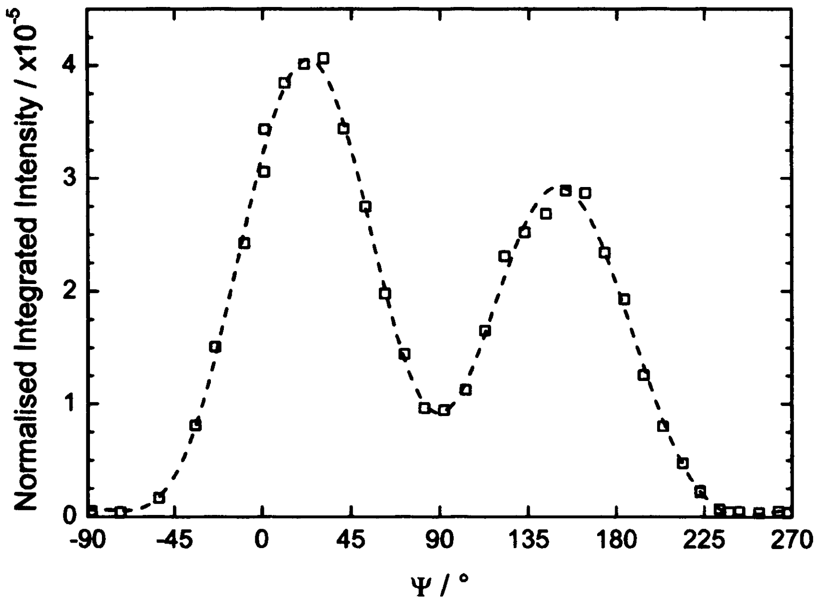

Figure 5.23: A free fit made to the azimuthal dependence of $\sigma\pi$ scattering intensity from the (103) reflection in UPd$_3$ at $T = 5.2$ K using a complex scattering tensor.

Parameter	Value	Parameter	Value	Parameter	Value
Intensity	8.31×10^{-5}	$\Re(P_{x^2-y^2})$	-1.02×10^{-1}	$\Im(P_{x^2-y^2})$	4.31×10^{-1}
$\Re(P_{xy})$	5.55×10^{-2}	$\Im(P_{xy})$	2.87×10^{-1}	P_{m_z}	-2.86×10^{-3}
$\Re(P_{zx})$	$1.88 \times 10^{+0}$	$\Im(P_{zx})$	$2.07 \times 10^{+0}$	P_{m_y}	-6.31×10^{-1}
$\Re(P_{yz})$	4.27×10^{-2}	$\Im(P_{yz})$	-6.47×10^{-1}	P_{m_x}	-3.79×10^{-1}
$\Re(P_{zz})$	$2.17 \times 10^{+0}$	$\Im(P_{zz})$	$2.47 \times 10^{+0}$	R^2	0.996

Table 5.5: Values of the parameters describing the scattering tensor for the fit to the $\sigma\pi$ (103) UPd$_3$ azimuthal data at $T = 5.2$ K shown in Figure 5.23.

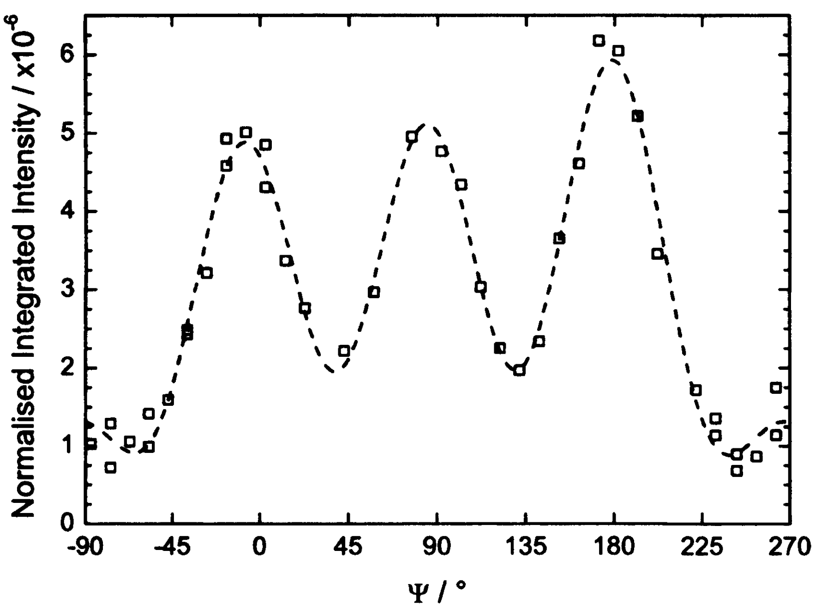

Figure 5.24: A free fit made to the azimuthal dependence of $\sigma\pi$ scattering intensity from the (104) reflection in UPd$_3$ at $T = 5.2$ K using a complex scattering tensor.

Parameter	Value	Parameter	Value	Parameter	Value
Intensity	8.26×10^{-6}	$\mathfrak{R}(P_{x^2-y^2})$	2.75×10^{-1}	$\mathfrak{I}(P_{x^2-y^2})$	5.48×10^{-2}
$\mathfrak{R}(P_{xy})$	6.46×10^{-1}	$\mathfrak{I}(P_{xy})$	-3.31×10^{-1}	P_{m_z}	-2.06×10^{-1}
$\mathfrak{R}(P_{zx})$	$1.46 \times 10^{+0}$	$\mathfrak{I}(P_{zx})$	-4.24×10^{-3}	P_{m_y}	-7.35×10^{-1}
$\mathfrak{R}(P_{yz})$	-4.41×10^{-1}	$\mathfrak{I}(P_{yz})$	-3.52×10^{-1}	P_{m_x}	-3.79×10^{-1}
$\mathfrak{R}(P_{zz})$	$4.20 \times 10^{+0}$	$\mathfrak{I}(P_{zz})$	$-2.15 \times 10^{+0}$	R^2	0.978

Table 5.6: Values of the parameters describing the scattering tensor for the fit to the $\sigma\pi$ (104) UPd$_3$ azimuthal data at $T = 5.2$ K shown in Figure 5.24.

our knowledge, there are as yet no publications suggesting octupolar order in hexagonal systems. However, magnetic octupolar order can only be observed directly through E_2 resonances [9,86].

We have assumed that the electric dipole transition $E1$ ($3d_{3/2} \rightarrow 5f$) dominates the scattering. Interference between the $E1$ and $E2$ resonances can provide another mechanism for explaining a complex azimuthal dependence of reflections as other types of multipolar order are probed, e.g. electric dipoles [86], while a pure $E2$ resonance would lead to possible octupolar order also being observed. However, an $E2$ resonance involves a momentum change $\Delta L = 2$, such that at the uranium M_{IV} edge an $E2$ resonance probes the unoccupied g bands, and it is believed that the matrix elements for such an event would be too small to allow for any observable signal [9]. An $E2$ event at the M_{II} and M_{III} edges would couple the $3p$ electrons to the $5f$ electrons, but the binding energies are greatly removed from that of the $3d$ electrons at 5.18 keV and 4.30 keV respectively [107], and so such events could not have been observed in our experiments. Therefore, the complicated azimuthal dependence observed at $T = 5.2$ K, is not the response of multipoles of order higher than $n = 2$.

Low point group symmetry

After recent discussions with the group of Amoretti at Università di Parma, the significant importance of the uranium point group symmetry in determining the crystal field operators has been brought to our attention. Neutron diffraction measurements have suggested that below T_{+1} the crystal symmetry is lowered from orthorhombic to monoclinic [108]. The lowering of the U point group symmetry will introduce imaginary terms in to the crystal field operators, which may help explain the observed azimuthal dependence of the scattering from the superlattice reflections in this phase and the resultant complex fits. We will be working with Amoretti *et al* to develop a new crystal field model, to address this point.

5.2.4 $T < T_2$

We have also investigated the lowest temperature phase through XRS measurements made at $T = 1.8$ K. Energy scans, Figure 5.25, performed on the (103) and (104) quadrupolar superlattice reflections reveal a resonance in the $\sigma\pi$ channel. These measurements were performed at an azimuth angle of $\Psi = -87°$, which unfortunately later proved to be a local intensity minimum in both channels at both reflections. The energy scan of the (103) reflection in $\sigma\sigma$ was repeated at $\Psi = -174°$, giving a large increase in the count rate and a change in the energy profile to give a resonance rather than a step, with non-resonant interference, and is comparable to that measured at 5.2 K, see Figure 5.15(b). Unfortunately there was insufficient time to repeat all the other measurements, so the preliminary energy scans are plotted together in Figure 5.25 for comparison purposes, while the repeated scan is shown in Figure 5.26.

Azimuthal measurements were made using the Stokes Method. This involves rocking the Au polariser crystal theta angle (θ_P) for $\eta = 0 : 30 : 180°$ at each azimuthal angle. The integrated intensity of the reflections is obtained by fitting a lorentzian squared peakshape, and then the variation in the intensity as a function of η is fitted using

$$I(\eta) = [\frac{1}{2}(1 + \mathrm{P}_1 \cos 2\eta + \mathrm{P}_2 \sin 2\eta)]I_0 = I_0 \cos^2(\eta + \delta), \tag{5.16}$$

to give the Stokes parameters P_1 and P_2, which are defined as:

$$\mathrm{P}_1 = \frac{I(\eta = 0) - I(\eta = \pi/2)}{I(\eta = 0) + I(\eta = \pi/2)} = \frac{I_{\sigma\sigma} - I_{\sigma\pi}}{I_{\sigma\sigma} + I_{\sigma\pi}}, \tag{5.17}$$

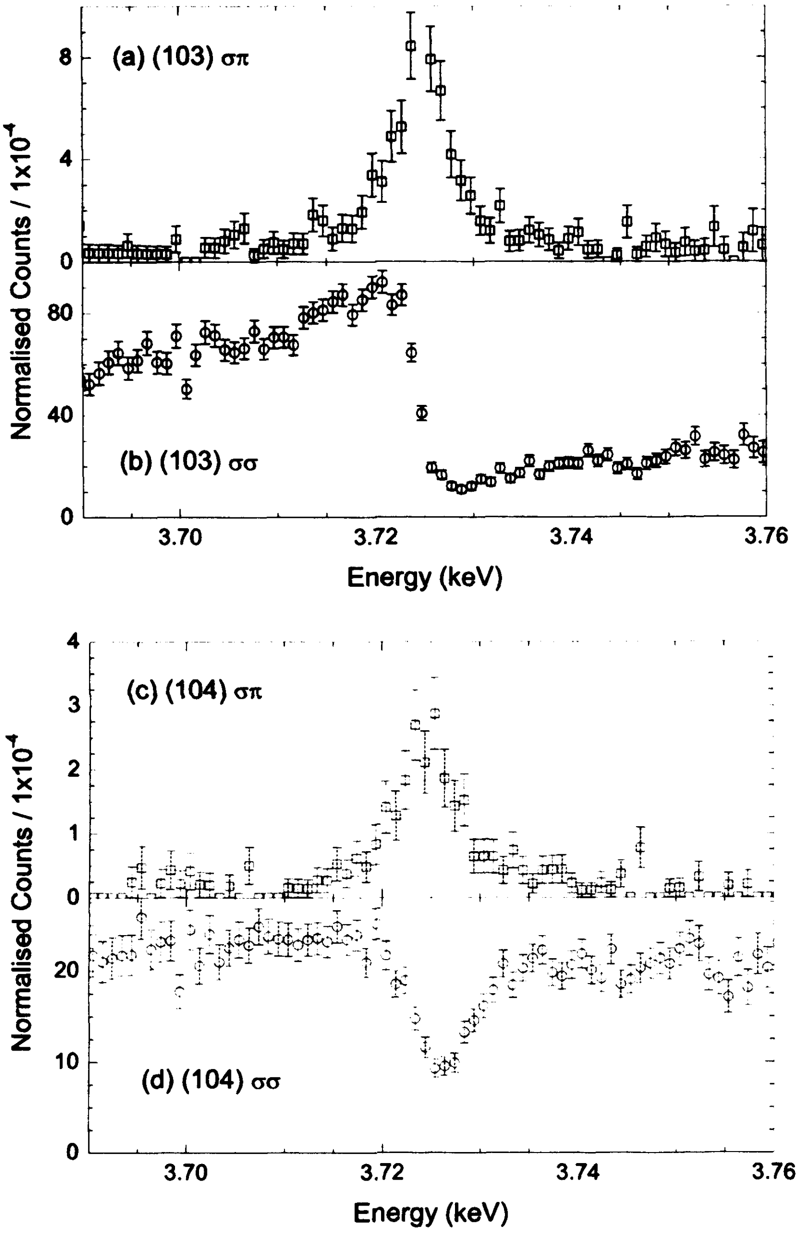

Figure 5.25: UPd$_3$ energy scans at $T = 1.8$ K of the (103) peak at $\Psi = -87°$ in (a) the $\sigma\pi$ channel showing resonance at $E = 3.725$ keV, and (b) the $\sigma\sigma$ channel showing an edge at the resonant energy; and of the (104) peak at $\Psi = -87°$ in (c) the $\sigma\pi$ channel also showing resonance at $E = 3.725$ keV, and (d) the $\sigma\sigma$ channel showing an anti-resonance.

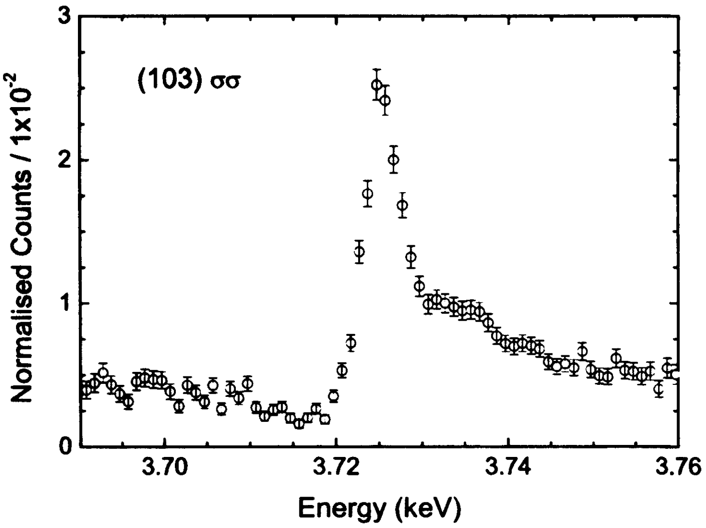

Figure 5.26: Energy scan at $T = 1.8$ K of the (103) peak in UPd$_3$ at $\Psi = -174°$ in the $\sigma\sigma$ channel.

$$P_2 = \frac{I(\eta = \pi/4) - I(\eta = 3\pi/4)}{I(\eta = \pi/4) + I(\eta = 3\pi/4)}. \qquad (5.18)$$

Hence when all the scattering is $\sigma\sigma$: $P_1 = 1$, and conversely when all the scattering is $\sigma\pi$: $P_1 = -1$. The variation in the intensity in the rotated and unrotated channels as a function of the azimuthal angle is also obtained. Figure 5.27 shows an example of the Stokes fit to the integrated intensities of the (103) reflection at $T = 1.8$ K as a function of η.

Figure 5.28 shows the azimuthal dependence of the $\sigma\pi$ scattering from the (103) reflection in UPd$_3$ at $T = 1.8$ K with two fits to the data. The dashed line corresponds to a real scattering tensor, which gives $R^2 = 0.986$, while the solid line is for a complex tensor, with $R^2 = 0.999$. The parameters for the two fits are given in Tables 5.13 and 5.14. It would appear that the complex tensor better describes the scattering. However, these measurements could only be performed over an azimuthal range of 200°, due to problems with collisions between the diffractometer and cryostat (these have now been remedied by the removal of an obsolete chi circle). In order to differentiate between the two

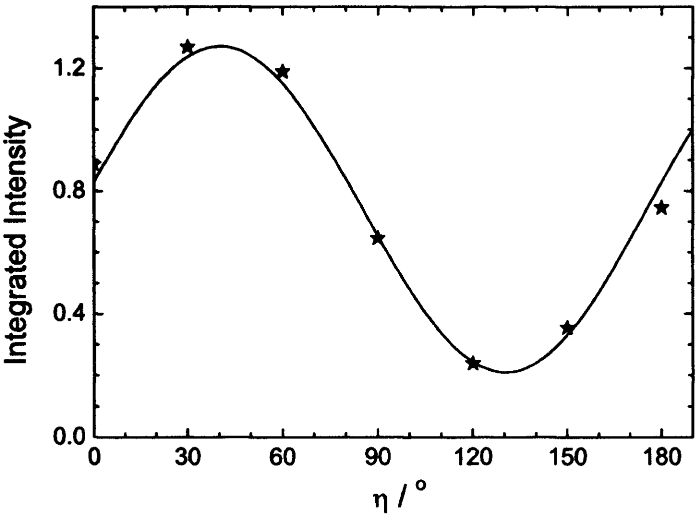

Figure 5.27: An example of the fit made to the integrated intensities of the peak shapes of the (103) reflection as a function of η at $T = 1.8$ K and $\Psi = -209°$ in $\mathrm{UPd_3}$ to obtain values for P_1 and P_2 at this azimuth angle. The fit showed by the line is described in equation (5.16).

tensors corresponding to the fits, it is clearly necessary to expand the range of Ψ investigated, to cover the region between $-45°$ and $90°$, where the two tensors give different results for the intensity.

The Stokes method also gives the azimuthal dependence of the $\sigma\sigma$ scattering, and this is shown in Figure 5.29 for the (103) reflection in $\mathrm{UPd_3}$ at $T = 1.8$ K. The form of the azimuthal dependence looks more complicated than for $\sigma\pi$, with possibly two different waveforms of different intensities present, one with a maxima centred at $\Psi \simeq 150°$ and another with a smaller maxima at $\Psi \simeq 210°$. Also shown in Figure 5.29 are fits for a real and a complex scattering tensor described by the parameters given in Tables 5.9 and 5.10. The real scattering tensor is strongly dominated by the yz elements, and if the more complicated details of the maxima are disregarded as being the result of instrumental error, gives a good description of the general periodicity of the scattering. With the freedom of eleven variable parameters in the complex tensor, the fit is greatly

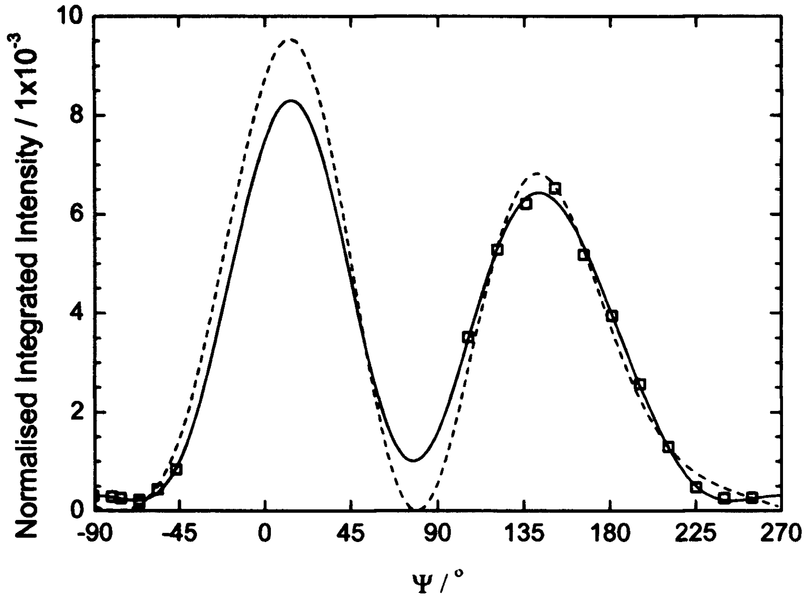

Figure 5.28: Two fits to the azimuthal dependence of $\sigma\pi$ scattering intensity from the (103) reflection in UPd$_3$ at $T = 1.8$ K.

Parameter	Value	Parameter	Value	Parameter	Value
$\Re(P_{zx})$	-4.20×10^1	$\Re(P_{xy})$	-9.23×10^0	$\Re(P_{yz})$	6.41×10^0
$\Re(P_{x^2-y^2})$	2.18×10^0	Intensity	7.54×10^{-6}	R^2	0.986

Table 5.7: Values of the parameters for the dashed line fit to the UPd$_3$ $T = 1.8$ K $\sigma\pi$ (103) data shown in Figure 5.28.

Parameter	Value	Parameter	Value	Parameter	Value
$\Re(P_{zx})$	-1.82×10^1	$\Re(P_{\mathrm{xy}})$	-8.75×10^0	$\Re(P_{yz})$	5.94×10^0
$\Re(P_{x^2-y^2})$	2.73×10^0	$\Re(P_{\mathrm{zz}})$	7.32×10^{-1}	$\Im(P_{zx})$	-7.20×10^0
$\Im(P_{xy})$	4.60×10^0	$\Im(P_{yz})$	-2.12×10^0	$\Im(P_{x^2-y^2})$	2.06×10^0
$\Im(P_{zz})$	1.37×10^1	Intensity	2.14×10^{-5}	R^2	0.999

Table 5.8: Values of the parameters for the solid line fit to the UPd$_3$ $T = 1.8$ K $\sigma\pi$ (103) data shown in Figure 5.28.

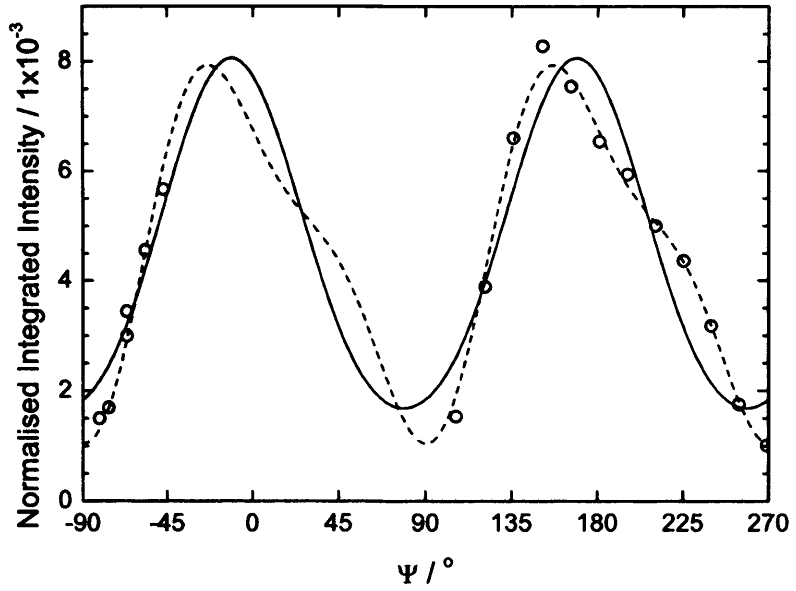

Figure 5.29: Two fits to the azimuthal dependence of $\sigma\sigma$ scattering intensity from the (103) reflection in UPd3 at $T = 1.8$ K.

Parameter	Value	Parameter	Value	Parameter	Value
$\mathfrak{R}(P_{zx})$	-4.84×10^0	$\mathfrak{R}(P_{xy})$	6.20×10^0	$\mathfrak{R}(P_{yz})$	1.98×10^1
$\mathfrak{R}(P_{x^2-y^2})$	-9.60×10^{-1}	Intensity	1.99×10^{-3}	R^2	0.888

Table 5.9: Values of the parameters for the solid line fit to the UPd3 $T = 1.8$ K $\sigma\sigma$ (103) data shown in Figure 5.29.

Parameter	Value	Parameter	Value	Parameter	Value
$\mathfrak{R}(P_{zx})$	3.927×10^1	$\mathfrak{R}(P_{xy})$	6.70×10^0	$\mathfrak{R}(P_{yz})$	2.05×10^1
$\mathfrak{R}(P_{x^2-y^2})$	1.13×10^1	$\mathfrak{R}(P_{zz})$	-1.72×10^0	$\mathfrak{I}(P_{zx})$	1.07×10^1
$\mathfrak{I}(P_{xy})$	-1.07×10^0	$\mathfrak{I}(P_{yz})$	9.20×10^0	$\mathfrak{I}(P_{x^2-y^2})$	5.06×10^0
$\mathfrak{I}(P_{zz})$	-9.89×10^0	Intensity	1.44×10^{-4}	R^2	0.988

Table 5.10: Values of the parameters for the dashed line fit to the UPd3 $T = 1.8$ K $\sigma\sigma$ (103) data shown in Figure 5.29.

improved, following the waveform more closely. It would be of interest to repeat these measurements to determine whether the waveform is truly intrinsic or not and to expand the data set, so as to help discriminate between different possible scattering tensors and their quadrupolar ordering models.

The dependence of the intensity on the scattering tensor and polarisation vectors, as described in equation (5.12), requires the tensor to be the same both for rotated and unrotated scattering. When the two parameter sets for each of the $\sigma\pi$ and $\sigma\sigma$ fits are compared, real for real and complex for complex, there is no obvious correlation. Looking at the parameters given for the complex fits to the two data sets in Tables 5.14 and 5.10 there is a similar trend in the relative values of the real elements with f_{zx} being large, while f_{xy} is the smallest, but there is a difference in the signs of the tensor elements. Comparison of the imaginary tensor elements shows that in both cases $\Im(f_{\mathrm{xy}})$ is negative while the other imaginary elements are all positive, but there is no similarity between the relative magnitudes of the different elements. It would be best if a fit could be made to the two data sets simultaneously, but the disparity in the two independent fits suggests that a least squares fit to both data sets would result in a significantly suppressed R^2 value.

The azimuthal dependence of the scattered intensity was also measured for the (104) reflection at $T = 1.8$ K. Figure 5.30 shows the rotated channel scattering data and a fit made to the data for a real scattering tensor (the fit parameters are given in Table 5.11), which indicates that the order is dominated by Q_{xy} and Q_{yz}. The same least squares fitting routine was used to vary the elements of a complex tensor, and while this appeared to obtain a slightly improved fit, R^2 was increased from 0.989 to 0.992, the complex tensor produced a negative scattering intensity for $-30 < \Psi < 40°$, which is unphysical and hence this fit is not shown.

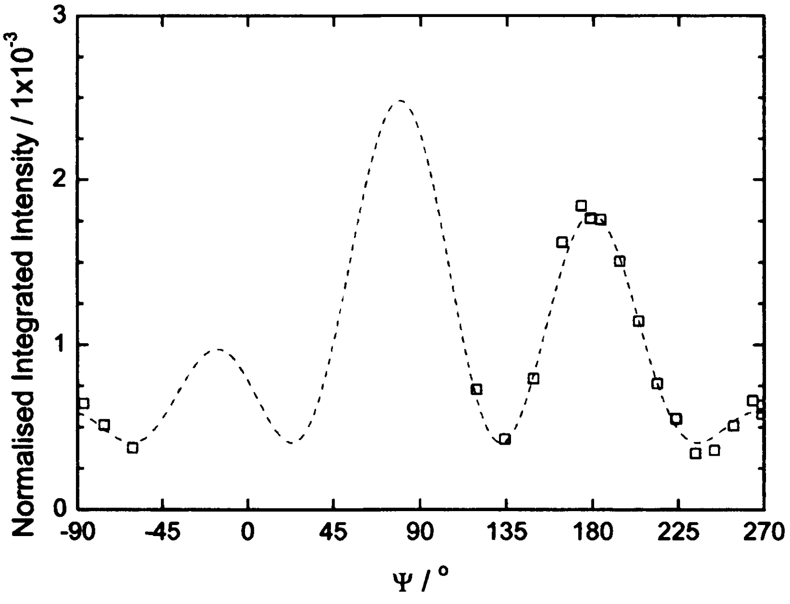

Figure 5.30: Fit to the azimuthal dependence of $\sigma\pi$ scattering intensity from the (104) reflection in UPd$_3$ at $T = 1.8$ K.

Parameter	Value	Parameter	Value	Parameter	Value
$\mathfrak{R}(P_{zx})$	5.74×10^{-1}	$\mathfrak{R}(P_{xy})$	-1.57×10^{0}	$\mathfrak{R}(P_{yz})$	1.15×10^{0}
$\mathfrak{R}(P_{x^2-y^2})$	-3.58×10^{-1}	Background	4.04×10^{-4}	Intensity	8.30×10^{-4}
R^2	0.989				

Table 5.11: Values of the parameters for the dashed line fit to the UPd$_3$ $T = 1.8$ K $\sigma\pi$ (104) data shown in Figure 5.30.

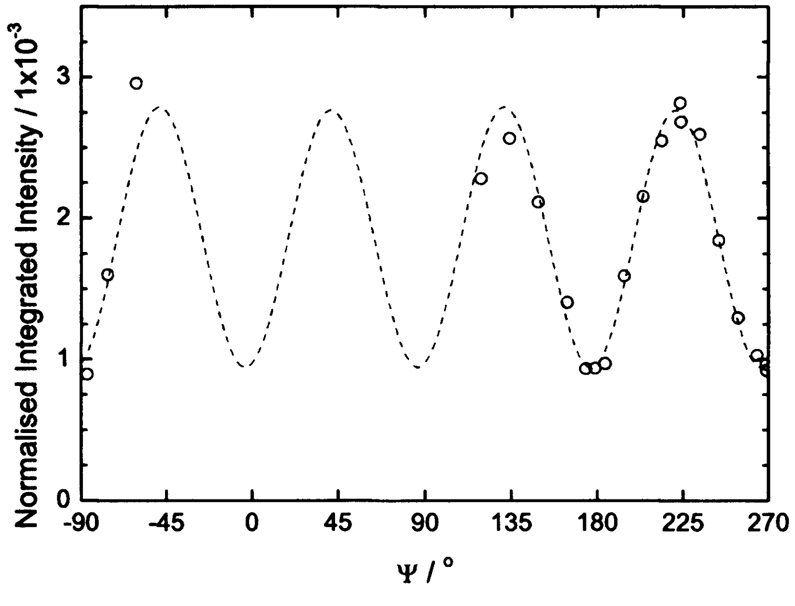

Figure 5.31: Fit to the azimuthal dependence of $\sigma\sigma$ scattering intensity from the (104) reflection in UPd$_3$ at $T = 1.8$ K.

Parameter	Value	Parameter	Value	Parameter	Value
$\mathfrak{R}(P_{zx})$	-2.76×10^{-2}	$\mathfrak{R}(P_{xy})$	1.37×10^{0}	$\mathfrak{R}(P_{yz})$	-6.30×10^{0}
$\mathfrak{R}(P_{x^2-y^2})$	3.96×10^{-1}	Background	9.43×10^{-4}	Intensity	1.72×10^{-4}
R^2	0.961				

Table 5.12: Values of the parameters for the dashed line fit to the UPd$_3$ $T = 1.8$ K $\sigma\sigma$ (104) data shown in Figure 5.31.

Figure 5.31 shows the unrotated scattering data and a least squares fit obtained for the real scattering tensor defined by the parameters in Table 5.12. The fit is reasonably good with $R^2 = 0.96$, and again indicates that the quadrupolar order is dominated by Q_{xy} and Q_{yz} components. When a least squares fit was made allowing the tensor elements to be complex no improvement was found.

It is interesting to note that for the (103) reflection an improved fit to the data is obtained using a complex scattering tensor, while for the (104) reflection a real scattering tensor is better. As discussed previously, the presence of quadrupole moments on the hexagonal sites can lead to a complex scattering tensor for (103), but not for (104). Hence the azimuthal dependence of the scattering from the two reflections at $T = 1.8$ K, may be compatible with the existence of hexagonal site quadrupoles.

Spin flip scattering, observed in polarised neutron diffraction measurements for $T < T_2$ [30], suggests the existence of magnetic order in this phase. A finite imaginary component for $\mathbf{Q} = (103)$ scattering but zero imaginary component at (104) could be indicative of a wave vector describing antiferromagnetic order, suggesting an antiphase stacking of dipole moments along the c-axis, as for the quadrupole stacking for $T_{+1} < T < T_0$. To investigate this possibility two fits have been made to the data in this phase. In one fit the imaginary elements of the scattering tensor are assumed to have purely magnetic origins, while in the other the imaginary elements originate from a combination of resonant magnetic and resonant anomalous scattering. Figure 5.32 shows that the quality of these fits to the (103) $\sigma\pi$ data at $T = 1.8$ K are very similar, $R^2 = 0.998$ and 0.999 respectively, but that the actual azimuthal waveforms are quite different. In order to determine whether there is magnetic scattering in this phase it will be necessary to extend the azimuthal range of the data set.

Attempts to make similar fits to the $\sigma\sigma$ data and both data sets for (104) have so far proved to be unsuccessful. Given that the magnitude of the moment in this phase has been estimated to be less than $0.02\,\mu_B$, and that unambiguous fits for magnetic order have not been successful, it is believed that another model may be required to more accurately explain the observed data. This phase also exhibits low symmetry and therefore these data sets will also be taken into consideration in the theoretical work of Amoretti *et al*, as discussed in section 5.2.3.

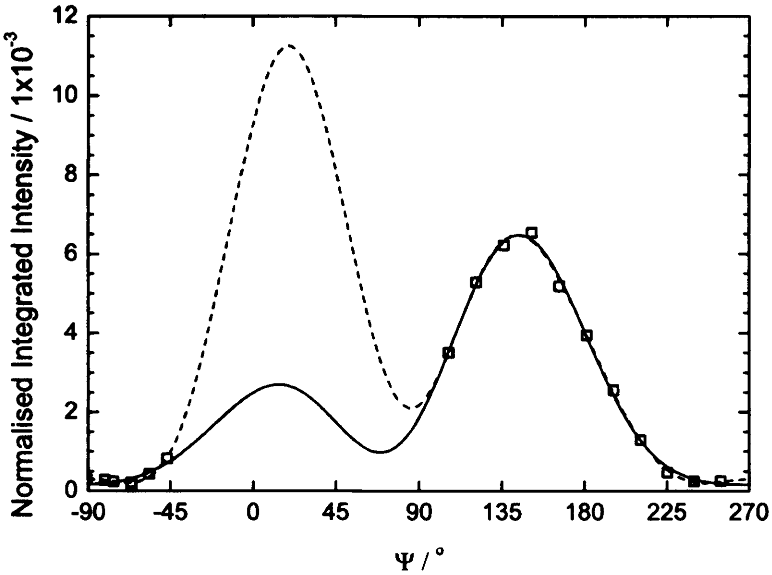

Figure 5.32: Two fits, with magnetic moments, to the azimuthal dependence of $\sigma\pi$ scattering intensity from the (103) reflection in UPd$_3$ at $T = 1.8$ K.

Parameter	Value	Parameter	Value	Parameter	Value
$\mathfrak{R}(P_{zx})$	1.49×10^{0}	$\mathfrak{R}(P_{xy})$	2.05×10^{-1}	$\mathfrak{R}(P_{yz})$	9.01×10^{-1}
$\mathfrak{R}(P_{x^2-y^2})$	8.20×10^{-1}	$\mathfrak{R}(P_{zz})$	8.13×10^{0}	P_{m_z}	1.67×10^{1}
P_{m_x}	5.46×10^{0}	P_{m_y}	6.61×10^{-2}	Intensity	8.53×10^{-4}
R^2	0.998				

Table 5.13: Parameter values for the solid line fit to the UPd$_3$ $T = 1.8$ K $\sigma\pi$ (103) data shown in Figure 5.32.

Parameter	Value	Parameter	Value	Parameter	Value
Intensity	2.24×10^{-4}	$\mathfrak{R}(P_{x^2-y^2})$	2.93×10^{0}	$\mathfrak{I}(P_{x^2-y^2})$	-1.41×10^{0}
$\mathfrak{R}(P_{xy})$	-1.89×10^{0}	$\mathfrak{I}(P_{xy})$	-4.91×10^{0}	P_{m_z}	6.92×10^{0}
$\mathfrak{R}(P_{zx})$	$2.50 \times 10^{+0}$	$\mathfrak{I}(P_{zx})$	-8.22×10^{0}	P_{m_y}	4.39×10^{-1}
$\mathfrak{R}(P_{yz})$	4.82×10^{-1}	$\mathfrak{I}(P_{yz})$	-7.39×10^{0}	P_{m_x}	-4.84×10^{0}
$\mathfrak{R}(P_{zz})$	$1.58 \times 10^{+1}$	$\mathfrak{I}(P_{zz})$	$-1.36 \times 10^{+1}$	R^2	0.999

Table 5.14: Parameter values for the dashed line fit to the UPd$_3$ $T = 1.8$ K $\sigma\pi$ (103) data shown in Figure 5.32.

5.3 $U(Pd_{1-x}Pt_x)_3$

UPt_3 is another very interesting uranium intermetallic, being a heavy fermion superconductor with $T_{SC} = 0.5$ K [45], where platinum, the uranium ligand ion, lies directly below palladium in the periodic table and hence has a more extended wave function. The crystal structures of UPd_3 and UPt_3 are slightly different (double hexagonal versus simple hexagonal close packed) but the Hill distance in each is very similar. This leaves questions about how the band structures of the two compounds differ to give different properties.

Experiments have been performed previously on samples with $x = 0.005$ [109]. Single crystal magnetic susceptibility data measured with the field applied parallel to the a-axis is reminiscent of that for UPd_3, suggesting that quadrupolar order has not been destroyed, while for $H||c$ there is a clear anomaly in the data at $T = 4.6$ K. This temperature is also associated with the development of a peak at $(\frac{1}{2}01)$ in polarised neutron diffraction experiments. Susceptibility data for a $x = 0.02$ sample showed no evidence of ordering above $T = 2$ K, indicating the high sensitivity of the quadrupolar order to ligand doping.

To further investigate the significance of Pd and Pt we have performed an XRS experiment on a single crystal of $U(Pd_{1-x}Pt_x)_3$ grown at Birmingham by Dave Fort with $x = 0.01$. As for the UPd_3 sample, it was cut with a reciprocal space (107) face and polished using diamond paste. The experiment was performed as for UPd_3 on the ID20 beamline.

Once the UB matrix had been defined at $E = 9$ keV at $T = 2$ K, and the lattice parameters set (in orthorhombic notation $a = 9.935$ Å, $b = 5.732$ Å, $c = 9.651$ Å), the energy was changed to the resonant energy, $E = 3.725$ keV, and then a rocking curve of the (004) Bragg peak performed. The peak was sharp,

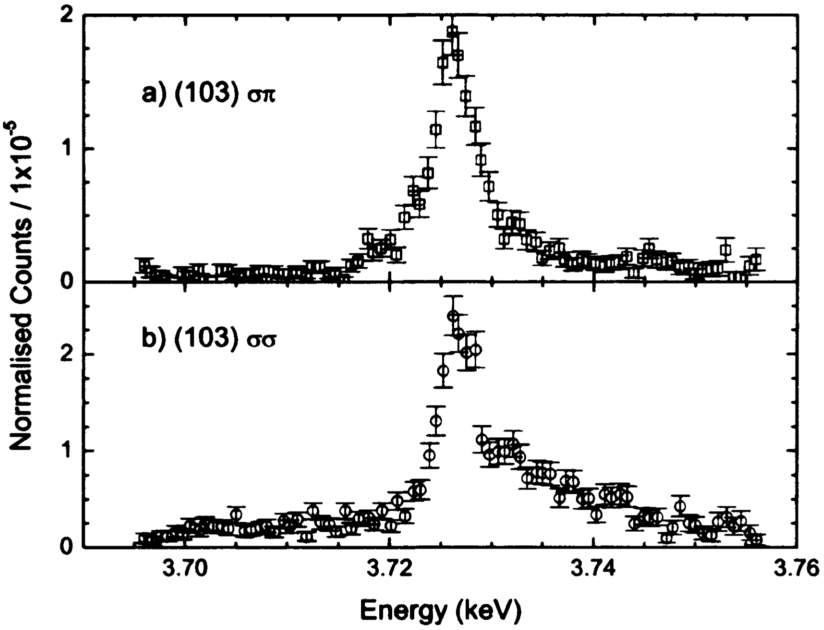

Figure 5.33: Energy scans of the (103) in $U(Pd_{0.99}Pt_{0.01})_3$ at T = 1.9 K and Ψ = 171° in a) the $\sigma\pi$ channel and b) the $\sigma\sigma$ channel both showing resonance.

i.e. the mosaic of the crystal is small, indicating the sample quality. Then we moved to (103) in reciprocal space to see if the quadrupolar superlattice reflection was present and varied the rho motor so as to find the azimuth angle which gave the maximum intensity reflection. This proved to be very difficult, due to the very weak intensity of the peak. A wide scan on the (004) peak was then performed to ensure that no other grains or crystallites were present, which could account for the poor signal.

On moving back to the (103) reflection all the motors were optimised revealing broad peaks in both channels in theta rocking curves, and energy scans were performed. Inspection of Figure 5.33 shows resonance in both channels without the significant nonresonant interference observed in the $\sigma\sigma$ channel in UPd_3 (Figure 5.11).

At the resonant energy, the sample stage was rotated through 10° and another theta rocking curve performed. The integrated intensity of the peak proved to be not significantly changed by this rotation, as one would expect for the azimuthal variation, which disproved that the broad peak could be the result of multiple scattering.

As discussed in Appendix A.2 the width of the measured peak is inversely related to the degree of correlation in real space, such that a broad diffraction peak corresponds to a small correlation suggesting short range order. Therefore we performed wide H and L scans (scans along the reciprocal space lattice vectors) with long counting times, to obtain good statistics, to determine the full-width half-maximum (FWHM) of the (103) reflection in $\sigma\pi$. The H and L scans are plotted in Figure 5.34. Making a lorentzian squared plus linear term fit to the peaks in the two scans gives a FWHM= 0.066 in units of τ_{100} and 0.063 in units of τ_{001}, or 0.042±0.003 Å and 0.041±0.003 Å respectively. These can be converted, see Appendix A.3.3, to give an indication of the degree of correlation in real space, which corresponds to 34 ± 2 Å, i.e. the quadrupolar ordering is short range only, extending over 3 - 4 unit cells.

Once the diffractometer alignment had been reoptimised on the (103) reflection in $\sigma\pi$ we performed theta rocking curves as we increased the sample temperature from $T = 2$ K to 13 K. Again the resultant peak shapes were fitted using a lorentzian squared plus linear lineshape to find the integrated intensity, peak centre and full-width half-maximum, which showed that for $T \leq 9$ K the peak centre and FWHM do not change significantly. Figure 5.35 shows the normalised integrated intensity decreasing as a function of temperature, until $T \geq 10$ K when there is no peak observed. Fitting $I = \alpha(T_C - T)^\beta$ gives $\beta = 0.60 \pm 0.06$ and $T_C = 9.1 \pm 0.1$ K, which is greater than the transition temperature we would expect from bulk measurements made for compositions at less than and greater than $x = 0.01$. The disparity in the transition temperatures may suggest that we do not have the Pt content that we expected,

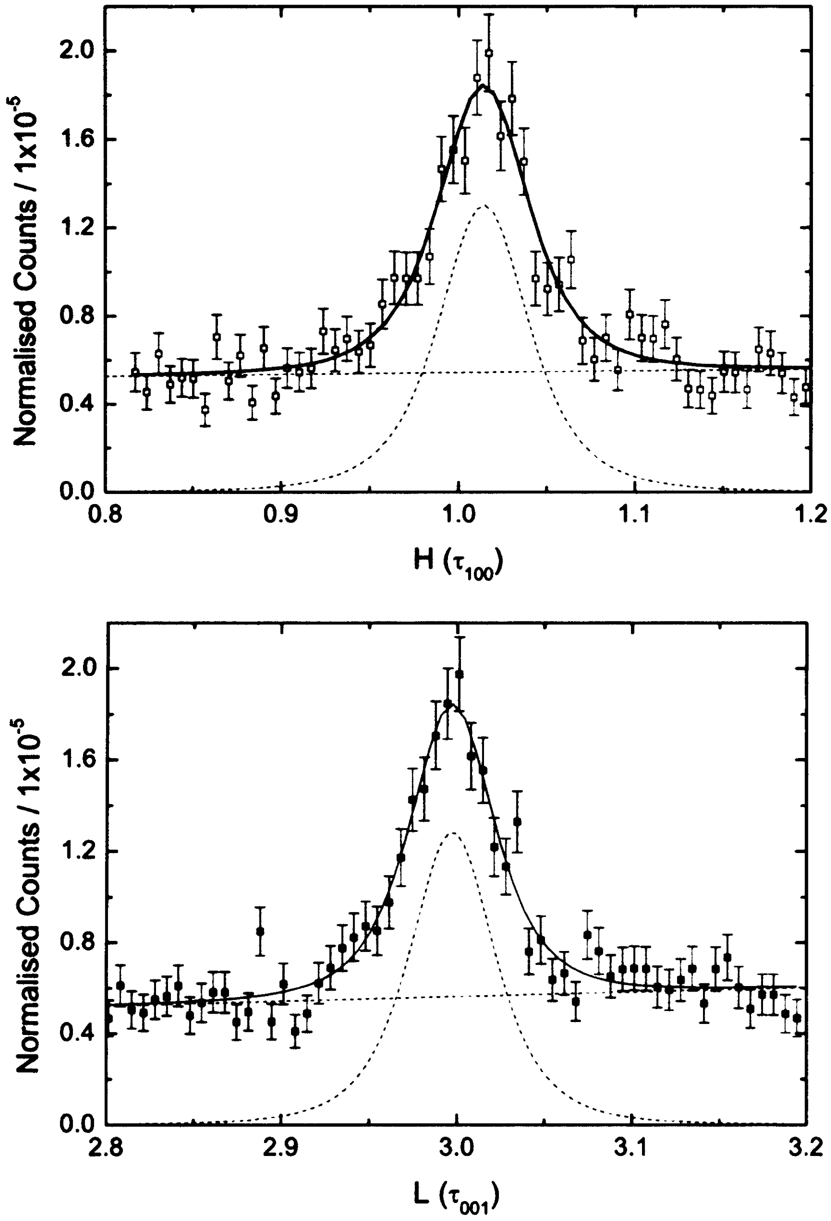

Figure 5.34: H scan and L scan across the (103) peak in U(Pd$_{0.99}$Pt$_{0.01}$)$_3$ at T = 1.8 K in $\sigma\pi$, with fits to the peak shapes indicating that the quadrupole order is short range, extending 3 - 4 unit cells.

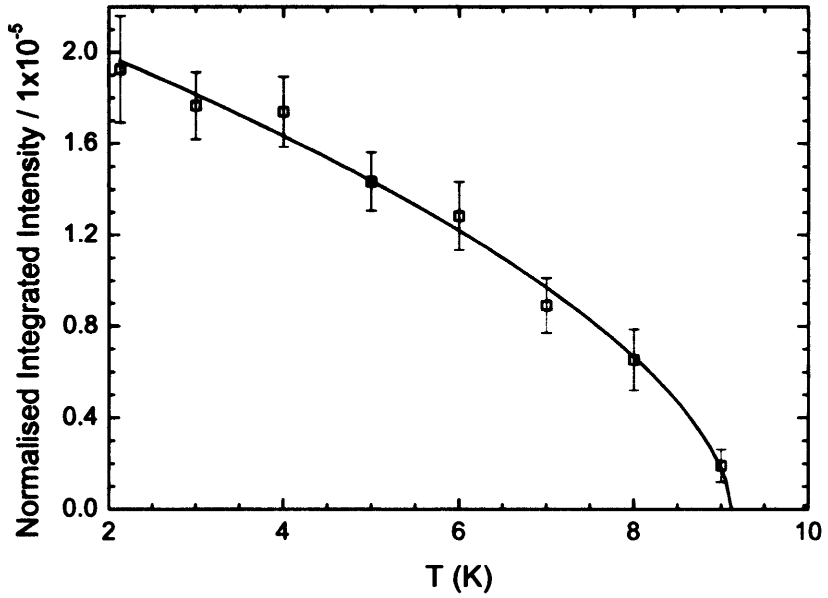

Figure 5.35: Temperature dependence of the integrated intensity of the (103) peak in $U(Pd_{0.99}Pt_{0.01})_3$ normalised to the monitor, calculated by fitting lorentzian squared plus a linear term to θ-scans. The red line through the data is a fit to $I \propto (T_C - T)^\beta$, where $T_C = 9.1 \pm 0.1$ K, and $\beta = 0.60 \pm 0.06$, which minimises chi squared.

and therefore we need to independently verify what the actual concentration of platinum is in the sample, which could be done using energy dispersive X-ray spectroscopy (EDX).

5.4 Conclusions

Our new high precision heat capacity measurements confirm the suggestion by Lingg *et al.* [25] from ultrasound that the transition at T_{+1} is second order, while that at T_{-1} is first order, and indicate an interesting evolution of features associated with the transition temperatures as a function of applied magnetic field.

We have identified the nature of the order in the first quadrupolar phase between T_0 and T_{+1} as being dominated by the Q_{zx} order parameter with quadrupole moments on quasi-cubic sites being stacked in antiphase along the c-axis, Fig. 5.13, which requires $B' \simeq 0$ in the matrix representing the quadrupolar operator. This is in agreement with calculations, based on the Hamiltonian

$$H = H_{CEF} + H_{Zeeman} - K_{\mathrm{zx}} \langle O_{\mathrm{zx}} \rangle O_{\mathrm{zx}}, \tag{5.19}$$

performed to reproduce the magnetic phase diagram for $H \parallel [001]$ and $T_{+1} < T < T_0$, obtained from high-field magnetisation and magnetostriction measurements [44]. It has been found that the fit to the data is further improved by the small admixture of a $Q_{\mathrm{x}^2-\mathrm{y}^2}$-type contribution to the scattering tensor, such that our data is consistent with the previous polarised neutron diffraction measurements [27], which were only able to detect $Q_{\mathrm{x}^2-\mathrm{y}^2}$ order in this phase.

It has not been possible to perform an experiment to determine the azimuthal dependence in the phase between T_{+1} and T_{-1}, due to the exceedingly narrow temperature range. Below T_{-1} the azimuthal dependence of the scattering is more complicated, and indicates that a more complicated model is required to describe the quadrupolar order. Excellent fits to the data for $\mathbf{Q} = (103)$ and (104) at $T = 5.2$ K have been obtained on allowing all the elements of the scattering tensor to vary freely, but no physical model has been found which recreates such a complex tensor. The addition of quadrupole moments on the uranium hexagonal sites to the ordering model, is unable to account for the scattering from $\mathbf{Q} = (104)$. While a structural distortion would introduce a complex scattering tensor for $\mathbf{Q} = (104)$, the magnitude of distortion required would lead to the destruction of the crystal, and therefore this seems an unsuitable solution. Another possible extension of the ordering model for this phase is the presence of additional multipole moments. Other measurement techniques have found no evidence of magnetic order. The fits to the data made allowing a symmetric imaginary tensor, associated with the quadrupolar order, and an antisymmetric imaginary tensor, associated with a magnetic moment, are unable to conclusively prove whether or not magnetic order may be present.

XRS measurements performed at T = 1.8 K, in the lowest temperature phase, again reveal a complicated azimuthal dependence to the scattering intensity from both the superlattice reflections. It has been interesting to note that the least squares fit to the experimental data is significantly improved for a complex scattering tensor for $\mathbf{Q}$ = (103), but that a better fit is obtained for a real scattering tensor for $\mathbf{Q}$ = (104). This could have significant implications, and could be interpreted as being due to quadrupole moments on the hexagonal sites, or an anti-phase stacking of magnetic moments along the c-axis.

Our XRS experiment on $U(Pd_{1-x}Pt_x)_3$ reveals a transition at $T_C \sim 9$ K to short range quadrupolar order with a correlation length of the order of 3 - 4 unit cells, indicating the sensitivity of the system to platinum doping. It will be necessary to check whether the Pt concentration is 1% or not.

5.5 Further Work

Heat capacity measurements are planned on single crystals in a field to follow the transitions in the basal plane and along the c-axis, enabling a better understanding of the peak splitting feature seen for the polycrystalline data, Fig. 5.5.

We hope to remeasure the temperature dependence of the (103) and (104) reflections over the quadrupolar transition temperatures using the cryomagnet on ID20, which has a much greater temperature stability. This is important to determine at which transition the scattering intensities from each reflection develop and to reinvestigate the feature at T^* seen in Figure 5.10 (a).

In order to distinguish definitively whether the quadrupolar structure at $T = 7.1$ K includes quadrupole moments located on the quasi-cubic sites or on both the quasi-cubic and hexagonal sites we would like to perform an XRS experiment to investigate the azimuthal dependence of the scattering from the (013) reflection. Using the $(0kl)$ reflections could also help to determine whether the azimuthal dependence of the scattering in the lower temperature phases is the result of hexagonal site quadrupoles or a crystallographic distortion.

It has been unfortunate that we have not, so far, been able to collect larger data sets over a wider range of Ψ in the phase $T < T_2$. The initial technical problems, which prevented us from extending the data range have been overcome, and it has only been due to lack of time that we have not returned to these measurements. It would be very interesting to re-perform these measurements, since fits based on different ordering models providing very similar results in the data region, give very different results in the unexplored region. Therefore, this would hopefully enable us to rule out different models for the ordering in this phase.

Theoretical work is now underway at the Università di Parma to establish the effect of the point group symmetry of the uranium in the lower temperature quadrupolar phases and to develop the associated crystal field model. This will prove to be particularly interesting since, so far, the multipolar systems investigated have tended to be high symmetry, and this work will provide new insight into low symmetry systems. To assist in this process, it will be important to carry out a full crystallographic investigation of UPd_3, which, to our knowledge, has been surprisingly absent up until this time. We plan to submit a proposal to ISIS to use the General Materials (GEM) diffractometer, to perform diffraction measurements in the different phases, to determine how the crystal symmetry evolves as a function of temperature.

So far all our experiments have concentrated on the uranium in UPd_3, and therefore it would be interesting to use the element selectivity of XRS to investigate any physics specific to the palladium ions. In other $5f$ compounds it has been shown that there is interesting behaviour also associated with the transition metal ions, such as the resonant enhancement observed at the gallium K-edge from electric dipole transitions in $UTGa_5$ (T=Ni, Pd and Pt) [110]. The azimuthal dependence of the scattering has been understood in terms of a model of orbital polarisation of the Ga sites compatible with the symmetry of the neighbouring U moments. These experiments have demonstrated that XRS provides information about the induced orbital polarisation on ligand ions in systems where there is significant valence-band hybridisation between U $5f$ and anion $4p$ states. The U $5f$ states in UPd_3 are well localised, but if resonant enhancement was observed at the palladium K-edge in UPd_3, performing experiments at this energy, rather than at the U M-edge, would allow access to a much larger region of reciprocal space and make it possible to perform experiments in complex sample environments, such as pressure cells, due to the much lower attenuation at higher energies. This could provide access to a whole new wealth of information about UPd_3.

Nuclear Magnetic Resonance (NMR) is another technique that directly probes quadrupolar order, but uranium NMR can only be done using ^{235}U, as ^{238}U has no unpaired nucleons and therefore zero nuclear magnetic moment. ^{235}U NMR is notoriously difficult due to the properties of the nuclei: a very small nuclear gyromagnetic ratio, a large nuclear quadrupole moment, the low natural abundance ($< 1\%$) and the strong radioactivity. In addition the relaxation times are commonly very short due to the strong hyperfine interaction with the $5f$ electrons, which makes the NMR signal detection very difficult using standard pulsed methods [111]. Quadrupolar order has only been studied directly using ^{235}U in the solid state in UO_2 [112]. In order to first determine whether it will be possible to use U-NMR in UPd_3 we will need to estimate the spin-lattice relaxation time $^{235}T_1$. This can be done indirectly using unlike spin-spin coupling which causes the T_1-modulated ^{235}U spins to contribute to the spin-echo decay process of the ligand nuclei, i.e. Pd nuclei [111].

Chapter 6

Results II - $NpPd_3$

In this chapter results of magnetisation, resistivity and heat capacity measurements performed on polycrystalline samples of dhcp $NpPd_3$ at the Actinide User Lab, Institute for Transuranium Elements, Karlsruhe, are discussed.

6.1 Magnetisation

Magnetisation measurements were carried out for $T = 2 - 300$ K in a range of fields up to 7 T on encapsulated samples using a SQUID magnetometer (Quantum Design MPMS-7), see section 4.2. In low applied fields, $H = 0.03$ T and 1.1 T, the isofield magnetic susceptibility shows a sharp increase below 35 K to a broad maximum centred at 20 K, as previously reported [50]. However, in addition we observe a shoulder at 10 K [113]. In higher fields: 4 T and 7 T, the form of M/H changes such that the 10 K feature becomes more pronounced, see Figure 6.1(a). The 30 K and 10 K anomalies could be attributed to two antiferromagnetic transitions, T_1 and T_2; these might occur separately on the locally hexagonal and quasi-cubic sites, similar to the tran-

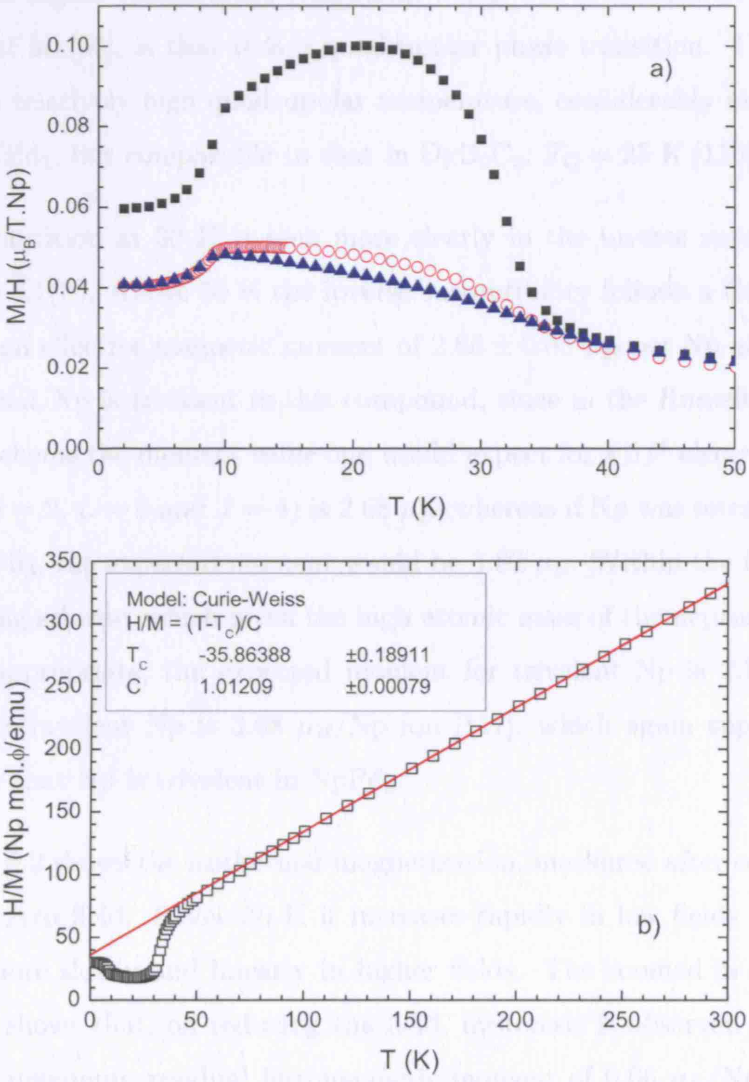

Figure 6.1: (a) $M/H(T)$ in NpPd$_3$ at $H = 1.1$ T (■), 4 T (○) and 7 T (▲), showing transitions at $T = 10$ K and 30 K. (b) Curie-Weiss fit to $H/M(T)$ for $H = 1.1$ T giving an effective moment of 2.85 μ_B/Np, which indicates that the neptunium ions in NpPd$_3$ are trivalent.

sitions observed in neodymium [114], or successively on only one of the site types, as in praseodymium [115]. Another possibility, considering the unusual form of the higher temperature transition, which was of considerable interest to Nellis *et al.* [50], is that it is a quadrupolar phase transition. This would result in a relatively high quadrupolar temperature, considerably higher than those in UPd_3, but comparable to that in DyB_2C_2: $T_Q = 25$ K [116].

The transition at 30 K is seen more clearly in the inverse susceptibility, see Figure 6.1(b). Above 50 K the inverse susceptibility follows a Curie-Weiss law, with an effective magnetic moment of 2.85 ± 0.05 μ_B per Np atom. This suggests that Np is trivalent in this compound, since in the Russell-Saunders coupling scheme the moment value one would expect for a $5f^4$ electron configuration ($S = 2$, $L = 6$ and $J = 4$) is 2.68 μ_B, whereas if Np was tetravalent, as U is in UPd_3, the expected moment would be 3.62 μ_B. Within the intermediate coupling scheme, which given the high atomic mass of the neptunium may be more appropriate, the expected moment for trivalent Np is 2.75 μ_B/Np ion, and tetravalent Np is 3.68 μ_B/Np ion [117], which again supports our conclusion that Np is trivalent in $NpPd_3$.

Figure 6.2 shows the isothermal magnetization, measured after cooling the sample in zero field. Below 30 K it increases rapidly in low fields before increasing more slowly and linearly in higher fields. The zoomed in section of the figure shows that, on reducing the field, hysteresis is observed below 0.1 T, with a maximum residual ferromagnetic moment of 0.06 μ_B/Np atom at $T = 15$ K. Below the 10 K transition, hysteresis is observed below 0.5 T but with a reduced residual ferromagnetic moment. Above 32 K, the isothermal magnetization increases linearly as a function of field over the entire range $H = 0 - 7$ T. At 7 T the maximum moment was 0.3 μ_B per Np atom. The absence of saturation in 7 T and the low remanent magnetisation, if an intrinsic property, may indicate that the structure below 30 K contains a small

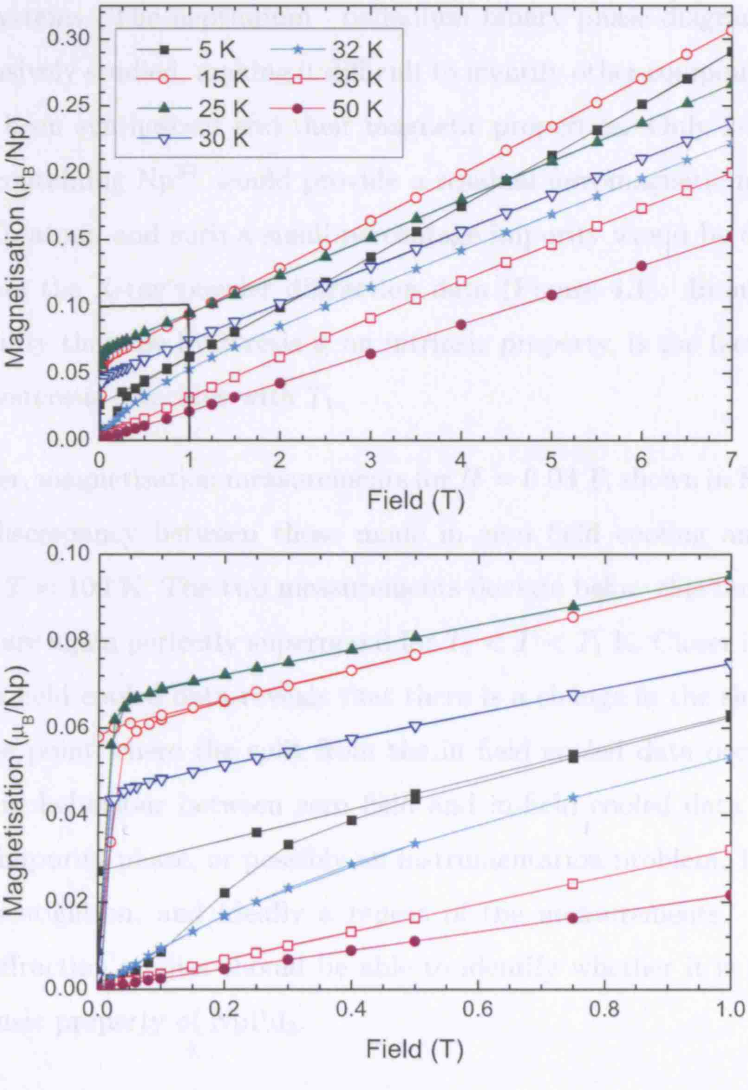

Figure 6.2: $M(H)$ in $NpPd_3$ up to 7 T at a range of temperatures, indicating that a 7 T field is insufficient for saturation; and the same data plotted up to 1 T showing hysteresis below 30 K, with a maximum residual ferromagnetic moment of 0.06 μ_B/Np atom for $T = 15$ K.

ferrimagnetic moment. An alternative explanation is the presence of some ferromagnetic impurity phase, but the isofield measurements appear to rule out either carbides or nitrides, commonly occurring ferromagnetic impurities in other systems. The neptunium palladium binary phase diagram has not been extensively studied, making it difficult to identify other compounds which may have been synthesized and their magnetic properties. Only 2-3 % of an impurity containing Np^{3+} would provide a residual ferromagnetic moment of 0.06 μ_B/Np atom, and such a small percentage impurity would be difficult to resolve from the X-ray powder diffraction data (Figure 4.1). In support for the possibility that the hysteresis is an intrinsic property, is the fact that the onset of hysteresis coincides with T_1.

However, magnetisation measurements for $H = 0.03$ T, shown in Figure 6.3, reveal a discrepancy between those made in zero field cooling and in-field cooling at $T = 100$ K. The two measurements deviate below this temperature until they are again perfectly superposed for $T_2 < T < T_1$ K. Closer inspection of the zero field cooled data reveals that there is a change in the slope of the data at the point where the split from the in field cooled data occurs. This difference in behaviour between zero field and in-field cooled data might be due to an impurity phase, or possibly an instrumentation problem. It requires further investigation, and ideally a repeat of the measurements. However, neutron diffraction studies should be able to identify whether it is the result of an intrinsic property of $NpPd_3$.

6.2 Electrical Resistivity

Electrical resistivity measurements were carried out using a Quantum Design PPMS-9 (section 4.3) for $T = 2-300$ K in zero field and 9 T. In $NpPd_3$ in zero

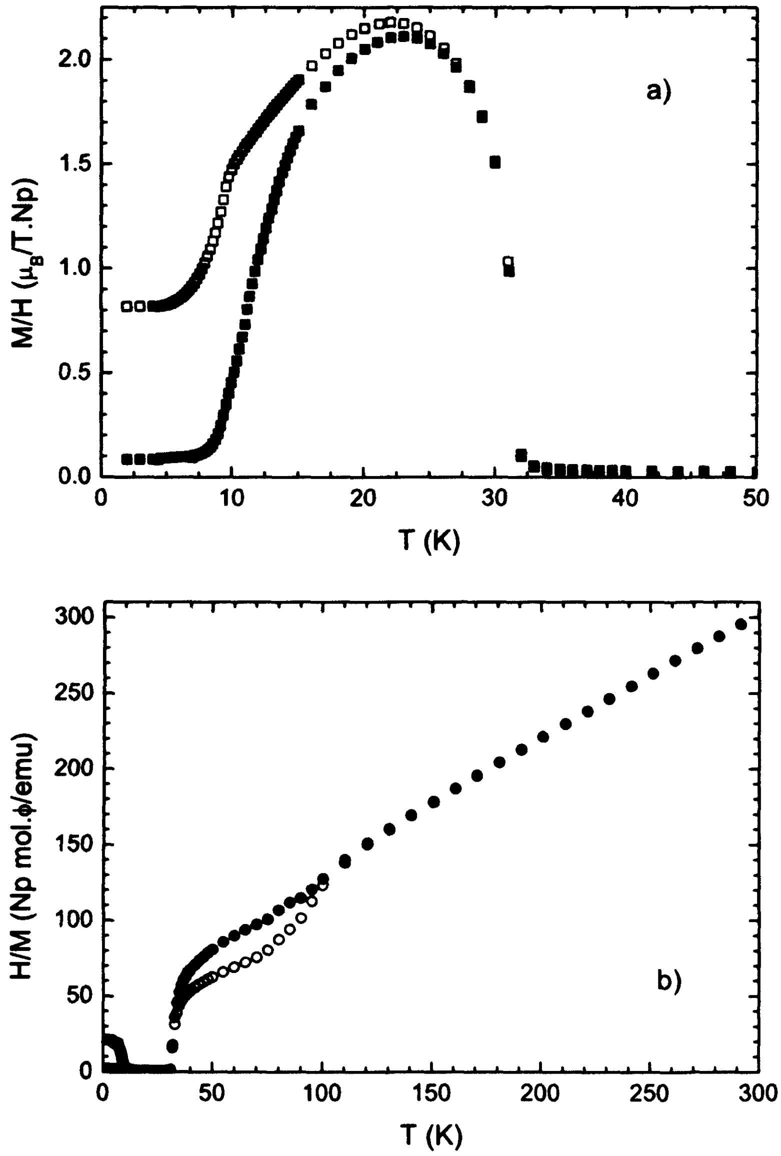

Figure 6.3: (a) $M/H(T)$ and (b) $H/M(T)$ in $NpPd_3$ at $H = 0.03$ T for zero field cooling and in field cooling (solid and open markers respectively).

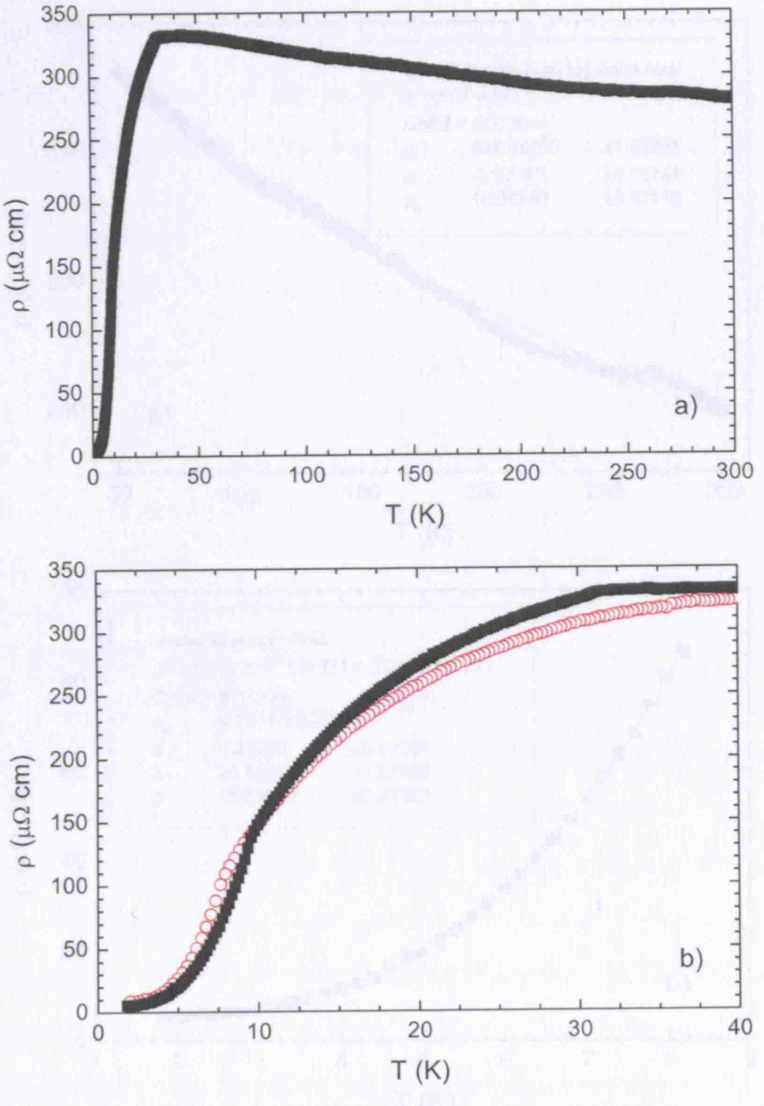

Figure 6.4: (a) $\rho(T)$ in NpPd$_3$ at $H = 0$ T for $T = 2 - 300$ K, showing a marked change in the gradient at $T = 30$ K. Below 30 K the resistivity decreases with decreasing temperature as for a normal metal, but above 30 K $d\rho/dT$ is negative. The 30 K transition appears to coincide with the onset of coherence. (b) $\rho(T)$ for $H = 0$ T (■) and 9 T (○). In zero field the two transitions at 10 and 30 K can be seen clearly. In 9 T the upper transition is smoothed away, while the lower transition is shifted down in temperature.

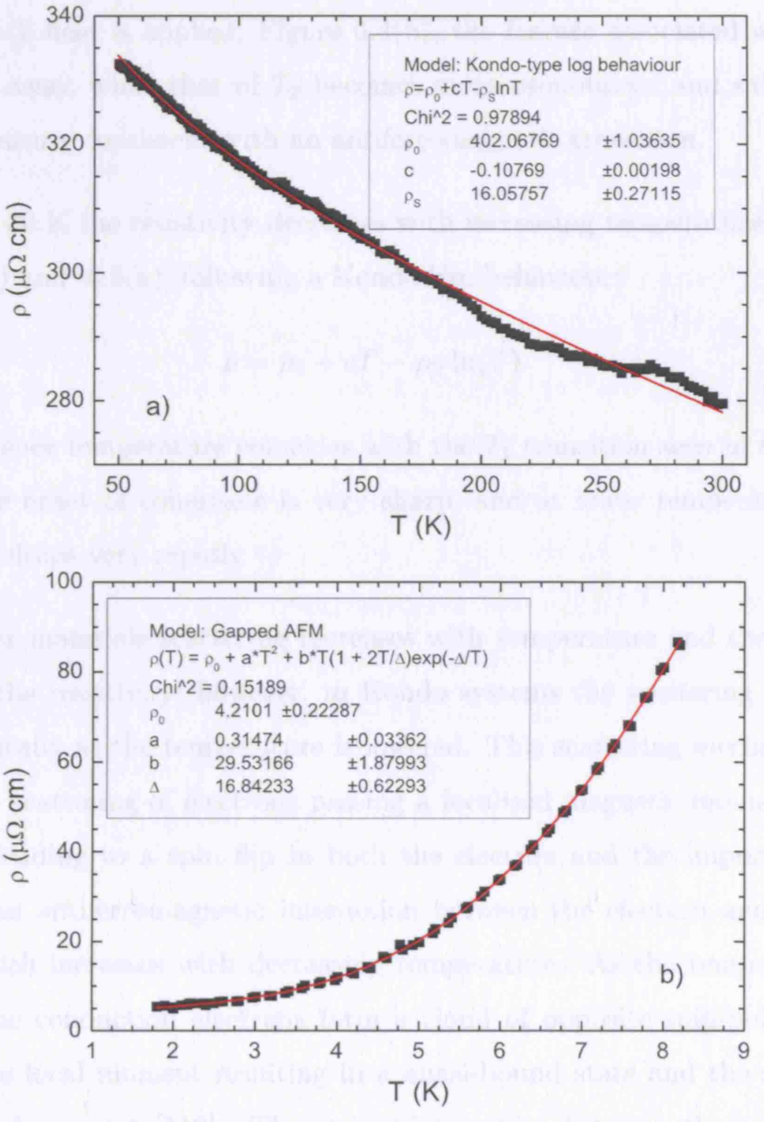

Figure 6.5: (a) A Kondo-type fit to $\rho(T)$ in NpPd$_3$ at $H = 0$ T for $T > 50$ K. (b) At low temperatures $\rho(T)$ is not proportional to T^2. Instead it can be modelled using an antiferromagnetic ground state with an energy gap $\Delta = 17$ K [123]. The fit made using this model gives a residual resistivity $\rho_0 \approx 4$ $\mu\Omega$ cm, and hence a residual resistivity ratio of 85, indicating the high quality of the sample.

field the data presented in Figure 6.4(a) shows two kinks at $T = 30$ K and 10 K corresponding to the transitions T_1 and T_2 seen in the magnetisation data. When a 9 T field is applied, Figure 6.4(b), the feature associated with T_1 is smoothed away, while that of T_2 becomes more pronounced and shifts down in temperature, consistent with an antiferromagnetic transition.

Above 30 K the resistivity decreases with increasing temperature, see Figures 6.4(a) and 6.5(a), following a Kondo-like behaviour:

$$\rho = \rho_0 + cT - \rho_S \ln(T). \qquad (6.1)$$

The coherence temperature coincides with the T_1 transition seen in the M/H data. The onset of coherence is very sharp, and at lower temperatures the resistivity drops very rapidly.

In most materials scattering increases with temperature and therefore so too does the resistivity; however, in Kondo systems the scattering increases logarithmically as the temperature is lowered. This scattering mechanism involves the scattering of electrons passing a localised magnetic moment on an impurity leading to a spin flip in both the electron and the impurity [118]. There is an antiferromagnetic interaction between the electron and the impurity which increases with decreasing temperature. As the temperature is lowered the conduction electrons form a cloud of opposite spin-polarisation around the local moment resulting in a quasi-bound state and the screening of the local moment [119]. The strong interaction between the conduction electrons and the moment leads to a strong enhancement of the electron scattering cross-section, which leads to the term proportional to $\mathcal{J} \ln T$ in the resistivity, where $\mathcal{J} < 0$ is the exchange coupling between the moment and conduction electrons. However, when a temperature $\sim T_K$ is reached, a bound singlet state is formed [51]. The crossover from incoherent inelastic scattering of conduction electrons from partially screened moments to coherent elastic electron-electron scattering is commonly referred to as the onset of Kondo lattice coherence. At high temperatures a Kondo lattice behaves as an ensemble of non-interacting Kondo impurities. At the lowest temperatures, the Kondo lattice can be described as a periodic Fermi liquid [120].

Kondo behaviour was initially observed in transition metal alloys where there is a resistivity minimum at low temperatures, but in heavy fermion systems the behaviour is commonly observed in the form of a maximum in the resistivity at a temperature T_M which generally lies below 40 K. For example, the resistivity of $NpRu_2Si_2$ is similar to that of $NpPd_3$ displaying a logarithmic variation with T above the ordering temperature, 27.5 K, and a precipitous drop below T_M understood as a huge magnetic contribution of an energy gap antiferromagnet [121]. The value of T_M is a function of the Kondo temperature T_K and the mean RKKY (Ruderman-Kittel-Kasuya-Yoshida) interaction strength between the magnetic ions [122]. The presence of a maximum in the resistivity data does not imply that magnetic ordering actually occurs. Instead T_M marks the temperature below which the RKKY interactions between the magnetic ions start to convert single-ion Kondo behaviour into correlated-ion behaviour.

The low temperature resistivity below 10 K does not vary as a simple Fermi Liquid $\rho(T) \propto T^2$, but instead behaves as an antiferromagnet with a 17 K energy gap [123]:

$$\rho(T) = \rho_0 + AT^2 + bT(1 + 2T/\Delta)\exp(-\Delta/T), \qquad (6.2)$$

see Figure 6.5(b). The residual resistivity ratio given by $\rho(T = 0\,\mathrm{K})/\rho(T = 300\,\mathrm{K})$ is 85, which is high for a neptunium bulk sample indicating the quality of the sample.

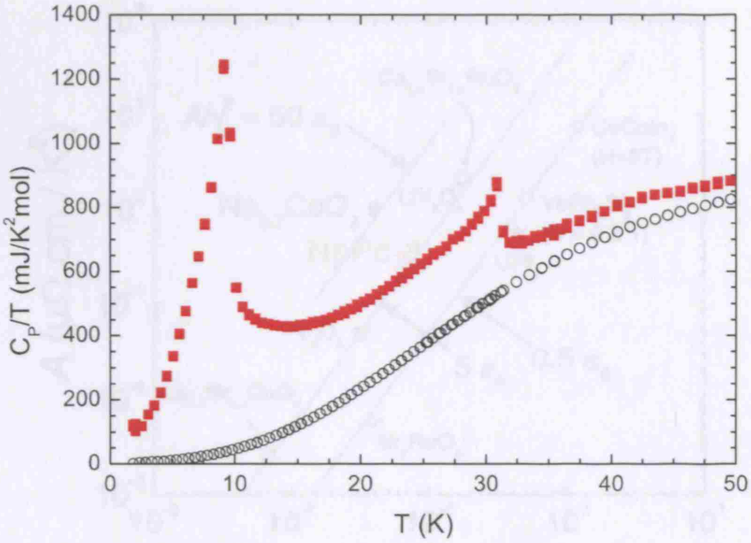

Figure 6.6: C_P/T vs T of NpPd$_3$ (■), showing peak features at $T = 10$ K and $T = 30$ K, and of ThPd$_3$ (○).

6.3 Heat Capacity

Heat capacity measurements were performed also using the PPMS-9 for $T = 2 - 300$ K in a range of applied magnetic fields. The NpPd$_3$ zero field data reveal two clear lambda anomalies at $T = 10$ K and 30 K, see Figure 6.6. Making a fit to the data for $2 < T < 5$ K using

$$C_P/T = \gamma T + \beta T^2, \tag{6.3}$$

gives the electronic heat capacity, $\gamma = 78 \pm 4$ mJK^{-2}mol^{-1}, however the value obtained for β determines the Debye Temperature to be 61 K, which is too low. This makes the estimate for γ less reliable. This is a very small data range over which to make a fit to determine γ and β, but a larger range of temperature leads to even smaller values for the Debye Temperature, since there is considerable curvature due to the lambda feature associated with T_2. Kadowaki and Woods [124] observed that the ratio of A/γ^2, where A is the coefficient of the quadratic term in the low temperature resistivity, has a com-

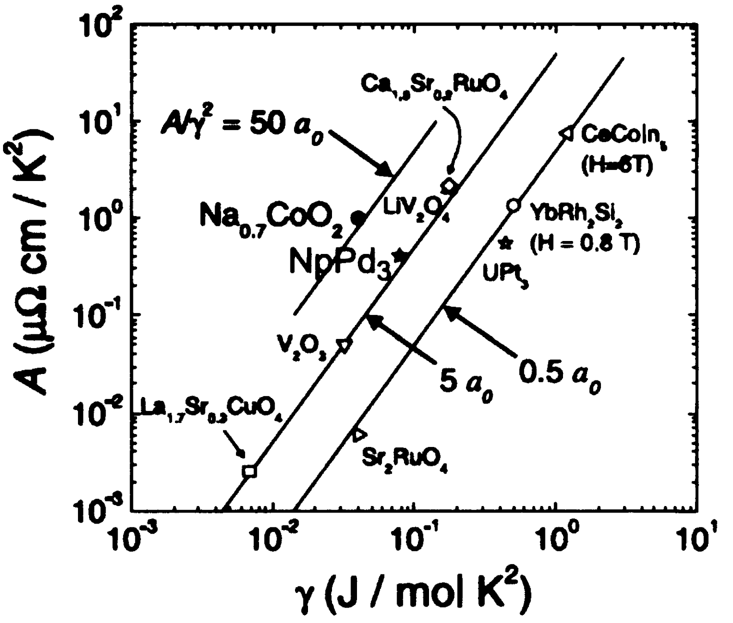

Figure 6.7: Kadowaki-Woods plot of A (where $\rho = \rho_0 + AT^2$) versus γ (electronic heat capacity coefficient) for a number of materials including $NpPd_3$, after Li *et al.* [125]. The three lines are lines of constant Kadowaki-Woods ratio, A/γ^2, for values of 0.5, 5 and 50 a_0, where $a_0 = 1 \times 10^{-5}$ $\mu\Omega\text{cm}(\text{mol.K/mJ})^2$. The first line at $a_0 = 0.5$ is characteristic of heavy fermion materials; the second line at $5a_0$, on which $NpPd_3$ lies, is typically found in systems with magnetic frustration or close to a Mott insulator; the third line at $50a_0$ is for the largest ratio found so far in $Na_{0.7}CoO_2$.

mon value of the order of 1.0×10^{-5} $\mu\Omega\text{cm}(\text{mol.K/mJ})^2$ in numerous heavy fermion materials, which is at least an order of magnitude greater than that for common d-metals. In $NpPd_3$, $A/\gamma^2 = 5.2 \pm 0.8 \times 10^{-5}$ $\mu\Omega\text{cm}(\text{mol.K/mJ})^2$, which when included on a Kadowaki-Woods plot, see Figure 6.7 after Li *et al.* [125] and references therein, lies on the $5a_0$ line with $La_{1.7}Sr_{0.3}CuO_4$ [126], V_2O_3 [127] and $Ca_{1.8}Sr_{0.2}RuO_4$ [128], which all lie close to a Mott transition and LiV_2O_4 [129], which exhibits geometric magnetic frustration.

Figure 6.8 does not show the magnetic entropy, from which quantitative conclusions can be drawn regarding the crystal field levels. Instead it shows

$$\int_2^T \left(\frac{C_P}{T}_{\mathrm{NpPd_3}} - \frac{C_P}{T}_{\mathrm{ThPd_3}} \right) dT,$$

where $\mathrm{ThPd_3}$ has been used as a phonon blank, but the electronic contribution has not been removed. This is due to the difficulties in estimating γ. Above $T = 100$ K the heat capacity data is less good with larger error bars, and if the thorium data and $\gamma = 78$ mJ/K^{2}mol are subtracted from the neptunium data the resultant difference is negative. As previously explained there is reason to doubt such a value for gamma. Regardless of this, it is still possible to draw qualtitative conclusions about the crystal field levels. Figure 6.8 shows the calculated entropy of $\mathrm{NpPd_3}$ to be almost double that of $\mathrm{UPd_3}$ below 40 K, suggesting occupation of a larger number of the crystal field levels. Since magnetisation measurements have indicated that neptunium is trivalent, this means that $J = 4$, as for uranium in $\mathrm{UPd_3}$, so that there will also be nine crystal field levels on the quasi-cubic and hexagonal sites. One possibility is that both site types have doublet ground states, which would lead to a ground state entropy of $R \ln 2$, as opposed to $\frac{1}{2} R \ln 2$ for $\mathrm{UPd_3}$, before the degeneracy is raised due to the mixing of levels caused by the quadrupole operators. Another cause of the increased entropy could be that the energy gaps to the first excited states on the cubic and hexagonal sites are low enough that both are thermally populated at 40 K, unlike in $\mathrm{UPd_3}$ where only the cubic excited state is partially occupied.

Inspection of Figure 6.9(a) reveals that in increasing applied magnetic fields the anomaly associated with T_2 shifts down in temperature, in agreement with the behaviour expected from an antiferromagnetic transition. The feature also decreases in size until $H = 7$ T after which it sharpens and increases in magnitude, behaviour which is as yet not explained. The application of a 1 T field broadens the T_1 transition feature and shifts it up in temperature by 2 K, while in fields greater than 4 T the feature has been smoothed away.

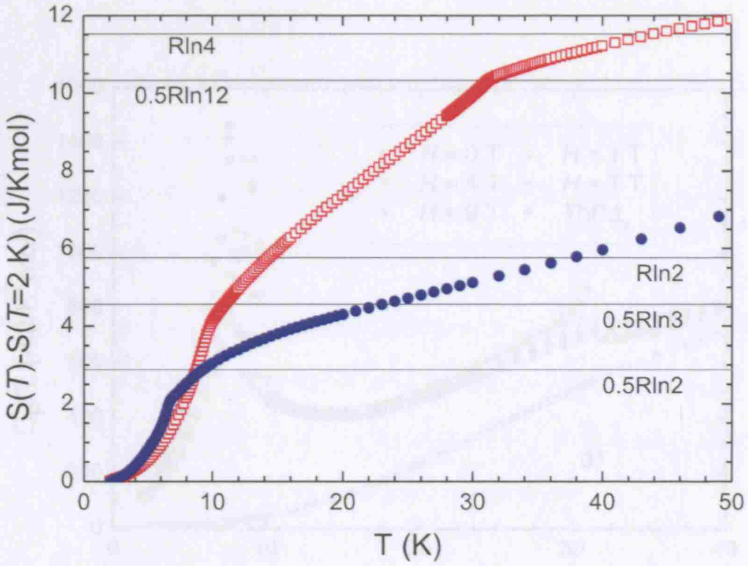

Figure 6.8: A comparison of the entropy of $NpPd_3$ (□) and UPd_3 (●), suggesting the occupation of a greater number of crystal field levels at low temperatures in $NpPd_3$ than UPd_3.

These are not the characteristics of an antiferromagnetic phase transition, however this could be consistent with a quadrupolar transition. The effect of the application of a magnetic field on the transitions is also seen clearly in the calculated entropy as shown in Figure 6.9(b).

6.4 Conclusions

In conclusion, magnetisation, electrical resistivity and heat capacity measurements reveal two transitions in dhcp $NpPd_3$ at $T_2 = 10$ K and $T_1 = 30$ K. The in-field behaviour of the features associated with the T_2 transition in different measurements indicates that it is most like an antiferromagnetic transition. The T_1 transition is that which was observed in the previous experiments by Nellis *et al.*, [50] but unattributed. It has proved more difficult using the current polycrystalline bulk property experimental data to assign the nature of

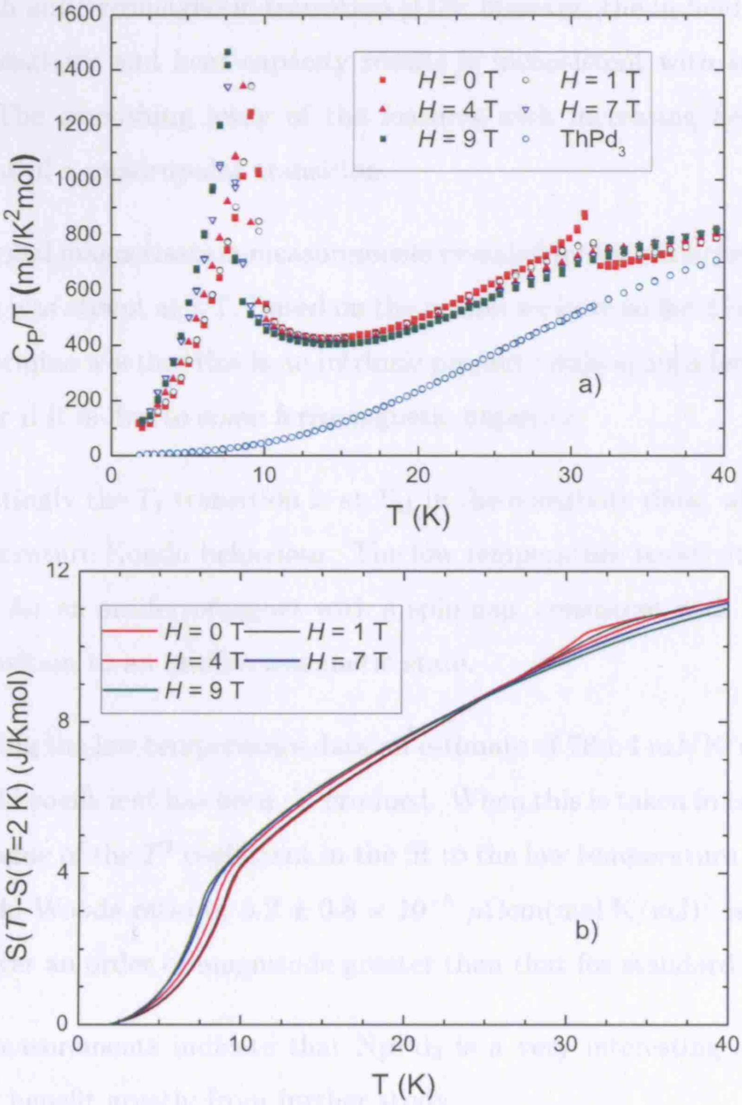

Figure 6.9: (a) Application of a magnetic field to $NpPd_3$ leads to the T_2 transition feature in C_P/T moving down in temperature, which is consistent with an antiferromagnetic transition, with an abrupt increase in peak height for $H \geq 7$ T. The T_1 feature broadens and moves up in temperature in low fields before being smoothed away for $H \geq 4$ T, behaviour more commonly associated with a quadrupolar transition. (b) The field-effect on the transitions is also seen clearly in the calculated entropy.

this transition. Initially, based on the magnetisation data, T_1 was also assessed as being an antiferromagnetic transition [113]; however, the in field behaviour seen in resistivity and heat capacity results is inconsistent with such a conclusion. The smoothing away of the features with increasing field is more reminiscent of a quadrupolar transition.

Isothermal magnetisation measurements revealed hysteresis below T_1, while saturation was absent at 7 T. Based on the results we have so far it is not possible to determine whether this is an intrinsic property indicating a ferrimagnetic moment or if it is due to some ferromagnetic impurity.

Interestingly the T_1 transition is at T_M in the resistivity data, which shows high temperature Kondo behaviour. The low temperature resistivity data fits the model for an antiferromagnet with a spin gap, consistent with T_2 being a phase transition to an antiferromagnetic state.

By fitting the low temperature data an estimate of 78 ± 4 mJ/K^{2}mol for the Sommerfeld coefficient has been determined. When this is taken in conjunction with the value of the T^2 coefficient in the fit to the low temperature resistivity, a Kadowaki-Woods ratio of $5.2 \pm 0.8 \times 10^{-5}$ $\mu\Omega$cm(mol.K/mJ)^2 is obtained, which is over an order of magnitude greater than that for standard $d-$metals.

Our measurements indicate that $NpPd_3$ is a very interesting compound, which will benefit greatly from further study.

6.5 Further Work

There are clearly many more experiments to be performed on $NpPd_3$. Once the glove box containing the new Czochralski puller at ITU has been commissioned, one of the first samples that they will attempt to grow will be single crystal

$NpPd_3$, which as far as we are aware has never been attempted before. It is hoped that, given it is isostructural to UPd_3, it should not prove to difficult to produce good quality samples. We will then be able to measure the magnetic and transport bulk properties of single crystals, which we hope will further elucidate our current data sets.

Neutron experiments will be of particular interest, but require large sample quantities, approximately $1 - 5$ g, which means that we are limited by the time taken to produce samples, but also in the long term by the fact that neptunium supplies are finite. It is planned to perform a neutron diffraction experiment in different fields at HMI on the E2 diffractometer to try and determine the nature of the transitions at T_1 and T_2. The previous diffraction experiment [50] observed no additional peaks at 4 K, which seems to rule out the possibility of an antiferromagnetic phase, since this would lead to magnetic Bragg peaks due to the increase in size of the unit cell. This led to discussions of some type of short range order, possibly in clusters. However, the experiment was performed on a very small quantity of polycrystalline $NpPd_3$ with poor instrumental flux and resolution. With the immense improvements in neutron sources and instrumentation that have taken place over the past thirty years we are confident that new diffraction data below 10 K will provide information about the ordering vector of the antiferromagnetic phase. Measurements in the phase between the two transitions at T = 10 K and 30 K will be particularly interesting. The absence of magnetic Bragg peaks would point to a non-magnetic origin for the transition at 30 K. Neutrons do not couple directly to quadrupole moments, but instead we may observe a lattice modulation vector associated with an induced lattice distortion as is seen in UPd_3.

A proposal to perform polarised neutron diffraction on D3 at ILL to follow the susceptibilities of the locally hexagonal and quasi-cubic sites individually has also been accepted. This will allow us to identify whether magnetic moments are developing on the site-types successively or simultaneously.

Inelastic Neutron Scattering (INS) experiments will provide a great deal of information about $NpPd_3$. We have had a proposal accepted on the HET spectrometer at ISIS to investigate $NpPd_3$, and it will also form part of the commissioning of the new MERLIN spectrometer. We will measure the crystal field excitations, giving us information about the valence state of the neptunium to compare with magnetisation data, and energy levels which can be used to calculate the heat capacity to compare with our data. The presence of the Kondo-type behaviour seen in the high temperature resistivity measurements suggest that $NpPd_3$ may not be as fully localised as UPd_3, which we can look for through the effect it would have on the crystalline field. A fit to the low temperature resistivity data indicates the presence of a spin gap $\Delta \sim 17$ K, which will also be investigated using INS.

If $T_1 = 30$ K is determined to be a transition to a quadrupolar phase, eventually we will perform an XRS experiment to look for "forbidden" superlattice reflections due to the order and to determine the azimuthal dependence of the scattering.

Chapter 7

Results III - $(U,Np)Pd_3$

Numerous studies of UPd_3 indicate that it undergoes four phase transitions at T_0 = 7.8 K, T_{+1} = 6.9 K, T_{-1} = 6.7 K and T_2 = 4.4 K, which have been attributed to a succession of antiferroquadrupolar orderings of the $5f^2$ localised U electrons on the quasi-cubic sites (see section 2.3). Magnetic susceptibility measurements on pure dhcp $NpPd_3$ indicate that it undergoes two magnetic phase transitions (see section 6.1). Since dhcp $NpPd_3$ and dhcp UPd_3 have almost identical lattice parameters and the same crystal structure we have anticipated complete solid solubility from UPd_3 to $NpPd_3$ allowing us to investigate the perturbation of the quadrupolar structures of UPd_3 by substitution of Np on some U sites. In this chapter the results for different measurements on the mixed actinide compounds are detailed, which for ease and clarity will often be identified by the percentage neptunium doping, such that 50%Np refers to $(U_{0.5}Np_{0.5})Pd_3$. The compositions investigated are 50%, 5%, 2% and 1% Np, with particular attention being focussed on $(U_{0.95}Np_{0.05})Pd_3$.

7.1 Magnetisation

7.1.1 $(\mathrm{U}_{0.5}\mathrm{Np}_{0.5})\mathrm{Pd}_3$

The 50%Np M/H data qualitatively resembles that for pure NpPd_3 shifted down in temperature, such that there is a sharp rise below 15 K to a broad maximum centred at 5 K, see Figure 7.1(a). In the H/M data, shown in Figure 7.1(b), the transition is seen clearly at 15 K, while above 100 K the data is linear, exhibiting Curie-Weiss behaviour with an effective paramagnetic moment of 2.976 ± 0.003 μ_B per actinide ion. Hysteresis is observed in magnetisation measurements as a function of applied magnetic field while saturation is absent, Figure 7.1(c). For $T < 15$ K the field below which hysteresis is observed increases with decreasing temperature to 1 T at 2 K, Figure 7.1(d). The maximum residual ferromagnetic moment is 0.05 μ_B/An. Again this leaves questions about the origin of this behaviour, whether it is an intrinsic ferrimagnetic effect or if it is due to a very small quantity of an impurity phase with a large ferromagnetic moment.

7.1.2 $(\mathrm{U}_{0.95}\mathrm{Np}_{0.05})\mathrm{Pd}_3$

The 5%Np magnetic measurements show no clear evidence of a magnetic transition. M/H data may show a slight upturn at the lowest temperatures, Figure 7.2(a), however, this could be an experimental artifact associated with the cryogenics. Figure 7.2(b) shows that above 100 K H/M may follow a modified Curie-Weiss Law, possibly indicative of a singlet ground state with a large energy gap to the first excited state, giving an effective paramagnetic of 3.06 ± 0.02 μ_B per actinide ion. There is no evidence of hysteresis in the isothermal magnetisation data.

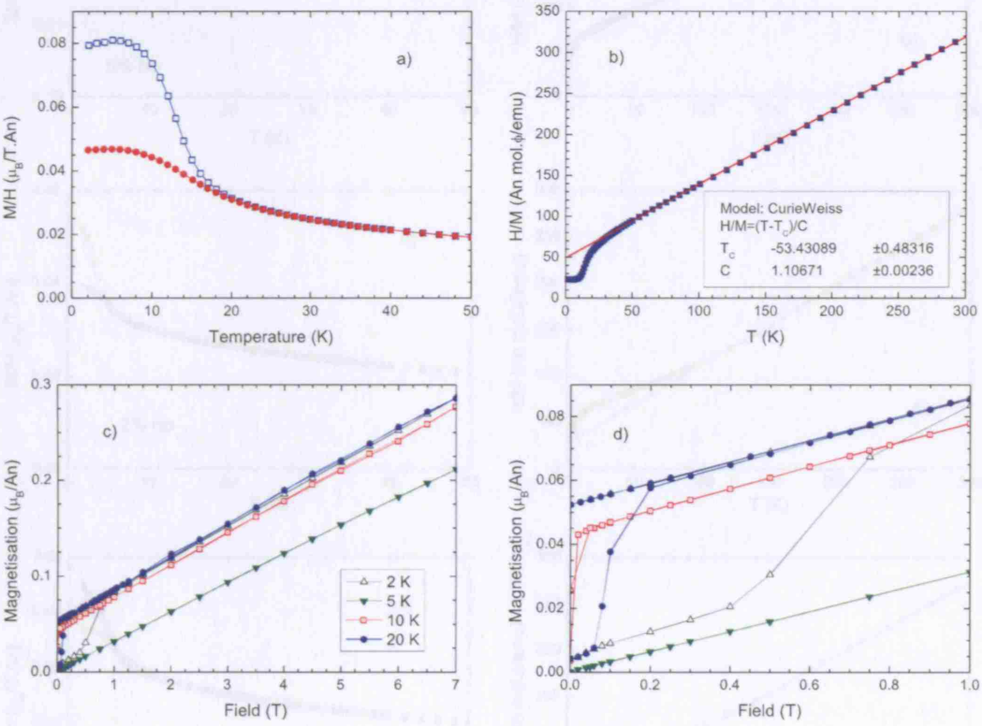

Figure 7.1: (a) $M/H(T)$ in $(\mathrm{U}_{0.5}\mathrm{Np}_{0.5})\mathrm{Pd}_3$ at $H = 1.1$ (□) and 4 T (●), showing a transition at $T \sim 12$ K. (b) Curie-Weiss fit to $H/M(T)$ for $H = 1.1$ T giving an effective moment of 2.976 ± 0.003 μ_B/An. (c) $M(H)$ in $(\mathrm{U}_{0.5}\mathrm{Np}_{0.5})\mathrm{Pd}_3$ up to 7 T at a range of temperatures, indicating that a 7 T field is insufficient for saturation; (d) the same data plotted up to 1 T showing hysteresis below 15 K, with a maximum residual ferromagnetic moment of 0.05 μ_B/An atom.

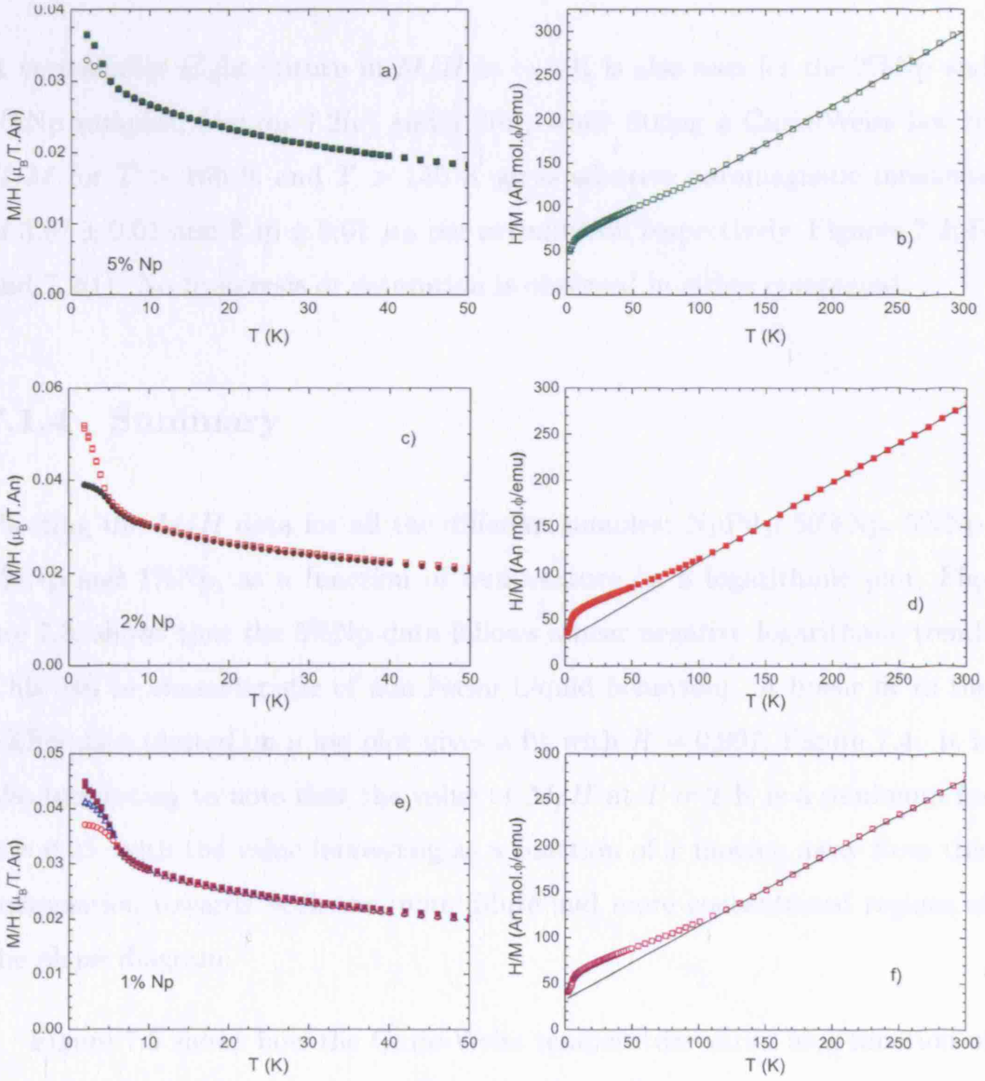

Figure 7.2: Isofield magnetisation measurements on dilute neptunium doped samples. (a) M/H in $(U_{0.95}Np_{0.05})Pd_3$ for $H = 1.1$ T (■) and 7 T (○). (b) H/M in $(U_{0.95}Np_{0.05})Pd_3$ for $H = 1.1$ T with the Curie-Weiss fit above 100 K shown as a black line. (c) M/H in $(U_{0.98}Np_{0.02})Pd_3$ for $H = 1.1$ T (□) and 7 T (•). (d) H/M in $(U_{0.98}Np_{0.02})Pd_3$ for $H = 1.1$ T with the Curie-Weiss fit above 100 K shown as a black line. (e) M/H in $(U_{0.99}Np_{0.01})Pd_3$ for $H = 1.1$ T (■), 4 T (△) and 7 T (○). (f) H/M in $(U_{0.99}Np_{0.01})Pd_3$ for $H = 1.1$ T with the Curie-Weiss fit above 150 K shown as a black line.

7.1.3 $(U_{1-x}Np_x)Pd_3$, $x = 0.02$, 0.01

A very similar slight upturn in M/H at ~ 5 K is also seen for the 2%Np and 1%Np samples, Figures 7.2(c) and 7.2(e), while fitting a Curie-Weiss law to H/M for $T > 100$ K and $T > 150$ K gives effective paramagnetic moments of 3.07 ± 0.01 and 3.16 ± 0.01 μ_B per actinide ion respectively, Figures 7.2(d) and 7.2(f). No hysteresis or saturation is observed in either compound.

7.1.4 Summary

Plotting the M/H data for all the different samples: $NpPd_3$, 50%Np, 5%Np, 2%Np and 1%Np, as a function of temperature on a logarithmic plot, Figure 7.3, shows that the 5%Np data follows a near negative logarithmic trend. This can be characteristic of non-Fermi Liquid behaviour. A linear fit to the 5%Np data plotted on a log plot gives a fit with $R = 0.997$, Figure 7.4. It is also interesting to note that the value of M/H at $T = 2$ K is a minimum for $x = 0.05$, with the value increasing as a function of x moving away from this composition towards both the more dilute and more concentrated regions of the phase diagram.

Figure 7.5 shows how the Curie-Weiss temperature varies as a function of the neptunium concentration in $(U_{1-x}Np_x)Pd_3$. The data point for $x = 0$ was obtained from single crystal data [26] using

$$\theta_{\text{poly}} = \frac{2}{3}\theta_a + \frac{1}{3}\theta_c, \tag{7.1}$$

where θ_i is the Curie-Weiss temperature determined from measurements with the applied field direction parallel to the i-axis. The sharp change in θ with low neptunium doping is unusual. The behaviour may be associated with the dramatic change in the lattice parameters, Figure 4.2. One possibility is that

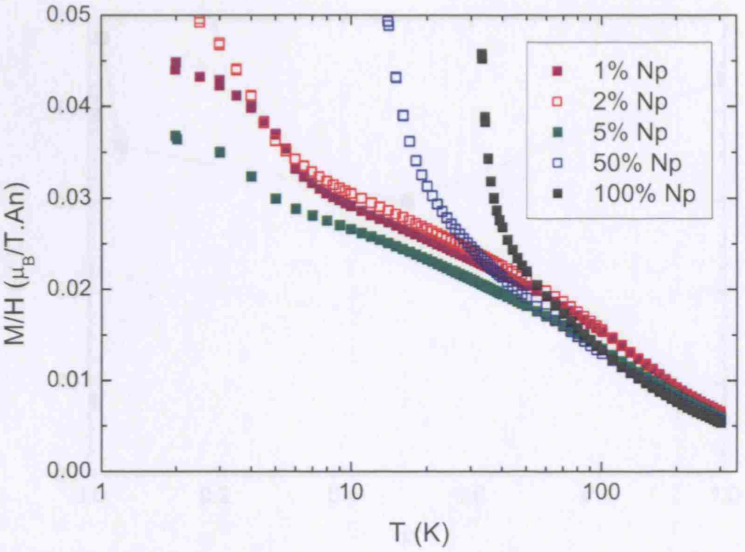

Figure 7.3: M/H in pure $NpPd_3$ and mixed $(U,Np)Pd_3$ at $H = 1.1$ T plotted vs $\log T$. $(U_{0.95}Np_{0.05})Pd_3$ shows a near negative log trend, possibly indicative of a non-Fermi Liquid.

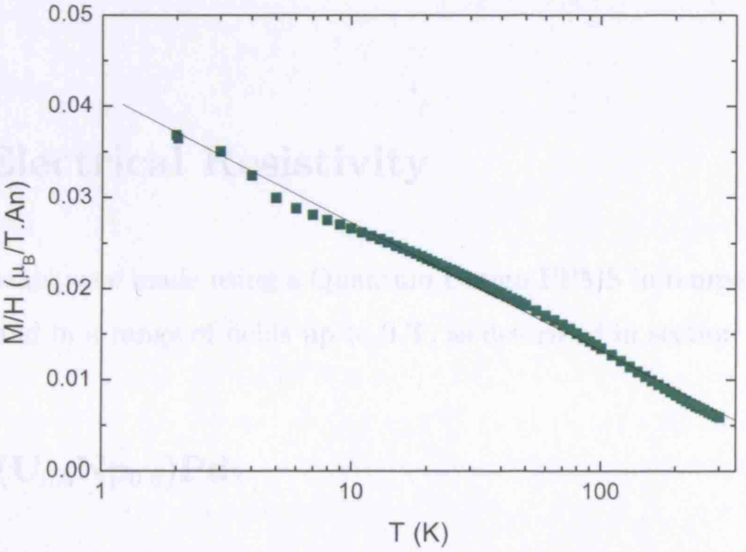

Figure 7.4: A linear fit to M/H in $(U_{0.95}Np_{0.05})Pd_3$ at $H = 1.1$ T plotted vs $\log T$.

the addition of a small quantity of Np leads to a sharp change in the cohesive energy, and hence the lattice constants, and the exchange interaction may be very sensitive to the lattice spacing due to changing bands near the Fermi

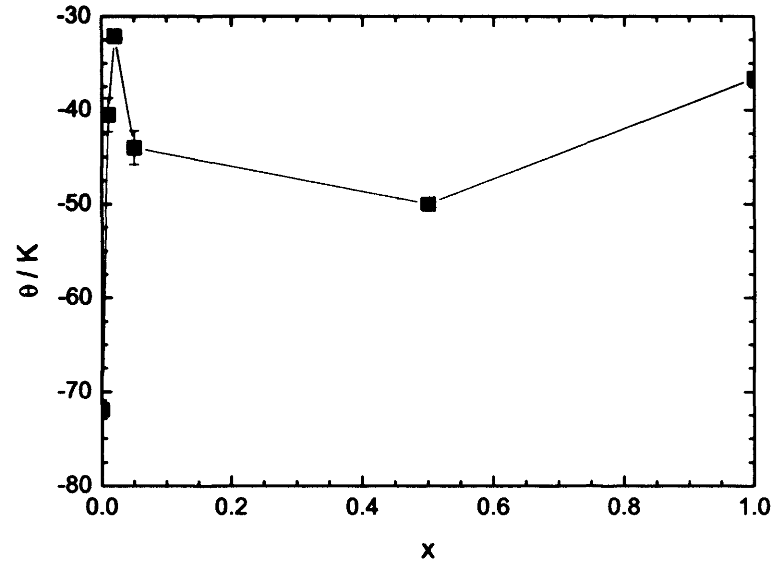

Figure 7.5: The Curie-Weiss temperature as a function of x in $(U_{1-x}Np_x)Pd_3$.

level.

7.2 Electrical Resistivity

Measurements were made using a Quantum Design PPMS in temperatures up to 300 K and in a range of fields up to 9 T, as described in section 4.3.

7.2.1 $(U_{0.5}Np_{0.5})Pd_3$

In the 50%Np sample the high temperature resistivity has a negative gradient, as seen in $NpPd_3$ (section 6.2). However the onset of coherence is not so sharp, varying over a broader range of temperatures, and is not associated with a transition temperature deduced from the magnetic measurements, see Figure 7.6(a). A kink is observed in the zero field resistivity at $T = 12$ K, which is smoothed away in a 9 T field, Figure 7.6(b).

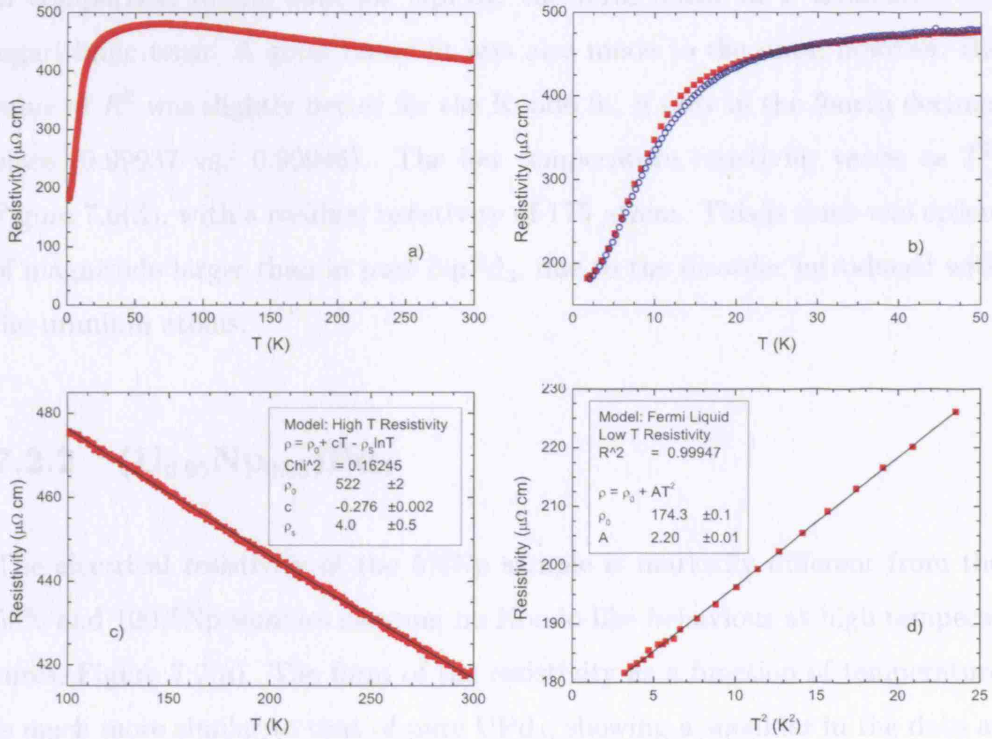

Figure 7.6: (a) $\rho(T)$ in $(\mathrm{U}_{0.5}\mathrm{Np}_{0.5})\mathrm{Pd}_3$ at $H = 0$ T for $T = 2 - 300$ K, showing a smooth change from a positive to a negative gradient at $T \sim 50$ K. (b) $\rho(T)$ for $H = 0$ (🟥) and 9 (○) T. In zero field a transition can be seen at 12 K. In 9 T the transition is smoothed away. (c) A Kondo-type fit (black line) to $\rho(T)$ in $(\mathrm{U}_{0.5}\mathrm{Np}_{0.5})\mathrm{Pd}_3$ at $H = 0$ T for $T > 100$ K. (d) Below 5 K the resistivity varies as T^2, in very good agreement ($R = 0.99965$) with Fermi-Liquid Theory.

A fit to the high temperature resistivity above 100 K, Figure 7.6(c), for

$$\rho = \rho_0 + cT - \rho_S \ln T, \tag{7.2}$$

is in good agreement with the data indicating Kondo-type behaviour. However, in comparison to the data for $NpPd_3$, the term linear in T dominates the logarithmic term. A good linear fit was also made to the data, however, the value of R^2 was slightly better for the Kondo fit, if only in the fourth decimal place (0.99937 vs. 0.99946). The low temperature resistivity varies as T^2, Figure 7.6(d), with a residual resistivity of 175 $\mu\Omega$cm. This is some two orders of magnitude larger than in pure $NpPd_3$, due to the disorder introduced with the uranium atoms.

7.2.2 $(U_{0.95}Np_{0.05})Pd_3$

The electrical resistivity of the 5%Np sample is markedly different from the 50% and 100%Np samples showing no Kondo-like behaviour at high temperatures, Figure 7.7(a). The form of the resistivity as a function of temperature is much more similar to that of pure UPd_3, showing a shoulder in the data at $T \sim 25$ K. This feature is associated with the thermal occupation of an excited crystal field level leading to an additional scattering channel. Application of a 9 T field has negligible effect on the resistivity.

Initial measurements made down to $T = 2$ K using the PPMS showed that at the lowest temperatures the resistivity trend was linear, see Figure 7.7(b). Such anomalous behaviour can be indicative of a non-Fermi liquid state or a mixed valence state, or can be attributed to the disruption of the periodic Bloch potential by the doping leading to a change in the scattering mechanism dictating the temperature dependence of the resistivity. To further investigate the low temperature resistivity the measurements were repeated using

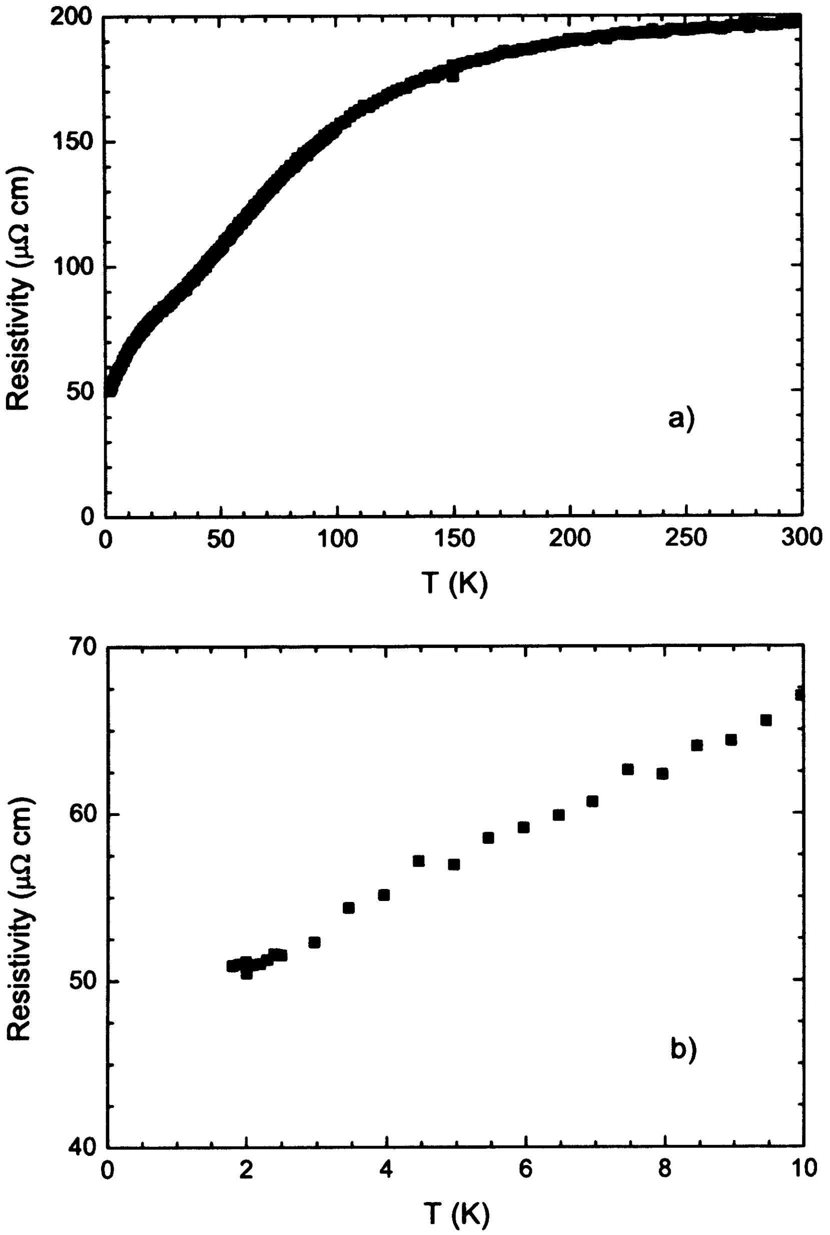

Figure 7.7: (a) $\rho(T)$ in $(U_{0.95}Np_{0.05})Pd_3$ at $H = 0$ T for $T = 2 - 300$ K, showing a standard metallic behaviour at high temperatures, with the resistivity increasing with increasing temperature. (b) For $T = 2 - 10$ K the temperature dependence of the resistivity does not appear to be that of a standard Fermi Liquid.

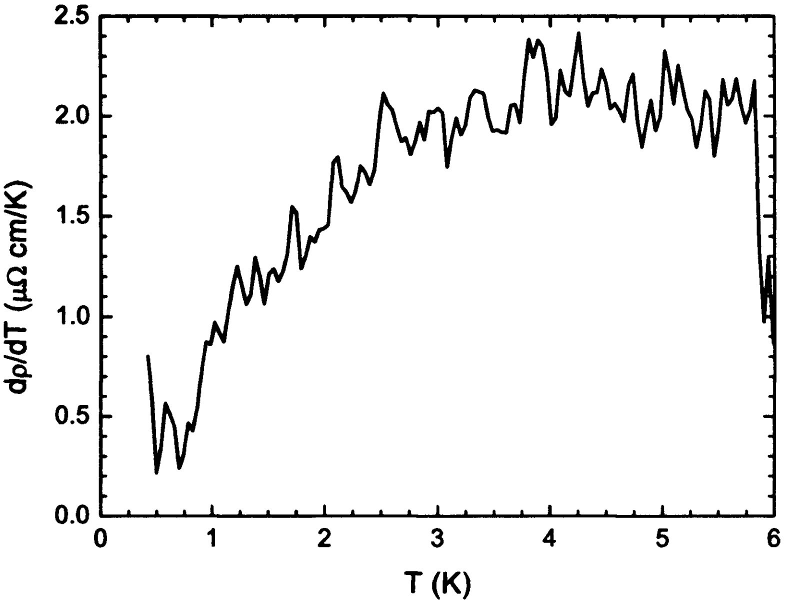

Figure 7.8: The maximum in dρ/dT as a function of temperature in $(U_{0.95}Np_{0.05})Pd_3$ indicating a change in regime.

the same encapsulated sample on a cryopumped system capable of attaining temperatures less than 1.5 K, see section 4.3.

The first derivative of the resistivity with respect to temperature was calculated and plotted, see Figure 7.8, to look for changes in the temperature dependence. A clear broad maximum centered on $T = 4$ K indicates that there is a change in the scattering regime. Below 1.6 K a fit made to the data using

$$\rho = \rho_0 + AT^c, \qquad (7.3)$$

gave a value of 2.11 ± 0.01 for the temperature exponent and $A = 0.418 \pm 0.003$ $\mu\Omega\mathrm{cmK}^{-2}$, see Figure 7.9, while for temperatures between 1.6 K and 4 K the exponent is 1.62 ± 0.01. This indicates that at the lowest temperatures $(U_{0.95}Np_{0.05})Pd_3$ is a Fermi liquid.

The resistivity of a 2%Np sample has not been measured, since the sample was used to make the 1%Np sample, and this sample has yet to be measured

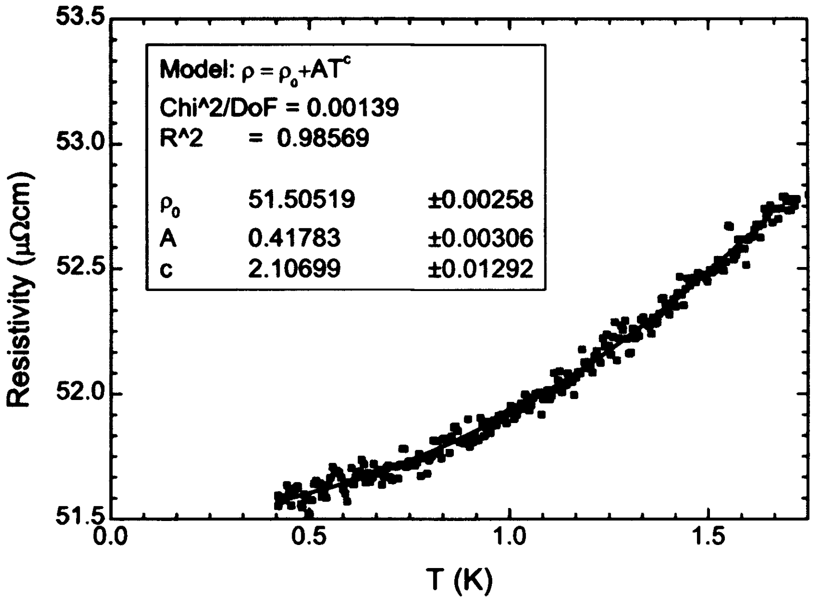

Figure 7.9: $\rho(T)$ in $(U_{0.95}Np_{0.05})Pd_3$ at $H = 0$ T for $T = 0.4 - 1.75$ K. A fit to $\rho = \rho_0 + AT^c$ for $T \leq 1.6$ K indicates that this composition in a Fermi liquid.

due to problems with encapsulation of the sample

7.3 Heat Capacity

7.3.1 $(U_{0.5}Np_{0.5})Pd_3$

Heat capacity measurements of $(U_{0.5}Np_{0.5})Pd_3$ and $ThPd_3$ in zero field (Figure 7.10(a)) show that below 100 K the heat capacity is dominated by magnetic contributions. A sharp cusp in the 50%Np data is seen at 12 K, corresponding to the transition seen in the magnetisation and resistivity data. However, there is also a broad peak centred on 5 K in C/T, a temperature at which no features were seen in the other measurements. The origin of this feature is unknown. One suggestion is that it is due to the neptunium moments ordering first leading to a rapid increase in the molecular field and therefore a slow

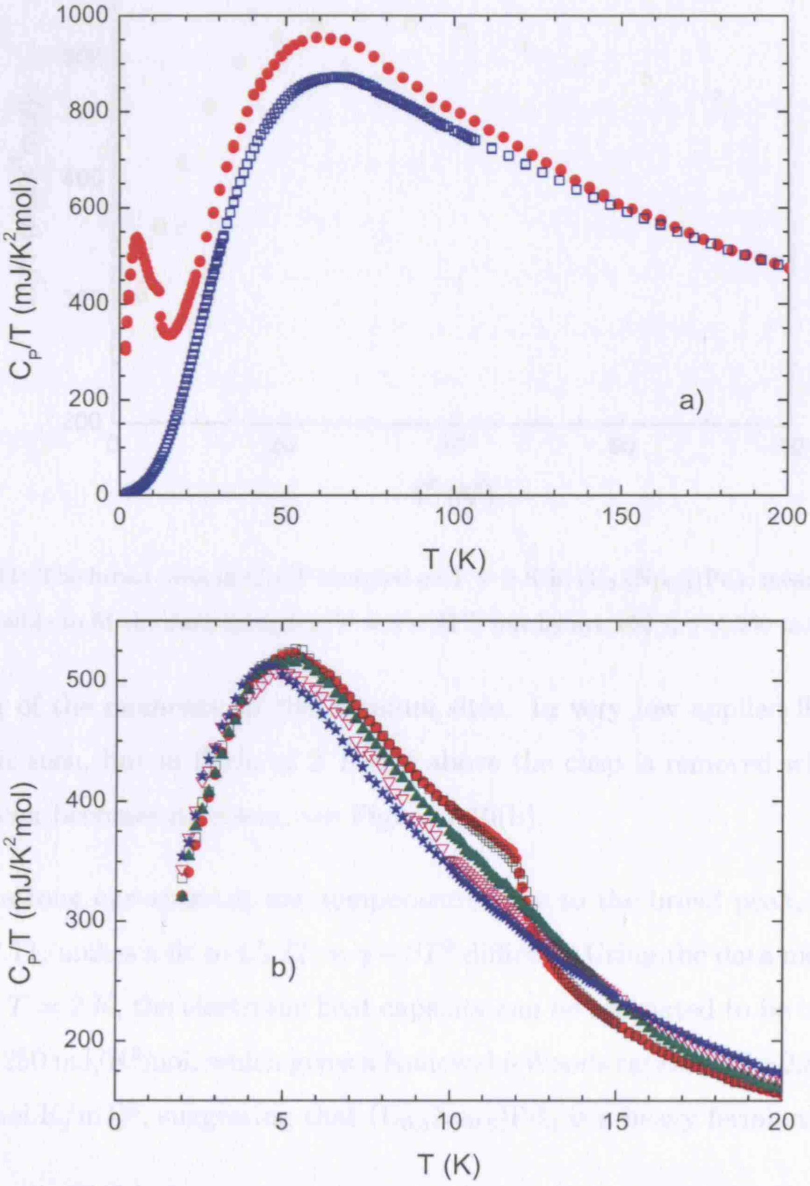

Figure 7.10: (a) C_P/T in $(U_{0.5}Np_{0.5})Pd_3$ (●) and $ThPd_3$ (□) at $H = 0$ T for $T = 2 - 200$ K. (b) In zero field (●) a cusp is seen in the data at 12 K, with a broad peak at 5 K. The application of field leads to the cusp being smoothed away ($H = 0.1$ T(□), $H = 2$ T (▲), $H = 5$ T (▽) and $H = 9$ T(★))

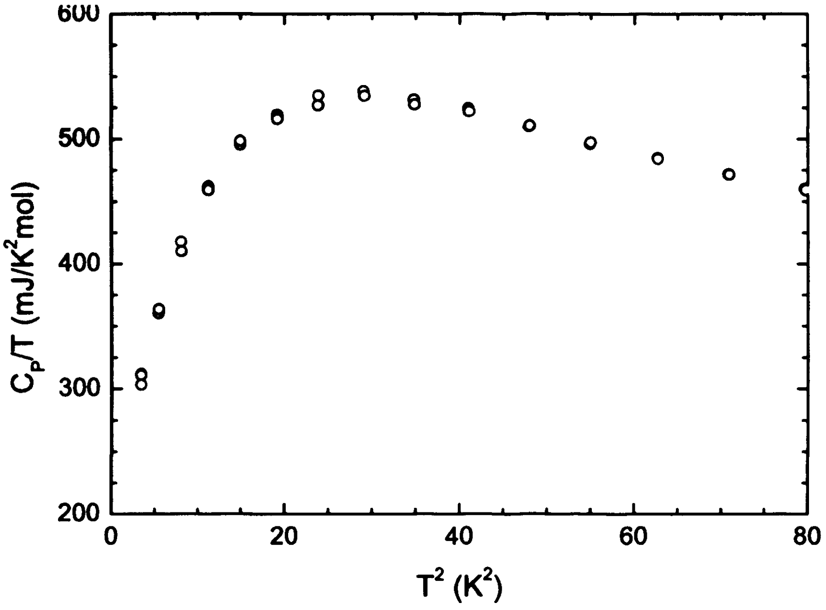

Figure 7.11: The broad peak in C_P/T centered on $T = 5$ K in $(U_{0.5}Np_{0.5})Pd_3$, means that it is not possible to fit the data using $C_P/T = \gamma + \beta T^2$, but by eye $150 \leq \gamma \leq 250$ mJ/K^{2}mol.

ordering of the moments on the uranium sites. In very low applied fields no change is seen, but in fields of 2 T and above the cusp is removed while the broad peak becomes narrower, see Figure 7.10(b).

The strong curvature at low temperatures due to the broad peak, seen in Figure 7.11, makes a fit to $C_P/T = \gamma + \beta T^2$ difficult. Using the data measured down to $T = 2$ K, the electronic heat capacity can be estimated to be between 150 and 250 mJ/K^{2}mol, which gives a Kadowaki-Woods ratio of $5.2 \pm 2.8 \times 10^{-5}$ $\mu\Omega$cm(mol.K/mJ)^2, suggesting that $(U_{0.5}Np_{0.5})Pd_3$ is a heavy fermion.

Using the $ThPd_3$ data as an estimate for the phonons in the 50%Np sample, an estimate for the magnetic entropy was calculated. However, the electronic heat capacity was not subtracted before the integration due to the difficulties in obtaining an estimate for γ. In addition it is not possible to extrapolate the data below 2 K with any degree of accuracy, and so the actual quantity plotted in Figure 7.15 is $S(T) - S(T = 2\text{K})$.

7.3.2 $(U_{0.95}Np_{0.05})Pd_3$

Initially the heat capacity of $(U_{0.95}Np_{0.05})Pd_3$ was measured for $T = 2 - 300$ K in applied magnetic fields of 0, 5 and 9 T. The broad peak feature below 5 K leads to significant curvature and a high value of $C_P/T \simeq 400$ mJ/K^{2}mol at $T = 2$ K [130]. Extrapolating back to $T = 0$ K from this data set would result in a highly elevated value for the Sommerfeld coefficient implying that 5%Np is a heavy fermion system. Two possible explanations for this are: 1) that this composition is in the vicinity of a quantum critical point (QCP) arising from the suppression of the quadrupolar transitions to zero temperature, or 2) that there are additional lower temperature transitions.

To investigate these possibilities the heat capacity was remeasured using a ^{3}He insert in the PPMS for $T = 0.6 - 20$ K (base temperature could not be obtained due to self-heating effects), see Figure 7.12 for the low temperature data. The new measurements have revealed several additional features. There is a shoulder in the $H = 0$ T data at $T = 8$ K, which is smoothed away with increasing field strength. The broad peak is still clear at $T \simeq 3.5$ K but there may be evidence of another peak centered on $T \simeq 2.5$ K explaining the feature on the low temperature side of the main peak. There is a further feature at $T \simeq 1.5$ K. The two lowest temperature features appear to stay at the same temperatures while being reduced in absolute value with increasing field, while the main peak centre moves to higher temperatures with increasing applied magnetic field. Such behaviour is inconsistent with an antiferromagnetic transition, and magnetisation measurements (section 7.1.2) rule out a ferromagnetic transition. Therefore this feature may be associated with a quadrupolar transition.

Even for $0.6 \leq T \leq 2$ K C_P/T is linear as a function of temperature, such that one cannot use the y-intercept of a plot of C_P/T vs T^2 to estimate

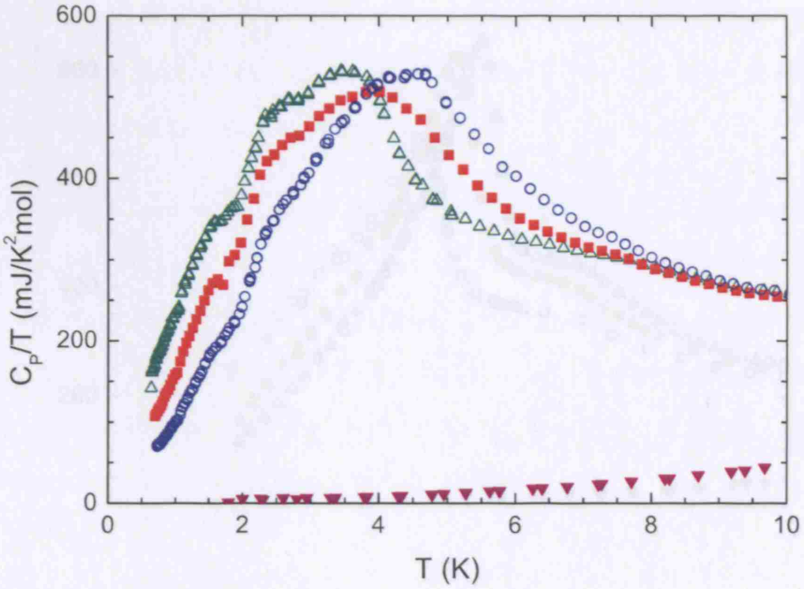

Figure 7.12: C_P/T in $(U_{0.95}Np_{0.05})Pd_3$ for $H = 0$ T (△), $H = 5$ T (■) and $H = 9$ T (○) and in $ThPd_3$ (▼).

the Sommerfeld coefficient. Assuming there are no further low temperature transitions, using the low temperature trend in C_P/T gives an estimate of $\gamma = 125 \pm 25$ mJ/K^{2}mol, which using the value of the quadratic temperature coefficient of the resistivity (section 7.2.2) gives a Kadowaki-Woods ratio of $2.7 \pm 1.1 \times 10^{-5}$ $\mu\Omega$cm.(mol.K/mJ)^2, indicating that the compound may also be a heavy fermion.

The low temperature form of the heat capacity means that it is very difficult to try extrapolate back to zero temperature, so that only $S(T) - S(T = 0.5\text{K})$ can be calculated, however, $S(T) - S(T = 2\text{K})$ is plotted in Figure 7.15 so as to be compared with the compounds for which lower temperature measurements have not yet been made.

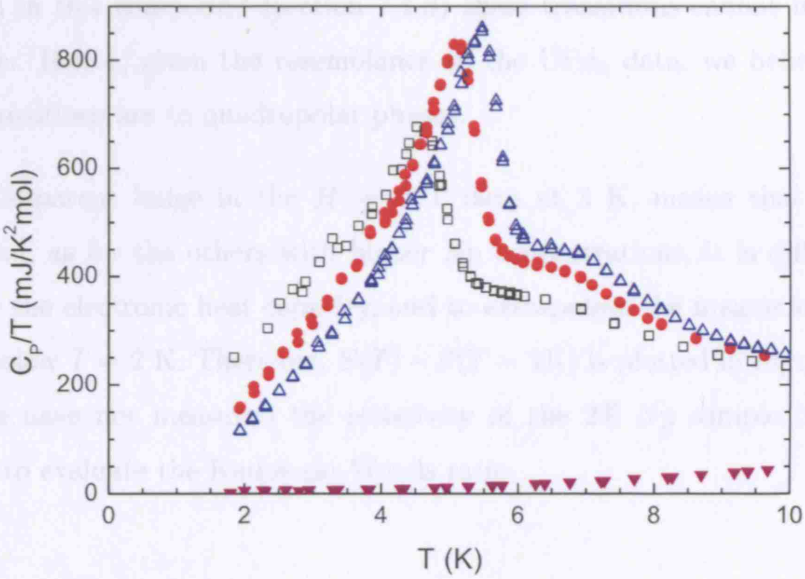

Figure 7.13: C_P/T in $(U_{0.98}Np_{0.02})Pd_3$ for $H = 0$ T (□), $H = 6$ T (●) and $H = 9$ T (△), and in $ThPd_3$ (▼).

7.3.3 $(U_{0.98}Np_{0.02})Pd_3$

The heat capacity of $(U_{0.98}Np_{0.02})Pd_3$, measured in applied magnetic fields of $H = 0$, 6 and 9 T, is shown in Figure 7.13. In zero field C_P/T increases rapidly to a peak at $T = 4.2$ K and then decreases to a shoulder at 7 K [130]. These features are similar to those observed in polycrystalline UPd_3 measurements (section 5.1), although the maximum value for C_P/T in $(U_{0.98}Np_{0.02})Pd_3$ is approximately half that in pure UPd_3, and considerably less sharp. The zero field data may also show evidence of a shoulder in the data at around 3 K.

When a magnetic field is applied, the peak is observed to move up in temperature to 5.5 K in $H = 9$ T. In addition the shoulder feature around 7 K becomes more pronounced as well as shifting up in temperature slightly. The positive shift in temperature with field indicates that the transitions are not antiferromagnetic in origin, and since no magnetic hysteresis has been observed in this compound (section 7.1.3) these transitions cannot be ferromagnetic. Hence, given the resemblance to the UPd$_3$ data, we believe that these transitions are to quadrupolar phases.

The apparent bulge in the $H = 0$ T data at 3 K, means that in this compound, as for the others with higher Np concentrations, it is difficult to estimate the electronic heat capacity, and to extrapolate the magnetic contribution below $T = 2$ K. Therefore, $S(T) - S(T = 2\text{K})$ is plotted in Figure 7.15. Since we have not measured the resistivity of the 2% Np sample it is not possible to evaluate the Kadowaki-Woods ratio.

7.3.4 $(\mathrm{U_{0.99}Np_{0.01}})\mathrm{Pd_3}$

The heat capacity of $(\mathrm{U_{0.99}Np_{0.01}})\mathrm{Pd_3}$ was measured as a function of temperature for $H = 0$, 5 and 9 T. As one might expect, the form of C_P/T, as shown in Figure 7.14, bears a strong resemblance to that of pure UPd$_3$, see section 5.1 and Figure 5.1 b). There is a sharp lambda transition at $T \simeq 6$ K, which is very similar to that associated with T_{-1} in UPd$_3$, and which moves to higher temperatures with increasing applied field. The "T_0" feature at 7.3 K in zero field, shifts up in temperature and becomes more prominent with increasing field. The "T_2" shoulder present at 4 K in zero field is smoothed away for $H \geq 5$ T.

Measurements also reveal a concave feature at $T \approx 2$ K in all fields. Possibly a similar smaller feature is observed in the addenda measurements, where the heat capacity of the sample holder without the sample is measured. However, the addenda is only 10% of the total heat capacity at this temperature, and so is unlikely to be responsible for the kink in the sample data. It is possible that the feature could be attributed to another lower temperature tran-

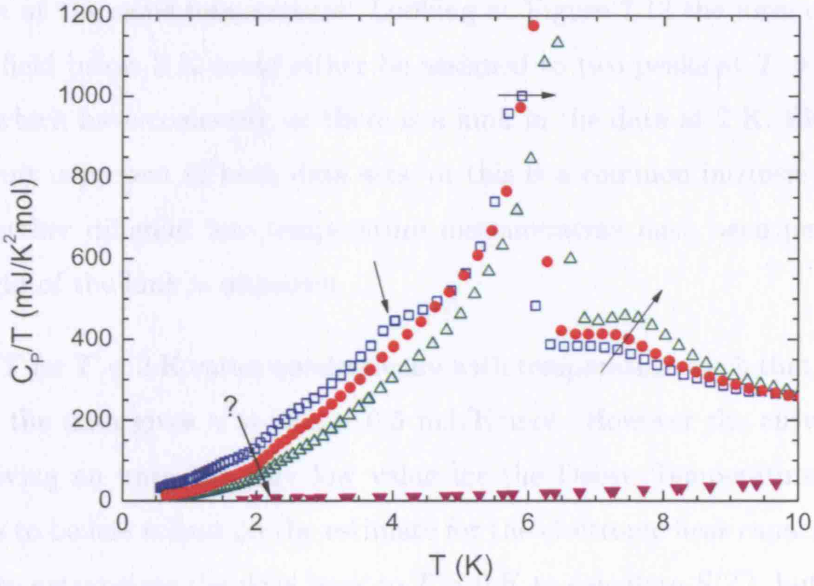

Figure 7.14: C_P/T in $(U_{0.99}Np_{0.01})Pd_3$ for $H = 0$ T (□), $H = 5$ T (●) and $H = 9$ T (△), and in $ThPd_3$ (▼). The general shape is very reminiscent of that for pure UPd_3, see Figure 5.1 b). The arrows show how the features associated with transitions evolve as a function of the applied field. The three higher temperature features could be associated with T_0, T_{-1} and T_2 using the nomenclature for UPd_3. The feature labeled with a question marked arrow may not be due to an intrinsic property of the system.

sition, but without further different measurements such a suggestion needs to be treated with care. Another possibility is that the feature is not an intrinsic property of the system, but instead due to some "bug" in the experimental apparatus. This is not a standard problem encountered when using a ^{3}He insert in a PPMS and cannot be easily assigned to a particular part of the measurements. The kink also bears some similarities to a feature in the 5% Np data at the same temperature. Looking at Figure 7.12 the form of C_P/T in zero field below 3 K could either be assigned to two peaks at $T = 1.5$ and 2.5 K, which have coalesced, or there is a kink in the data at 2 K. Either the same fault is present in both data sets, or this is a common intrinsic feature. Until further different low temperature measurements have been performed the origin of the kink is unknown.

C_P/T for $T < 2$ K varies quadratically with temperature, such that making a fit to the data gives $\gamma = 26.0 \pm 0.5$ mJ/K^{2}mol. However the curvature is large giving an unrealistically low value for the Debye Temperature, which leads us to be less reliant on the estimate for the electronic heat capacity. It is simple to extrapolate the data back to $T = 0$ K to calculate $S(T)$, but for the reason given above this may not be a reliable estimate for the heat capacity. In addition, since for most of the other compounds it is not easy to extrapolate to $T = 0$ K, for comparison purposes only $S(T) - S(T = 2\text{K})$ is plotted in Figure 7.15.

7.3.5 Entropy summary

In all cases the heat capacity of ThPd$_3$ has been subtracted from each data set to remove the phonon contribution. To obtain the magnetic entropy the electronic heat capacity needs to also be removed. However, in several cases, most notably for (U$_{0.5}$Np$_{0.5}$)Pd$_3$, it has not been possible to determine γ accu-

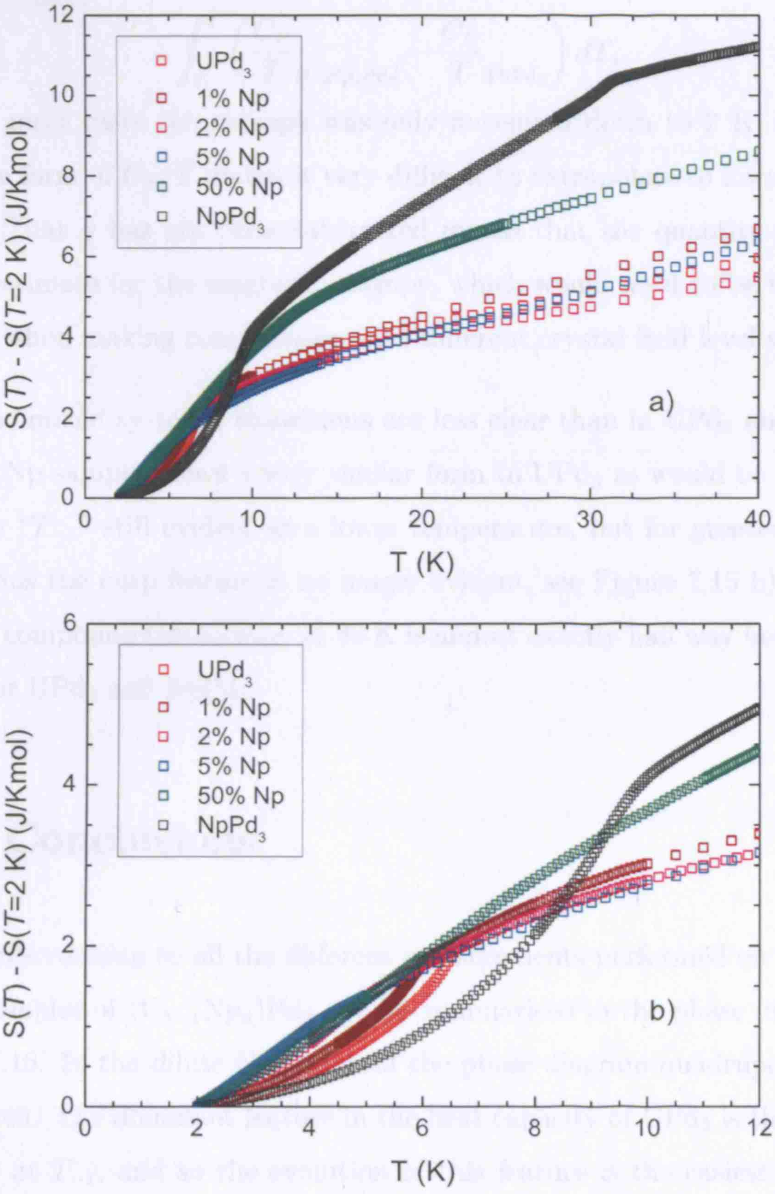

Figure 7.15: a) The calculated entropy of $(U_{1-x}Np_x)Pd_3$ for $x = 0$, 0.01, 0.02, 0.05, 0.5 and 1.0, showing that at $T = 40$ K the 50% Np entropy lies almost exactly half way between that of UPd_3 and $NpPd_3$. b) A low temperature zoom in of the same plot showing how dilute Np concentrations smooth the UPd_3 T_{-1} transition.

rately and only estimates with large error bars can be obtained. Figures 7.15 a) and b) show

$$\int_2^T \left(\frac{C_P}{T}_{\text{(U,Np)Pd}_3} - \frac{C_P}{T}_{\text{ThPd}_3} \right) dT, \tag{7.4}$$

since in most cases the entropy was only measured down to 2 K, and quite often the form of C_P/T makes it very difficult to extrapolate to lower temperatures. That γ has not been subtracted means that the quantity plotted is an overestimate for the magnetic entropy, which would need to be taken into account when making comparisons with different crystal field level schemes.

In the mixed systems, transitions are less clear than in UPd_3 and $NpPd_3$. The 1% Np sample shows a very similar form to UPd_3 as would be expected, with the "T_{-1}" still evident at a lower temperature, but for greater Np concentrations the cusp feature is no longer evident, see Figure 7.15 b). For the 50% Np compound the entropy at 40 K is almost exactly half way between the values for UPd_3 and $NpPd_3$.

7.4 Conclusions

The results relating to all the different measurements performed on polycrystalline samples of $(U_{1-x}Np_x)Pd_3$ can be summarised in the phase diagram in Figure 7.16. In the dilute Np region of the phase diagram quadrupolar order is observed. The dominant feature in the heat capacity of UPd_3 is the lambda anomaly at T_{-1}, and so the evolution of this feature is the easiest to follow with increasing Np doping. The heat capacity of 1% Np is very similar to that of pure UPd_3, while that for 2% Np also has common features, but by 5% Np doping there are significant differences in the form. The "T_{-1}" feature moves to lower temperatures as x is increased to 0.05, suggesting the possibility that at some critical doping concentration this transition will be suppressed to zero

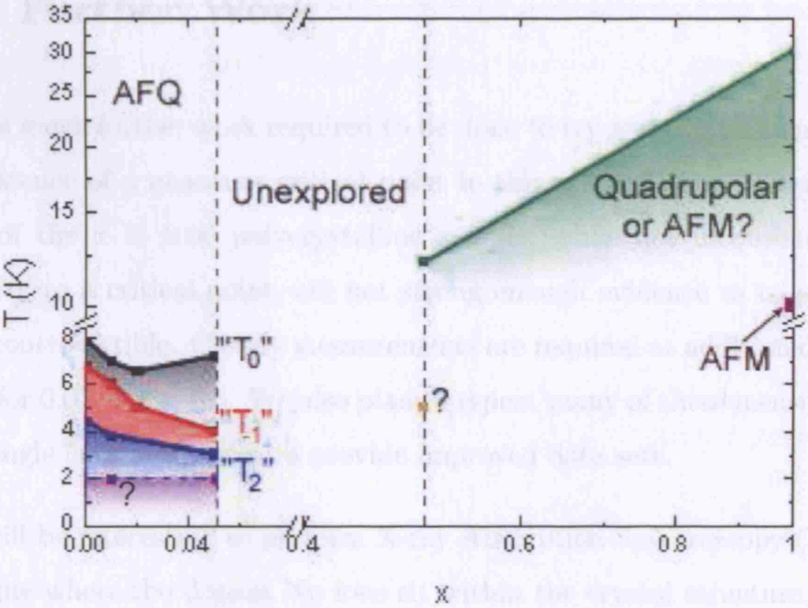

Figure 7.16: Temperature T versus Neptunium concentration x phase diagram for $(U_{1-x}Np_x)Pd_3$ obtained from bulk property measurements. Points marked with "?" are from features in the heat capacity data, which either have yet to be assigned to a transition, or are considered dubious. AFQ: antiferroquadrupolar, AFM: antiferromagnet.

temperature leading to a quantum critical point of quadrupolar origin.

Proximity to a quantum critical point at $x = 0.05$ could be consistent with the apparent heavy fermion and possible non-Fermi liquid behaviours at this composition observed in the bulk thermodynamic measurements. It would be very interesting to have discovered a QCP associated with the suppression of quadrupolar order. So far, as far as the author is aware, there have been no theoretical models developed for such an occurrence, but we see no reason why this system should not present quantum criticality as the doping destroys the quadrupolar order.

7.5 Further Work

There is much further work required to be done to try and establish or exclude the existence of a quantum critical point in this system. The bulk measurements of the $x = 0.05$ polycrystalline sample, while not inconsistent with proximity to a critical point, are not strong enough evidence as to prove the idea incontrovertible. Clearly measurements are required at additional compositions for $0.05 < x < 0.5$. We also plan to repeat many of these measurements using single crystal samples to provide improved data sets.

It will be interesting to perform X-ray Absorption Spectroscopy (XAS) to determine where the dopant Np ions sit within the crystal structure, i.e. are they randomly arranged throughout the unit cell, or do they preferentially occupy one of the symmetry type sites, and the valence of the uranium and neptunium ions. By tuning to the uranium and neptunium absorption edges it will be possible to analyse the properties of the elements individually.

We have had proposals accepted to use INS to look at how the crystal field levels of UPd_3 have been perturbed with the addition of Np, again looking at the valence states. We also plan to look for E/T scaling associated with non-Fermi Liquid behaviour in the vicinity of a Quantum Critical Point for the 5%Np sample.

Our measurements suggest that quadrupolar order is present at least up to 5% Np concentrations, and so eventually it will be of great interest to use XRS to investigate how the quadrupolar order evolves as a function of Np doping. XRS will also allow us to investigate the possibility that the broad peak seen in the heat capacity of the 50% Np sample (Figure 7.10(b)) reflects the ordering of the Neptunium moments, increasing the Molecular Field, causing the slow ordering of the uranium moments. Using the elemental selectivity of the probe, it would be possible to follow the temperature dependence of the intensity of previously forbidden reflections, to determine whether there was a succession of ordering temperatures related to the two elements.

Chapter 8

Conclusions

This project forms a concerted effort to further our understanding of the unusual antiferroquadrupolar compound UPd_3, both through direct measurements of the quadrupolar order in UPd_3, and by investigating how the properties change with the substitution of neptunium for uranium. We have built on the knowledge from the considerable wealth of UPd_3 literature and have many suggestions for further experiments to perform arising from the analysis of our results presented in this thesis. Our new X-ray Resonant Scattering experiments have made use of new developments in instrumentation at the European Synchrotron Radiation Facility. While, as far as we know, no experimental data has been published by other authors on the mixed system $(U,Np)Pd_3$, presumably partially due to the inherent difficulties in using neptunium. In this chapter, I will summarise the conclusions drawn in the previous chapters.

Our X-ray resonant scattering measurements, discussed in Chapter 5, have allowed us to probe the quadrupolar order directly in three of the four quadrupolar phases of UPd_3. At $T = 7.1$ K, in the highest temperature quadrupolar phase, our data is consistent with a dominant antiferro-stacking of Q_{zx}

quadrupoles along the c-axis, with an admixture of $Q_{x^2-y^2}$ quadrupoles. This result taken in combination with our high precision heat capacity measurements has enabled us to further the crystal field model for UPd_3. The azimuthal dependence of the scattering in the lower temperature phases has proved much more complicated, and cannot be explained using simple models of quadrupolar order on the quasi-cubic uranium sites in an orthorhombic structure alone. Least squares fits made to these data sets by allowing the tensor elements to vary freely indicate that the scattering tensors are complex. A number of possibilities to extend the model have been investigated, but fits to the data have so far proved inconclusive. UPd_3 may exhibit multipolar order, but we cannot use the azimuthal dependence of XRS to investigate whether there is a primary order parameter driving quadrupolar order as a secondary order parameter, since the transition matrix elements, equation (3.8), for electric quadrupole ($E2$) and higher order transitions are zero at the uranium M_{IV}-edge.

In Chapter 6 we reinvestigated $NpPd_3$ through magnetisation, electrical resistivity and heat capacity measurements on polycrystalline samples. In addition to the transition at $T_1 = 30$ K, identified by Nellis *et al.* [50], we have found a second transition at $T_2 = 10$ K. The behaviour of the anomaly associated with this transition in different measurements is consistent with an antiferromagnetic transition. The nature of the T_1 transition is more problematic, but the in-field behaviour of the heat capacity feature at this temperature could be consistent with a transition to quadrupolar order. Interestingly, the T_1 transition coincides with the very sharp change in electrical resistivity regimes to a high temperature Kondo-type behaviour. The bulk measurements have not enabled us to distinguish between two possible scenarios for the transitions: 1) the transitions occur successively on only one of the site types, or 2) the transitions occur separately on the two neptunium sites, but this will be determined by polarised neutron diffraction measurements on single crystal samples in which we will be able to follow the different site susceptibilities. By combining heat capacity and resistivity measurements, performed down to a base temperature of 2 K, the Kadowaki-Woods ratio has been calculated to be $5.2 \pm 0.8 \times 10^{-5}$ $\mu\Omega$cm(mol.K/mJ)^2, suggesting that $NpPd_3$ may be a heavy Fermion compound. Clearly $NpPd_3$ is a very interesting compound, which could benefit from further study.

Chapter 7 details the first measurements made, to our knowledge, on the mixed system $(U_{1-x}Np_x)Pd_3$. Special interest has been paid to the dilute neptunium end of the phase diagram, as we have been investigating the disruption of quadrupolar order through chemical pressure. It has been shown that the T_{-1}-type transition moves to lower temperatures with increasing neptunium content, and that for $x = 0.05$ there is a suggestion of heavy Fermion and non-Fermi liquid behaviour, which may be consistent with being in the vicinity of a quantum critical point. It will be very interesting to use inelastic neutron scattering to determine whether there is E/T scaling at this composition, to investigate the possibility of local quantum criticality [59, 63]. Further compositions will need to be examined to look for non-Fermi liquid behaviour and other signifiers of possible proximity to quantum criticality.

Bibliography

[1] D. F. McMorrow, K. A. McEwen, U. Steigenberger, H. M. Rønnow, and F. Yakhou. *Phys. Rev. Lett.* **87**, 057201 (2001).

[2] Y. Murakami, H. Kawada, H. Kawata, M. Tanaka, T. Arima, Y. Moritomo, and Y. Tokura. *Phys. Rev. Lett.* **80**, 1932 (1998).

[3] Y. Murakami, J. P. Hill, D. Gibbs, M. Blume, I. Koyama, M. Tanaka, H. Kawata, T. Arima, Y. Tokura, K. Hirota, and Y. Endoh. *Phys. Rev. Lett.* **81**, 582 (1998).

[4] K. J. Thomas, J. P. Hill, S. Grenier, Y.-J. Kim, P. Abbamonte, L. Venema, A. Rusydi, Y. Tomioka, Y. Tokura, D. F. McMorrow, G. Sawatzky, and M. van Veenendaal. *Phys. Rev. Lett.* **92**, 237204 (2004).

[5] S. B. Wilkins, P. D. Spencer, P. D. Hatton, S. P. Collins, M. D. Roper, D. Prabhakaran, and A. T. Boothroyd. *Phys. Rev. Lett.* **91**, 167205 (2003).

[6] R. Shiina, H. Shiba, and P. Thalmeier. *J. Phys. Soc. Japan* **66**, 1741 (1997).

[7] Y. Aoki, T. Namiki, T. D. Matsuda, K. Abe, H. Sugawara, and H. Sato. *Phys. Rev. B* **65**, 064446 (2002).

[8] K. Izawa, Y. Nakajima, J. Goryo, Y. Matsuda, S. Osaki, H. Sugawara, H. Sato, P. Thalmeier, and K. Maki. *Phys. Rev. Lett.* **90**, 117001 (2003).

[9] J. A. Paixão, C. Detlefs, M. J. Longfield, R. Caciuffo, P. Santini, R. J. Bernhoeft, N. and, and G. H. Lander. *Phys. Rev. Lett.* **89**, 187202 (2002).

[10] S. B. Wilkins, J. A. Paixão, R. Caciuffo, P. Javorsky, F. Wastin, J. Rebizant, C. Detlefs, N. Bernhoeft, P. Santini, and G. H. Lander. *Phys. Rev. B* **70**, 214402 (2004).

[11] T. Matsumura, N. Oumi, K. Hirota, H. Nakao, Y. Murakami, Y. Wakabayashi, T. Arima, S. Ishihara, and Y. Endoh. *Phys. Rev. B* **65**, 094420 (2002).

[12] P. Morin and D. Schmitt, *Ferromagnetic Materials*, vol. 5, pp. 1 132. North-Holland, 1990.

[13] J. L. Smith and E. A. Kmetko. *J. Less Common Metals* **90**, 83 (1983).

[14] S. S. Hecker. *Met. Mat. Trans. A* **35**, 2209 (2004).

[15] J. M. Wills and O. Eriksson. *Los Alamos Science* **26**, 128 (2000).

[16] P. Link, A. Gukasov, J.-M. Mignot, T. Matsumura, and T. Suzuki. *Phys. Rev. Lett.* **80**, 4779 (1998).

[17] Y. Tokura and N. Nagaosa. *Science* **288**, 462 (2000).

[18] G. Gehring and K. Gehring. *Rep. Prog. Phys.* **38**, 1 (1975).

[19] M. Sera, H. Ichikawa, T. Yokoo, J. Akimitsu, M. Nishi, K. Kakurai, and S. Kunii. *Phys. Rev. Lett.* **86**, 1578 (2001).

[20] D. Schmitt and P. M. Levy. *J. Magn. Magn. Mater.* **49**, 15 (1985).

[21] P. Fazekas, A. Kiss, and K. Radnóczi. *Prog. Theor. Phys. Suppl.* **160**, 114 (2005).

[22] R. Caciuffo, J. A. Paixão, C. Detlefs, M. J. Longfield, P. Sanitini, N. Bernhoeft, J. Rebizant, and G. H. Lander. *J. Phys. Condens. Matter* **15**, S2287 (2003).

[23] P. Santini, S. Carretta, N. Magnani, G. Amoretti, and R. Caciuffo. *Phys. Rev. Lett.* . accepted for publication.

[24] T. Takimoto. *J. Phys. Soc. Jpn.* **75**, 259 (2006).

[25] N. Lingg, D. Maurer, V. Müller, and K. A. McEwen. *Phys. Rev. B* **60**, R8430 (1999).

[26] K. A. McEwen, J.-G. Park, A. J. Gipson, and G. A. Gehring. *J. Phys. Condens. Matter* **15**, S1923 (2003).

[27] K. A. McEwen, U. Steigenberger, K. N. Clausen, J.-G. P. J. Kulda, and M. B. Walker. *J. Magn. Magn. Mater.* **177-181**, 37 (1998).

[28] W. J. L. Buyers, A. F. Murray, T. M. Holden, E. C. Svensson, P. de V. DuPlessis, G. H. Lander, and O. Vogt. *Physica B+C* **102**, 291 (1980).

[29] M. B. Walker, C. .Kappler, K. A. McEwen, U. Steigenberger, and K. N. Clausen. *J. Phys. Condens. Matter* **6**, 7365 (1994).

[30] U. Steigenberger, K. A. McEwen, J. L. Martinez, and D. Fort. *J. Magn. Magn. Mater.* **108**, 163 (1992).

[31] K. A. McEwen, U. Steigenberger, and J. L. Martinez. *Physica B* **186-188**, 670 (1993).

[32] K. A. McEwen, U. Steigenberger, K. Clausen, Y. Bi, M. Walker, and C. Kappler. *Physica B* **213&214**, 128 (1995).

[33] M. Bull, K. A. McEwen, R. Osborn, and R. S. Eccleston. *Physica B* **223 & 224**, 175 (1996).

[34] Y. Baer, H. R. Ott, and K. Andres. *Solid State Comm.* **36**, 387 (1980).

[35] R. Eloirdi, T. Gouder, F. Wastin, J. Rebizant, and F. Huber. *J. Alloy Compd.* **374**, 265 (2004).

[36] H. R. Ott, K. Andres, and P. H. Schmidt. *Physica* **102B**, 148 (1980).

[37] S. W. Yun, H. Sugawara, J. Itoh, M. Takashita, T. Ebihara, N. Kimura, P. Svoboda, R. Settai, Y. Ōnuki, and H. Sato. *J. Phys. Soc. Jpn* **63**, 1518 (1994).

[38] K. A. McEwen, M. Ellerby, and M. de Podesta. *J. Magn. Magn. Mater.* **140-144**, 1411 (1995).

[39] Y. Tokiwa, K. Sugiyama, T. Takeuchi, M. Nakashima, R. Settai, Y. Inada, Y. Haga, E. Yamamoto, K. Kindo, H. Harima, and Y. Ōnuki. *J. Phys. Soc. Japan* **70**, 1731 (2001).

[40] S. W. Zochowski, M. de Podesta, C. Lester, and K. A. McEwen. *Physica B* **206 & 207**, 489 (1995).

[41] M. Lenkewitz, S. Corsepius, E. W. Scheidt, and G. R. Stewart. *J. Alloys Comp.* **232**, 67 (1996).

[42] S. W. Zochowski and K. A. McEwen. *Physica B* **199-200**, 416 (1994).

[43] T. Takeuchi, Y. Tokiwa, R. Settai, Y. Haga, E. Yamamoto, T. Honma, and Y. Ōnuki. *Physica B* **281 & 282**, 602 (2000).

[44] Y. Tokiwa, K. Sugiyama, T. Takeuchi, R. Settai, Y. Inada, Y. Haga, E. Yamamoto, T. Honma, K. Sakurai, M. Nakashima, K. Miyake, K. Kindo, and Y. Ōnuki. *Physica B* **281** & **282**, 604 (2000).

[45] G. R. Stewart, Z. Fisk, J. O. Willis, and J. L. Smith. *Phys. Rev. Lett.* **52**, 679 (1984).

[46] M. R. Norman, T. Oguchi, and A. J. Freeman. *J. Magn. Magn. Mater.* **69**, 27 (1987).

[47] T. Ito, H. Kumigashira, H.-D. Kim, T. Takahashi, N. Kimura, Y. Haga, E. Yamamoto, Y. Ōnuki, and H. Harima. *Phys. Rev. B* **59**, 8923 (1999).

[48] T. J. Heal and G. I. Williams. *Acta Cryst.* **8**, 494 (1955).

[49] A. Schenck, F. N. Gygax, and K. A. McEwen. *J. Phys. Condens. Matter* **14**, 4595 (2002).

[50] W. J. Nellis, A. R. Harvey, G. H. Lander, B. D. Dunlap, M. B. Brodsky, M. H. Mueller, J. F. Reddy, and G. R. Davidson. *Phys. Rev. B* **9**, 1041 (1974).

[51] A. J. Schofield. *Contemporary Physics* **40**, 95 (1999).

[52] H. v. Löhneysen, T. Pietrus, G. Portisch, H. G. Schlager, A. Schröder, M. Sieck, and T. Trappmann. *Phys. Rev. Lett.* **72**, 3262 (1994).

[53] J. Hertz. *Phys. Rev. B* **14**, 1165 (1976).

[54] S. S. Saxena, P. Agarwal, K. Ahilan, F. M. Grosche, R. K. W. Haselwimmer, M. J. Steiner, E. Pugh, I. R. Walker, S. R. Julian, P. Monthoux, G. G. Lonzarich, A. Huxley, I. Sheikin, D. Braithwaite, and J. Flouquet. *Nature* **406**, 587 (2000).

[55] C. Pfleiderer, G. J. McMullan, S. R. Julian, and G. G. Lonzarich. *Phys. Rev. B* **55**, 8330 (1997).

[56] F. M. Grosche, C. Pfleiderer, G. J. McMullan, G. G. Lonzarich, and N. R. Bernhoeft. *Physica B* **206-7**, 20 (1995).

[57] M. C. Aronson, R. Osborn, R. A. Robinson, J. W. Lynn, R. Chau, C. L. Seaman, and M. B. Maple. *Phys. Rev. Lett.* **75**, 725 (1995).

[58] J. G. Park, D. T. Adroja, K. A. McEwen, and A. P. Murani. *J. Phys. Condens. Matter* **14**, 3865 (2002).

[59] A. Schröder, G. Aeppli, E. Bucher, R. Ramazashvili, and P. Coleman. *Phys. Rev. Lett.* **80**, 5623 (1998).

[60] A. Rosch, A. Schröder, O. Stockert, and H. v. Löhneysen. *Phys. Rev. Lett.* **79**, 159 (1997).

[61] D. Belitz, T. R. Kirkpatrick, and J. Rollbuhler. *Phys. Rev. Lett.* **93**, 155701 (2004).

[62] T. Senthil, A. Vishwanath, L. Balents, S. Sachdev, and M. P. A. Fisher. *Science* **303**, 1490 (2004).

[63] Q. Si, S. Rabello, K. Ingersent, and J. L. Smith. *Nature* **413**, 804 (2001).

[64] O. Stockert, H. v. Löhneysen, A. Rosch, N. Pyka, and M. Loewenhaupt. *Phys. Rev. Lett.* **80**, 5627 (1998).

[65] J. S. Kang, J. W. Allen, M. B. Maple, M. S. Torikachvili, W. P. Ellis, B. B. Pate, Z. X. Shen, J. J. Yeh, and I. Lindau. *Phys. Rev. B* **39**, 13529 (1989).

[66] C. L. Seaman, M. B. Maple, B. W. Lee, S. Ghamaty, M. S. Torikachvili, J.-S. Kang, L. Z. Liu, J. W. Allen, and D. L. Cox. *Phys. Rev. Lett.* **67**, 2882 (1991).

[67] B. Andraka and A. M. Tsvelik. *Phys. Rev. Lett.* **67**, 2886 (1991).

[68] S. Süllow, T. J. Gortenmulder, G. J. Nieuwenhuys, A. A. Menovsky, and J. A. Mydosh. *J. Alloys Compd.* **215**, 223 (1994).

[69] D. A. Gajewski, R. Chau, and M. B. Maple. *Phys. Rev. B* **62**, 5496 (2000).

[70] S. D. Wilson, P. Dai, D. T. Adroja, S.-H. Lee, J.-H. Chung, J. W. Lynn, N. P. Butch, and M. B. Maple. *Phys. Rev. Lett.* **94**, 56402 (2005).

[71] J.-A. Nielsen and D. F. McMorrow, *Elements of Modern X-ray Physics.* Chichester: John Wiley and Sons Ltd., 2001.

[72] "http://xdb.lbl.gov/section2/sec_2-2.html,".

[73] E. Burkel. *J. Phys. Condens. Matter* **13**, 7477 (2001).

[74] "http://www.adams-institute.ac.uk/graduate_lectures/ted_wilson/acins14(electrons)r1.ppt,".

[75] J. Baruchel, J.-L. Hodeau, M. S. Lehmann, J.-R. Regnard, and C. Schlenker, eds., *Neutron and Synchrotron Radiation for Condensed Matter Studies Volume 1: Theory, Instruments and Methods.* Springer-Verlag GmbH, 1993.

[76] S. W. Lovesey. *J. Phys. C: Solid State Phys.* **20**, 5625 (1987).

[77] M. Blume. *J. Appl. Phys.* **57**, 3615 (1985).

[78] S. W. Lovesey and S. Collins, *X-ray Scattering and Absorption by Magnetic Materials.* Oxford University Press, 1996.

[79] F. de Bergevin and M. Brunel. *Acta Crystall.* **A37**, 314 (1981).

[80] D. T. Keating. *Phys. Rev.* **178**, 732 (1969).

[81] M. Amara, R. M. Galera, P. Morin, and J. F. Bérar. *J. Phys.: Condens. Matter* **10**, L743 (1998).

[82] D. Gibbs, D. R. Harshman, E. D. Isaacs, D. B. McWhan, D. Mills, and C. Vettier. *Phys. Rev. Lett.* **61**, 1241 (1988).

[83] T. A. W. Beale, P. D. Spencer, P. D. Hatton, S. B. Wilkins, M. v. Zimmermann, S. D. Brown, D. Prabhakaran, and A. T. Boothroyd. *Phys. Rev. B* **72**, 064432 (2005).

[84] S. B. Wilkins, R. Caciuffo, C. Detlefs, J. Rebizant, E. Colineau, F. Wastin, and G. H. Lander. *Phys. Rev. B* **73**, 060406(R) (2006).

[85] T. Arima, J.-H. Jung, M. Matsubara, M. Kubota, J.-P. He, Y. Kaneko, and Y. Tokura. *J. Phys. Soc. Jpn.* **74**, 1419 (2005).

[86] S. D. Matteo, Y. Joly, and C. R. Natoli. *Phys. Rev. B* **72**, 144406 (2005).

[87] J. P. Hannon, G. T. Trammell, M. Blume, and D. Gibbs. *Phys. Rev. Lett.* **61**, 1245 (1988).

[88] J. P. Hill and D. F. McMorrow. *Acta Crystall.* **A52**, 236 (1996).

[89] V. E. Dmitrienko. *Acta Cryst.* **A39**, 29 (1983).

[90] S. Ji, C. Song, J. Koo, K.-B. Lee, Y. J. Park, J. Y. Kim, J.-H. Park, H. J. Shin, J. S. Rhyee, B. H. Oh, and B. K. Cho. *Phys. Rev. Lett.* **91**, 257205 (2003).

[91] D. Mannix, Y. Tanaka, D. Carbone, N. Bernhoeft, and S. Kunii. *Phys. Rev. Lett.* **95**, 117206 (2005).

[92] T. Nagao and J. ichi Igarashi. *Phys. Rev. B* **74**, 104404 (2006).

[93] "www.esrf.fr/usersandscience/experiments/xasms/id20,".

[94] M. Blume and D. Gibbs. *Phys. Rev. B* **37**, 1779 (1988).

[95] H. Kleykamp and S. G. Kang. *Z. Metallkd* **82**, 544 (1991).

[96] L. Vegard. *Z. Phys.* **5**, 17 (1921).

[97] D. Fort. *Rev. Sci. Instrum* **68**, 3504 (1997).

[98] B. D. Josephson. *Physics Letters* **1**, 251 (1962).

[99] "http://www.qdusa.com/products/ppms.html,".

[100] J. S. Hwang, K. J. Lin, and C. Tien. *Rev. Sci. Instrum.* **68**, 94 (1997).

[101] P. Javorský, F. Wastin, E. Colineau, J. Rebizant, P. Boulet, and G. Stewart. *J. Nucl. Mat.* **344**, 50 (2005).

[102] N. W. Ashcroft and N. D. Mermin, *Solid State Physics*, ch. 23, 458. Harcourt College Publishers, 1976.

[103] M. D. Le, K. A. McEwen, M. Rotter, A. Barcza, M. Doerr, J. Brooks, E. Jobiliong, and D. Fort, "Magnetostriction of UPd_3 up to 33 T," in *Proceedings 36ièmes Journées des Actinides*, 2006.

[104] J. G. Conway. *J. Chem. Phys* **31**, 1002 (1959).

[105] H. C. Walker, K. A. McEwen, D. F. McMorrow, S. B. Wilkins, F. Wastin, E. Colineau, and D. Fort. *Phys. Rev. Lett.* **97**, 137203 (2006).

[106] K. A. McEwen, H. C. Walker, M. D. Le, D. F. McMorrow, E. Colineau, F. Wastin, S. B. Wilkins, J.-G. Park, R. I. Bewley, and D. Fort. *J. Magn. Magn. Mater.* (to be published).

[107] J. A. Bearden and A. F. Burr. *Rev. Mod. Phys.* **39**, 125 (1967).

[108] K. A. McEwen private communication.

[109] A. Martin-Martin, *Magnetism in uranium intermetallic compounds.* PhD thesis, University College London, 2000.

[110] K. Kuzushita, K. Ishii, S. B. Wilkins, B. Janousova, T. Inami, K. Ohwada, M. Tsubota, Y. Murakami, K. Kaneko, N. Metoki, S. Ikeda, Y. Haga, Y. Ōnuki, N. Bernhoeft, and G. H. Lander. *Phys. Rev. B* **73**, 104431 (2006).

[111] Y. Tokunaga, R. E. Walstedt, S. Kambe, H. Kato, H. Sakai, E. Yamamoto, Y. Haga, and Y. Ōnuki. *J. Magn. Magn. Mater.* **272-276**, E49 (2004).

[112] K. Ikushima, S. Tsutsui, Y. Haga, H. Yasuoka, R. E. Walstedt, N. M. Masaki, A. Nakamura, S. Nasu, and Y. Ōnuki. *Phys. Rev. B* **63**, 104404 (2001).

[113] H. C. Walker, K. McEwen, P. Boulet, E. Colineau, and F. Wastin. *Physica B* **359-361**, 1156 (2005).

[114] T. W. Roberts, S. W. Zochowski, F. Tasset, and K. A. McEwen. *Physica B* **267-268**, 243 (1999).

[115] K. A. McEwen and W. Stirling. *J. Phys. C* **14**, 157 (1981).

[116] H. Yamauchi, H. Onodera, K. Ohoyama, T. Onimaru, M. Kosaka, M. Ohashi, and Y. Yamaguchi. *J. Phys. Soc. Jpn* **68**, 2057 (1999).

[117] J. M. Fournier, *Structure and Bonding*, vol. 59/60, pp. 127 196. Berlin: Springer-Verlag, 1985.

[118] J. Kondo. *Prog. Theor. Phys.* **32**, 37 (1964).

[119] S. Blundell, *Magnetism in Condensed Matter.* Oxford, 2001.

[120] M. C. Aronson, J. D. Thompson, J. L. Smith, Z. Fisk, and M. W. McElfresh. *Phys. Rev. Lett.* **63**, 2311 (1989).

[121] F. Wastin, E. Bednarczyk, J. Rebizant, S. Zwirner, and G. H. Lander. *J. Alloys Comp.* **262-263**, 124 (1997).

[122] J. S. Schilling. *Phys. Rev. B* **33**, 1667 (1986).

[123] N. H. Andersen, *Crystalline Electric Field and Structural Effects in f-electron Systems*, 373. New York: Plenum, 1980.

[124] K. Kadowaki and S. B. Woods. *Solid State Comm.* **58**, 507 (1986).

[125] S. Y. Li, L. Taillefer, D. G. Hawthorn, M. A. Tanatar, J. Paglione, M. Sutherland, R. W. Hill, C. H. Wang, and X. H. Chen. *Phys. Rev. Lett.* **93**, 56401 (2004).

[126] S. Nakamae, K. Behnia, N. Mangkorntong, M. Nohara, H. Takagi, S. J. C. Yates, and N. E. Hussey. *Phys. Rev. B* **68**, 100502(R) (2003).

[127] J. Spałek, A. Datta, and J. M. Honig. *Phys. Rev. Lett.* **59**, 728 (1987).

[128] S. Nakatsuji, D. Hall, L. Balicas, Z. Fisk, K. Sugahara, M. Yoshioka, and Y. Maeno. *Phys. Rev. Lett.* **90**, 137202 (2003).

[129] C. Urano, M. Nohara, S. Kondo, F. Sakai, T. S. H. Takagi and, and T. Okubo. *Phys. Rev. Lett.* **85**, 1052 (2000).

[130] H. C. Walker, K. McEwen, P. Boulet, E. Colineau, and F. Wastin. *Physica B* **378-380**, 981 (2006).

Appendix A

Fourier Analysis and Correlation Functions

A.1 Introduction

Fourier Transforms decompose a spatially varying function into its different sinusoidally varying frequency components and in scattering theory transfer between direct and reciprocal space. The Fourier transform of a function $f(x)$ is defined as

$$\tilde{f}(q) = \frac{1}{\sqrt{2\pi}} \int_{-\infty}^{\infty} f(x) \exp(-\imath q x)\, \mathrm{d}x. \tag{A.1.1}$$

The inverse Fourier transform converts the function $\tilde{f}(q)$ back into the spatially varying function:

$$f(x) = \frac{1}{\sqrt{2\pi}} \int_{-\infty}^{\infty} \tilde{f}(q) \exp(\imath q x)\, \mathrm{d}q. \tag{A.1.2}$$

An important feature of Fourier transforms is the way they transform convoluted functions. The convolution of a function $f(x)$ with the function $g(x)$

is defined as

$$h(z) = \int_{-\infty}^{\infty} f(x)g(z-x)\,\mathrm{d}x. \tag{A.1.3}$$

The Fourier transform $\tilde{h}(q)$ of the convolution is given by:

$$\begin{aligned} \tilde{h}(q) &= \frac{1}{\sqrt{2\pi}} \int_{-\infty}^{\infty} \mathrm{d}z\, e^{-\imath qz} \left\{ \int_{-\infty}^{\infty} f(x)g(z-x)\,\mathrm{d}x \right\} \\ &= \frac{1}{\sqrt{2\pi}} \int_{-\infty}^{\infty} f(x)e^{-\imath qx}\,\mathrm{d}x \int_{-\infty}^{\infty} g(u)e^{-\imath qu}\,\mathrm{d}u \\ &= \sqrt{2\pi}\tilde{f}(q)\tilde{g}(q), \end{aligned} \tag{A.1.4}$$

i.e. the product of the separate Fourier transforms multiplied by $\sqrt{2\pi}$. This result is significant since a crystal lattice in direct space can be modelled as a periodic array of atoms represented by Dirac delta functions convolved with the charge density at each atom. The convolution theorem states therefore that the Fourier transform of the system will be the product of the Fourier transform of the periodic lattice and the Fourier transform of the charge density of a single atom.

A.2 Correlation Functions

A.2.1 Introduction

In an ideal system, in the ordered state the magnetic moments in a linear chain would all be perfectly aligned with respect to one another, with an infinite degree of correlation. However, in a real system there will be a degree of disorder such that the magnetic moments vary slightly in orientation. The probability that a moment situated at x will be in the same orientation as one at the origin is described by the correlation function. In this section the Fourier transforms of several direct space correlation functions are derived.

A.2.2 Lorentzian

One of the simplest models assumes that the correlation at a point x decays exponentially from an initial value, A at the origin, defining a correlation function $C(x)$ as

$$C_L(x) = A\exp(-\kappa|x|), \tag{A.2.5}$$

i.e. the correlation decreases by a factor of e in a length $x = 1/\kappa$. Since the function is even, the Fourier transform can be evaluated using the cosine transform:

$$\begin{aligned} \tilde{C}_L(q) &= \frac{2A}{\sqrt{2\pi}} \int_0^\infty \exp(-\kappa x)\cos(qx)\,\mathrm{d}x \\ &= \frac{2A}{\sqrt{2\pi}} \Re\left\{ \int_0^\infty e^{-(\kappa - \imath q)x}\,\mathrm{d}x \right\} \\ &= \frac{2A}{\sqrt{2\pi}} \Re\left\{ \frac{\kappa + \imath q}{\kappa^2 + q^2} \right\} = \sqrt{\frac{2}{\pi}} \frac{A\kappa}{\kappa^2 + q^2}. \end{aligned} \tag{A.2.6}$$

This is the equation for a lorentzian centred at $q = 0$ with height $H = \sqrt{2/\pi}A/\kappa$ and a half width half maximum equal to κ. Therefore if there is a high degree of correlation in real space, such that κ is small, the transform in reciprocal space will be very narrow, see Figure A.1 for the real space correlation function and its Fourier transform for different values of κ. It also means that by measuring the width of the diffraction peak in reciprocal space the degree of correlation in real space can be determined.

The integrated area (I) of a lorentzian is given by

$$I = \pi\kappa H \propto \kappa \cdot \frac{1}{\kappa}, \tag{A.2.7}$$

and is therefore independent of the inverse correlation length κ. Thus the integrated area of the diffraction peak gives the amplitude of scattering with infinite correlation.

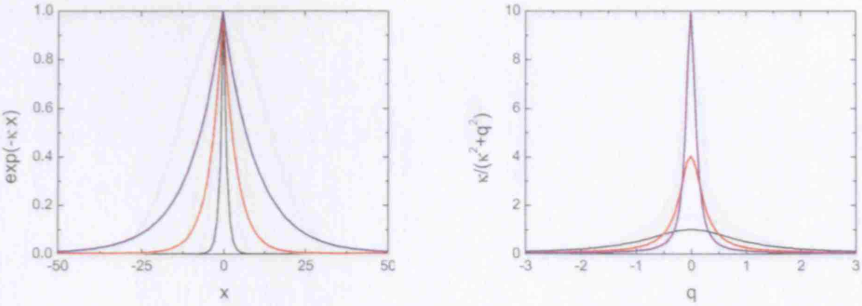

Figure A.1: The correlation function $\mathcal{C}_L(x) = \exp(-\kappa|x|)$ (left) and its Fourier transform $\tilde{\mathcal{C}}_L(q) = \frac{\kappa}{\kappa^2+q^2}$ (right) for $\kappa = 1$ (black), 0.25 (red) and 0.1 (blue).

A.2.3 Gaussian

Here the properties of a Gaussian correlation function:

$$\mathcal{C}_G(x) = a \exp\left[-\frac{x^2}{2\sigma^2}\right], \tag{A.2.8}$$

where σ is the standard deviation of the distribution, are derived as above. By completing the square and using standard integrals the Fourier transform can be shown to be

$$\tilde{\mathcal{C}}_G(q) = A\sigma \exp\left[-\frac{\sigma^2 q^2}{2}\right], \tag{A.2.9}$$

another Gaussian function.

Figure A.2 shows the direct space Gaussian function $\mathcal{C}_G(x)$ (left) and the Fourier transform $\tilde{\mathcal{C}}_G(q)$ (right) for $\sigma = 1$, 2 and 5. Again the integrated area is independent of the real space standard deviation.

A.2.4 Lorentzian Squared

The correlation function in section A.2.2 is quite unphysical since the back to back exponential functions lead to a singularity at $x = 0$. A modified correlation function which falls off more slowly with the spatial variable and

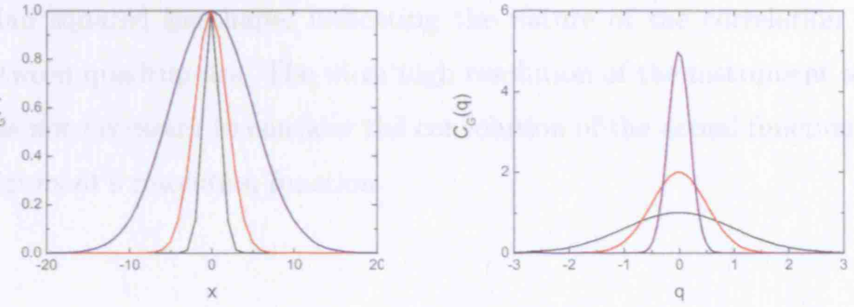

Figure A.2: The correlation function $\mathcal{C}_G(x) = \exp(-x^2/2\sigma^2)$ (left) and its Fourier transform $\tilde{\mathcal{C}}_G(q) = \sigma \exp(-\sigma^2 q^2/2)$ (right) for $\sigma = 1$ (black), 2 (red) and 5 (blue).

which smooths the singularity is given by

$$\mathcal{C}(x) = A(1 + \kappa|x|)\exp(-\kappa|x|). \tag{A.2.10}$$

The computed Fourier transform of this function is

$$\tilde{\mathcal{C}}(q) \propto \frac{A\kappa^3}{(\kappa^2 + q^2)^2}, \tag{A.2.11}$$

which describes a Lorentzian squared peak shape. Figure A.3 shows the direct space correlation function and the Fourier transform for different values of the inverse correlation length.

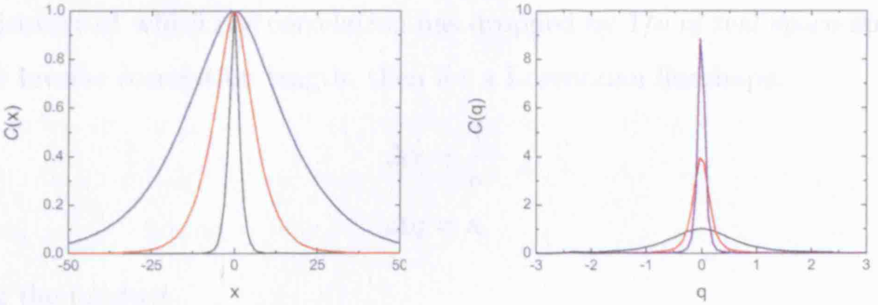

Figure A.3: The correlation function $\mathcal{C}(x) = (1 + \kappa|x|)\exp(-\kappa|x|)$ (left) and its Fourier transform $\tilde{\mathcal{C}}(q) = \kappa^3/(\kappa^2 + q^2)^2$ (right) for $\kappa = 1$ (black), 0.25 (red) and 0.1 (blue).

The lineshape of the quadrupolar order superlattice diffraction peaks measured as a function of theta, as in chapter 5.2, are fitted best using the lorentzian squared lineshape, indicating the nature of the correlation function between quadrupoles. The ultra high resolution of the instrument means that it is not necessary to consider the convolution of the actual function with the instrument's resolution function.

A.3 Correlation Lengths

Fitting one of the above peak shapes to a peak in reciprocal space from a scattering experiment gives the inverse correlation length κ, which is equal to the half width at half maximum. In real space the correlation length is defined as the distance over which the degree of correlation has decreased by a factor of 1/e. Using Fourier transforms it is possible to derive the relationship between the two correlation lengths.

A.3.1 Lorentzian

The relationship is simplest for a Lorentzian peak shape. If we define Δx as the distance at which the correlation has dropped by 1/e in real space and Δq as the inverse correlation length, then for a Lorentzian lineshape:

$$\begin{aligned} \Delta x &= \frac{1}{\kappa} \\ \Delta q &= \kappa, \end{aligned}$$

giving the product

$$\Delta x \Delta q = 1. \tag{A.3.12}$$

A.3.2 Gaussian

Using equations (A.2.8) and (A.2.9) Δx and Δq are given by

$$\Delta x = \sigma\sqrt{2}$$
$$\Delta q = \frac{\sqrt{2\ln 2}}{\sigma},$$

such that the product is $2\sqrt{\ln 2}$.

A.3.3 Lorentzian Squared

Δx for the function $C(x) = A(1 + \kappa|x|)\exp(-\kappa|x|)$ can be calculated numerically to be

$$\Delta x = \frac{2.14619}{\kappa},$$

while Δq can be solved analytically:

$$\Delta q = \kappa\sqrt{\sqrt{2} - 1}.$$

Therefore the product of the two is

$$\Delta x \Delta q = 1.38128, \qquad (A.3.13)$$

which gives the numerical factor required when converting between the inverse correlation length, identified from fitting the reciprocal space peak shape, and the real space correlation length.

Appendix B

Azimuthal dependence calculations

B.1 Quadrupolar tensor construction

The quadrupolar tensor is calculated by considering ellipsoids on the four quasi-cubic uranium sites at (000), ($\frac{1}{2}\frac{1}{2}0$), (000), and ($\frac{1}{2}\frac{1}{2}\frac{1}{2}$) and is given by

$$C^{\alpha\beta} = \sum_{\mathbf{r}_i} \exp(i\mathbf{Q}\cdot\mathbf{r}_j)C_j^{\alpha\beta} \tag{B.1.1}$$

If the major axis is c_l, and the minor axis is c_s then for $Q_{\mathrm{x}^2-\mathrm{y}^2}$ order in the cubic different structure the individual second rank tensors are given by:

$$C_1, C_4 = \begin{pmatrix} c_l & 0 & 0 \\ 0 & c_s & 0 \\ 0 & 0 & c_s \end{pmatrix} \text{ and } C_2, C_3 = \begin{pmatrix} c_s & 0 & 0 \\ 0 & c_l & 0 \\ 0 & 0 & c_s \end{pmatrix}$$

Therefore for the (103) quadrupolar superlattice reflection the scattering tensor used in azimuthal calculations is given by

$$\begin{aligned} C &= C_1 + C_2 \exp(i\pi) + C_3 \exp(3i\pi) + C_4 \exp(4i\pi) \\ &= C_1 - C_2 - C_3 + C_4 \\ &= \begin{pmatrix} 2(c_l - c_s) & 0 & 0 \\ 0 & 2(c_s - c_l) & 0 \\ 0 & 0 & 0 \end{pmatrix} \end{aligned} \tag{B.1.2}$$

To calculate the scattering tensor for combinations of other order parameters which tilt the ellipsoids off axis, $3D$ rotation matrices are applied to each individual site tensor before combining them according to equation (B.1.1).

B.2 Azimuthal calculations

Given below are the details of the Matlab program used to calculate the azimuthal scattering dependence in UPd_3, based on a program written by Stuart Wilkins, one of the beamline scientists on ID20 at the ESRF. The "runscript.m" program calls the function "fitazimuth", which is given below the program, for a specific choice of order parameter described by the tensor C, scattering vector, q, energy and reference vector from which the azimuthal angle, psi, is measured, and then calculates the intensity for the different polarization channels as a function of psi.

```
% script to use the fitazimuth function for choice of q, az_ref,
% energy and quadrupolar tensor

q = [1 0 3]
```

```
lattice = [sqrt(3).*5.77 5.77 9.66]
energy = 3.73;
az_ref = [0 -1 0];
psi = -180:1:180;

C = [1 0 0; 0 -1 0; 0 0 0]  % tensor for Q_x^2-y^2

sp = [];
ss = [];
pp = [];
ps = [];

for mypsi=(psi.*pi./180);
sp = [ sp; fitazimuth(C,energy,q,az_ref,lattice,[1 0],[0 1],mypsi)];
ss = [ ss; fitazimuth(C,energy,q,az_ref,lattice,[1 0],[1 0],mypsi)];
pp = [ pp; fitazimuth(C,energy,q,az_ref,lattice,[0 1],[0 1],mypsi)];
ps = [ ps; fitazimuth(C,energy,q,az_ref,lattice,[0 1],[1 0],mypsi)];
end

Sp = sp.*conj(sp); % mod squared to get intensity
Ss = ss.*conj(ss);
Pp = pp.*conj(pp);
Ps = ps.*conj(ps);

figure
plot(psi',Sp,'r');
hold on
plot(psi',Ss,'b');
```

```
legend('\sigma - > \pi','\sigma - > \sigma');
ylabel('Intensity','Fontsize',14);
xlabel('\psi [degrees]','Fontsize',14);
title('(103) Q_x^2-y^2','Fontsize',14);

figure
plot(psi',Pp,'r');
hold on
plot(psi',Ps,'b');
legend('\pi - > \pi','\pi - > \sigma');
ylabel('Intensity','Fontsize',14);
xlabel('\psi [degrees]','Fontsize',14);
title('(103) Q_x^2-y^2','Fontsize',14);
```

The "fitazimuth" function sets up the basis vectors for the reference frame to define the polarization vectors for a given value of the azimuthal angle.

```
function out = fit_azimuth (tensor, energy, q, azref, lattice, ein,
eout, phi)

% Convert to reciprocal space using inverse lattice parameters

d_hkl = 1./sqrt((q(1)./lattice(1)).^2 + (q(2)./lattice(2)).^2 ...
+ (q(3)./lattice(3)).^2);
theta = asin(12.39842./(2*d_hkl*energy));

qprime = (2.*pi./lattice).*q; az_refprime = (2.*pi./lattice).*azref;
```

```
% Define a set of crystal basis vectors on q and the azimuth
% reference vector c1,c2,c3


c3 = -1.*qprime;
c2 = cross(c3,az_refprime);
c1 = cross(c2,c3);


c3 = c3./vecmag(c3);
c2 = c2./vecmag(c2);
c1 = c1./vecmag(c1);
% getting unit vectors by dividing through by modulus


% Now do an azimuth rotation about the c3 vector to the u
% vectors from Blume and Gibbs



u3 = c3;
u2 = (sin(phi).*c1) + (cos(phi).*c2);
u1 = (cos(phi).*c1) - (sin(phi).*c2);


% Now define a 2 element matrix for the incident and exit
% polarisation.  For sigma polarisation in both cases this is just
% eps_sigma = u2.  For pi polarisation there is a dependence on
% theta bragg.
% First make a set of unit basis vectors


eps_in = (ein(1).*u2) + ein(2).*((sin(theta).*u1) - ...
```

```
(cos(theta).*u3));
eps_out = (eout(1).*u2) + eout(2).*((-cos(theta).*u3) - ...
(sin(theta).*u1));


out = eps_out * tensor * eps_in';
```

Figures B.1- B.5 show the plots for the calculated azimuthal dependence of the scattering dependence for the different allowed quadrupolar order parameters using the above program.

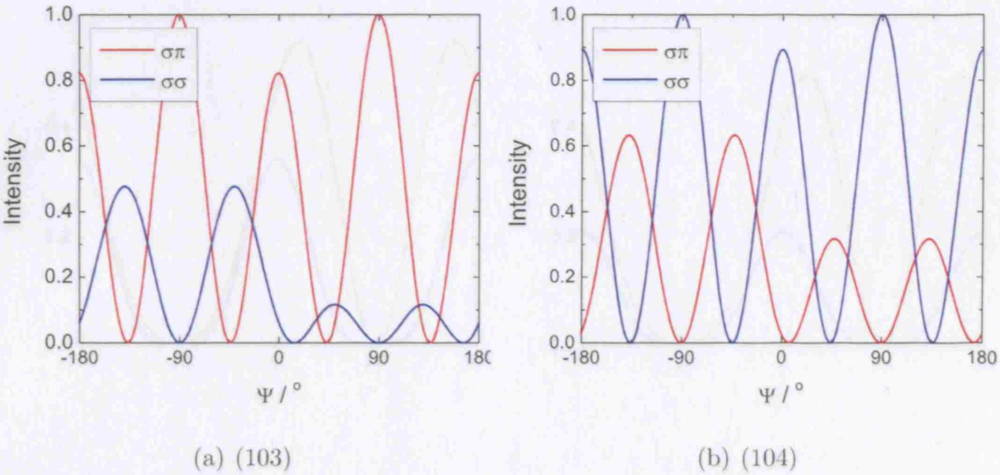

(a) (103) (b) (104)

Figure B.1: Calculated azimuthal dependence of scattering from superlattice reflections in UPd$_3$ for $Q_{x^2-y^2}$ order.

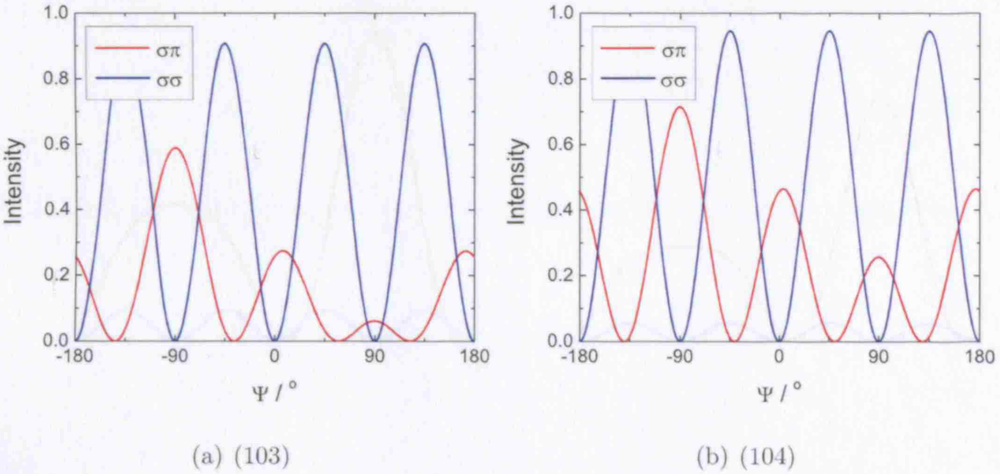

(a) (103) (b) (104)

Figure B.2: Calculated azimuthal dependence of scattering from superlattice reflections in UPd$_3$ for Q_{xy} order.

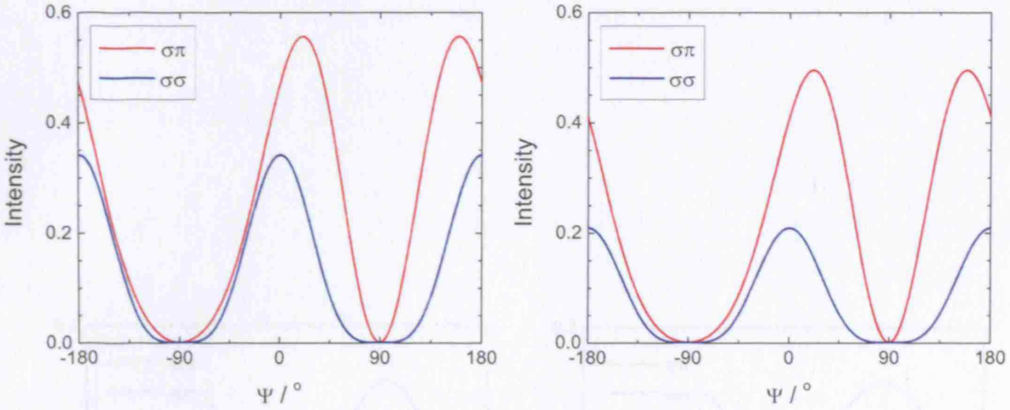

(a) (103) (b) (104)

Figure B.3: Calculated azimuthal dependence of scattering from superlattice reflections in UPd_3 for Q_{zx} order.

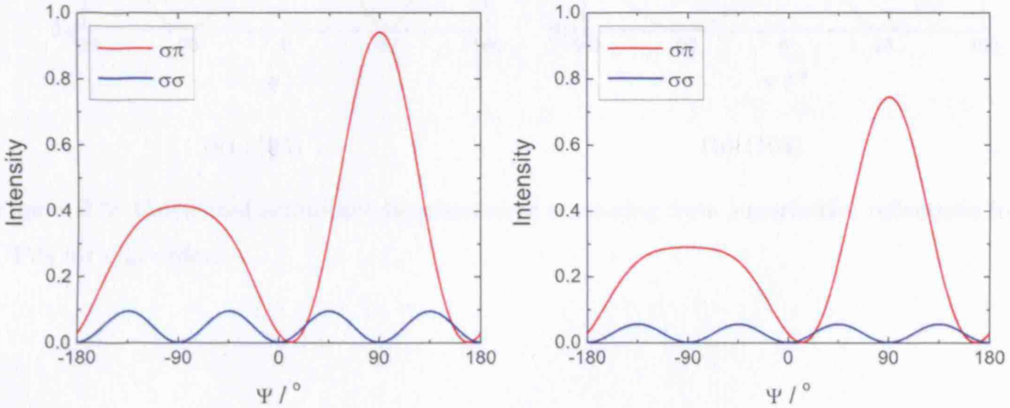

(a) (103) (b) (104)

Figure B.4: Calculated azimuthal dependence of scattering from superlattice reflections in UPd_3 for Q_{yz} order.

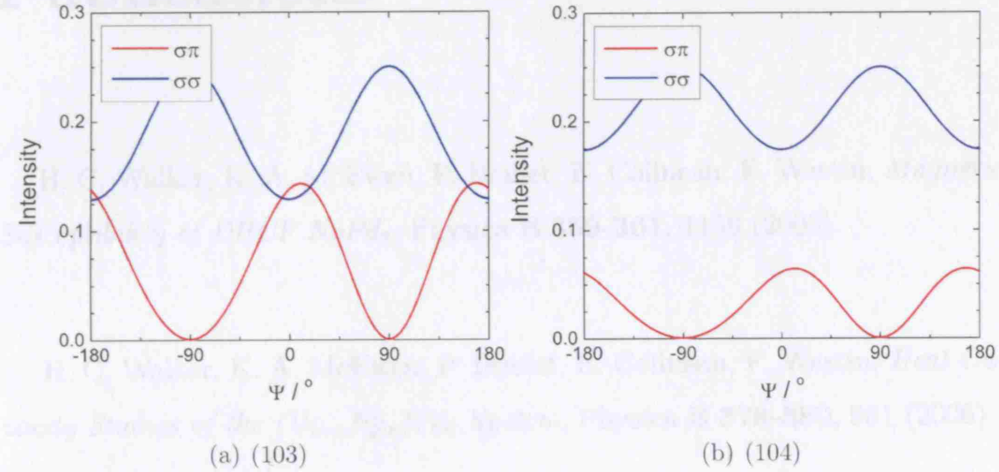

(a) (103)

(b) (104)

Figure B.5: Calculated azimuthal dependence of scattering from superlattice reflections in UPd$_3$ for Q_{zz} order.

Appendix C

Publications

H. C. Walker, K. A. McEwen, P. Boulet, E. Colineau, F. Wastin, *Magnetic Susceptibility of DHCP* $NpPd_3$, Physica B **359-361**, 1156 (2005).

H. C. Walker, K. A. McEwen, P. Boulet, E. Colineau, F. Wastin, *Heat Capacity Studies of the* $(U_{1-x}Np_x)Pd_3$ *System*, Physica B **378-380**, 981 (2006)

K. A. McEwen, H. C. Walker, P. Boulet, E. Colineau, F. Wastin, S. B. Wilkins, D. Fort, *Quadrupolar and Magnetic Ordering in* $(U,Np)Pd_3$, J. Phys. Soc. Jpn. **75** Suppl, 20 (2006)

H. C. Walker, K. A. McEwen, D. F. McMorrow, S. B. Wilkins, F. Wastin, E. Colineau, D. Fort, *Determination of the antiferroquadrupolar order parameters in* UPd_3, Phys. Rev. Lett. **97**, 137203 (2006)

H. C. Walker, K. A. McEwen, D. T. Adroja, J.-G. Park, Y. S. Kwon, J.-

Y. So, W. Kockelmann, M. Meissner, *Inelastic Neutron Scattering and Heat Capacity Studies of Ferromagnetic* $PrInNi_4$, Physica B **385-386, Part 1**, 41 (2006)

H. C. Walker, K. A. McEwen, E. Colineau, J.-C. Griveau, F. Wastin, *A New Route to Quantum Criticality in* $(U,Np)Pd_3$, to be published in J. Magn. Magn. Mater.

K. A. McEwen, H. C. Walker, M. D. Le, D. F. McMorrow, E. Colineau, F. Wastin, S. B. Wilkins, J.-G. Park, R. I. Bewley, D. Fort, *Understanding the quadrupolar structures of* UPd_3, to be published in J. Magn. Magn. Mater.

D. T. Adroja, J.-G. Park, K.-H. Jang, H. C. Walker, K. A. McEwen, T. Takabatake, *Study of Non-Fermi Liquid Behaviour near the Ferromagnetic Quantum Critical Point in* $CePd_{0.15}Rh_{0.85}$, to be published in J. Magn. Magn. Mater.

D. T. Adroja J. -G. Park, E. A. Goremychkin, K. A. McEwen, N. Takeda, B. D. Rainford, K. S. Knight, J. W. Taylor, Jeongmi Park, H. C. Walker, R. Osborn, *Observation of two spin gap energies in the filled skutterudite compound* $CeOs_4Sb_{12}$, Phys. Rev. B **75**, 014418 (2007)